



Expedition UT-GOM2-2

Site H

Terrebonne Basin (Walker Ridge Block 313)
WR313 H002 (API 608124014800) and WR313 H003 (API 608124014900)
30 July–28 September 2023

Expedition UT-GOM2-2 Scientists

Publisher's notes

This work was supported by the U.S. Department of Energy (DOE), National Energy Technology Laboratory (NETL), under Contract No. DE-FE00223919.

This work was the result of scientific collaboration between the following institutions The University of Texas at Austin (UT), DOE, NETL, the United States Geological Survey (USGS), the Bureau of Ocean Energy Management (BOEM), The Ohio State University, Columbia University, University of New Hampshire, Oregon State University, University of Washington, Tufts University, Colorado School of Mines, and Geotek Ltd.

Disclaimer

This report was prepared as an account of work sponsored by the U.S. Department of Energy. The U.S. Department of Energy, nor any of their employees, makes any warranty, express or implied, or assumes any legal liability or responsibility for the accuracy, completeness, or usefulness of any information, apparatus, product, or process disclosed, or represents that its use would not infringe privately owned rights. Reference herein to any specific commercial product, process, or service by trade name, trademark, manufacturer, or otherwise does not necessarily constitute or imply its endorsement, recommendation, or favoring by the U.S. Department of Energy or any agency thereof. The views and opinions of authors expressed herein do not necessarily state or reflect those of the U.S. Department of Energy or any agency thereof. This report has been peer reviewed and approved for publication consistent with United States Geological Survey (USGS) Fundamental Science Practices (<https://pubs.usgs.gov/circ/1367/>).

Authorship and citation

Peter B. Flemings, Carla Thomas, Stephen C. Phillips, Timothy S. Collett, Ann E. Cook, Evan Solomon, Frederick S. Colwell, Joel E. Johnson, David Awwiller, Irita Aylward, Athma R. Bhandari, Donald Brooks, Jessica Z. Buser-Young, Alejandro Cardona, Michael A. Casso, Rachel Coyte, Tom Darrah, Marcy Davis, Brandon Dugan, Dan Duncan, John T. Germaine, Melanie Holland, Jesse Houghton, Saffron Martin, N. Tanner Mills, Michael Mimitz, Daniel Minarich, Yuki Morono, Zachary Murphy, Joshua O'Connell, Ethan Petrou, Tom Pettigrew, John W. Pohlman, Alexey Portnov, Marcie Purkey Phillips, Thomas Redd, Derek E. Sawyer, Peter Schultheiss, Kelly Shannon, Camille Sullivan, Cathal Small, Kayla Tozier, Man-Yin Tsang, Camila Van Der Maal, William F. Waite, Taylor Walton, 2025, Expedition UT-GOM2-2 Site H. In Flemings et. al., Proceedings of the UT-GOM2-2 Deepwater Hydrate Coring Expedition, University of Texas Institute for Geophysics, <https://doi.org/10.5281/zenodo.13971276>.

Copies of these proceedings can be found on OSTI.gov ([Search for UT-GOM2-2 | OSTI.GOV](#)), Zenodo.org ([Search Terrebonne Basin Deepwater Hydrate Coring](#)), and the UT-GOM2-2 website ([UT-GOM2-2: Deepwater Hydrate Coring Expedition - UT Institute for Geophysics](#)).

Cover photos

Left: University of Texas at Austin professor and expedition chief scientist Peter B. Flemings ready to lead the day's activities. Photo Credit: Jackson School of Geosciences

Right: The Helix Q4000 deepwater well intervention vessel and the 290-foot *Harvey Hermes* supply boat, carrying UT-GOM2-2 labs, pipe, fluids, and equipment, during a rendezvous on site. Photo credit: Peter B. Flemings

Table of contents

Publisher's notes	2
Disclaimer	2
Authorship and citation	2
Cover Photos	2
Table of contents	3
List of figures	5
List of tables	7
List of equations	8
Note	8
Introduction	9
Operations	10
Operational summary WR313 Site H	10
Surface location	15
Water depth and rig floor elevation	15
Borehole deviation survey	15
True vertical depth below seafloor	15
Projection of Hole H001 to Site H measured depth	17
Drilling fluids	18
Drilling challenges	19
Plug and abandonment	23
Coring	27
Overview	27
Pressure coring	34
PCTB performance	35
Conventional coring	41
Lithostratigraphy	45
Lithologic units	45

<u>Detailed sedimentology from visual core description</u>	55
<u>Sediment composition from smear slides</u>	57
<u>Environment of deposition</u>	58
<u>Lithostratigraphy post-expedition analysis plan</u>	60
Calcareous nannofossil biostratigraphy	62
<u>0-296.4 mbsf (Hole H003)</u>	62
<u>644.6 to 859.6 mbsf (Hole H002)</u>	63
<u>Biostratigraphy post-expedition analysis plan</u>	66
Physical properties	67
<u>Thermal conductivity</u>	67
<u>In-situ temperature / thermal gradient</u>	69
<u>Pressure coring logging and imaging</u>	74
<u>Conventionalized whole core logging</u>	75
<u>Conventional whole core logging and imaging</u>	75
<u>Split core logging and imaging</u>	79
<u>Undrained shear strength</u>	82
<u>Index properties</u>	85
<u>Dissolved gas concentrations and hydrate saturation</u>	95
Microbiology	101
<u>Curation of microbiology samples</u>	106
<u>Extraction and amplification of DNA</u>	106
<u>Microbiology post-expedition analysis plan</u>	109
Geochemistry	110
<u>Pore water geochemistry</u>	100
<u>Gas geochemistry</u>	119
<u>Sedimentary geochemistry</u>	123
Appendices	131
References	132

List of figures

Figure F1: Measured depth of the bit as a function of time	11
Figure F2: Bathymetry map of Walker Ridge Block 313	16
Figure F3: The locations, distances, and azimuths of the boreholes at Site H.....	16
Figure F4: Sketch of Hole H003 deviation	18
Figure F5: Cross plot of events in Hole H003 vs Hole H001	18
Figure F6: Demonstration of the projection of Hole H001 to Hole H003	20
Figure F7: Examples of particle size distribution of sands encountered	23
Figure F8: Images of the sandy seafloor	24
Figure F9: Visual core description (VCD) of the grain size at the top of Site H.....	25
Figure F10: Plug and abandonment schematic for Hole H003	25
Figure F11: Plug and abandonment schematic for Hole H002	26
Figure F12: Core deployments and temperature measurements.....	28
Figure F13: Expanded view of the core deployments and temperature measurements.....	29
Figure F14: Expanded view of core deployments at the Red sand in Hole H003	30
Figure F15: Core deployments in Hole H002.....	31
Figure F16: Expanded view of the core deployments from above and in the Upper Blue sand.....	32
Figure F17: Expanded view of the core deployments in and below the Orange sand	33
Figure F18: Depth of pressure core sealing.....	38
Figure F19: Examples of rig data from two G-APC deployments	42
Figure F20: Examples of G-APC cores with damage	44
Figure F21: Photos of G-APC coring during UT-GOM2-2.....	44
Figure F22: Interpreted Site H lithologic units and lithofacies	46
Figure F23: Ternary plots of sediment grain size and composition.....	47
Figure F24: Lithostratigraphy examples of Lithologic Unit II.....	49
Figure F25: Comparison of Hole H001 LWD data with Hole H003 core data	50
Figure F26: Representative interval of Lithostratigraphic Unit IV.....	51
Figure F27: Expanded view of Lithologic Unit IV	52
Figure F28: Expanded view of Lithologic Unit IV	53

<u>Figure F29:</u> View of Lithologic Units V, VI and VII	54
<u>Figure F30:</u> Expanded view of Lithologic Unit VI	56
<u>Figure F31:</u> Example smear slide photomicrographs	58
<u>Figure F32:</u> H003 and H002 downhole smear slide results	60
<u>Figure F33:</u> Biostratigraphy plate under polarized light	64
<u>Figure F34:</u> Composite time-depth plot of calcareous nannofossil biohorizons	65
<u>Figure F35:</u> Thermal conductivity with compressed measured depth.....	68
<u>Figure F36:</u> Temperature record for each Advanced Piston Corer Temperature Tool (APCT-3) deployment	71
<u>Figure F37:</u> Interpreted in-situ temperatures from seafloor to 150 mbsf.....	72
<u>Figure F38:</u> Temperatures with true vertical depth	72
<u>Figure F39:</u> Image from a remote operating vehicle showing the Temperature Dual Pressure Penetrometer	73
<u>Figure F40:</u> Temperature Dual Pressure Penetrometer (T2P) and rig data during T2P water column test	74
<u>Figure F41:</u> Example pressure core log for Core H003-08CS	76
<u>Figure F42:</u> Conventionalized core magnetic susceptibility	77
<u>Figure F43:</u> Example conventional core log for Core H003-01H.....	78
<u>Figure F44:</u> Downcore trends in MSCL-S measured conventional core properties.....	79
<u>Figure F45:</u> Color spectrophotometry results.....	80
<u>Figure F46:</u> Point magnetic susceptibility from split cores	81
<u>Figure F47:</u> Major and minor elements as measured by X-ray fluorescence on split cores	83
<u>Figure F48:</u> Trace elements as measured by X-ray fluorescence on split cores.....	84
<u>Figure F49:</u> Undrained shear strength measurements.....	85
<u>Figure F50:</u> Ternary diagrams of particle size distribution using different measurements and classifications	86
<u>Figure F51:</u> Sand, silt and clay fractions with depth	87
<u>Figure F52:</u> Cumulative laser particle size distributions for Hole H003.....	89
<u>Figure F53:</u> Cumulative laser particle size distributions from Hole H002	90
<u>Figure F54:</u> Cumulative hydrometer particle size distributions	91
<u>Figure F55:</u> Measured moisture and density properties	92
<u>Figure F56:</u> Expanded view of the measured moisture and density properties.....	93
<u>Figure F57:</u> Comparison of the (A) wet (bulk) density	94

Figure F58: Cross plot of the water content measurements	94
Figure F59: Cross plot of porosity.....	95
Figure F60: Magnetic susceptibility with compressed measured depth	96
Figure F61: Dissolve methane and hydrate saturation with compressed measured depth.....	99
Figure F62: Total volume of methane produced from a pressure core	100
Figure F63: Geochemistry summary	111
Figure F64: Expanded view of the Geochemistry Summary 0-300 mbsf.....	112
Figure F65: Uncorrected salinity and alkalinity with depth	118
Figure F66: Composition of headspace gas samples	120
Figure F67: Constituent ratios from headspace gas samples	120
Figure F68: Composition of void gas samples	121
Figure F69: Composition of pressure core gas samples.....	122
Figure F70: Composition of void, pressure core, and hydrate gas samples.....	122
Figure F71: Carbon isotopes of methane ($\delta^{13}\text{C}$) and molecular ratios.....	124
Figure F72: $\delta^{13}\text{C}$ isotopic ratio of methane and molecular ratios 0-1601 mbsf.....	125
Figure F73: $\delta^{13}\text{C}$ isotopic ratio of methane and molecular ratios 280-300 mbsf	126
Figure F74: $\delta^{13}\text{C}$ isotopic ratio of methane and molecular ratios 674-678 mbsf	127
Figure F75: $\delta^{13}\text{C}$ isotopic ratio of methane and molecular ratios 800-820 mbsf	128
Figure F76: Initial CHNS element analysis results	129
Figure F77: Initial Total Sulfur (TS) vs Total Organic Carbon (TOC)	131

List of Tables

Table T1: Final surface and bottom-hole locations and water depth	16
Table T2: Hole H003 and H002 borehole deviation surveys.....	17
Table T3: Comparison of Hole H001 logging while drilling (LWD) to Hole H003 lithofacies transitions.....	19
Table T4: Seismic horizons and stratigraphic surface depths	21
Table T5: Three incidents where tools became stuck inside the bottom hole assembly	22
Table T6: Summary of pressure coring deployments.....	34
Table T7: Summary of operational parameters for all pressure coring deployments	36
Table T8: Pressure coring tool performance	37

Table T9: Hole H003 Conventional G-APC and G-XCB cores.....	43
Table T10: Lithofacies classification at Site H.....	48
Table T11: UT-GOM2-2 Split core sample post-expedition work	61
Table T12: Calcareous nannofossil biohorizons	66
Table T13: Thermal conductivity measurements	69
Table T14: Summary for all Advance Piston Corer Temperature Tool (APCT-3) deployments	70
Table T15: Interpreted in-situ temperature for Site H	72
Table T16: Quantitative degassing results for pressure cores.....	97
Table T17: Interpreted methane concentration and hydrate saturation.....	98
Table T18: Investigator and analysis for each microbiology whole-round subsample	102
Table T19: Types and collection dates of microbiology control samples.....	107
Table T20: Extracted DNA.....	108
Table T21: Routine whole-round pore water sample results	113
Table T22: Organic whole-round pore water sample results	115
Table T23: Seawater drilling fluid sample results.....	116
Table T24: Water -based mud drilling fluid sample results	116
Table T25: PCATS fluid sample results	117
Table T26: Sediment geochemistry results.....	130

List of equations

Equation E1. Used to calculate of true vertical depth below seafloor for Hole H003.....	16
Equation E2. Used to correlate Hole H003 measured depth with H001 measured depth.....	17
Equation E3. Used to correlate Holes H001 and H002 depths below the seafloor	17

Note

These results are summarized in Expedition UT-GOM2-2 Summary (Flemings et al., [2025a](#)). Methods are described in Expedition UT-GOM2-2 Methods (Flemings et al., [2025b](#)). Lists of all acronyms, abbreviations, symbols, units, conversion factors, and sample codes used in these proceedings are also provided in Methods (Flemings et al., [2025b](#)).



The sun rises on another day on location at Walker Ridge Block 313 during the drilling of Hole H002. The *Harvey Spirit* has arrived to provide additional support. Photo credit: Peter B. Flemings

Introduction

In the summer and fall of 2023, The University of Texas Deepwater Hydrate Coring Expedition (UT-GOM2-2) drilled, cored, collected downhole measurements, and analyzed samples from the seafloor to the base of the gas hydrate stability zone at Site H in Walker Ridge Block 313 (Site H, WR313) in the deepwater Terrebonne basin, Gulf of America (Gulf of Mexico), herein “the Gulf”.

A summary of the scientific motivation and the geological overview of Site H are provided in the UT-GOM2-2 Summary (Flemings et al., [2025a](#)). UT-GOM2-2 drilled and cored two boreholes at Site H WR313. Site H was originally drilled (Hole H001) using logging while drilling (LWD) during the 2009 Gas Hydrates Joint Industry Project Leg II (JIP II) (Boswell et al., [2012a](#); Boswell et al., [2012b](#); Frye et al., [2012](#); Hutchinson et al., [2008](#); Shedd et al., [2010](#)).

This report describes the operations, samples obtained, and initial analyses for Site H. Analyses include results from Hole UT-GOM2-2-WR313-H002 (Hole H002) and Hole UT-GOM2-2-WR313-H003 (Hole H003). Analyses include results for pressure coring, conventional coring, lithostratigraphy and biostratigraphy, physical properties, geochemical analysis, and gas hydrate saturation.



The sun sets on the Gulf of America (Gulf of Mexico) as *Harvey Spirit* makes its way back to Port Fourchon with UT-GOM2-2 chilled laboratories carrying samples and core. Photo credit: Geotek Ltd.

Operations

Operational summary WR313 Site H

A graphical presentation of all operations at Site H is shown in Figure [F1](#). Operations in support of the drilling and coring started with moving the Helix *Q4000* deepwater well intervention vessel (*Q4000*) over the planned position of Hole H003 and conducting dynamic positioning surveys for the vessel (See [Surface location](#)). The Pressure Coring Tool with Ball Valve in the Cutting Shoe configuration (PCTB-CS) bottom hole assembly (BHA) and drill pipe were run into the ocean to a depth of 2,029 ft RKB by 2400 hr on 02 August 2023. The *Q4000* Remotely Operated Vehicles (ROVs) were also deployed to conduct a systematic search for the surface location of Hole H001 that was previously drilled in the Walker Ridge Block 313 during the 2009 Joint Industry Project Leg II (JIP II) (Collett et al., [2009](#)). The seafloor search for Hole H001 was unsuccessful and the decision was made to mark the seafloor location for the proposed Hole H002 and Hole H003 based on the coordinates as proposed in the expedition Operations Plan (Flemings et al., [2023](#)).

After running the PCTB-CS BHA to a depth of 6,365 ft RKB in the water column, the Probe Deployment Tool (PDT) with the Temperature Dual Pressure Penetrometer (T2P) was deployed in the drill pipe for testing.

Hole H003 was drilled first. Operations for each borehole are reported in Hole H003 and Hole H002 below. More details can be found in Appendix A: UT-GOM2-02 post-drill operation report and daily log (executed activities, drilling and coring statistics, and an event drilling-log), and Appendix B: Daily science reports.

Hole H003

The PTCB-CS BHA was lowered until the coring bit tagged the seafloor mud line at a depth of 6,506 ft RKB (water depth of 6,454 ft, rig height of 52 ft, See [Water depth and rig floor elevation](#)). Core H003-01H was acquired at

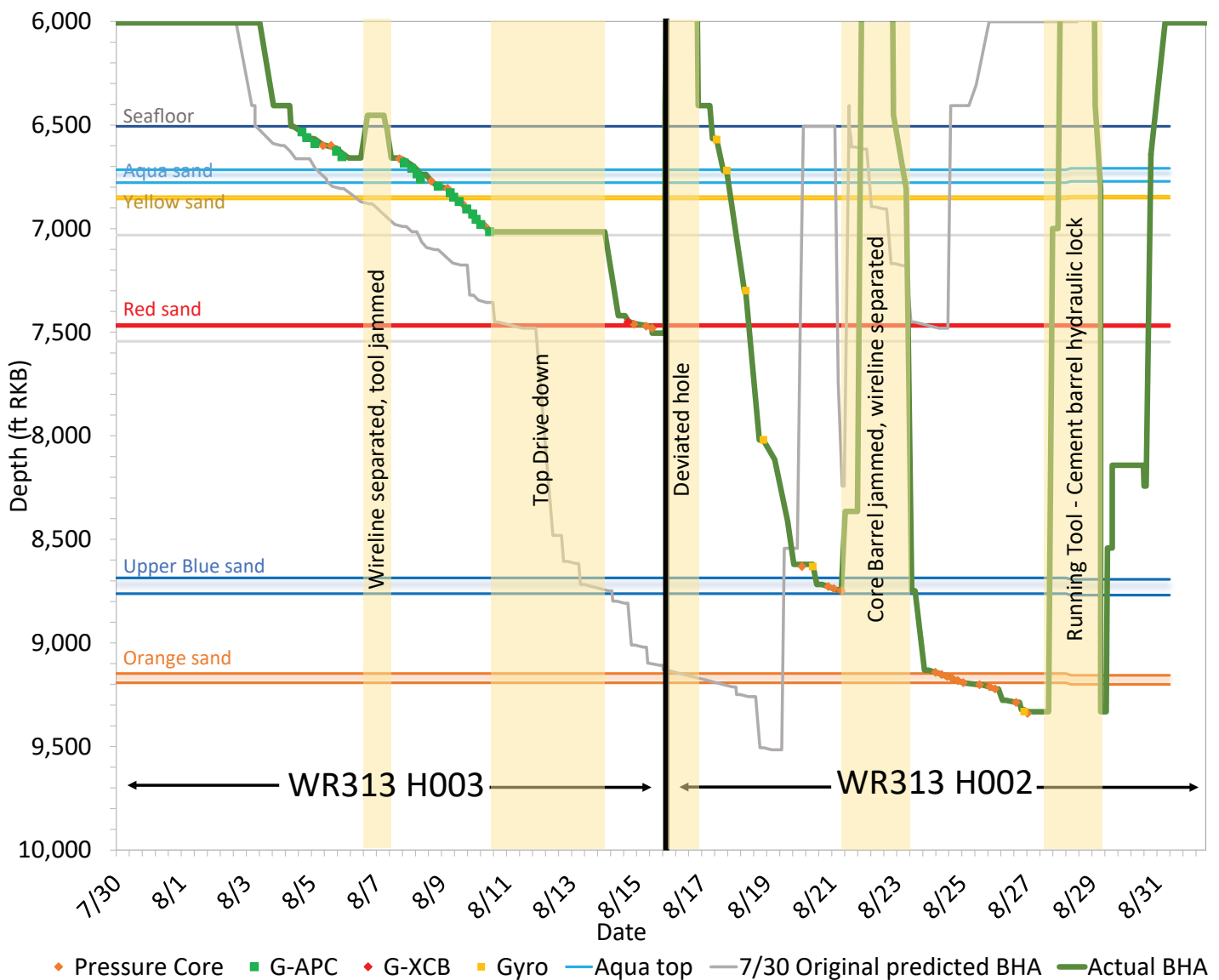


Figure F1: Measured depth of the bit as a function of time at Walker Ridge Block 313 (WR313) for Hole H002 and Hole H003. The original operational plan is shown as a light gray line. The measured depth of the bit is shown as a green line. On top of the green line, stops are shown for pressure coring as orange dots, conventional coring as green squares and red diamonds, and gyroscopic measurements as dark yellow squares. Operational downtime is shown as transparent yellow columns. Projected sands from Hole H001 (Table T4) are shown as aqua blue, yellow, red, blue, and orange horizontal lines. Dataset: <https://doi.org/10.5281/zenodo.14680104>

0800 hr on 04 August 2023 using the Geotek Advanced Piston Corer (G-APC). Eventually, three successive G-APC cores were acquired and sampled at a high resolution (Core H003-01H to H003-03H). A standard set of whole-round time-sensitive core subsamples were collected from each core section. Undrained strength was monitored along each G-APC core as it was sectioned.

On 05 August 2023, the first pressure core was acquired: Core H003-04CS. This core was recovered at atmospheric pressure. Because of this, the decision

was made to acquire an additional PCTB-CS core immediately below Core H003-04CS. Core H003-05CS was recovered at an internal pressure of 3,475 psi. This pressure was close to the pressure boost setting. The hole was then advanced to a depth of 6,659 ft RKB (46.6 mbsf) with the acquisition of two G-APC cores (Cores H003-06H to H003-07H). Temperature measurements were also acquired using the Advance Piston Corer Temperature Tool (APCT-3) during the coring of Cores H003-03H, H003-06H, and H003-07H. Undrained strength was monitored along each G-APC core.

On the morning of 06 August 2023, while preparing to core H003-08CS, the wireline separated under tension while deploying the PCTB-CS using the PCTB running tool. After recovering and attaching the separated wireline to a fishing tool, the fishing tool assembly was run into the hole to recover the lost PCTB-CS running tool. After recovering the PCTB-CS running tool from the hole, an emergency pulling tool was run into the hole and successfully latched to the PCTB-CS core barrel. After numerous attempts, however, the PCTB-CS could not be removed from the BHA. It was interpreted that the PCTB-CS was packed-off in the BHA with mud and sand (See [Drilling challenges](#)). The decision was made to pull the BHA out of the hole; however, after the BHA cleared the seafloor, it was determined that the mud/sand had cleared, and the PCTB-CS core barrel was no longer stuck. The PCTB-CS core barrel was recovered to the vessel by wireline. On the morning of 07 August 2023, the *Q4000* was moved back into position over Hole H003 and Hole H003 was re-entered at the mudline. After tripping the PCTB-CS BHA to the bottom of the hole at 6,659 ft RKB (46.6 mbsf), Core H003-08CS was acquired at an internal pressure of 2,075 psi. The hole was next advanced to a total depth of 6,715 ft RKB (63.7 mbsf) with the acquisition of two G-APC cores (H003-09H and H003-10H). APCT-3 temperature measurements were also acquired with Cores H003-09H and H003-10H. Undrained strength was monitored.

Operations on 08 August 2023 included advancing Hole H003 to a total depth of 6,806 ft RKB (91.4 mbsf) through the recovery of three G-APC and two PCTB-CS cores. The three G-APC cores (H003-11H, H003-12H, and H003-14H) were recovered without any problems. APCT-3 temperature measurements were also acquired with Cores H003-12H and H003-14H. The first pressure core acquired from this section was Core H003-13CS. This core was recovered at an internal pressure of 3,531 psi. The next acquired pressure core, Core H003-15CS, failed to seal.

On 09 August 2023, Hole H003 was advanced to a total depth of 6,930 ft RKB (129.2 mbsf) through five deployments of the G-APC and the recovery of one

PCTB-CS core. The conventional cores H003-16H to H003-18H H003-20H, and H003-21H were processed in the core receiving lab using standard UT-GOM2-2 core processing techniques (See Methods: Conventional core processing (Flemings et al., [2025b](#))). APTC-3 temperature measurements were also acquired while coring Core H003-17H and H003-21H. Core H003-019CS was recovered at an internal pressure of 3042 psi.

Operations on 10 August 2023 included advancing Hole H003 to a depth of 7,015 ft RKB (155.1 mbsf) with the deployment and recovery of three G-APC cores (H003-22H, H003-23H, and H003-25H) and one PCTB-CS core (H003-24CS). The first evidence of significant challenges associated with the G-APC coring operations was observed in Core H003-022H, where the core contained numerous gas voids and a partially collapsed core liner. Core H003-23H and H003-25H were also expansive in nature with numerous gas voids. Core H003-025H also exhibited evidence of possible inflow of sediment into the core barrel. The core liner was damaged and proved to be very difficult to remove from the inner core barrel. The decision was made to switch from the G-APC to the G-XCB coring systems to further advance the conventional coring operations in Hole H003. APCT-3 temperature measurements were also acquired with Core H003-25H. Within this sequence, an additional PCTB-CS pressure core (H003-24CS) was acquired without problems and was sealed at an internal pressure of 3,091 psi.

After the recovery of Core H003-25H on 10 August 2023, it was discovered that the Top Drive System (TDS) was showing a “high temperature alarm” for the drill motor. It was determined that the TDS blower motor (cooling fan motor) had electrically grounded. The blower motor was removed from the TDS and transported by supply vessel to shore for repairs. After further inspection of the damaged *Q4000* TDS blower motor at the Houma Armature Works, it was determined that the motor could not be repaired. The new replacement blower motor was delivered to the *Q4000* and installed in the TDS by 1930hr on 13 August 2023. It was decided to advance the hole from its

current depth of 7,015 ft RKB (155.1 mbsf) by drilling (without coring) to a core point depth of 7,420 ft RKB (278.6 mbsf), thought to be just above the Red sand.

On 14 August 2023, the first G-XCB core (H003-26X) of the UT-GOM2-2 Expedition was acquired over the core depth interval from 7,420 to 7,448 ft RKB (278.6 to 287.1 mbsf), with a total recovery of 27.9 ft of core (or 100% recovery). Also, on 14 August 2023 and into 15 August 2023, three additional PCTB-CS pressure cores were acquired. Core H003-27CS was recovered at an internal pressure of 3,091 psi, Core H003-28CS was recovered at an internal pressure of 3,478 psi, and Core H003-29CS was recovered at an internal pressure of 3,480 psi.

After advancing the hole from 7,480 to 7,505 ft RKB (296.9 to 304.55 mbsf) by drilling (no coring) and conducting a borehole directional survey, it was determined that the borehole was inclined by 7.75° at an azimuth of 124.38° (See [Borehole deviation survey](#)). BSEE considers any borehole with an inclination of more than 3° to be deviated, which requires additional approvals and the acquisition of more frequent directional surveys (every 500 ft). Because of concerns associated with targeting the deeper critical “Orange sand” interval, the decision was made at 2000 hr on 15 August 2023 to terminate operations in Hole H003 and move over and drill/core Hole H002. After receiving approval from the BSEE Houma District office, the crew of the *Helix Q4000* moved ahead to abandon Hole H003 by pumping into the hole 115 bbls of 11.0 ppg water-based mud (WBM), followed by 110 bbls of 8.6 ppg seawater (See [Plug and abandonment](#)). The PCTB-CS BHA was recovered to the *Q4000* at 0900 hr on 16 August 2023, marking the end of Hole H003 and the start of Hole H002.

The *Q4000* ROVs continuously monitored the borehole for any evidence of water or gas flow during operations in Hole H003. After the hole was completed, the ROV performed an “as left” seafloor survey.

Hole H002

Operations in support of the drilling and coring

Hole H002 started with running the PCTB in the Face Bit configuration (PCTB-FB) BHA to just above the seafloor. The *Helix Q4000* used dynamic positioning to move over the planned position of Hole H002. This was completed by 0600 on 17 August 2023.

Hole H002 was spudded at 0600 hr on 17 August 2023 at a depth of 6,506 ft RKB (water depth of 6,454 ft, rig height of 52 ft, See Water depth and rig floor elevation). Hole H002 was then advanced throughout the remainder of the day to a depth of 6,923 ft RKB (127.1 mbsf). Because of the borehole deviation concerns associated with the Hole H003, the spud-in program and initial “top-hole” drilling phase of Hole H002 featured the use of controlled drilling parameters designed to reduce borehole deviations. These measures included maintaining a slow rate of penetration and a low circulation rate. In addition, two directional surveys were conducted in the shallow section of Hole H002. The first survey was at the seafloor and the second at 6,714 ft RKB (63.4 mbsf). These surveys yielded measured borehole inclinations of 0.24° and 0.82° at an azimuth of 110°, respectively (See [Borehole deviation survey](#)). Next, Hole H002 was advanced by drilling (no coring) on 18 August 2023 from 6,923 to 7,852 ft RKB (127.1-410.2 mbsf). An additional directional survey was conducted at a depth of 7,666 ft RKB (353.6 mbsf), which yielded a measured inclination of only 0.35° at an azimuth of 96.79°. This was well within the directional drilling tolerances planned for the hole.

Operations on 19 August 2023 included advancing Hole H002 to a total depth of 8,620 ft RKB (644.3 mbsf) by drilling (no coring) and slowly switching from drilling with seawater to 10.5 ppg water-based mud (See Drilling fluids). By 0210 hr on 20 August 2023, core H002-01FB was recovered without pressure. Next, an additional directional survey was conducted at a depth of 8,577 ft RKB (631.2 mbsf), which yielded a measured inclination of only 0.60° at an azimuth of 99.31° (See [Borehole deviation survey](#)). Hole H002 was then advanced by drilling (no coring) to the next PCTB-FB core point at 8,718 ft RKB (674.2 mbsf). Core H002-02FB was recovered at 4,543 psi. By 0100 hr on 21 August 2023, Core H002-03FB was recovered

at a pressure of 4,530 psi. After coring Core H002-04FB and making multiple attempts to unlatch the PCTB-FB from the BHA, the wireline separated under tension at the packer in the TDS. It was decided that the PCTB-FB could not be removed from the BHA. The pipe and PCTB-FB BHA were pulled from the hole and recovered to the *Q4000* by 1200 hr on 22 August 2023. Upon recovery of the BHA, it was determined that a piece of the wireline was stuck in the PCTB latch collet, preventing the PCTB from unlatching from the BHA. Core H002-04FB did not maintain pressure.

By 2400 hr on 22 August 2023, the PCTB-FB BHA was replaced with the PCTB-CS BHA and the BHA was run to just above the seafloor at 6,506 ft RKB. From 0000-0600 hr on 23 August 2023, the *Q4000* crew conducted operations in support of re-entering Hole H002, which allowed the PCTB-CS BHA to be advanced to the previous total depth of the hole at 8,748 ft RKB (683.3 mbsf). The hole was then advanced by drilling (no coring) to a depth of 9,132 ft RKB (800.4 mbsf), which was the core point for the first PCTB-CS core associated with the Orange sand continuous pressure coring campaign.

On 24 August 2023, Hole H002 was advanced from a depth of 9,132 to 9,192 ft RKB (800.4 to 818.7 mbsf) with the acquisition and recovery of the first six of an attempted nine PCTB-CS pressure cores targeting the Orange sand and bounding mud. The first two cores (Core H002-05CS and H002-06CS) were interpreted to be mud-rich and located above the Orange sand. In addition, both Cores H002-05CS and H002-06CS were recovered at near in situ pressure at 4,566 to 3,784 psi, respectively. Core H002-07CS was recovered at a pressure of 4,503 psi and may have cored a sediment contact between a mud-dominated and hydrate-bearing sedimentary section. Core H002-08CS was recovered at an internal pressure of 4,503 psi. Core H002-09CS failed to maintain pressure. However, it did yield important sedimentologic data (mostly silt to mud-rich sediment core) that helped to direct the ongoing coring program. By 0055 hr on 25 August 2023, Core H002-10CS had been recovered to the *Q4000* at a measured pressure of 2,777 psi. Three additional PCTB-CS pressure cores were recovered on

25 August 2023 from the Orange sand and associated mud-rich sedimentary section (Cores H002-11CS to H002-13CS). Core H002-11CS was recovered at a pressure of 4,708 psi. Cores H002-12CS and H002-13CS were recovered without pressure and processed as conventional core. Core H002-13CS was the ninth and final core within the Orange sand pressure coring campaign.

On 26 August 2023, Hole H002 was advanced by drilling (no coring) to the next core point at 9,277 ft RKB (844.6 mbsf) by 2400 hr and the PCTB-CS was run into the hole. In response to the failure of the PCTB-CS to seal pressure with the last two runs, Cores H002-14CS and H002-15CS were deployed with boost pressure settings increased to 5,200 and 5,500 psi, respectively. Cores H002-14CS and H002-15CS both failed to hold pressure. Coring operations in Hole H002 ended at 0548 hr on 27 August 2023 with the recovery and processing of Core H002-15CS from the depth interval from 9,322 to 9,332 ft RKB (858.3-861.3 mbsf), which also marked the total depth of Hole H002. An additional directional survey was also conducted at depth of 9,268 ft RKB (841.8 mbsf), which recorded a borehole inclination at 0.47° at an azimuth of 78.33° (See [Borehole deviation survey](#)).

While preparing to place the regulatory-required cement plug in Hole H002, a BHA cement liner was lowered to the BHA with the PCTB running tool. The cement liner became stuck in the BHA, and the *Q4000* lost the ability to circulate drilling fluids through the BHA. After making several attempts to pull the cement liner from the BHA, the decision was made to cut the wireline connected to the cement liner at the surface and slip/cut wireline while tripping the BHA back to near the seafloor. After cutting the wireline, several attempts were again made to try and pull the cement liner from the BHA before tripping was started. These additional attempts to pull the liner free also failed. After several more failed attempts to pull the liner free at about 3,000 ft RKB, the BHA was pulled back to the *Q4000*. Upon the recovery of the BHA to the vessel, it was discovered that the running tool was stuck inside the BHA drill collars and that a great deal of barite drilling mud sediment was packed off around the

running tool.

By 2230 hr on 28 August 2023, a new standard cementing BHA had been run to the seafloor where, because of extensive planning by the UT Drilling Staff and the *Q4000* operational crew, the BHA entered the seafloor without problems and was run into the hole at 6,918 ft RKB (125.6 mbsf) by midnight. After running the cementing BHA to a depth of 9,332 ft RKB (861.3 mbsf) the cementing program was started (See [Plug and abandonment](#)). By 0640 hr on 29 August 2023, 105 bbls of 11.5 ppg high-viscosity pad mud was spotted in the hole from 9,332 to 8,548 ft RKB (861.3 to 622.4 mbsf) followed by 209 bbls of 10.5 ppg spacer. Next, the *Q4000* crew pulled the BHA back to 8,548 ft RKB (622.4 mbsf) and pumped 71 bbls (369 sacks) of 16.4 ppg Class H Cement, followed by 8.7 bbls of spacer, and 5 bbls of seawater. Cement was in place at 1400 hr and the 24-hour “wait on cement” period was started. At 1415 hr on 30 August 2023, the cementing BHA was run into the hole to a depth of 8,105 ft RKB (487.4 mbsf) and tagged the top of the cement plug with 15,000 lbs of bit weight. Next, the cementing BHA was pulled from the seafloor to a depth of 6,352 ft RKB by 1730 hr. The vessel was placed on demobilization status at 2400 hr on 30 August 2023. The coring BHA cleared the rig floor on the *Q4000* by 0400 hr on 31 August 2023. The backloading of coring equipment and laboratory containers, along with the transfer of all Geotek crew and remaining shipboard scientists, to the *Harvey Hermes* supply boat was completed. The *Q4000* was located over the location of Hole H002 until moving 1-mile off location at the 2400 hr on 1 September 2023; thus, ending demobilization operations and the UT-GOM2-2 Expedition.

Surface location

The surface locations of Hole H002 and Hole H003 are shown in Table [T1](#) and Figures [F2](#) and [F3](#) as surveyed by Fugro U.S.A. Marine Inc (Fugro). Fugro provided its own positioning system and precisely located the position of the vessel over the proposed hole locations. The ROV was then maneuvered directly beneath the vessel using the *Q4000* navigation system. Buoys were then placed at the borehole

locations. Before each borehole was spudded, the respective buoys were moved to allow the BHA to spud the borehole at the precise location of the buoy. See also Methods: Determining hole locations (Flemings et al., [2025b](#)).

Hole H002 is located 65 ft (19.8 m) SSW and Hole H003 is located 66 ft (20.12 m) NNE of the original WR313-H001 (Hole H001) hole, as drilled during JIP II (Collett et al., [2012](#)) (Figure [F3](#)).

Water depth and rig floor elevation

As described in Operational summary WR313 Site H and shown in Table [T1](#), in Hole H003, the coring bit touched the seafloor mud line at a measured depth of 6,506 ft RKB on 04 August 2023 (Table [T1](#)). The rig floor elevation above sea level was 52 feet, and therefore the water depth was 6,454 ft.

In Hole H002, the bit also touched the seafloor mud line at a measured depth of 6,506 ft RKB on 17 August 2023. The rig floor elevation above sea level was 52 feet. Thus, the Hole H002 water depth was 6,454 ft.

Borehole deviation survey

One deviation survey was conducted in Hole H003 after the hole was advanced to a depth of 7,505 ft RKB (304.5 mbsf) (Table [T2](#)). The survey was conducted from inside the drill pipe, above the BHA. One measurement was made near the mudline at 6,600 ft RKB (28.6 mbsf) and one near the BHA at 7,451 ft RKB (288.0 mbsf). The borehole was found to trend ESE with inclination increasing from 6.06 degrees near the mudline to 7.75 degrees near the bottom of the borehole. The significant deviation of the borehole drove the decision to terminate drilling operations in Hole H003 and permanently abandon the borehole.

Four deviation surveys were conducted in Hole H002 throughout the drilling and coring of the hole (Table [T2](#)). The surveys were conducted from inside the drill pipe above the BHA. Deviation was consistently less than 1 degree.

True vertical depth below seafloor

For Hole H003, we assumed a constant Hole H003

Borehole	API No.	Top-Hole Location		Bottom-Hole Location		Top-Hole Depth		
		Latitude	Longitude	Latitude	Longitude	Pipe Length to Seafloor	Sea Surface	Water depth
		(NAD27)	(NAD27)	(NAD27 N)	(NAD27 W)	(ft RKB)	(ft RKB)	(ft)
H001	608124004000	26° 39' 44.85"	-91° 40' 33.75"	26° 39' 44.99"	-91° 40' 33.17"	6502	51	6451
H002	608124014800	26° 39' 44.22"	-91° 40' 33.90"	26° 39' 44.18"	-91° 40' 33.63"	6506	52	6454
H003	608124014900	26° 39' 45.45"	-91° 40' 33.59"	26° 39' 44.84"	-91° 40' 32.61"	6506	52	6454

Table T1: Final surface and bottom-hole locations and water depth at the time of drilling Walker Ridge Block 313 (WR313) Holes H001, H002, and H003. Hole H001 was drilled during the 2009 Joint Industry Project Leg II (JIP II) logging-while-drilling (LWD) program. Holes H002 and H003 were drilled during this expedition. H002 and H003 top-hole locations are as surveyed by Fugro on 02 August 2023. Hole H002 and H003 bottom-hole locations are from Gyrodata, as surveyed on 14 August 2023 and 26 August 2023, respectively (Table T2). Hole H001 top and bottom-hole locations are from BSEE (2024). NAD27 = North America Datum of 1927.

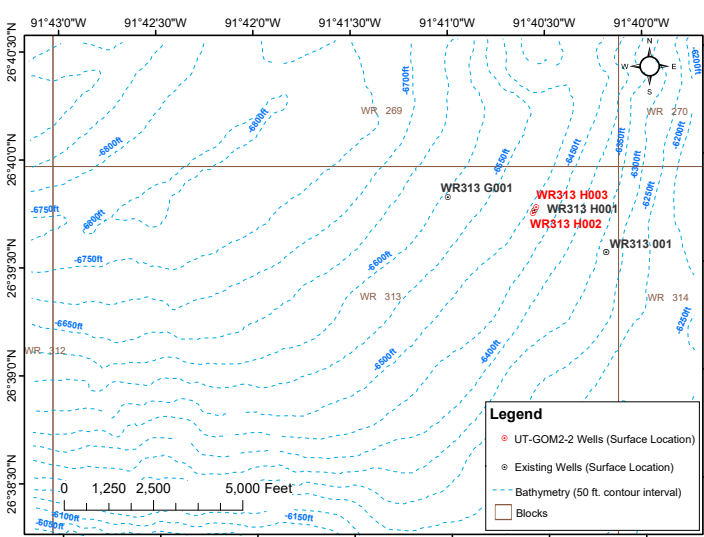


Figure F2: Bathymetry map of Walker Ridge Block 313 (WR313) study area showing the surface locations of previously drilled holes (black circles) and UT-GOM2-2 holes (red circles). Coordinate System: NAD 1927 UTM Zone 15N.

inclination of 7 degrees (See [Borehole deviation survey](#)) to calculate the Hole H003 vertical depth below the seafloor (True Vertical Depth from the Hole H003 measured depth below the seafloor (Equation E1).

$$\text{Hole H003 True Vertical Depth} = 7^{\circ} * \text{Hole H003 Depth (mbsf)}$$

Equation E1.

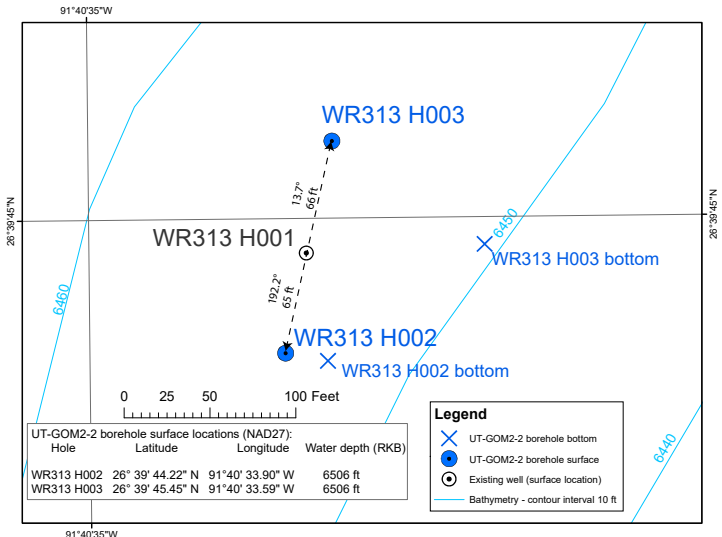


Figure F3: The locations, distances, and azimuths of the boreholes at Site H. Hole H001 location coordinates are from BSEE (2024). The locations of Hole H002 and Hole H003 as surveyed by Fugro (top-hole) and Gyrodata (bottom-hole) during UT-GOM2-2 (Table T2). Bathymetry was derived from the seafloor reflector in three-dimensional seismic data. WR313 = Walker Ridge Block 313; NAD27 = North America Datum of 1927.

The seafloor at the top of Hole H003 is 5 feet lower than the seafloor vertically above the bottom of Hole H003. This was not considered in the calculation. The true vertical depth in Hole H002 is the measured depth since Hole H002 was vertical.

(A)	(B)	(C)	(D)	(E)	(F)	(G)		(H)	
BOREHOLE	DEPTH	INCL	AZIMUTH	DOGLEG SEVERITY	VERTICAL DEPTH	CLOSURE		HORIZONTAL COORDINATES	
	ft RKB	deg.	deg.	deg./100 ft	ft RKB	Dist. (ft)	Az. (deg.)	Y (ft)	X (ft)
WR313 H003	6600	6.06	123.32	6.45	6599.82	4.97	123.32	-2.73	4.15
	7451	7.75	124.38	0.2	7444.63	107.23	123.89	-59.79	89.02
WR313 H002	6667	0.82	110.19	0.51	6666.99	1.15	110.19	-0.4	1.08
	7667	0.35	96.79	0.05	7666.94	11.31	106.57	-3.23	10.84
	8577	0.6	99.24	0.03	8576.91	18.83	103.27	-4.32	18.32
	9268	0.47	78.33	0.03	9267.88	25.04	99.95	-4.33	24.67

Table T2: Hole H003 and H002 borehole deviation surveys performed at Walker Ridge Block 313 (WR313) by Gyrodata. A) Borehole; B) Measured depth of the gyroscope in feet below the rig floor (ft RKB); C) through H) Gyroscopic survey results taken inside the 9-7/8" drill pipe; Both measurements in Hole H003 were taken during the same deployment of the gyroscope at the end of Hole H003 drilling on 15 August 2023. All measurements shown for Hole H002 were taken during the same deployment of the gyroscope at the end of Hole H002 drilling on 26 August 2023; C) Inclination (INCL); F) Calculated vertical depth of the gyroscope assuming the drill pipe is vertical (0-degree inclination) from the RKB to the seafloor (6,506 ft RKB). Dataset: <http://doi.org/10.5281/zenodo.14680104>.

Projection of Hole H001 to Site H measured depth

Projection of Hole H001 to Hole H003 measured depth

We projected Hole H001 Logging While Drilling (LWD) measured depths to Hole H003 measured depth as illustrated in Figure F4. Three factors impact the projection of depths in Hole H001 LWD data to equivalent stratigraphic depths in Hole H003. First, to what extent was the drill pipe within the water column longer than the vertical depth between the rig floor and the top of the hole at the sea floor? This could be due to bending of the pipe, or the ship's positioning. Second, what was the effect of the Hole H003 deviation below the seafloor. Third, what was the impact of the stratigraphy rising, relative to the seafloor, between the vertical Hole H001 and deviated Hole H003?

Table T3 lists five events in Hole H003 that we could correlate directly to the H001 LWD data. We cross plotted the "Compressed Depth Adjusted for Voids and Fall-in" of each event in Hole H003 against their equivalent measured depth in Hole H001 (Figure F5). We found that stratigraphic surfaces in Hole H003 measured depth below sea floor, H003 MDBSF, could

be correlated from H001 measured depth below sea floor, H001 MDBSF, with Equation E2:

$$H003 \text{ MDSBF} = (C * H001 \text{ MDSBF}) + B$$

Equation E2.

Equation E2 states that to project stratigraphic surfaces from Hole H001 to equivalent stratigraphic levels onto Hole H003 a static shift (B), and a depth-dependent correction (C) must be applied. By regression, we determined C = 0.988 and B = 3.32 m. Figure F6 illustrates the improvement in correlation obtained.

Projection of Hole H001 to Hole H002 measured depth

Both Hole H002 and Hole H001 were essentially vertical. Furthermore, they were located along strike with each other with the intention that stratigraphic surfaces would be at the same depth in the two boreholes. Thus, stratigraphic surfaces in Holes H001 and H002 are assumed to exist at equivalent depths below the seafloor with Equation E3:

$$Hole \ H002 \ Depth \ mbsf = \\ Hole \ H001 \ Depth \ (mbsf)$$

Equation E3.

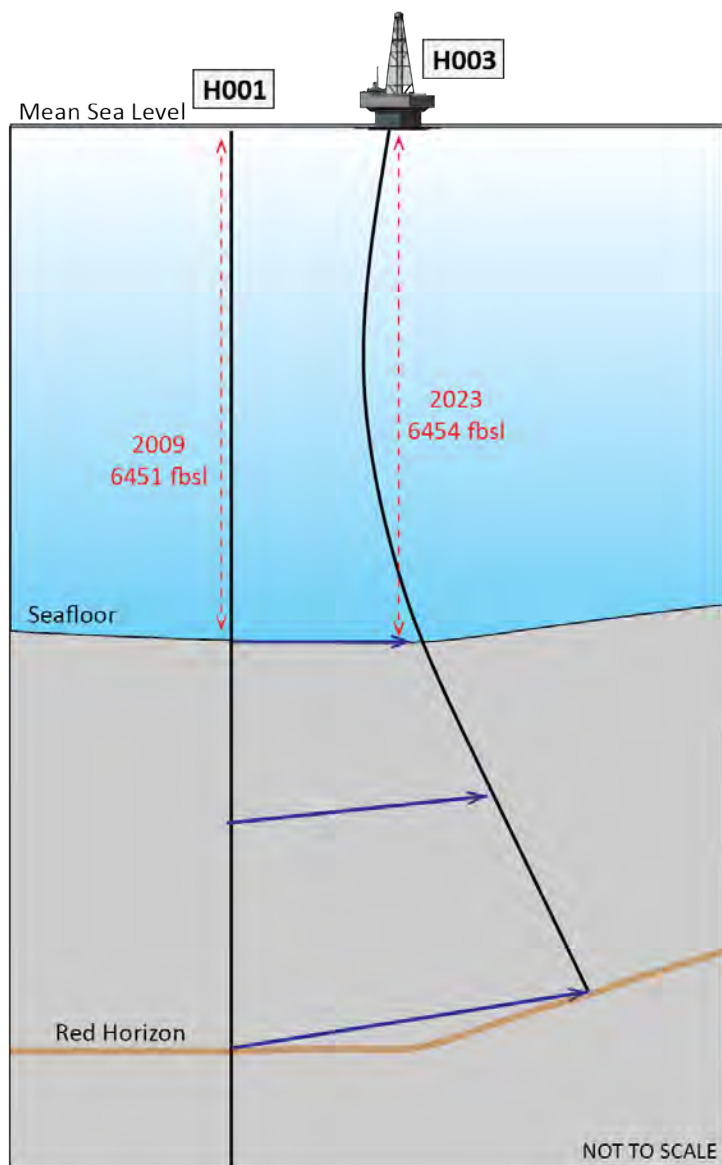


Figure F4: Sketch of Hole H003 deviation and the projection of Hole H001 to Hole H003 measured depth.

Plotting H001, H002, and H003 downhole data

When Hole H001 LWD data and stratigraphic tops are plotted with Hole H002 and Hole H003 downhole data in Hole H002 and Hole H003 measured depth, all Hole H001 depths to 300 mbsf are first converted to Hole H003 measured depths using Equation E2. The depth conversion is only applied down to 300 mbsf for the following reasons. Only Hole H003 was deviated. Hole H003 was only cored to a measured depth of 7,470 ft RKB (296.9 mbsf). And the calculated shift in the depth rounds to zero at and around 300 mbsf. Using this method, the resulting projected depths of seismic

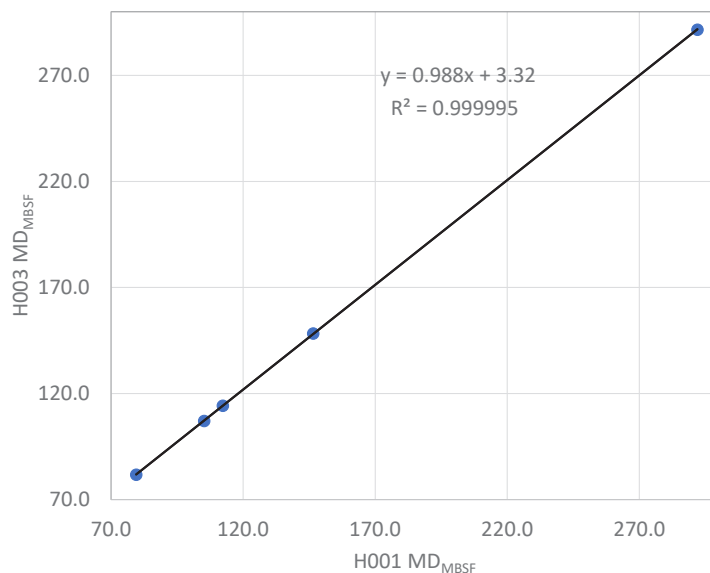


Figure F5: Cross plot of events in Hole H003 vs Hole H001. Hole H003 measured depth in meters below the seafloor (H003 MD_MBSF, vertical axis) are from Table T3, column F. Hole H001 measured depth in meters below the seafloor (H001 MD_MBSF, horizontal axis) are from Table T4, column WR313 H001.

horizons and stratigraphic surfaces were calculated and are shown in Table T4.

Drilling fluids

Hole H003 was drilled and cored from the seafloor to total depth using seawater and high-viscosity sweeps as needed.

Hole H002 was spudded using seawater while staging up pumps from 100 gpm to 175 gpm at 90 psi from the seafloor to 6,570 ft RKB (19.5 mbsf). Drilling from 6,570 to 8,115 ft RKB (19.5 to 490.4 mbsf) was completed with seawater increasing from 200-350 gpm; pumping 15-40 bbls of high-viscosity sweep mud as needed.

At a measured depth of 8,115 ft RKB (490.4 mbsf), the drilling fluids program in Hole H002 was slowly switched over from the use of seawater to the continuous use of 10.5 ppg water-based weighted drilling mud. Drilling mud was mixed on-the-fly from 16.0 ppg water-based mud (WBM) with seawater. While drilling ahead, mud was pumped at 300-350 gpm using the rig pumps. While coring, mud was pumped at 84-207 gpm using the cement pumps.

A. Strata	B. Hole H001 Depth	C. Hole H003 Core	D. Hole H003 Depth	E. Hole H003 Compressed Depth	F. Hole H003 Adjusted Compressed Depth
	mbsf		mbsf	mbsf	mbsf
density transition	79.49	H003-14H^	82.04	81.80	81.86
density transition	105.21	H003-18H*^	109.28	107.76	107.27
density transition	112.26	H003-20H	114.27	114.23	114.23
density transition	146.52	H003-25H*^	151.39	150.33	148.08
Red sand	292.00	H003-28CS	292.00	291.60	291.82

Table T3: Comparison of Hole H001 logging while drilling (LWD) to Hole H003 lithofacies transitions. A) Observation or Strata; B) Hole H001 LWD low-to-high density transitions and Red sand top in Hole H001 measured depth; C) Hole H003 cores with observed Hole H003 ooze-to-clay transitions (See [Lithostratigraphy](#)) and Red sand top. Some of these cores had fall-in (see * on core name) and/or voids (see ^ on core name) in the core above the observed transition; D) Hole H003 measured depth of transition; E) Hole H003 compressed measured depth of transition; F) Hole H003 compressed measured depth of the transition adjusted for observed fall-in and voids by subtracting the compressed thickness of fall-in and voids from the compressed depth of the observed transition.

Higher pump rates than anticipated were required to keep the borehole clean. The seafloor was sandy (Figures [F7](#), [F8](#), and [F9](#); also See [Drilling challenges](#) and [Lithostratigraphy](#)). This sand was at least 4.5 m thick. Core images indicated that Sections 1 and 2 of core H003-01H (Figure [F9](#)) were about half-full of sediment before splitting and the rest of the core liner was full of water. Thus, the actual thickness of this seafloor sand may be thicker than the recovered amount. As a result of this sand layer, a crater developed in the top section of the borehole (Figure [F8](#)) producing a dramatic drop in annular velocity (vertical speed of drilling fluid returning up through the annulus between the drill pipe and the formation) throughout the top section, making removal of the sand-sized particles more difficult. Several operational events described above and below also prevented circulation for significant periods of time, exacerbating the problem. Periods of non-circulation may have also caused barite to fall out of high-viscosity sweeps in Hole H003 and the water-based mud and high-viscosity sweeps in Hole H002.

Drilling challenges

Tools became stuck inside the BHA three times. As a result, we had to either partially (06 August 2023) or completely (21 August 2023 and 27 August 2023)

retrieve the BHA to the rig floor (Figure [F1](#) and Table [T5](#)).

In the 06 August 2023 and 27 August 2023 cases, it was determined that the tool became stuck because sediment packed off around the tool within the BHA. It is possible that this sediment was from the shallow sand encountered at the top of the hole (Figure [F7](#) yellow curve, and Figure [F8](#)) and/or fallout of the barite from the drilling mud (See [Drilling fluids](#)).

The 21 August 2023 event was the result of a piece of the wireline stuck in the PCTB latch collet preventing the coring tool from unlatching from the BHA.

06 August 2023

While preparing for the deployment of the coring tool for Core H003-08CS, the wireline separated under tension while deploying the PCTB-CS pulling tool before coring. After recovering the PCTB-CS pulling tool from the borehole, an emergency pulling tool was run into the borehole and successfully latched to the PCTB-CS core barrel. However, the PCTB-CS could not be removed from the BHA, and it was interpreted that the PCTB-CS was packed-off in the BHA with sediment. The BHA was pulled out of the borehole. However, after the BHA cleared the seafloor, the sediment had cleared, and the PTCB-CS core barrel was no longer stuck.

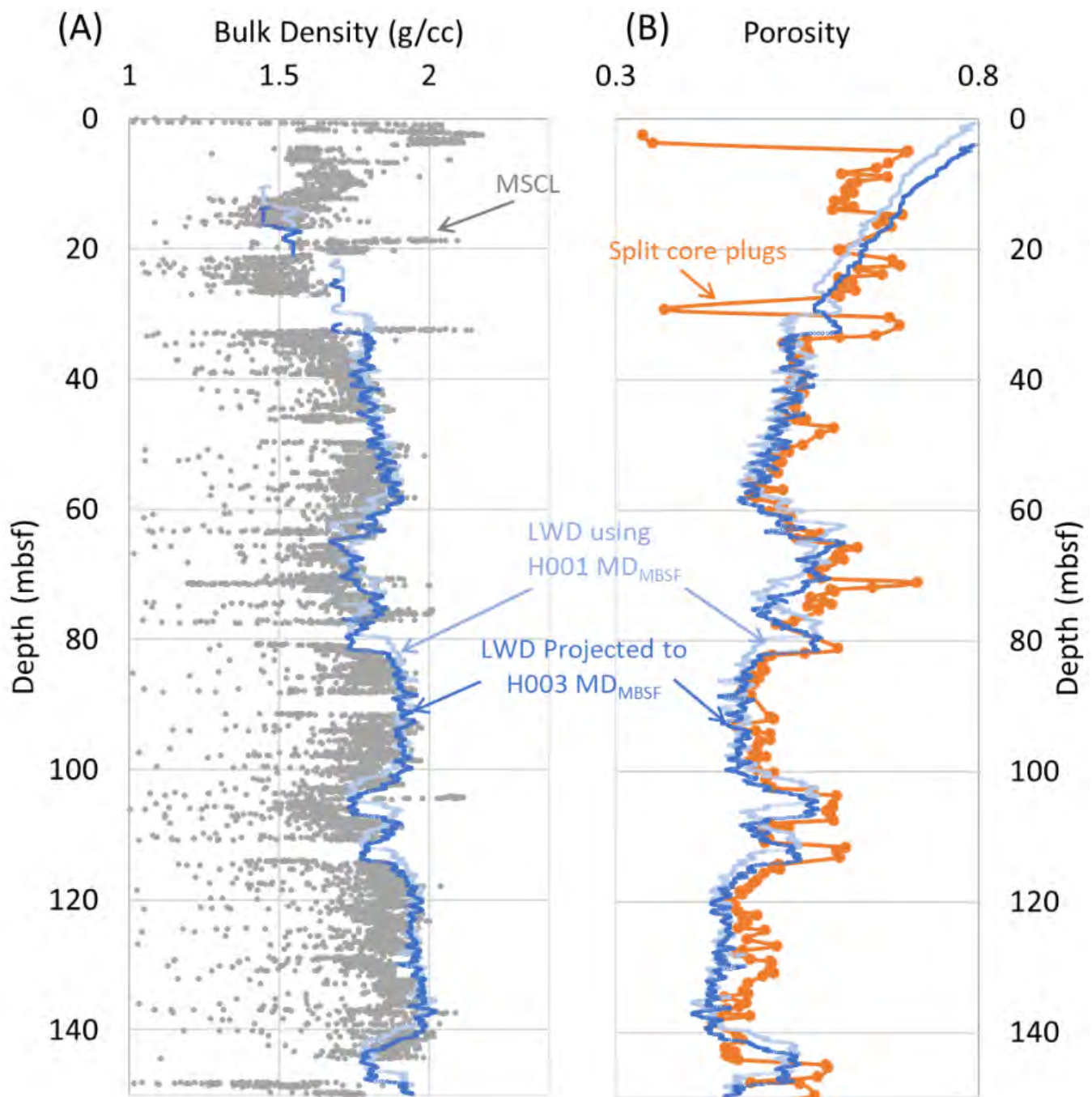


Figure F6: Demonstration of the projection of Hole H001 to Hole H003 using Equation E2. A) Gray dots: Hole H003 Multi-Sensor Core Logger (MSCL) whole-round gamma density measurements (See Conventional whole core logging) plotted using Hole H003 compressed measured depth. Light Blue line: H001 logging while drilling (LWD) bulk density plotted using Hole H001 measured depth (H001 MD_{MBSF}, no projection). Dark Blue line: Hole H001 LWD bulk density projected from Hole H001 measured depth to Hole H003 measured depth (H003 MD_{MBSF}) using Equation E2 ($B = 3.32$ m, $C = 0.988$); B) Orange circles: Hole H003 porosity from moisture and density measurements of split core plug samples (See Index properties, sample code MDX) using compressed measured depth. Core porosity was determined assuming a fresh-water saturation of 100% and a grain density of 2.7 g/cm^3 . Light Blue line: Hole H001 LWD porosity plotted using Hole H001 measured depth (no projection). The method for calculating the porosity from LWD data is discussed in Flemings et al. (2025a). Dark Blue line: H001 LWD porosity using Hole H001 measured depth projected to Hole H003 measured depth using Equation E2 ($B = 3.32$ m, $C = 0.988$); The peaks in the darker blue line correlate more closely to the measured data.

			WR313 H001		WR313 H002		WR313 H003		
Events, Sands & LWD Units			Depth (mbsf)	Depth (ft RKB)	Depth (mbsf)	Depth (ft RKB)	Depth (mbsf)	Depth (ft RKB)	
Seafloor			-	6,513	-	6,506	-	6,506	
Hrz 1200		LWD Unit 1	61	6,715	61	6,708	64	6,716	
Water-bearing Aqua sand	Top		61	6,715	61	6,708	64	6,716	
	Base		80	6,777	80	6,770	83	6,778	
Hrz 1100			101	6,846	101	6,839	104	6,846	
Water-bearing Yellow sand	Top		101	6,846	101	6,839	104	6,846	
	Base		105	6,857	105	6,850	107	6,857	
Hrz 1000			158	7,033	158	7,026	160	7,031	
JIP mud unit with low concentration hydrate		Top	LWD Unit 2	158	7,033	158	7,026	160	7,031
Hrz 0900				292	7,471	292	7,464	292	7,463
Hydrate-bearing Red sand	Top	292		7,471	292	7,464	292	7,463	
	Base	294		7,479	294	7,472	294	7,471	
JIP mud unit with low concentration hydrate		Base		316	7,551	316	7,544		
Hrz 0800				316	7,551	316	7,544		
Water-bearing coarse-grained interval	Top	LWD Unit 3	334	7,609	334	7,602			
	Base		335	7,613	335	7,606			
Hydrate-bearing marine mud	Top		523	8,229	523	8,222			
	Base		525	8,235	525	8,228			
Hydrate-bearing marine mud	Top		558	8,345	558	8,338			
	Base		563	8,359	563	8,352			
Hrz 0500			610	8,513	610	8,506			
Water-bearing coarse-grained interval	Top	LWD Unit 4	615	8,530	615	8,523			
	Base		622	8,555	622	8,548			
Hydrate-bearing Upper Blue sand	Top		664	8,693	664	8,686			
	Base		688	8,769	688	8,762			
Hrz 400			696	8,798	696	8,791			
Hydrate-bearing marine mud	Top	LWD Unit 5	786	9,091	786	9,084			
	Base		786	9,093	786	9,086			
Hrz 0300			805	9,155	805	9,148			
Hydrate-bearing Orange sand	Top		805	9,155	805	9,148			
	Base		819	9,199	819	9,192			
Interpolated BSR				895	9,448	895	9,441		

Table T4: Seismic horizons and stratigraphic surface depths. WR313 H001 measured (and true vertical) depths are from the 2009 Joint Industry Project Leg II (JIP). WR313 H002 depths are measured (and true vertical) depths determined using Equation E3. WR313 H003 depths are measured depths determined using Equation E2. The true vertical depth can be calculated from the measured depth using Equation E1. LWD = logging while drilling; Hrз = horizon. Horizons and sands are discussed in Expedition UT-GOM2-2 Summary (Flemings et al., 2025a).

6 August 2023	While preparing for the deployment of the coring tool for Core H003-08CS, the wireline separated under tension while deploying the PCTB-CS pulling tool before coring. After recovering the PCTB-CS pulling tool from the borehole, the emergency pulling tool was run into the borehole and successfully latched to the PCTB-CS core barrel. However, the PCTB-CS could not be removed from the BHA, and it was interpreted that the PCTB-CS was packed-off in the BHA with sediment. The BHA was pulled out of the borehole. However, after the BHA cleared the seafloor, the sediment had cleared, and the PTCB-CS core barrel was no longer stuck.
21 August 2023	After deploying the PCTB-FB tool and cutting Core H002-04FB, multiple attempts were made to unlatch the PCTB-FB tool. The wireline separated under tension, and it was decided that the PCTB-FB inner barrel was stuck and could not be removed from the BHA. The PCTB-FB coring BHA was pulled from the borehole and recovered to the Q4000 by 1200 hr on 22 August 2023. A piece of the wireline was found stuck in the PCTB latch collet preventing the coring tool from unlatching from the BHA.
27 August 2023	The cement liner was lowered into the BHA, became stuck in the BHA, and the Q4000 lost the ability to circulate drilling fluids through the BHA. It was interpreted that a "hydraulic lock" had occurred with the pressure in the drill pipe above the liner being greater than the pressure below. After making a number of attempts to pull the cementing liner from the BHA, the decision was made to cut the wireline connected to the cement liner at the surface and slip/cut wireline while tripping the BHA back to near the seafloor and to try again to pull the cement liner from the BHA. These additional attempts to pull the liner free also failed. After several more failed attempts to pull the liner free, the BHA was pulled back to the Q4000. Upon the recovery of the BHA to the vessel, it was discovered that the running tool on the wireline was stuck inside the BHA drill collars and that a great deal of barite drilling mud sediment was packed off around the running tool.

Table T5: Three incidents where tools became stuck inside the bottom hole assembly (BHA). Dataset: <http://doi.org/10.5281/zenodo.14680104>.

21 August 2023

After deploying the PCTB-FB tool and cutting Core H002-04FB, multiple attempts were made to unlatch the PCTB-FB tool. The wireline separated under tension, and it was decided that the PCTB-FB inner barrel was stuck and could not be removed from the BHA. The PCTB-FB coring BHA was pulled from the borehole and recovered to the Helix Q4000 by 1200 hr on 22 August 2023. A piece of the wireline was found stuck in the PCTB latch collet preventing the coring tool from unlatching from the BHA.

27 August 2023

A cement liner was lowered into the BHA, became stuck in the BHA, and the Q4000 lost the ability to circulate drilling fluids through the BHA. It was

interpreted that a "hydraulic lock" had occurred with the pressure in the drill pipe above the liner being greater than the pressure below. After making a number of attempts to pull the cementing liner from the BHA, the decision was made to cut the wireline connected to the cement liner at the surface and slip/cut wireline while tripping the BHA back to near the seafloor and to try again to pull the cement liner from the BHA. These additional attempts to pull the liner free also failed. After several more failed attempts to pull the liner free, the BHA was pulled back to the Q4000. Upon the recovery of the BHA to the vessel, it was discovered that the running tool on the wireline was stuck inside the BHA drill collars and that a great deal of barite drilling mud sediment was packed off around the running tool.

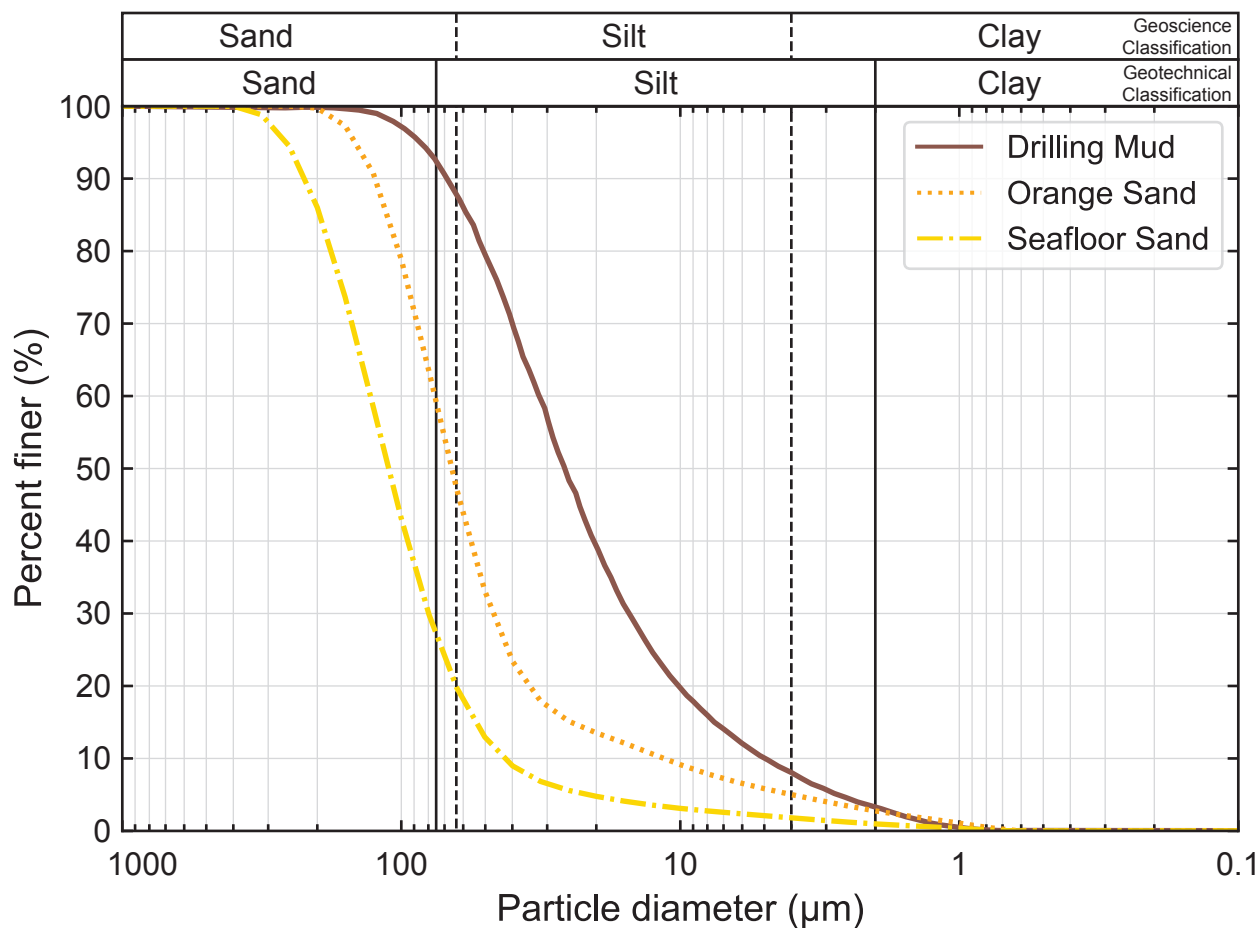


Figure F7: Examples of particle size distribution of sands encountered during the drilling of Site H. The particle size distribution of a representative sample of barite (data provided by MI-SWACO in an email communication) is shown as a solid brown line. Measured data from a sample in the Hole H002 Orange interval (sample H002-09CS-4b, 64-65cm) is shown as a dotted orange line. Measured data from a sample at the top of Hole H003 (sample H003-01H-3a, 64-65cm) is shown as a dash-dotted yellow line. Particle size cutoffs shown are for the geotechnical (solid vertical lines; clay = <2 μm, silt = 2-75 μm, sand = >75 μm) and geoscience (dashed vertical lines; clay = <3.9 μm, silt = 3.9-62.5 μm, sand = >62.5 μm) classifications. See Methods: Laser particle analysis (Flemings et al., 2025b) for measurement method. Dataset: <http://doi.org/10.5281/zenodo.14109861>.

Plug and abandonment

Per 30 CFR 250.1715, the normal requirement for permanent well abandonment of an open hole is to emplace a cement plug(s) from at least 100 feet below the seafloor to 100 feet above the top of oil, gas, and freshwater zones to isolate fluids in the strata. However, with hydrate-bearing zones/sands, the heat of formation of the cement has the potential to dissociate the hydrate and make the borehole unstable. Therefore, as with UT-GOM2-1, we proposed to place a cement plug above the hydrate interval to reduce the risk of dissociating hydrate causing a gas flow and destabilizing the formation around the cement.

The plug and abandonment plans for Holes H003 and H002 were reviewed and certified by J. Connor Consulting, Inc. and were subsequently reviewed and approved by BSEE. Any deviation from the BSEE-approved Plug And Abandonment Plans (as described below) required additional written authorization from BSEE prior to enacting these changes. At the conclusion of abandonment activities for Holes H002 and H003, BSEE deemed the abandonment of both wells to be compliant with federal regulations (30 CFR 250 Subpart Q).

Hole H003

The plug and abandonment plan for Hole H003 required emplacement of a 300-ft cement plug approximately 150 feet above the uppermost

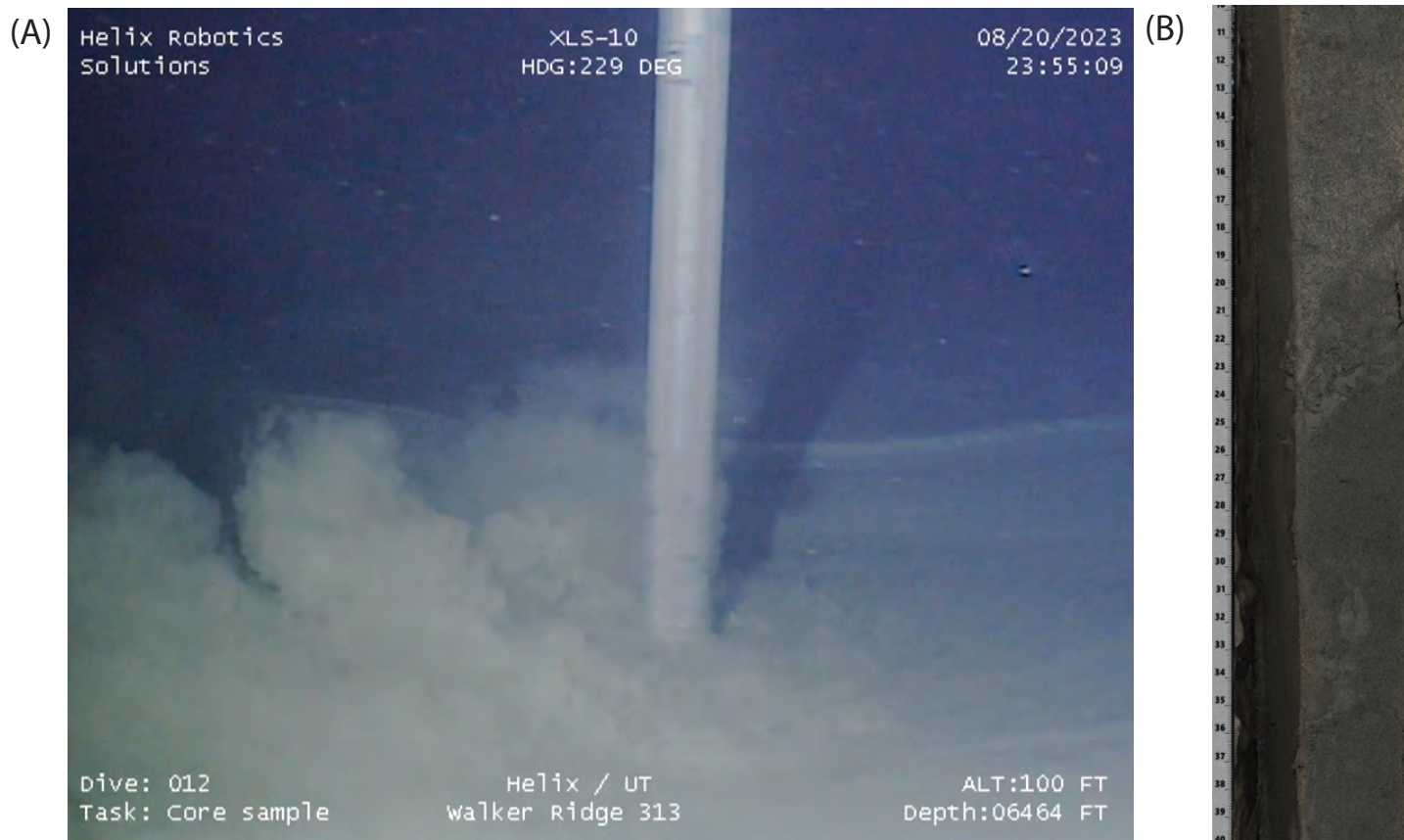


Figure F8: Images of the sandy seafloor. A) Frame capture from a video of the drill pipe in Hole H002 during coring showing the outline of the seafloor 'crater' and billowing sandy sediment. Pipe is blurred because of its rotation; B) Line Scan of a 30 cm interval of split core, Section H003-01H-2 acquired from within the seafloor 'crater.'

significant gas hydrate-bearing zone (the Upper Blue sand). However, the total drilled measured depth of 7,505 ft RKB (304.5 mbsf) was significantly shallower than planned. UT submitted a request to BSEE to permanently abandon Hole H003 by filling the borehole with 11.0 ppg WBM (See Methods: Drilling fluids (Flemings et al., [2025b](#))) from total depth to seafloor. UT provided the technical justification that the weight and pumping pressure of cement in the shallow section would have exceeded the fracture gradient of the formation. BSEE subsequently approved UT's request.

Hole H003 was abandoned on 15 August 2023 by displacing the borehole from the total depth of 7,505 ft RKB (304.5 mbsf) to the seafloor with 115 bbls of 11.0 ppg water-based mud (Figure [F10](#)).

Hole H002

As with Hole H003, the plug and abandonment plan for Hole H002 also required emplacement of a cement

plug in the borehole beginning at approximately 150 feet above the uppermost significant gas hydrate-bearing zone (the Upper Blue sand) and extending upward for a minimum of 300 feet.

Upon achieving a total borehole measured depth of 9,332 ft RKB (861.3 mbsf) on 26 August 2023, the decision was made to plug and abandon Hole H002. A cementing liner was deployed into the BHA by wireline in preparation for cementing. Upon landing the cementing liner in the BHA, the BHA became blocked, and pressure increased to approximately 500 psi. Repeated attempts to retrieve the cement liner were unsuccessful and the BHA was tripped out of the borehole to the rig floor by pulling double lengths of drill pipe and cutting the wireline below the top drive system. A new cementing BHA was assembled, and the borehole was successfully re-entered with assistance from both Q4000 ROVs. The BHA was then placed at 9,332 ft RKB (861.3 mbsf) on 29 August 2023.

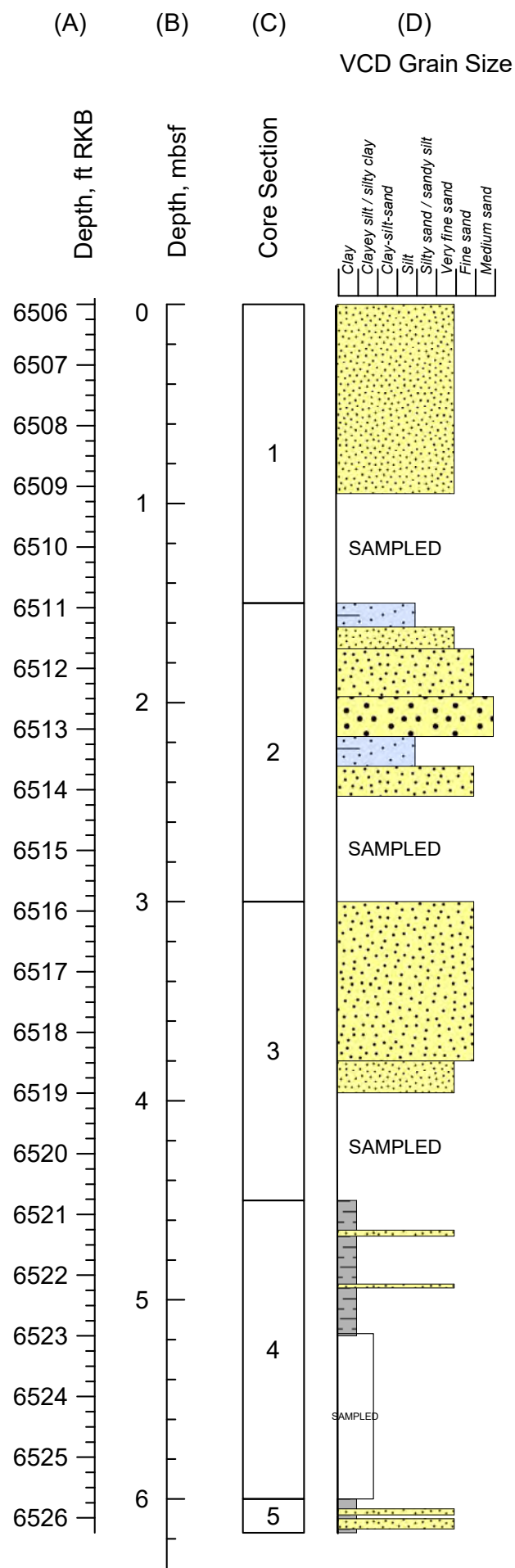


Figure F9: Visual core description (VCD) of the grain size at the top of Site H. Core H003-01H was taken at the seafloor and was the first core taken during drilling. A) Measured depth in feet below rig floor (ft RKB), B) Measured depth in meters below seafloor (mbsf), C) Core Section number, D) VCD of grain size. Yellow is sand. Blue is silt. Gray is clay. See Methods: Grain size (Flemings et al., 2025b).

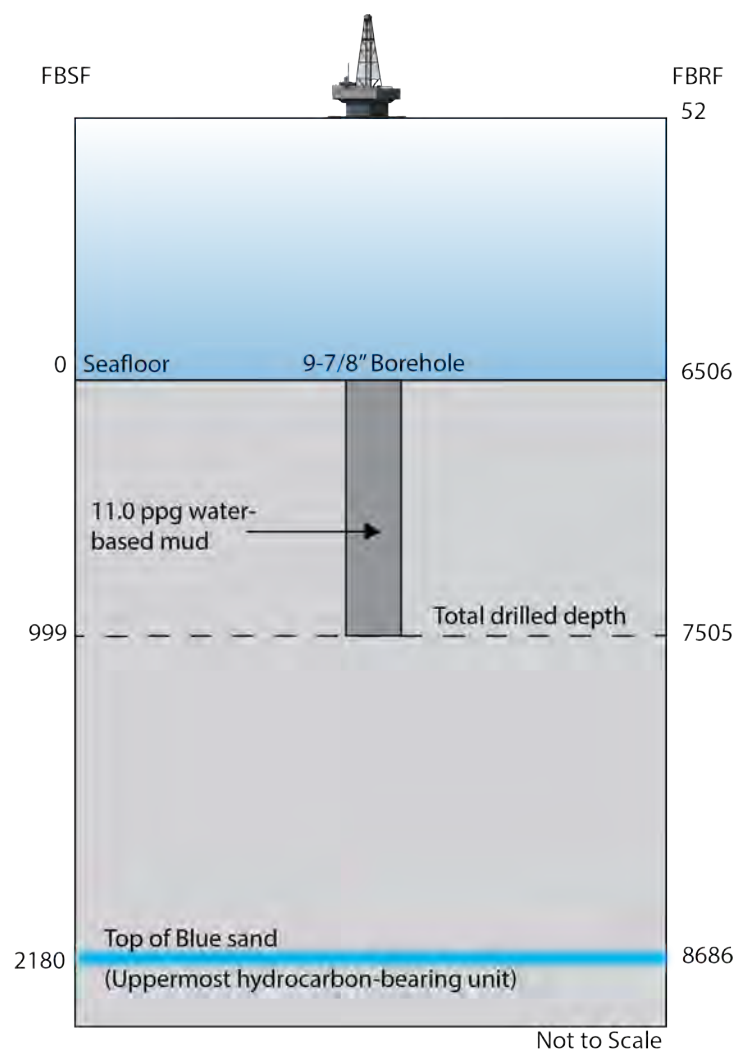


Figure F10: Plug and abandonment schematic for Hole H003. To be consistent with permitting, depths are expressed in feet below the seafloor (FBSF) and were calculated assuming a seafloor depth of 6,506 ft RKB.

Hole H002 was plugged on 29 August 2023 by first pumping 11.5 ppg high-viscosity pad mud followed by 10.5 ppg spacer at total depth. The bit was then raised to the measured depth of 8,497 ft RKB (606.8 mbsf). At this depth, an additional 10.5 ppg spacer mud, followed by 71 bbls of 16.4 ppg Class H cement, followed by additional spacer mud was pumped to set the cement at 8,105 to 8,548 ft RKB (487.4 to 622.4 mbsf) (Figure F11). After the cementing job was completed, the cement was allowed to cure

for 24 hours as required by BSEE. On 30 August 2023, after the cement had cured, the BHA was run back downhole to determine the measured depth of the cement plug. The top of the cement plug was encountered at a depth of 8,105 ft RKB (487.4 mbsf); 443 ft above the base of the cement plug. The integrity of the cement plug was tested with 15,000 lbs of weight on bit, as required by BSEE. After confirming the integrity of the cement, the remaining upper section of the open borehole was displaced with 11.0 ppg WBM from 8,105 ft RKB (487.4 mbsf) to seafloor. The cementing BHA was then retrieved to the deck of the *Q4000*.

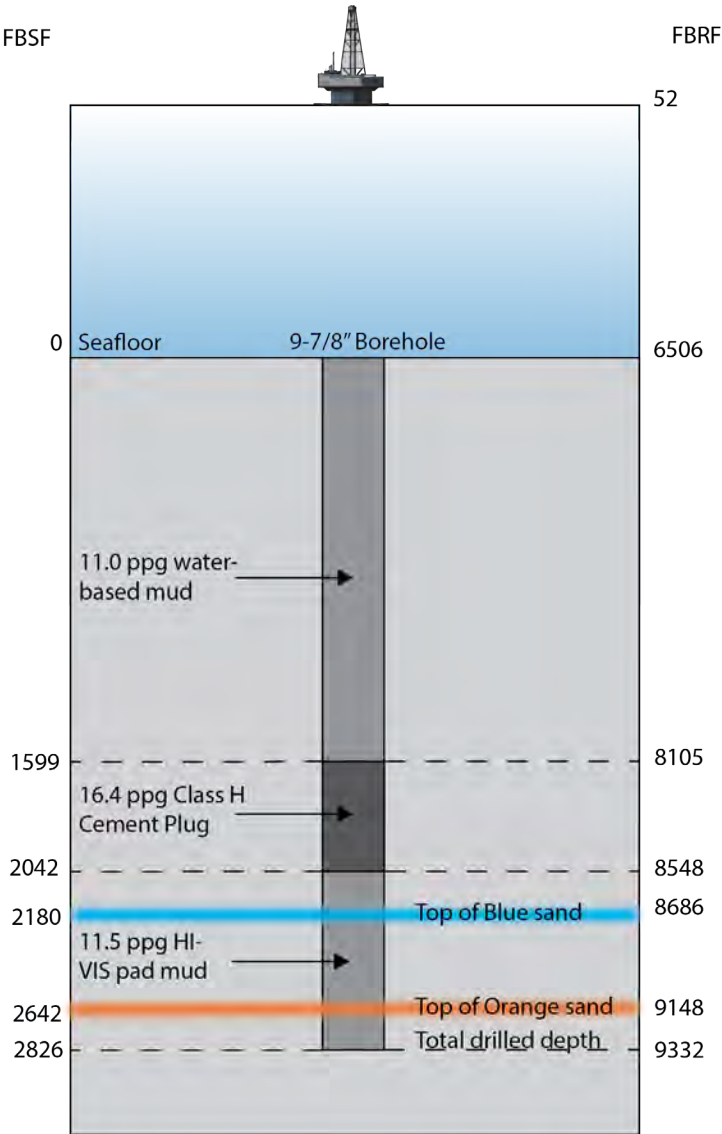


Figure F11: Plug and abandonment schematic for Hole H002. To be consistent with permitting, depths are expressed in feet below the seafloor (FBSF) and were calculated assuming a seafloor depth of 6,506 ft RKB.



Pressure coring tool closed ball valve. Photo Credit: Geotek Ltd.

Coring

Overview

Figure [F12](#) illustrates the integrated coring program for Site H in Hole H002 and Hole H003 measured depth (See [Plotting H001, H002, and H003 downhole data](#)). Hole H003 was drilled and cored to 7,480 ft RKB (296.8 mbsf, Figure [F12](#), column G). Eighteen G-APC, one G-XCB, and ten PCTB cores were taken in Hole H003 using the Cutting Shoe configuration of the tool (PCTB-CS) (Figure [F12](#), column I).

In Hole H003, continuous piston coring with intermittent pressure coring was performed from the seafloor to 7,015 ft RKB (155.1 mbsf) (Figure [F13](#), column I) and from 7,420 to 7,480 ft RKB (278.6 to 296.8 mbsf). Twelve temperature measurements were made in conjunction with some of the piston cores (APCT-3, Figure [F13](#), column H; See [Thermal conductivity](#)). Pressure cores were taken at about 100 ft (31 m) intervals from the seafloor down to 6,990 ft RKB (147.6 mbsf) to measure the buildup of the dissolved methane concentration with depth (Figure [F13](#), column I; also See [Dissolved gas concentrations and hydrate saturation](#)). Pressure coring was also used to try and capture the Red sand interval (Figure [F14](#)).

Hole H002 was drilled and cored to a total measured depth of 9,332 ft RKB (861.3 mbsf) (Figure [F15](#), column G). Only pressure cores were taken in Hole H002, and these were focused in and around the Upper Blue (Figure [F16](#)) and Orange hydrate-bearing sands (Figure [F17](#)). Fifteen pressure cores were taken using two different configurations of the tool (PCTB-CS and PCTB-FB) (Figure [F15](#), column I).

533 ft (162.6 m) of conventional core was obtained from both boreholes. Cores were mostly expansive and generally had recoveries above 100% (Figure [F12](#), J and [Conventional core recovery](#)). The performance of the

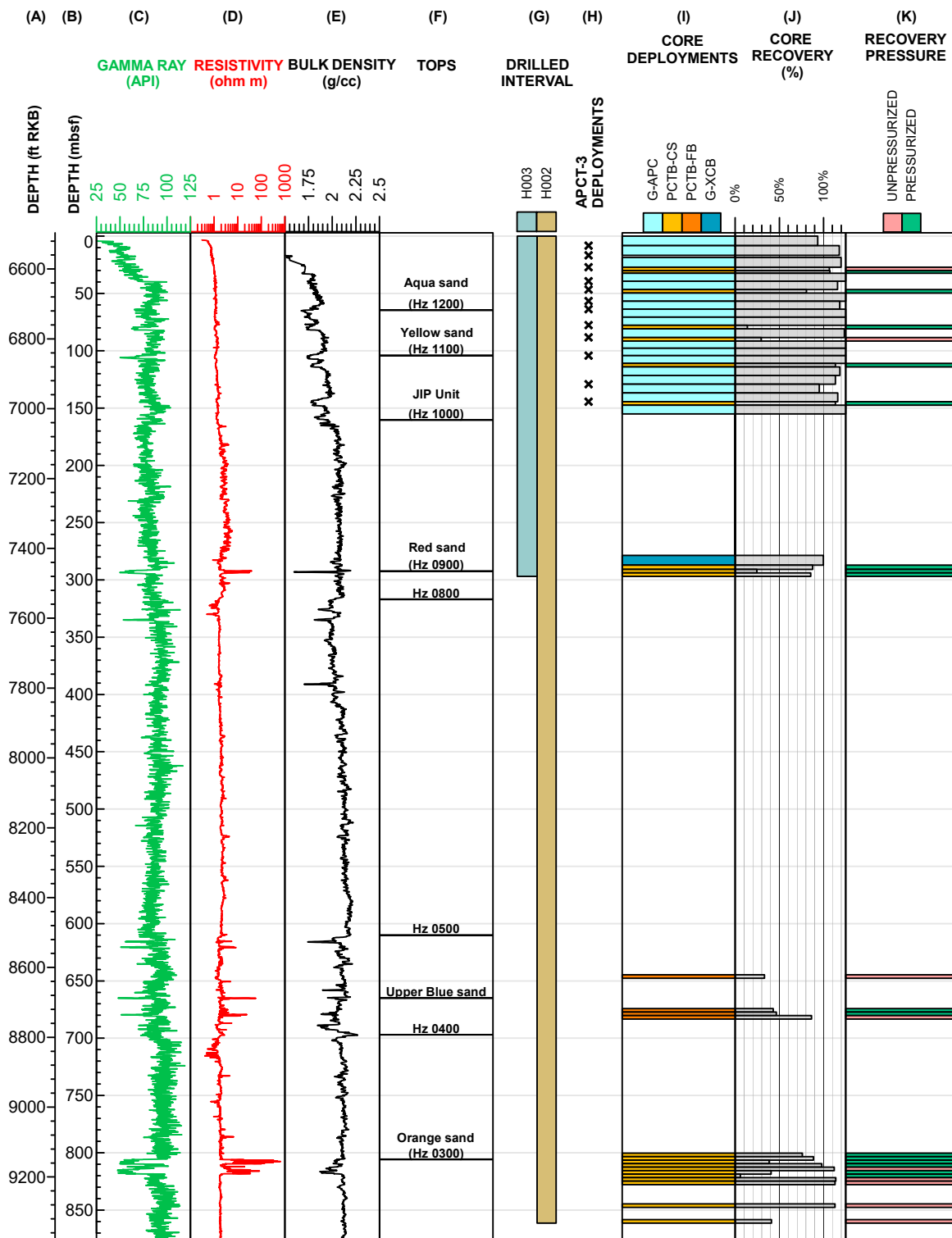


Figure F12: Core deployments and temperature measurements made during UT-GOM2-2. A) Measured depth in feet below rig floor (ft RKB); B) Measured depth in meters below the seafloor (mbsf); C) Projected Hole H001 logging while drilling (LWD) gamma ray in green. The depth projection of Hole H001 LWD data onto Hole H002 and Hole H003 is discussed in Plotting H001, H002, and H003 downhole data; D) Projected LWD resistivity in red; E) Projected LWD bulk density in black; F) Seismic horizons (Hz) and stratigraphic tops as described in (Table T4); G) Drilled interval for Hole H003 in blue and Hole H002 in tan; H) In-situ temperature measurement locations using the Advanced Piston Corer Temperature Tool (APCT-3) in H003; I) Core deployments. Advanced Piston (G-APC) cores are shown in light aqua blue. Extended Core Barrel (G-XCB) cores are shown in dark aqua blue. Pressure Coring Tool with Ball Valve in the Cutting Shoe configuration (PCTB-CS) are shown in dark yellow and in the Face Bit configuration in orange; J) Percent core recovery (Table T6 and Table T9); K) Recovery pressure for the pressure cores measured with a pressure gauge on the rig. Cores recovered at elevated pressure are shown as green, and atmospheric pressure as pink (Data in [Pressure coring summary](#), See [PCTB performance](#) for discussion about PCTB sealing).

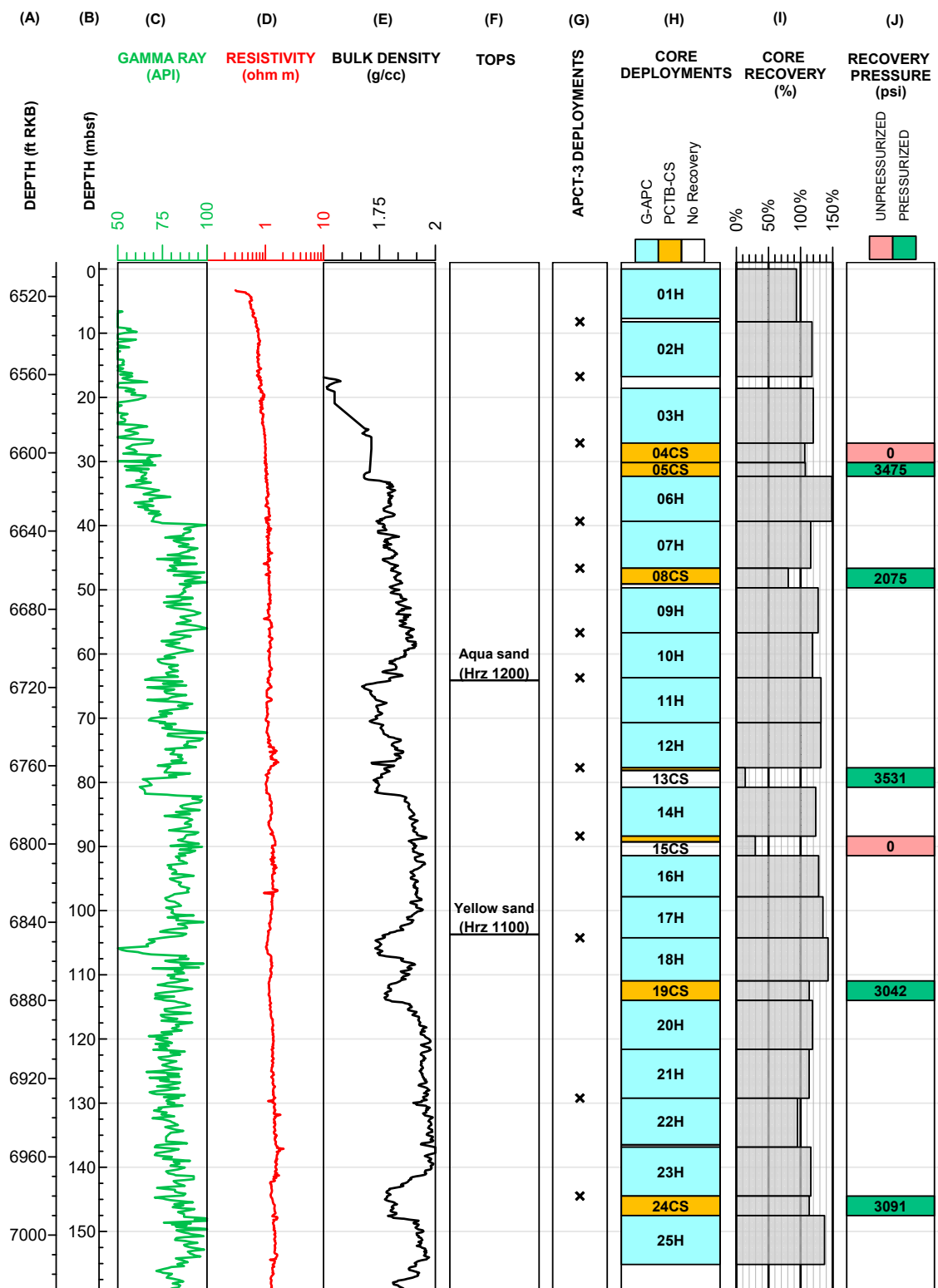


Figure F13: Expanded view of the core deployments and temperature measurements in Hole H003 to 7,015 ft RKB (155.1 mbsf) A) Measured depth in feet below rig floor (ft RKB); B) Measured depth in meters below the seafloor (mbsf). C) Projected Hole H001 logging while drilling (LWD) gamma ray in green. The depth projection of Hole H001 LWD data onto Hole H002 and Hole H003 is discussed in [Plotting H001, H002, and H003 downhole data](#); D) Projected LWD resistivity in red; E) Projected LWD bulk density in black; F) Seismic horizons (Hrz) and stratigraphic tops as described in (Table T4); G) In-situ temperature measurement locations made with the Advanced Piston Corer Temperature Tool (APCT-3); H) Core deployments. Advanced Piston cores (G-ACP) are shown in light aqua blue. Extended Core Barrel (G-XCB) cores are shown in dark aqua blue. Pressure Coring Tool with Ball Valve in the Cutting Shoe configuration (PCTB-CS) are shown in dark yellow; I) Percent core recovery (Tables T6 and T9); J) Recovery pressure for the pressure cores measured with a pressure gauge on the rig. Cores recovered at elevated pressure are shown as green, and atmospheric pressure as pink (Data from [Pressure coring summary](#)).

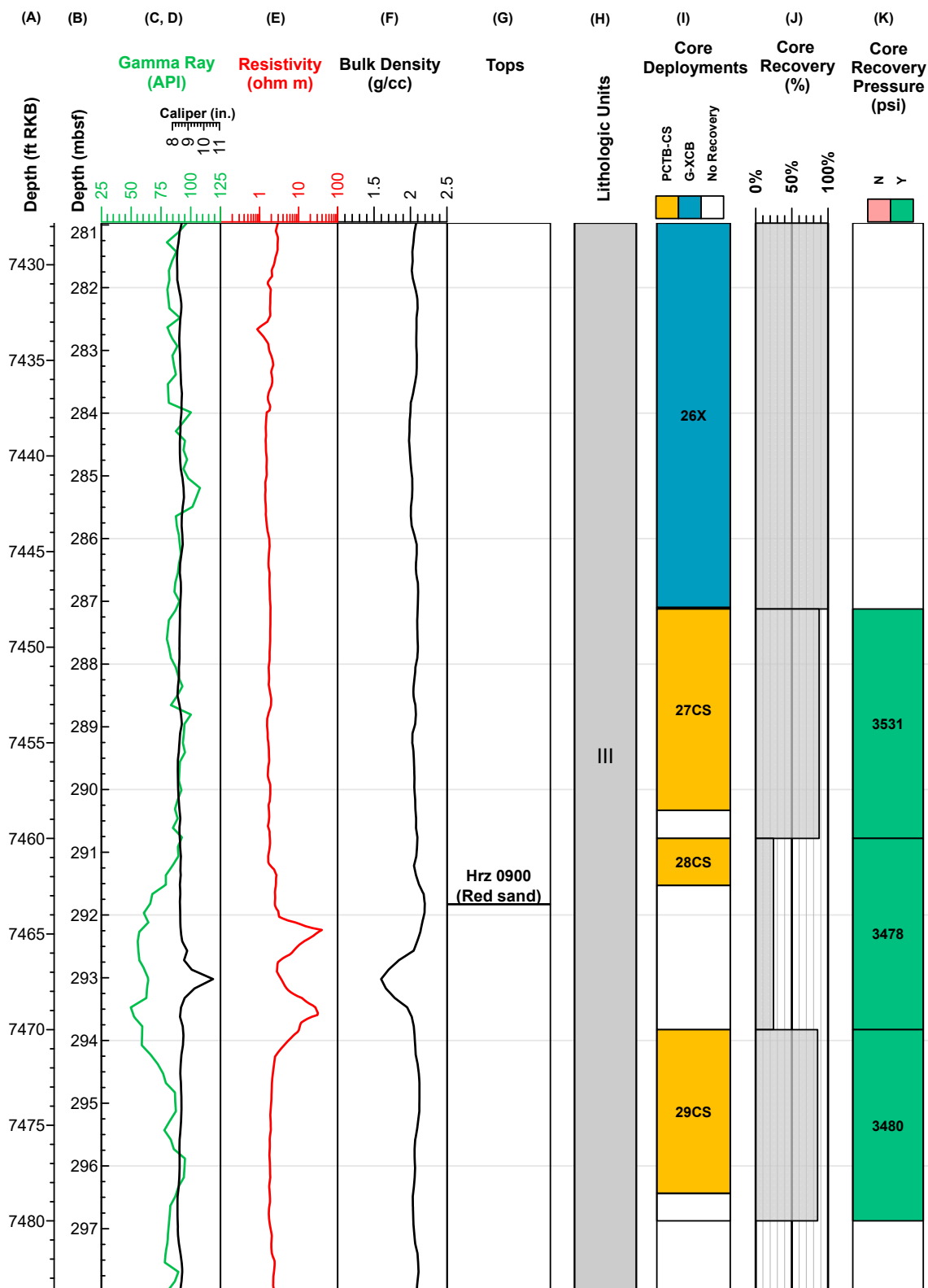


Figure F14: Expanded view of core deployments at the Red sand in Hole H003. A) Measured depth in feet below rig floor (ft RKB), B) Measured depth in meters below the seafloor (mbsf). C) Projected Hole H001 logging while drilling (LWD) gamma ray in green. The depth projection of Hole H001 LWD data onto Hole H002 and Hole H003 is discussed in [Plotting H001, H002, and H003 downhole data](#); D) Projected LWD caliper data in black; E) Projected LWD resistivity in red; F) Projected LWD bulk density in black; G) Seismic horizons (Hrz) and stratigraphic tops as described in (Table T4); H) Lithologic Units; I) Core deployments. Extended Core Barrel (G-XCB) cores are shown in dark aqua blue, Pressure Coring Tool with Ball Valve in the Cutting Shoe Configuration (PCTB-CS) cores are shown in dark yellow. Area cored but no recovery is shown with gray diagonal hatches; J) Percent core recovery (Tables T6 and T9); K) Recovery pressure for the pressure cores measured with a pressure gauge on the rig. Cores recovered at elevated pressure are shown as green (Data from [Pressure coring summary](#)).

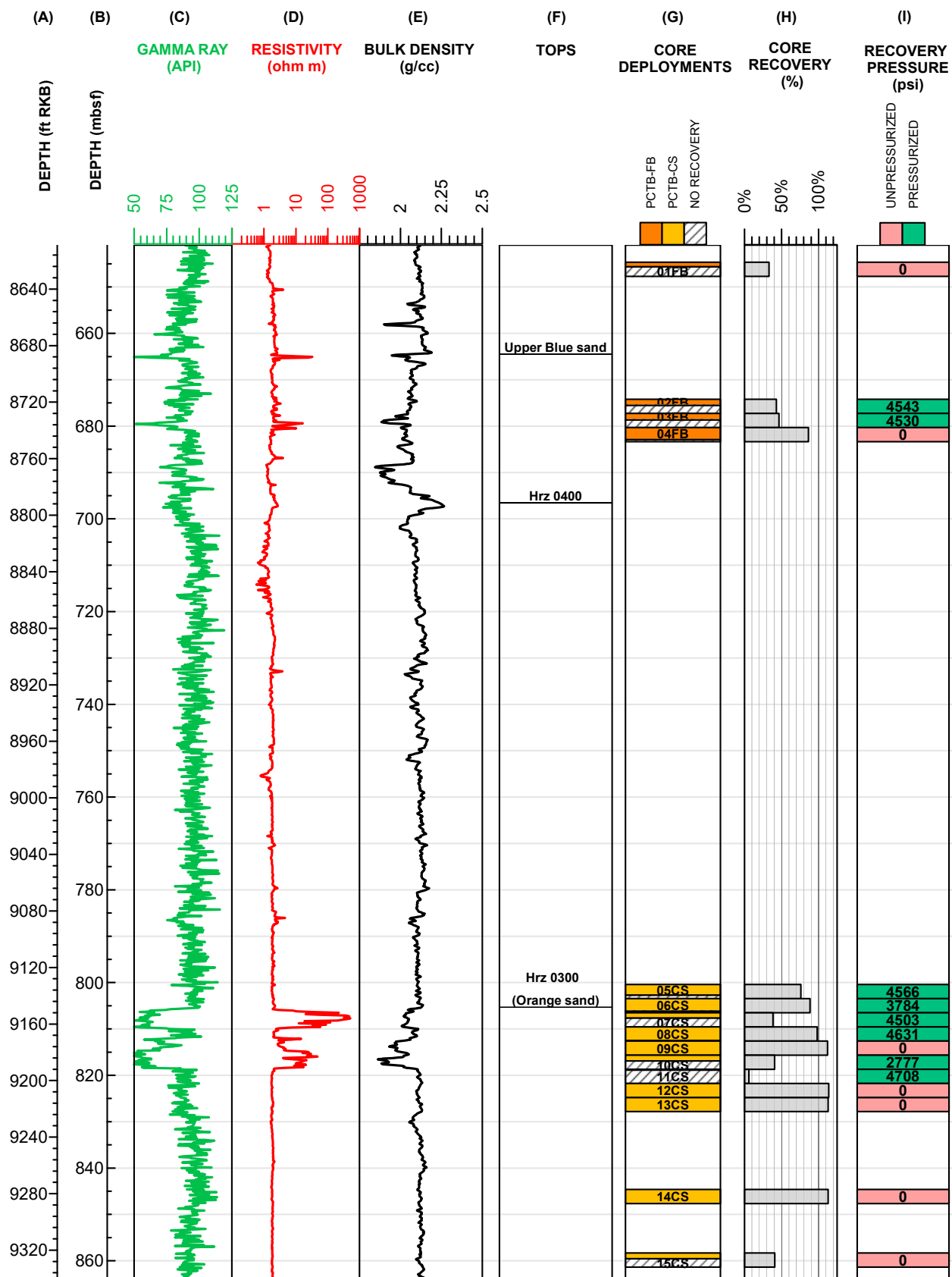


Figure F15: Core deployments in Hole H002. A) Measured depth in feet below rig floor (ft RKB); B) Measured depth in meters below the seafloor (mbsf); C) Logging while drilling (LWD) gamma ray in green; D) LWD resistivity in red; E) LWD bulk density in black; F) Seismic horizons (Hrz) and stratigraphic tops as described in (Table T4); G) Core deployments. Pressure Coring Tool with Ball Valve in the Face Bit configuration (PCTB-FB) are shown in orange and in the Cutting Shoe configuration (PCTB-CS) are shown in dark yellow; H) Percent core recovery (Table T6); I) Recovery pressure for the pressure cores; cores recovered at elevated pressure are shown as green, and atmospheric pressure as pink (Data from [Pressure coring summary](#)).

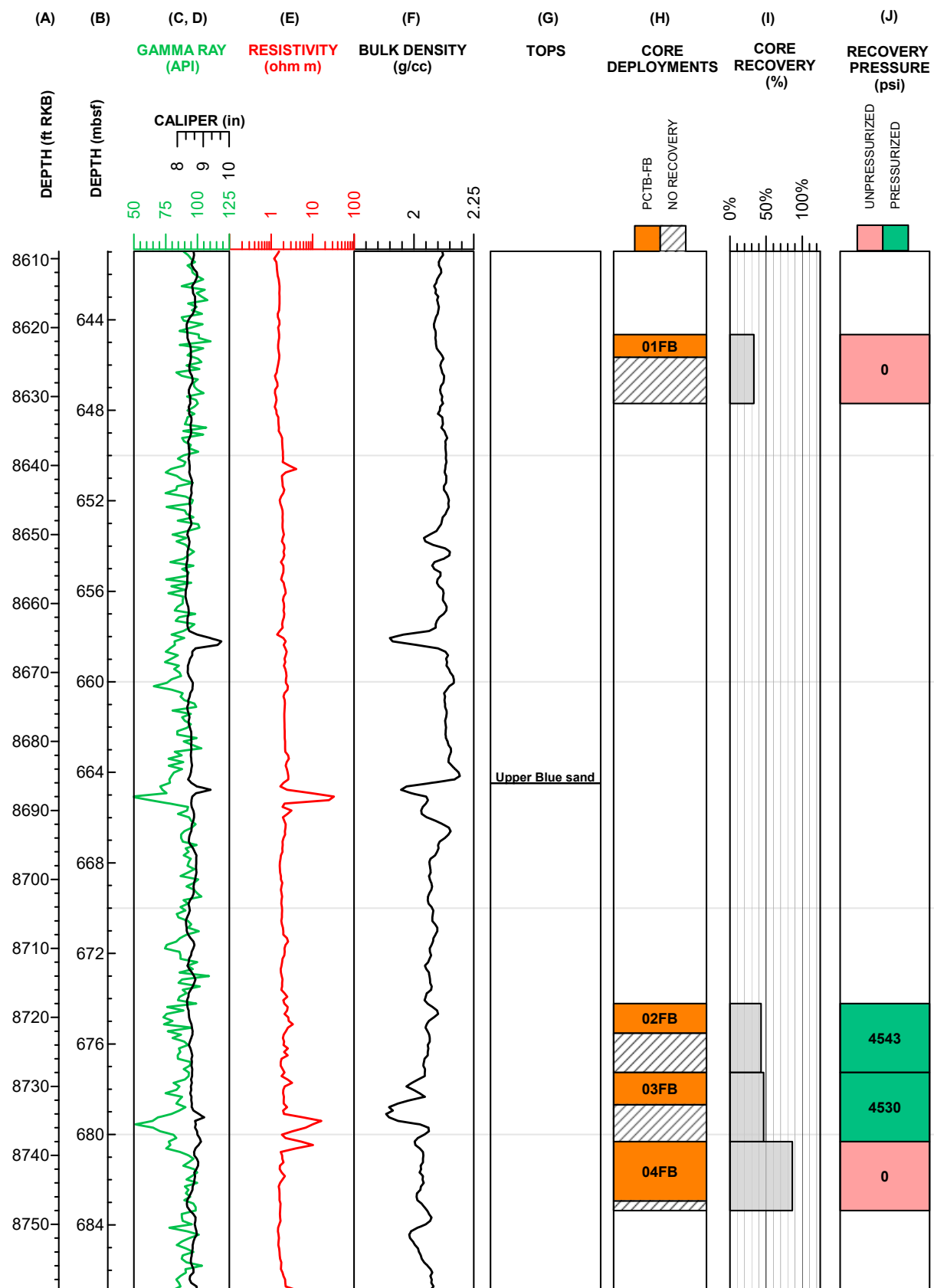


Figure F16: Expanded view of the core deployments from above and in the Upper Blue sand. A) Measured depth in feet below rig floor (ft RKB); B) Measured depth in meters below the seafloor (mbsf); C) Logging while drilling (LWD) gamma ray in green; D) LWD caliper in black; E) LWD resistivity in red; F) LWD bulk density in black; G) Seismic horizons (Hrz) and stratigraphic tops as described in (Table T4); H) Core deployments. Pressure Coring Tool with Ball Valve in the Face Bit configuration (PCTB-FB) are shown in orange; I) Percent core recovery (Table T6); J) Recovery pressure for the pressure cores; cores recovered at elevated pressure are shown as green, and atmospheric pressure as pink (Data from [Pressure coring summary](#)).

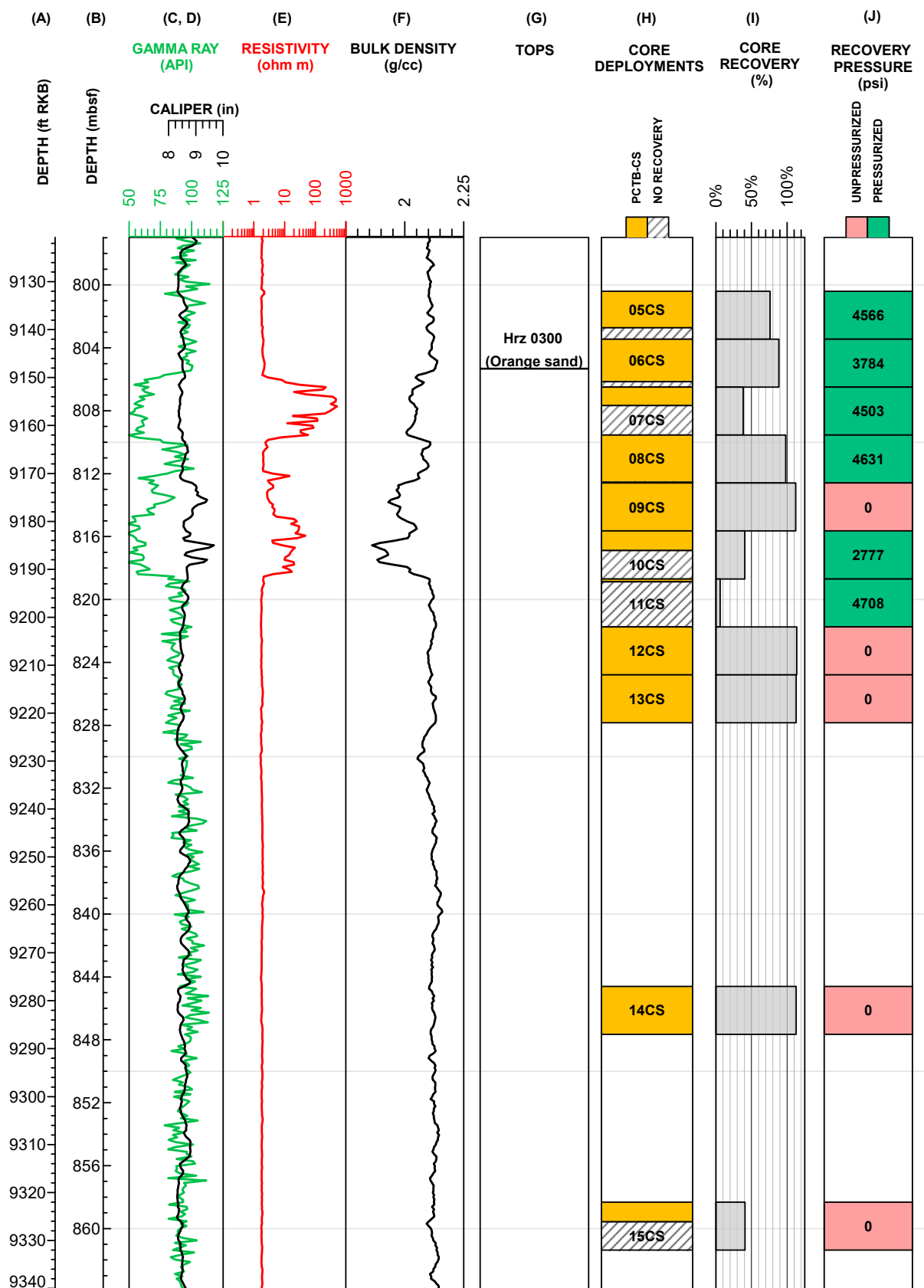


Figure F17: Expanded view of the core deployments in and below the Orange sand. A) Measured depth in feet below rig floor (ft RKB); B) Measured depth in meters below the seafloor (mbsf); C) Logging while drilling (LWD) gamma ray in green D) LWD caliper in black; E) LWD resistivity in red; F) LWD bulk density in black; G) Seismic horizons (Hrz) and stratigraphic tops as described in (Table T4); H) Core deployments. Pressure Coring Tool with Ball Valve in the Cutting Shoe configuration (PCTB-CS) are shown in dark yellow; I) Percent core recovery (Table T6); J) Recovery pressure for the pressure cores; cores recovered at elevated pressure are shown as green, and atmospheric pressure as pink (Data from [Pressure coring summary](#)).

A. Core	B. Depth, Top		C. Core Advance		D. Curated Length	E. Recovery	F. In-situ Pressure	G. Recovery Pressure
	mbsf	ft RKB	ft	m	m	%	psi	psi
H003-Test	-	2047	NA	NA	NA	NA	928	2672
H003-04CS	27.1	6595	10	3.0	3.2	107%	3042	0
H003-05CS	30.2	6605	7	2.1	2.3	107%	3047	3475
H003-08CS	46.6	6659	10	3.0	2.5	81%	3072	2075
H003-13CS	77.7	6761	10	3.0	0.4	14%	3120	3531
H003-15CS	88.4	6796	10	3.0	0.9	30%	3136	0
H003-19CS	110.9	6870	10	3.0	3.5	114%	3170	3042
H003-24CS	144.5	6980	10	3.0	3.5	114%	3222	3091
H003-27CS	287.1	7448	12	3.7	3.2	88%	3439	3531
H003-28CS	290.8	7460	10	3.0	0.7	25%	3445	3478
H003-29CS	293.8	7470	10	3.0	2.6	86%	3449	3480
H002-01FB	644.6	8621	10	3.0	1.0	33%	3985	0
H002-02FB	674.2	8718	10	3.0	1.3	43%	4030	4543
H002-03FB	677.2	8728	10	3.0	1.4	47%	4034	4530
H002-04FB	680.3	8738	10	3.0	2.6	86%	4039	0
H002-05CS	800.4	9132	10	3.0	2.3	76%	4222	4566
H002-06CS	803.4	9142	10	3.0	2.7	89%	4227	3784
H002-07CS	806.5	9152	10	3.0	1.2	38%	4232	4503
H002-08CS	809.5	9162	10	3.0	3.0	98%	4236	4631
H002-09CS	812.6	9172	10	3.0	3.4	112%	4241	0
H002-10CS	815.6	9182	10	3.0	1.2	41%	4245	2777
H002-11CS	818.7	9192	10	3.0	0.2	6%	4250	4708
H002-12CS	821.7	9202	10	3.0	3.5	114%	4255	0
H002-13CS	824.7	9212	10	3.0	3.4	113%	4259	0
H002-14CS	844.6	9277	10	3.0	3.4	113%	4290	0
H002-15CS	858.3	9322	10	3.0	1.3	41%	4311	0

Table T6: Summary of pressure coring deployments using the Pressure Coring Tool with Ball Valve (PCTB); A) Core/core barrel deployment. CS= PCTB in the Cutting Shoe configuration. FB= PCTB in the Face Bit configuration; B) Core top measured depth in meters below the seafloor (mbsf) and feet below the rig floor (ft RKB); C) Reported cored interval/core throw, yellow highlighted numbers differed from the rig data by more than 20%; D) Curated length; E) Calculated % recovery; F) In-situ pressure calculated from the measured depth assuming a pressure gradient of 0.465 psi/ft; G) Recovery pressure as recorded by a pressure gauge when the autoclave was extracted from the core barrel at the PCTB service area. Values were determined as discussed in Methods: Pressure coring results (Flemings et al., [2025b](#)). Dataset: <http://doi.org/10.5281/zenodo.14104224>.

conventional core barrels is discussed in G-APC and G-XCB performance.

Combining the two boreholes, a total of 179.8 ft (54.8 m) of core was acquired from 25 deployments of the PCTB: there were four deployments of the Face Bit configuration (PCTB-FB), and 21 deployments of the

Cutting Shoe configuration (PCTB-CS) (See [Pressure core recovery](#)).

Pressure coring

The following sections summarize pressure coring and discuss pressure coring operations, PCTB

performance, pressure core recovery, and pressure core quality. Pressure core logging is discussed under [Physical Properties](#). A detailed discussion of the pressure coring tool and coring tool deployment method is presented in Methods: Pressure Coring Tool with Ball Valve (Flemings et al., [2025b](#)). Detailed pressure coring deployment figures for all cores are shown in Appendix C: Pressure coring Deployments.

Pressure coring summary

Table [T6](#) summarizes PCTB deployments. The PCTB was deployed ten times in Hole H003 using the Cutting Shoe configuration (PCTB-CS), plus an additional test in the water column. Coring targets included background muds and the hydrate-bearing Red sand. A pre-expedition review of Hole H001 LWD data showed the possibility of hydrate-filled fractures in mud. Three continuous pressure cores, covering a total interval of 30 ft (9.1 m), were used to attempt to capture the thin (8 ft, 2.4 m) hydrate-bearing Red sand (Figure [F14](#)).

The PCTB was deployed fifteen times in Hole H002 (Figure [F15](#)). It was deployed four times using the face-bit configuration (PCTB-FB) and eleven times using the Cutting Shoe configuration (PCTB-CS). Core depths were targeted to capture background muds, bounding muds, and the Upper Blue and Orange hydrate-bearing sands. Three continuous pressure cores covering a total interval of 30 ft (10 m) targeted one hydrate-bearing section of the 76 ft-thick (23.1 m) Upper Blue sand (Figure [F16](#)). Nine pressure cores, covering a total interval of 90 ft (27.4 m), targeted the 44 ft-thick (13.4 m) Orange sand interval and surrounding muds. Two final cores targeted background muds close to the bottom simulating reflection (BSR) (Figure [F17](#)). See Summary: Background (Flemings et al., [2025a](#)) for more information about the predicted BSR.

Pressure coring operations

Table [T7](#) summarizes the operational parameters for each pressure coring deployment.

Drilling fluid was pumped at a rate above what is optimal for core recovery (<100 gpm) (Table [T7](#),

<https://doi.org/10.5281/zenodo.13971276>

column D) to keep sediment from infiltrating the borehole and packing-off the core barrel in the BHA (See [Drilling challenges](#)). When very low flow rates were used (<50 gpm, Cores H003-04CS and H003-15CS), the PCTB ball was packed with material (mud/sand) and the ball valve did not close.

High-viscosity mud sweeps just before coring, while the BHA was set just above the bottom of the hole (within 2 ft), were only planned for pressure coring deployments after an interval of drilling ahead without coring. The design of the sweeps was planned before the expedition to keep sediment fall-in out of the core barrel. However, due to issues with pack-off mentioned above, the addition of a high-viscosity sweep, just before coring, was implemented after the first pressure core (Core H003-04CS) and for all pressure cores cored with seawater (Table [T7](#), column I).

PCTB performance

A summary of the PCTB performance is shown in Figure [F18](#) and Table [T8](#). Details are included in Appendix C: Pressure Coring Deployments.

Autoclave sealing

For the autoclave to hold pressure (seal), the PCTB ball valve and the upper seal must both close when the tool is actuated.

Sealing failures

In nine UT-GOM2-2 deployments, the PCTB did not seal (Table [T8](#), column K). Five of these nine were because the ball valve did not close. Three, possibly four, of these nine were because the upper seal did not close.

Ball valve failures

During five deployments in Hole H002 and H003, the autoclave did not seal because the ball valve did not close (Table [T8](#), column I). Two of these five deployments did not close because sediment from borehole fall-in entered above the drill bit and became packed in the ball. This sediment was still present in the ball when the core barrel was recovered

A. Core	B. Depth, Top	C. Drilling Fluid	D. Avg. Flow rate	E. Avg. RPM	F. WOB	G. Avg. ROP	H. Avg. wireline velocity POOH	I. High-Vis Gel Sweep Front estimated arrival at the BHA
	ft RKB		gpm	1/min	lbm	ft/hr	ft/min	
H003-04CS	6595	8.6 ppg SW	43	20	1-5k	48	325	No Hi-Vis Sweep
H003-05CS	6605	8.6 ppg SW	101	60	1-5k	69	No data	Before pump shutoff
H003-08CS	6659	8.6 ppg SW	84	63	1-5k	89	329	During latching
H003-13CS	6761	8.6 ppg SW	89	64	1-5k	96	374	Before pump shutoff
H003-15CS	6796	8.6 ppg SW	47	62	1-3k	65	218	Before latching
H003-19CS	6870	8.6 ppg SW	106	62	4-5k	93	373	After pump shutoff
H003-24CS	6980	8.6 ppg SW	116	63	4-5k	104	266	During latching
H003-27CS	7448	8.6 ppg SW	137	82	8-10k	94	286	Before pump shutoff
H003-28CS	7460	8.6 ppg SW	134	62	8-10k	41	247	Before pump shutoff
H003-29CS	7470	8.6 ppg SW	142	86	8-10k	156	404	Before latching
H002-01FB	8621	10.3 ppg WBM	134	83	10-14k	39	361	No Hi-Vis Sweep
H002-02FB	8718	10.3 ppg WBM	124	83	6-10k	34	354	No Hi-Vis Sweep
H002-03FB	8728	10.3 ppg WBM	122	83	6-10k	31	344	No Hi-Vis Sweep
H002-04FB	8738	10.3 ppg WBM	120	82	6-10k	60	-	No Hi-Vis Sweep
H002-05CS	9132	10.5 ppg WBM	207	84	13-18k	21	326	No Hi-Vis Sweep
H002-06CS	9142	10.5 ppg WBM	129	81	10-13k	27	317	No Hi-Vis Sweep
H002-07CS	9152	10.5 ppg WBM	125	82	10-13k	50	357	No Hi-Vis Sweep
H002-08CS	9162	10.5 ppg WBM	114	79	13-20k	42	354	No Hi-Vis Sweep
H002-09CS	9172	10.5 ppg WBM	94	82	10-20k	102	282	No Hi-Vis Sweep
H002-10CS	9182	10.5 ppg WBM	84	79	12-20k	112	231	No Hi-Vis Sweep
H002-11CS	9192	10.5 ppg WBM	85	83	10-15k	31	269	No Hi-Vis Sweep
H002-12CS	9202	10.5 ppg WBM	124	84	12-20k	32	320	No Hi-Vis Sweep
H002-13CS	9212	10.5 ppg WBM	110	80	15-21k	33	313	No Hi-Vis Sweep
H002-14CS	9277	10.5 ppg WBM	117	83	20-28k	40	347	No Hi-Vis Sweep
H002-15CS	9322	10.5 ppg WBM	139	81	7-13k	28	315	No Hi-Vis Sweep

Table T7: Summary of operational parameters for all pressure coring deployments A) Core; B) Core Top measured depth in feet below the seafloor (ft RKB); C) Drilling fluid and weight (SW = seawater, WBM = water-based mud); D) Average flow rate during coring; E) Average rotations per minute (RPM) during coring; F) Driller's shack weight on bit (WOB) during coring from Driller and Company Man daily reports. See Methods: Weight on bit (Flemings et al., [2025b](#)) for a discussion of WOB; G. Average rate of penetration (ROP). H) Average wireline velocity in the water column while pulling the coring tool up the drill pipe; G) Estimated time of arrival of the high-viscosity sweep front at the BHA relative to other steps in the pressure coring process. Pumps are shut off before coring while the running tool is swapped for the pulling tool. Details are in Methods: Pressure coring tool deployments (Flemings et al., [2025b](#)). Values were determined as discussed in Methods: Pressure coring operations (Flemings et al., [2025b](#)). Dataset: <http://doi.org/10.5281/zenodo.14104224>.

to the rig floor (Cores H003-04CS and H003-15CS). One deployment did not close because debris from the rig floor (a piece of wireline) was caught in the coring tool, preventing the tool from actuating (Core H002-

04FB).

The last two ball valve failures are from the deepest coring deployments (Core H002-14CS and H002-

A. Core	B. Depth, Top	C. Seal Depth	D. In-situ pressure, calculated	E. Boost setting	F. Seal Pressure, DST	G. Boosted pressure, DST	H. Recovery pressure, gauge	I. Ball valve closed	J. Upper seal closed	K. Autoclave sealed	L. Sealed at ~ in-situ pressure	M. Stayed in Hydrate stability zone	N. Comments
	ft RKB	ft RKB	psi	psi	psi	psi	psi						
H003-Test	2047	-	927.675	3500	-	-	2672	Yes	Yes	Yes	Likely	-	No DST or rig data
H003-04CS	6595	-	3042.495	3550	-	-	0	No	-	No	-	No	No DST data, ball packed with mud
H003-05CS	6605	5846	3047.145	3507	2570	3249	3475	Yes	Yes	Yes	No	Yes	No Wireline data; seal depth estimate from seal pressure
H003-08CS	6659	-	3072.255	3517	-	-	2075	Yes	Yes	Yes	No	-	No DST data
H003-13CS	6761	6208	3119.685	3548	2781	3700	3531	Yes	Yes	Yes	No	Yes	Late seal with boost above coring depth
H003-15CS	6796	-	3135.96	3490	-	-	0	No	-	No	-	No	Ball packed with mud
H003-19CS	6870	6747	3170.37	3497	3092	3663	3042	Yes	Yes	Yes	Yes, but late	Yes	Late seal with boost at ~in-situ pressure
H003-24CS	6980	6696	3221.52	3490	3040	3636	3091	Yes	Yes	Yes	Yes, but late	Yes	Late seal with boost at ~in-situ pressure
H003-27CS	7448	6464	3439.14	3503	2919	3706	3531	Yes	Yes	Yes	No	No	Late seal with boost above coring depth, delay at seafloor
H003-28CS	7460	7412	3444.72	3482	3418	3738	3478	Yes	Yes	Yes	Yes, but late	Yes	Late seal with boost ~ at coring depth
H003-29CS	7470	4854	3449.37	3493	3047	3578	3480	Yes	Yes	Yes	No	Yes	Late complete seal with boost ~ above coring depth; delay at seafloor
H002-01FB	8621	-	3984.585	4540	-	-	0	Yes	No	No	-	No	Wireline ops issue, incomplete trigger
H002-02FB	8718	6559	4029.69	4537	3427	4501	4543	Yes	Yes	Yes	No	Yes	Late seal with boost
H002-03FB	8728	8704	4034.34	4572	3880	4670	4530	Yes	Yes	Yes	Yes	Yes	Seal with boost
H002-04FB	8738	-	4038.99	4523	-	-	0	No	-	No	-	No	Piece of wireline in latch collet prevented unlatching, tool not triggered
H002-05CS	9132	0	4222.2	4522	-	-	4566	Yes	Yes	Yes	Likely	Yes	> DST data limit
H002-06CS	9142	6433	4226.85	4493	4146	no boost	3784	Yes	Yes	Yes	No	Yes	boost may be hidden by DST data limit, possibly leaky seal
H002-07CS	9152	9090	4231.5	4470	4317	> DST limit	4503	Yes	Yes	Yes	Yes	Yes	Seal with boost
H002-08CS	9162	9128	4236.15	4538	4114	> DST limit	4631	Yes	Yes	Yes	Yes	Yes	Seal with boost
H002-09CS	9172	-	4240.8	4508	-	-	0	Yes	No	No	-	No	Incomplete trigger
H002-10CS	9182	7594	4245.45	4462	3511	no boost	2777	Yes	Yes	Yes	No	Yes	Late, possibly leaky seal, no boost
H002-11CS	9192	8943	4250.1	4565	4171	> DST limit	4708	Yes	Yes	Yes	Yes, but late	Yes	Late seal with boost, core pulled out with emergency tool
H002-12CS	9202	-	4254.75	4450	-	-	0	Yes	No	No	-	No	Incomplete trigger
H002-13CS	9212	-	4259.4	4485	-	-	0	Yes	?	No	-	No	Incomplete trigger? BV closed
H002-14CS	9277	-	4289.625	5540	-	-	0	No	-	No	-	No	Ball valve only partially closed
H002-15CS	9322	-	4310.55	5408	-	-	0	No	-	No	-	No	Ball valve not closed

Table T8: Pressure coring tool performance. A) Core deployment; B) Core top measured depth in feet below the rig floor (ft RKB); C) Depth of sealing; D) In-situ pressure; E) Pressure boost setting on the PCTB; F) Autoclave DST pressure at sealing; G) Autoclave boosted pressured after sealing as recorded by pressure sensors in data storage tags (DSTs); H) Recovery pressure as measured on the rig after recovery; I) Ball valve closure; J) Upper seal closed; K) Autoclave sealing (ball valve and upper seal combined); L) Did core seal above the in-situ pressure; M) Determination of core hydrostatic condition vs the hydrate stability zone; N) Comments related to tool performance. All values were determined as discussed in Methods: Pressure coring results (Flemings et al., [2025b](https://doi.org/10.5281/zenodo.14104224)). Dataset: <https://doi.org/10.5281/zenodo.14104224>.

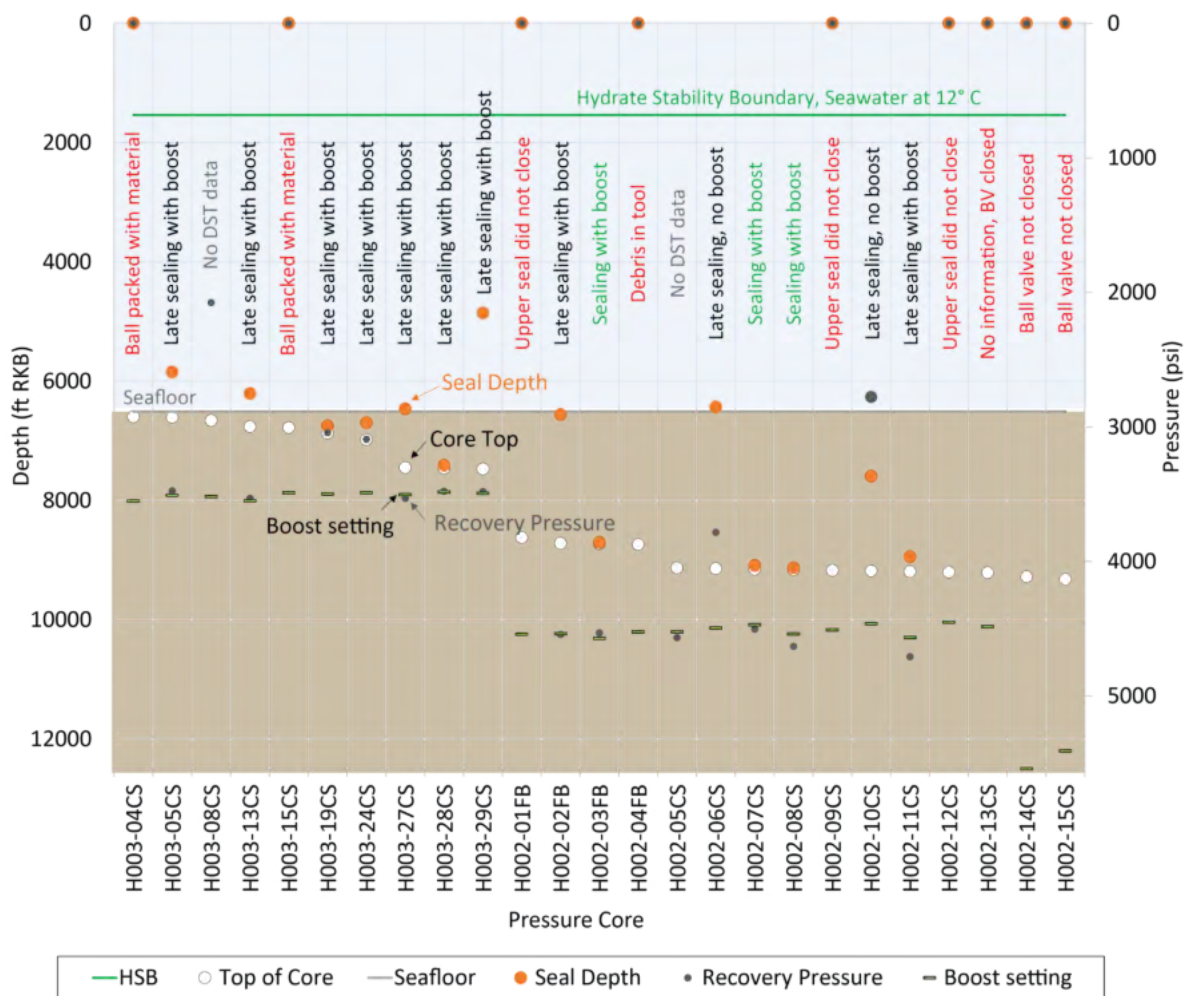


Figure F18: Depth of pressure core sealing for each of the 26 coring deployments with Data Storage Tag (DST) pressure and temperature data. Core top measured depths in feet from the rig floor (ft RKB) are shown as white circles. Boost pressure settings are shown as green dashes. Seal depths are shown as orange circles. Seal depths and seal times were determined from DST data. Recovery pressures were measured with a pressure gauge on the rig and are shown as dark gray circles. Two cores did not seal (H003-04CS and -15CS) because the ball was packed with mud and the ball valve did not close. Values were determined as discussed in Methods: Pressure coring results (Flemings et al., [2025b](https://doi.org/10.5281/zenodo.14104224)). Dataset: [http://doi.org/10.5281/zenodo.14104224](https://doi.org/10.5281/zenodo.14104224).

15CS). The cause of the ball valve failure for these two cores is unknown at this time and no information on the source of the ball valve failure was recorded in the logs.

Possible causes for the ball valve not closing

Possible causes for the ball valve not closing are 1) jamming of the ball with sediment that washes away before arriving at the rig floor; and 2) trying to operate the tool at pressures greater than its workable limit.

Related to the workable limit: the PCTB was successfully tested in a borehole pressured to 5,000 psi (no flow) (Appendix E and F in Flemings, [2020](https://doi.org/10.5281/zenodo.13971276)). Recorded autoclave pressures for these two cores

were less than 5,000 psi (4,400 to 4,500 by DST with a calculated expected in-situ pressure of 4,290 and 4,311 psi). Drill string pressures were not captured for these two deployments and may have been over 5,000 psi.

Related to the sediment jamming the ball or ball valve; many PCTB deployments show surges in the drill string pressure (200-500 psi, measured by a pressure sensor on the wireline) but not the autoclave pressure (measured by a pressure sensor in the PCTB, See Methods: Pressure Coring Tool with Ball Valve (Flemings et al., [2025b](https://doi.org/10.5281/zenodo.14104224))). This indicates some type of blockage of the flow through the bit and possibly just up from the bit between the PCTB and the drill

pipe. Similar to UT-GOM2-1, even when most of the sediment clears, small particles can remain jammed in the mechanisms leaving the ball valve open or partially open as was noted for Core H002-14CS (Flemings et al., [2020](#); Price et al., [2021](#); Thomas et al., [2020](#)).

Also, the ball valve on Core H003-13CS was closed when it arrived at the rig floor and the measured recovery pressure was 3,531 psi. We assumed in this assessment that the PCTB did not seal because of a possible issue with the upper seal (See [Upper seal failures](#)). However, no notes on Core H002-13CS indicated that the upper seal did not trigger. It is instead possible that during the recovery of Core H002-13CS, the ball was temporally jammed with sediment, but the sediment cleared, and the ball valve closed long after the boost pressure (required for sealing) was exhausted (See [Possible causes for late sealing](#)).

Upper seal failures

Three, possibly four, deployments did not seal because the upper seal was not triggered and did not close (Cores H002-01FB, H002-09CS, H002-12CS, and possibly H002-13CS, Table [T8](#), column J).

The reason the tool was not triggered is unknown at this time, but at least one deployment noted a wireline operational error (Core H002-01FB).

Sealing

Ideally, the PCTB seals at coring depth with a pressure equal to the core in-situ pressure and is immediately followed by a pressure boost.

Seventeen UT-GOM2-2 deployments sealed (Table [T8](#), column K). Three of the seventeen deployments sealed on time and twelve sealed late. Two could not be assessed.

Cores H002-03FB, H002-07CS, H002-08CS sealed on time (Table [T8](#), column L, Yes). They sealed at coring depth and at a pressure approximately equal to the estimated core in-situ pressure (Table [T8](#), columns D and F, in-situ and seal pressure). In all three cases the

pressure was immediately boosted (Table [T8](#), column G, boosted pressure).

H003-test and Core H002-05CS did not have usable DST pressure or temperature data and the performance could not be fully assessed. However, based solely on the recovery pressure (gauge pressure measured on the rig floor), which was higher than the core in-situ pressure, they are close to in-situ pressure (Table [T8](#), columns D and H, in-situ and recovery pressure).

Late sealing

Of the twelve deployments that sealed late, seven sealed below in-situ pressure (Table [T8](#), column L), four sealed close to in-situ pressure, and one could not be fully assessed.

Late sealing below in-situ pressure

Seven of the twelve deployments that sealed late, sealed at pressure lower than in-situ pressure. In five of these deployments, pressures were boosted above in-situ (Cores H003-05CS, H003-13CS, H003-27CS, H003-29CS, H002-02FB). In two of these deployments, there was no increase in pressure from the pressure boost (Core H002-06CS and H002-10CS). A slow bleed of the pressure is also visible in the data for these two cores.

One deployment did not have usable DST pressure and temperature data, and the performance could not be fully assessed. It is, however, likely that the core sealed late based solely on the recovered pressure which was much lower than the in-situ pressure (H003-08CS, Table [T8](#), column H).

Late sealing close to in-situ pressure

Four of the twelve late-sealing deployments sealed at approximately in-situ pressure (Table [T8](#), column L). In two of these deployments, the coring tool was temporarily stuck in the BHA (Core H003-11CS and H003-28CS). The PCTB was actuated sometime during the attempted extractions. The cores sealed and a pressure boost was applied.

In the other two of these deployments, the drill string

pressure was elevated above the core in-situ pressure (Cores H003-19CS, H003-24CS). So, even though the core sealed above coring depth, the pressure at which they sealed was still close to in-situ pressure.

Possible causes for late sealing

Possible causes for late sealing are 1) temporary jamming of the ball with sediment that washes away before arriving at the rig floor (See [Possible causes for the ball valve not closing](#)); and 2) late release of the pressure boost.

Engineering tests have shown that a significant pressure differential on the upper seal is required for the autoclave upper seal to rapidly close and fully/tightly seal (Price et al., [2021](#)). This pressure differential is provided by the pressure boost if the borehole pressure is lower than the boost setting. In all deployments, the boost was set higher than in-situ pressure (Table [T7](#), column E), so the boost would be released when the tool was actuated.

Related to the sediment temporarily jamming the ball or ball valve: if sediment was in the ball but washed away very quickly, the boost pressure would have been released before the ball valve closed. The boost could still help close the upper seal, but no boost would likely be visible in the pressure data and the seal would probably not have been tight. This is what we see in Cores H002-06CS and H002-10CS.

Related to late release of the pressure boost: the autoclave upper seal will not close until the boost is released. This is what we observed in most cases with late sealing. Additionally, many of these cores appear to seal when the PCTB clears the BHA. Thus, the late boost may be caused by some amount of friction or minimum activation pressure differential in the pressure boost section that must be overcome before the pressure boost is released.

Temperature history and the hydrate stability zone

For all the Hole H002 cores that sealed, the pressure and temperature of the cores remained continuously at conditions where gas hydrate is stable (Table [T8](#), column M). All temperature measurements of the

autoclave, as measured by a temperature sensor on the IT plug (See Methods: Pressure Coring Tool with Ball Valve (Flemings et al., [2025b](#))), stayed within the hydrate stability zone.

Hole H003 cores are harder to assess. Temperature measurements of the autoclave rose higher and crossed the hydrate stability temperature boundary for several minutes in all deployments. However, temperature measurements of the sensor on the rabbit more closely mimic the temperature of the core (See Methods: Pressure Coring Tool with Ball Valve (Flemings et al., [2025b](#))). Only three Hole H003 cores captured the core temperature of the sensor on the rabbit (H003-27CS through H003-29CS). Of these three cores, two stayed within the hydrate stability zone (H003-28CS and H003-29CS) and one (H003-27CS) may have left the hydrate stability zone for several minutes (assuming the sensor was in thermal contact with the core).

Pressure core recovery

Pressure core recovery is summarized in Table [T6](#). Combining the two boreholes, a total of 179.8 ft (54.8 m) of core was acquired from 25 deployments of the PCTB: there were 4 deployments of the Face Bit configuration (PCTB-FB), and 21 deployments of the Cutting Shoe configuration (PCTB-CS).

There was 105.0 ft (32.0 m) of core retrieved at elevated pressure (green zones, Figure [F12](#), column K) and the remaining 74.8 ft (22.8 m) was processed as conventional core (pink zones, Figure [F12](#), column K). After pressure coring, most of the pressure core was quantitatively degassed (See [Dissolved gas concentrations and hydrate saturation](#)) and processed as conventional core. There was 29.3 ft (8.92 m) of core kept at elevated pressure and transferred to UT Austin for further testing.

The average recovery for the pressure cores in Hole H003 was 76% with a bimodal distribution and peaks around 23% and 99%. Cores H003-05CS, H003-08CS, H003-19CS, and H003-24CS had no fall-in. Core H003-04CS was dominated by chaotic sandy fall-in and the recovery was 107%. In Core H003-13CS, recovery was

14% with over half (26 cm) appearing to be fall-in. Core H003-15CS recovery was 30% with just under half (42 cm) appearing to be fall-in. Recovery for the deeper cores in H003, Cores H003-27CS, H003-28CS, and H003-29CS, was 88%, 25%, and 86%, respectively. H003-29CS might have 10 cm of fall-in at the top.

Fall-in appears to be controlled by the flow rate and not the sweeps. Fall-in was greatest when the flow rate was low (< 50 gpm). Fall-in was not present in Core H003-08CS where the flow rate was higher (84 gpm).

The average recovery for the pressure cores in Hole H002 was 70% with a bimodal distribution and peaks around 36% and 100%. There was no apparent fall-in in any of the Hole H002 cores with the possible exception of H002-10CS, with 30 cm of fall-in or highly disturbed core at the top.

Pressure core recovery was highly dependent on the nature of the sediment. Recovery was low in sand-prone sections. Figure [F14](#) shows an example of the cores across the Red sand. In this case, 3 continuous pressure cores were taken (Core H003-27CS, H003-28CS, and H003-29CS). In sands, where the LWD Gamma ray values are low (Figure [F14](#), column C), borehole calipers record washout (Figure [F14](#), column D), and recovery is low (Figure [F14](#), Core H003-28CS). In contrast, where the section is more mud dominant, recovery is much higher (Figure [F14](#), Core H002-27CS, and H003-29CS). These same characteristics were repeated during pressure coring of the Blue and Orange sands (Figures [F16](#) and [F17](#)). We interpret that these sands were poorly indurated and were washed away during coring.

Conventional coring

This section summarizes the conventional coring results, discusses G-APC and G-XCB performance, and describes conventional core recovery. Conventional core logging is discussed under Physical properties in [Conventional whole core logging](#).

Conventional coring summary

Conventional cores were acquired with G-APC and the

G-XCB tools (Table [T9](#) and example Figure [F19](#)), coring method details are in Methods: Conventional coring Tools (Flemings et al., [2025b](#)). Eighteen G-APC and 1 G-XCB cores were acquired in Hole H003 between 6,506-7,448 ft RKB (0-287.1 mbsf, Table [T9](#)). All of the G-APC cores were acquired from 6,506-7,015 ft RKB (0-155.1 mbsf); the last G-APC core was Core H003-25H. No coring occurred between 7,015-7,420 ft RKB (155.1-278.6 mbsf). A single G-XCB core (Core H003-26X) was acquired at 7,420-7,448 ft RKB (278.6-287.1 mbsf, Figure [F12](#)).

G-APC and G-XCB performance

G-APC deployments achieved full penetration through Core H003-21H (129 mbsf) (e.g. Figure [F19](#), column A). Signs of G-APC refusal began in Core H003-22H (129.2 mbsf) with a partial penetration and partial core liner collapse (Figure [F20](#), column A). The following core, Core H003-23H, had full penetration. G-APC refusal occurred with the acquisition of H003-25H; full stroke was not achieved when firing the tool with all 3 shear pins and all 4 speed control valves fully open (Figure [F19](#), column B). Core H003-25H was also difficult to remove from the core barrel and ultimately had to be cut into sections before core processing. Severe core disturbances were observed including vertical fractures and vertical layering (Figure [F20](#), column B).

G-XCB coring was used to acquire core H003-26X (7,420-7,448 ft RKB, 278-287 mbsf) after drilling (no coring) from 7,015-7,420 ft RKB (155.1-278.6 mbsf, Table [T9](#)) with no issues.

Conventional core recovery

Table [T9](#), column I, shows the core recovery (%) for each core. Core expansion resulted in a conventional core average recovery of 122%. G-APC cores were planned at less than the 31 ft (9.5 m) core liner length to account for expansion. This was accomplished by firing the G-APC a short distance above the top of the formation. G-XCB coring was used to acquire Core H003-26X (278 – 287 mbsf).

The first core (Core H003-01H) had a 93% recovery. All subsequent piston cores to Core H003-21H expanded

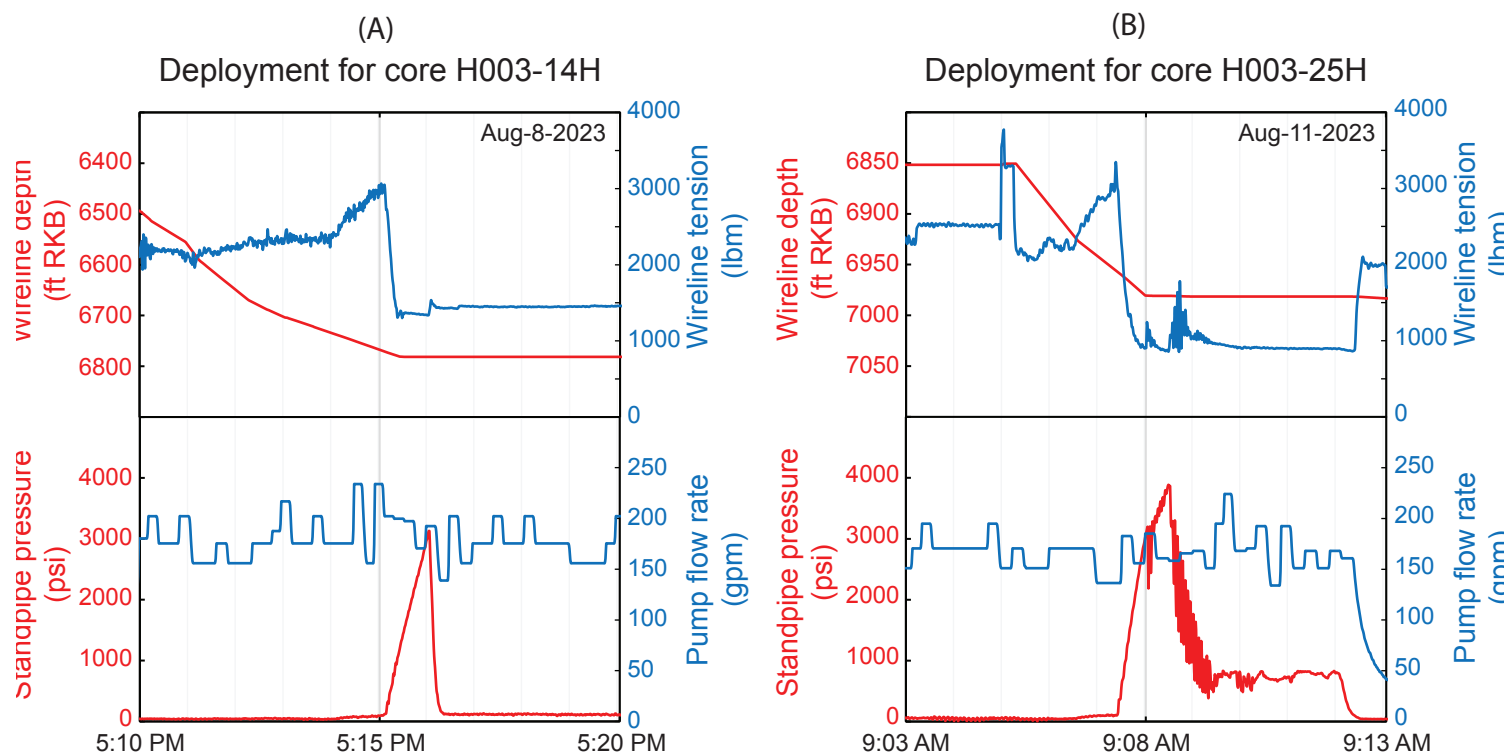


Figure F19: Examples of rig data from two G-APC deployments. A) a complete stroke in Core H003-14H and (B) an incomplete stroke, or G-APC refusal, in Core H003-25H. The top plots show the measured wireline tool depth (red) in feet below the rig floor (ft RKB) and tension (blue) of G-APC tool during acquisition of each core. The bottom plots show the corresponding standpipe pressure buildup (red) and the pump flow rate (blue). In Core H003-14H (A) there is a full stroke and corresponding complete pressure relief. This behavior contrasts with the final G-APC core (Core H003-25H) shown in Core 25H; B) In Core 25H there is incomplete pressure relief after maximum pressure and firing, signaling G-APC refusal and incomplete penetration. The deployment method is discussed in Methods: Downhole tools (Flemings et al., 2025b). Dataset: <https://doi.org/10.5281/zenodo.14518080>.

beyond the cored length (Table T9, column I and Figure F12, column J). Core H003-22H recovered only 95%, but the liner collapsed (See [G-APC and G-XCB performance](#)). Core H003-03H, H003-06H, H003-12H, H003-18H, and H003-25H contained 42 to 213 cm of fall-in at the top.

Cracking and voids could be observed through the core liners (e.g., Figure F21, column C) and pressure relief holes were drilled for safety through the liners.

The first and only conventional rotary core was Core H003-26X and was successful with 100% recovery. Core quality was generally good in this core, despite some biscuited sections.

A. Core	B. Firing Pressure	C. BHA offset	D. Shear Pins	E. Speed Control Valves	F. Depth, Top		G. Cored interval		H. Recovered Length	I. Recovery	J. Comments
	psi	m	1-3	1-4	mbsf	ft RKB	ft	m	m	%	
H003-01H	2300	1.5	2	1	0.0	6506	27	8.2	7.7	93	Mudline core - no voids -H2S at bottom
H003-02H	2100	1.2	2	1	8.2	6533	28	8.5	10.1	118	Slightly expansive-cracks in lower half-slight H2S-SMI likely top fall-in?
H003-03H	2292	1.2	2	1	18.6	6567	28	8.5	10.2	120	Expansive throughout - top fall-in ? - APTC-3 dwell time ~5 mins
H003-06H	1900	2.7	2	1	32.3	6612	23	7.0	10.4	149	Mud sweep - APTC-3 10 min dwell - expansive + sandy fall-in
H003-07H	1950	2.4	2	1	39.3	6635	24	7.3	8.5	116	Pump until just before 'land & fire' - clean hole - expansive
H003-09H	2048	2.7	2	2	49.7	6669	23	7.0	8.9	127	APTC-3 10 min dwell - expansive - voids throughout
H003-10H	2042	2.7	2	2	56.7	6692	23	7.0	8.3	118	APTC-3 10 min dwell - expansive -voids throughout
H003-11H	2100	2.7	2	2	63.7	6715	23	7.0	9.2	132	No APTC-3 expansive -voids throughout
H003-12H	2250	2.7	2	2	70.7	6738	23	7.0	9.2	132	APTC-3 10 min dwell - Delays on rig floor - not full pressure release - expansive - voids at bottom
H003-14H	3060	2.1	3	4	80.8	6771	25	7.6	9.4	124	Full penetration voids throughout
H003-16H	3100	3.4	3	4	91.4	6806	21	6.4	8.2	128	Full penetration voids throughout
H003-17H	3150	3.4	3	4	97.8	6827	21	6.4	8.6	135	Full penetration voids throughout
H003-18H	3147	3.0	3	4	104.2	6848	22	6.7	9.6	143	Full penetration voids throughout
H003-20H	3200	2.1	3	4	114.0	6880	25	7.6	9.0	119	Full penetration voids throughout
H003-21H	3100	2.1	3	4	121.6	6905	25	7.6	8.6	113	Full penetration
H003-22H	3600	2.1	3	4	129.2	6930	25	7.6	7.3	95	Partial penetration - partial collapsed liner at top
H003-23H	3800	2.1	3	4	136.9	6955	25	7.6	8.8	116	Partial penetration - no flow-in
H003-25H	3750	2.1	3	4	147.5	6990	25	7.6	10.5	137	Partial penetration stuck liner - hydraulic extraction -possible flow-in -APC Refusal - change to XCB
H003-26X	n/a	n/a	n/a	n/a	278.6	7420	28	8.5	8.5	100	Good core, voids throughout, likely biscuited

Table T9: Hole H003 Conventional G-APC and G-XCB cores. A) Core/core barrel deployment. H = Advanced Piston Corer. X = Extended Core Barrel; B) Standpipe pressure at firing; C) BHA offset above total depth; D) Number of shear pins used; E) Number of open speed control valves; F) Measured depth of the top of the core in meters below the seafloor (mbsf) and feet below the rig floor (ft RKB); G) Cored interval/core throw in ft and m; H) Archived length; I) Recovery; J) Comments. The code 'H', as in 09H, refers to G-APC cores whereas 'X' refers to G-XCB core. Values were determined using the methods in Methods: Conventional coring results (Flemings et al., 2025b). Dataset: <https://doi.org/10.5281/zenodo.14518080>.

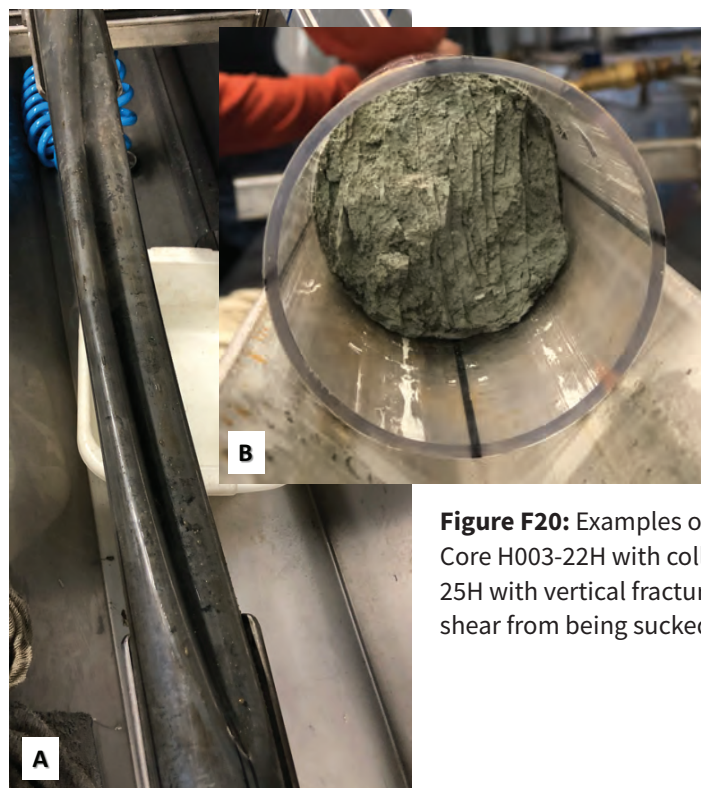


Figure F20: Examples of G-APC cores with damage. A) Core H003-22H with collapsed liner; and B) Core H003-25H with vertical fractures, possibly due to pervasive shear from being sucked into the liner.



Figure F21: Photos of G-APC coring during UT-GOM2-2. A) G-APC core barrel with core liner being prepared for removal; B) Core being removed from barrel and entering the core receiving lab; C) Typical G-APC core with full or nearly full recovery, minor voids and expansion cracks; D) G-APC core on receiving track before sampling, cutting, and curation.



Members of the science party inspect core at the Geotek Coring Inc. facilities in Salt Lake City, Utah. Pictured left to right: The Ohio State University professor Ann E. Cook, University of New Hampshire students Kayla Tozier and Camille Sullivan, U.S. Geological Survey scientist Timothy S. Collett, and University of New Hampshire professor Joel E. Johnson. Photo credit: Peter B. Flemings

Lithostratigraphy

Lithologic units

The lithostratigraphy was divided into seven lithologic units (Unit I to VII, Figure [F22](#) H and I). Each unit is composed of one or more lithofacies (Figure [F22](#) H and I, Figure [F23](#), and Table [T10](#)). Both the core data from Holes H002 and H003 and the logging while drilling (LWD) data from Hole H001 were used to define the lithologic units and the lithofacies. In cored intervals, the lithofacies could be described directly and compared to the LWD data. In intervals where no core was present, the lithofacies were interpreted from the LWD data.

Lithologic Unit I – Seafloor Sand (0-4.5 mbsf)

Unit I is the sand at the seafloor (Figure [F22](#)). This sand was sampled by the first core, Core H003-01H, which recovered a sandy interval from 0-4.5 mbsf. Slab images from computed tomography (CT) suggest a fairly uniform coarse-grained lithology (Figure [F8](#)). More than 80% of the sediment is sand (yellow circles Figure [F23](#) A.). These sediments are composed of quartz and feldspar and lithics in equal proportions (yellow circles Figure [F23](#) B.).

Lithologic Unit II – Interbedded Mud & Silt with Ooze (4.5-160 mbsf)

Unit II is composed of interbedded Ooze and Mud & Silt (Figure [F22](#), Figure [F24](#) (D, E, F, and G), and Figure [F25](#)). The Ooze has a high percentage of calcareous nannofossils, a high porosity, a low bulk density, and a low clay content (white circles and triangles Figure [F23](#) B, Figure [F24](#) D, F and G, and Figure [F25](#)) sediment with variably

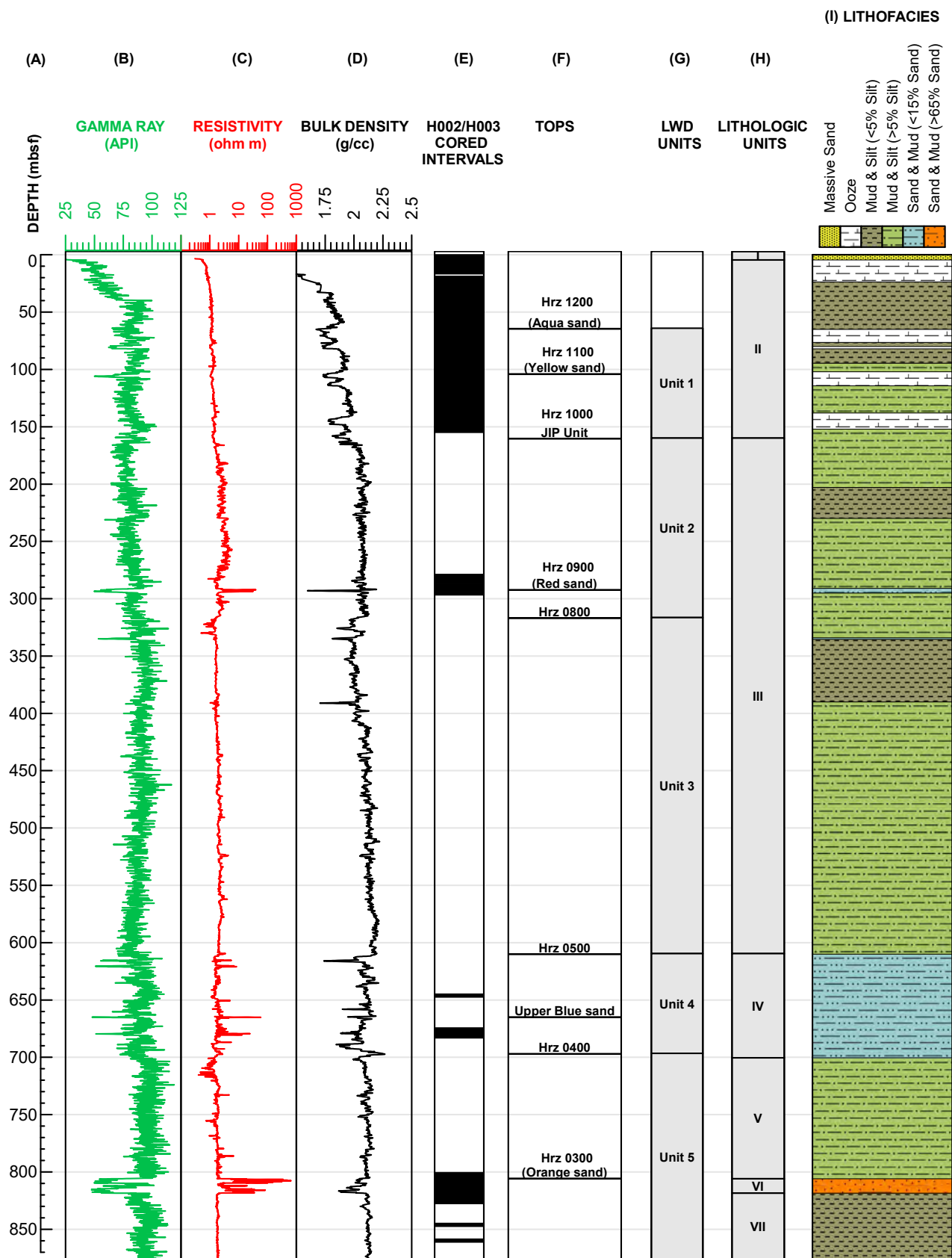
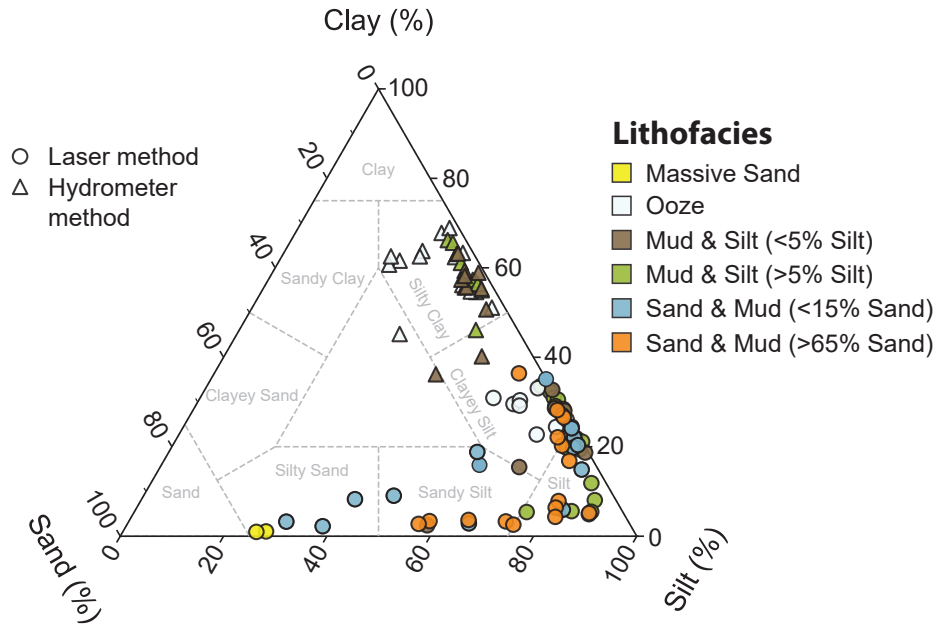


Figure F22: Interpreted Site H lithologic units and lithofacies. A) Measured depth in meters below the seafloor (mbsf); B) Projected Hole H001 logging while drilling (LWD) gamma ray in green. The depth projection of Hole H001 LWD data onto Hole H002 and Hole H003 is discussed in [Plotting H001, H002, and H003 downhole data](#); C) Projected LWD resistivity in red; D) Projected LWD bulk density in black; E) Cored interval for Hole H003 and Hole H002 in black; F) Seismic reflectors (Hrz = Horizon) and stratigraphic tops as described in Table [T4](#); G) LWD units (See Summary (Flemings et al., [2025a](#))); H) Lithologic Units; I) Lithofacies at Site H, as defined in Table [T10](#).

(A) Grain Size



(B) Composition

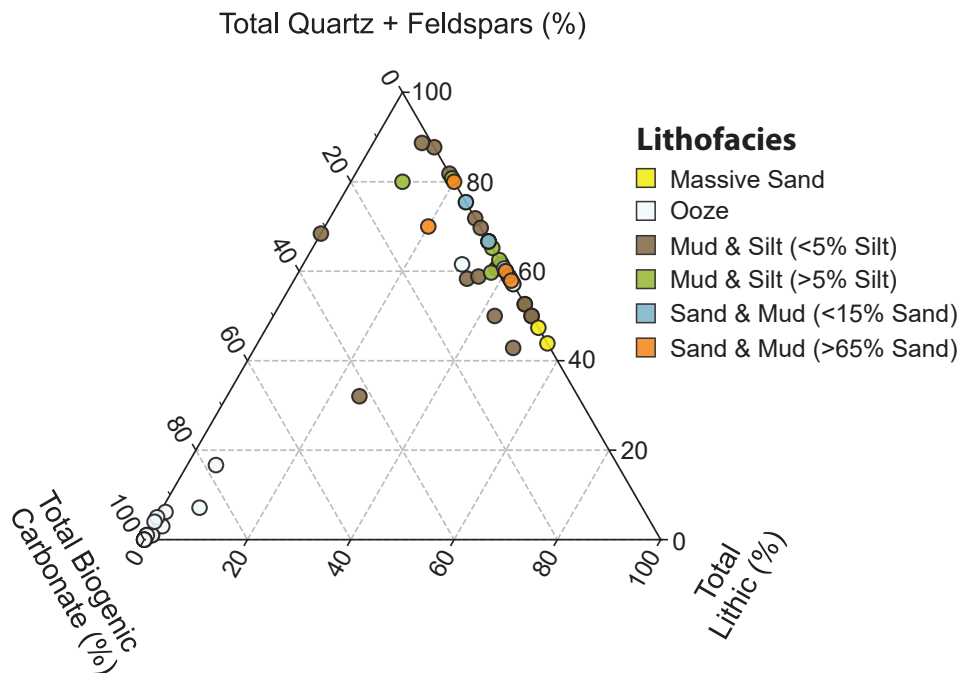


Figure F23: Ternary plots of sediment grain size and composition. Results are colored by lithofacies (e.g. Figure F22, column I and Table T10); A) Ternary diagram modeled after Shepard's diagram (Shepard, 1954). In this representation, the clay-sized particles are assumed to be smaller than 2 μm and the silt-sized particles are assumed to be smaller than 75 μm as described in the Unified Soil Classification System (ASTM International, 2017). This approach is commonly used in geotechnical engineering and contrasts the approach commonly used by geoscientists wherein clay-sized particles are smaller than 3.9 μm and silt-sized particles are smaller than 62.5 μm (Shepard, 1954). Two methods were used to determine particle size distribution: laser particle analysis (circles) and hydrometer (triangles). See Methods: Grain size (Flemings et al., 2025b). The mud within the finer-grained lithofacies (Mud & Silt) plot as a clayey silt when measured with the laser method whereas they plot as silty clay with the hydrometer method. Systematic laser and hydrometer method comparison studies have shown that the laser method typically reports a larger particle size for plate-shaped clay particles than does the hydrometer method (Di Stefano et al., 2010; Ferro and Mirabile, 2009; Wen et al., 2002). This is because the laser method reports a value weighted towards the average particle dimension, whereas the hydrometer method reports a value weighed towards the thin (short) dimension (Di Stefano et al., 2010; Ferro and Mirabile, 2009). Ternary plots for each method can be found in Particle size distribution; B) Ternary plot of the sediment composition derived from smear slide analysis. Grain size dataset: <http://doi.org/10.5281/zenodo.14109861>, Composition Dataset: <http://doi.org/10.5281/zenodo.14518170>.

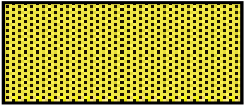
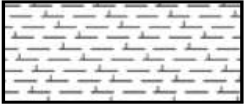
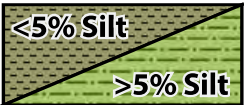
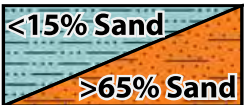
A) Lithofacies Legend	B) Lithofacies Name	C) Lithofacies Description
	Massive Sand	Massive sand lithology
	Ooze	Ooze lithology
	Mud & Silt	Interbedded mud and silt lithologies. If the total thickness of the silt beds is less than 5% of the total thickness, it is colored green. If the total thickness of the silt beds is more than 5% of the total thickness, it is colored light green.
	Sand & Mud	Interbedded sand and mud lithologies. If the total thickness of the sand beds is less than 15% of the total thickness, it is colored blue. If the total thickness of the sand beds is more than 65% of the total thickness, it is colored orange.

Table T10: Lithofacies classification at Site H. Four lithofacies composed of one or more lithologies were defined.

present foraminifera. Figure F24 images show that the Mud & Silt lithofacies is dominated by clayey silt, but it can have a few very thin layers of silt present. Determinations of the classification of grains in Figure F24 was based on the hydrometer particle size distribution using the geotechnical classification of sediment (See Methods: Grain size (Flemings et al., 2025b)). A comparison of the resulting classifications using laser particle analysis versus the hydrometer, as well as the geotechnical versus the geoscientific classification, is discussed in Particle size distribution.

Lithologic Unit III – Mud & Silt (160-610 mbsf)

Unit III is dominated by mud with minor silt layers (Figure F22). Within this interval, only the mud with around the single thin sand at ~300 mbsf, the Red sand (Figures F14 and F22), has been sampled to date. This mud is a silty clay grain size when analyzed with the hydrometer method.

Lithologic Unit IV – Interbedded Sand & Mud (610-700.5 mbsf)

Unit IV is composed of the Sand & Mud lithofacies

(Figures F22 and F26, and expanded Figure F27 and Figure F28). This lithologic unit represents the Blue sand and includes the hydrate-bearing Upper Blue sand (Figure F22). The analyzed samples show a bimodal distribution with the sand beds ranging from silty sand to sandy silt and the mud beds being a clayey silt (blue circles in Figure F23 A, and Figures F27 and F28).

Lithologic Unit V – Mud & Silt (700.5-805.75 mbsf)

Unit V is composed of the Mud & Silt lithofacies and is similar to Unit III (Figure F22). Two pressure cores sampled the bottom of this unit.

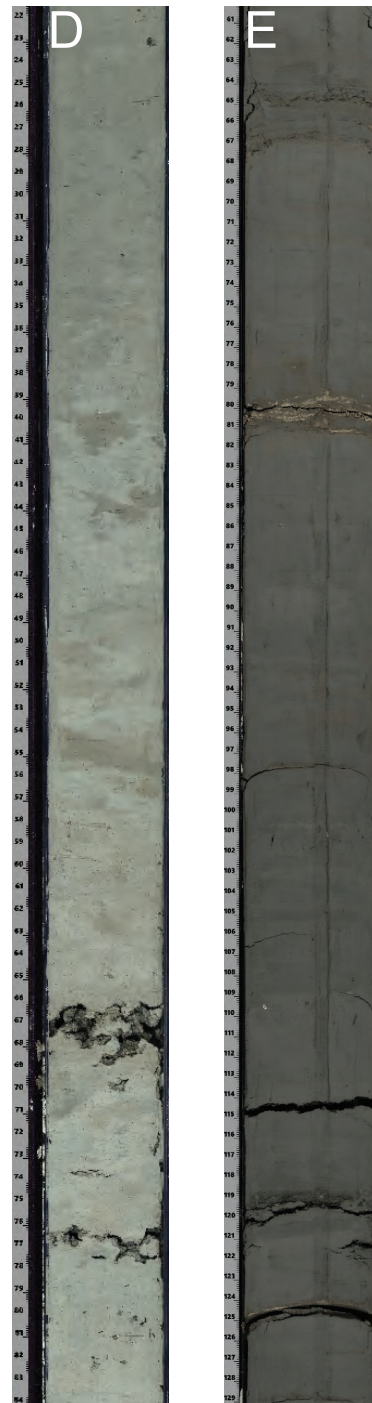
Lithologic Unit VI – Interbedded Sand & Mud (805.75-818.5 mbsf)

Unit VI is composed of the Interbedded Sand & Mud lithofacies. The percent of the sand is much larger than in the overlying Unit IV (Figures F22 and F29). This unit is called the Orange sand (Figure F22). One conventionalized (depressurized pressure core) core, Core H002-09CS, was described and sampled for grain size analysis from the lower quality sand (812.6 mbsf,

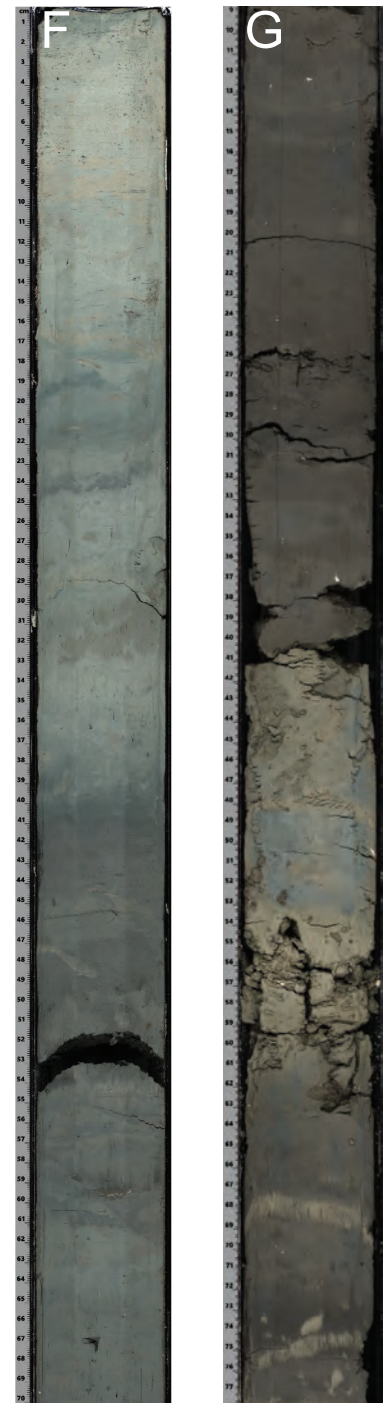
Sedimentary Structures



Lithology



Contacts



Diagenesis

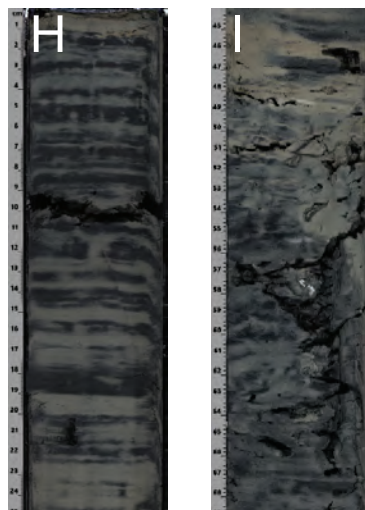


Figure F24: Lithostratigraphy examples of Lithologic Unit II. Sedimentary structures: A) Lithologic Unit II Laminations (Section H003-03H-7); B) Bioturbation (Section H003-03H-2); C) and Graded beds (Section H003-12H-5); Lithology: D) Foraminifera-bearing calcareous nannofossil ooze, with bioturbation (Section H003-19CS-4); E) Mud with silt beds (Section H003-20H-3); Contacts: F) Gradational contact within a bioturbated carbonate ooze dominated interval (Section H003-12H-4); G) Sharp contact between bioturbated carbonate ooze, lower, and mud, upper (Section H003-25H-10-1); Diagenesis: H) Iron sulfide precipitation within laminated sediments (Section H003-14H-5); I) bioturbated sediments (Section H003-02H-4). Rulers show the archived depth in the section. Images are from split core line scan camera imagery. See Methods: Split core logging and imaging (Flemings et al., [2025b](#)). Dataset: <http://doi.org/10.5281/zenodo.14261688>.

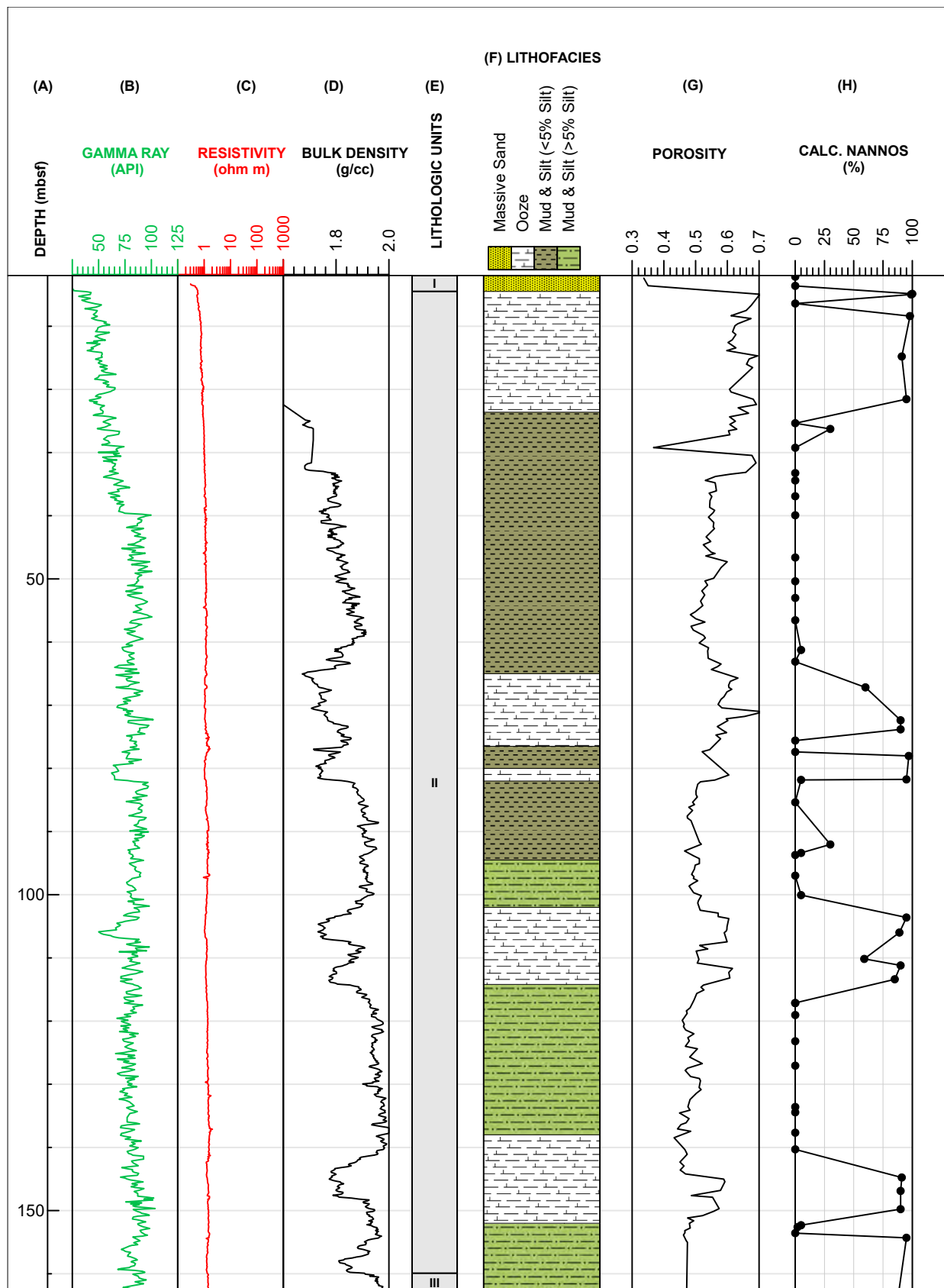


Figure F25: Comparison of Hole H001 LWD data with Hole H003 core data within Lithologic Unit II. A) Measured depth in meters below seafloor (mbsf); B) Projected Hole H001 logging while drilling (LWD) gamma ray in green. The depth projection of Hole H001 LWD data onto Hole H002 and Hole H003 is discussed in Plotting H001, H002, and H003 downhole data; C) Projected LWD resistivity in red; D) Projected LWD bulk density in black; E) Lithologic units; F) Lithofacies (Table T10); G) Porosity derived from moisture and density measurements on core using compressed measured depths (See Index properties); H) Fraction of calcareous nannofossils based on smear slide analysis using compressed measured depths.

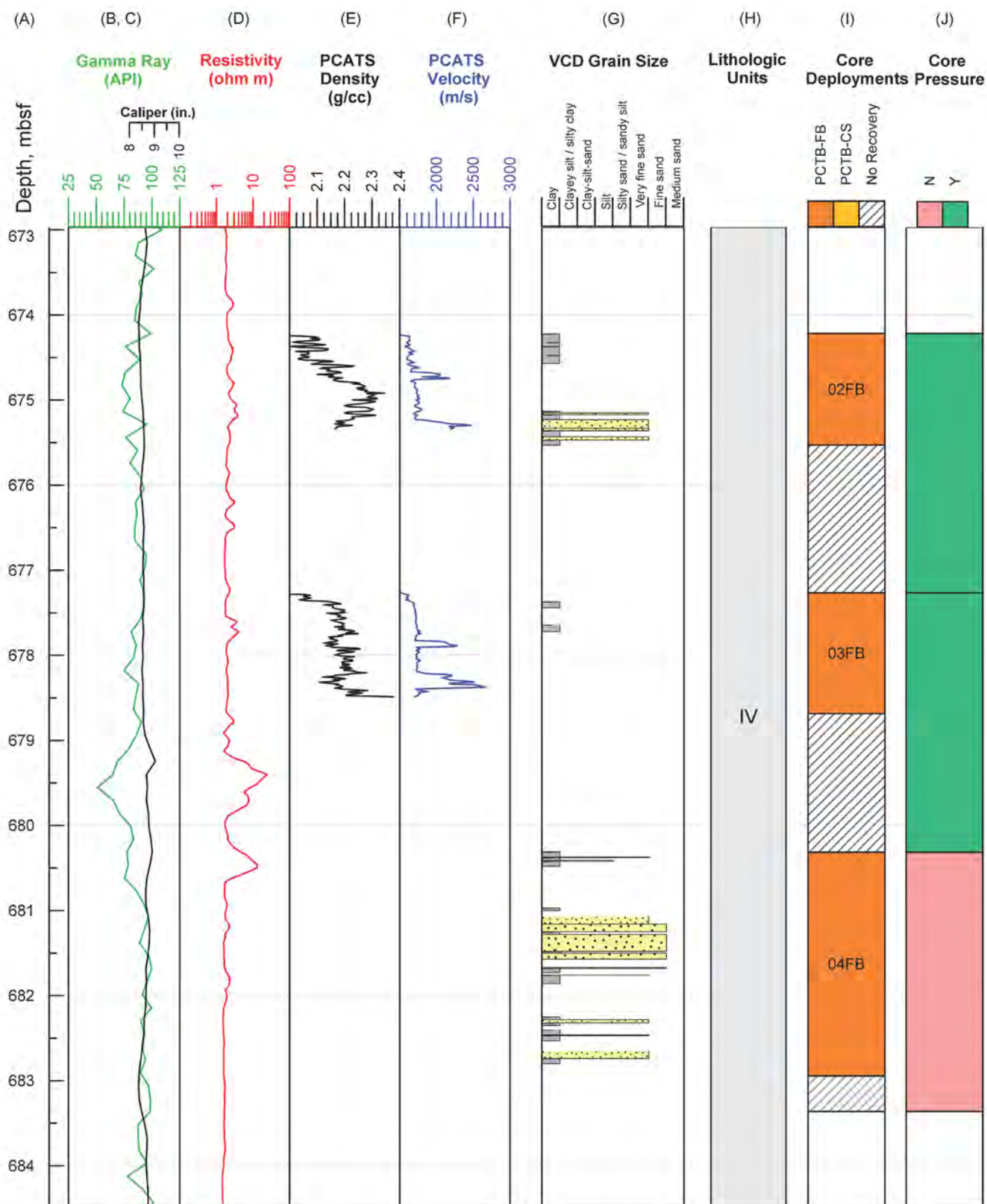


Figure F26: Representative interval of Lithostratigraphic Unit IV (the Upper Blue sand interval). A) Measured depth in meters below the seafloor (mbsf); B) Logging while drilling (LWD) gamma ray in green; C) LWD caliper in black; D) LWD resistivity in red; E) Pressure Core Analysis and Transfer System (PCATS) pressure core gamma density in black; F) PCATS pressure core P-wave velocity in blue; G) Visual Core Description (VCD) of grain size: sands = yellow, silts = blue, clay = gray; H) Lithologic unit; I) Core deployments using the Pressure Coring Tool with ball valve in the Face Bit configuration (PCTB-FB) in orange; J) Recovery pressure for the pressure cores measured with a pressure gauge on the rig. Cores recovered at elevated pressure are shown as green and at atmospheric pressure are shown as pink.

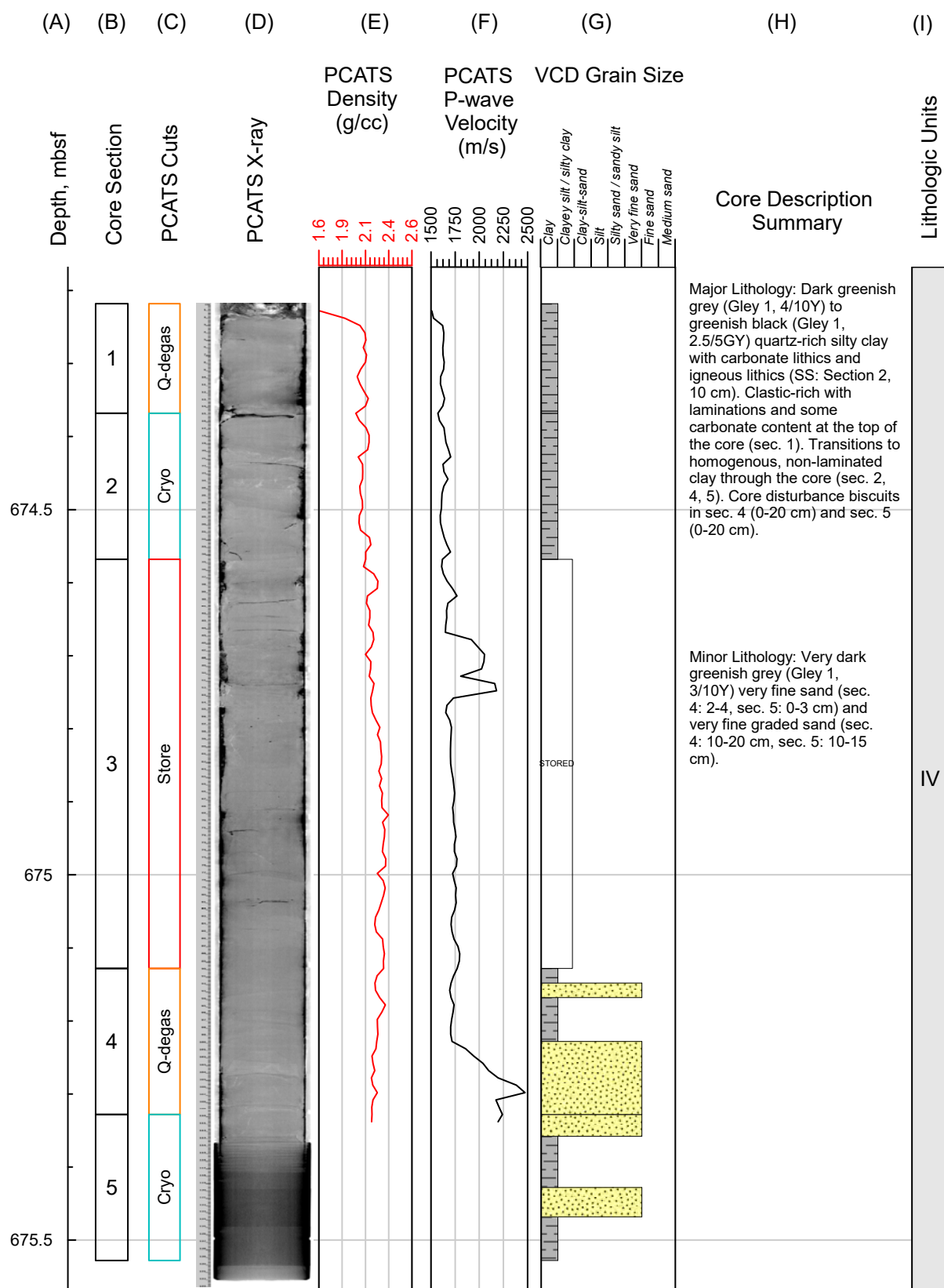


Figure F27: Expanded view of Lithologic Unit IV (the Upper Blue sand interval), which is composed of the Sand and Mud lithofacies (Table T10) showing Core H002-02FB, 674.2-677.3 mbsf (the larger interval is illustrated in Figure F16 above). A) Measured depth in meters below the seafloor (mbsf); B) Core section; C) Core allocation either to quantitative degassing (Q-degas), storage and later transported to UT (Store), or cryogenic freezing followed by depressurization for microbiology studies (Cryo); D) Pressure Core Analysis and Transfer System (PCATS) X-ray image (slab view of Computed Tomography (CT) data); E) PCATS pressure core P-wave velocity in red; F) PCATS pressure core gamma density in black; G) Visual Core Description (VCD) of grain size: sands = yellow, silts = blue, clay = gray; H) VCD summary; I) Lithologic unit.

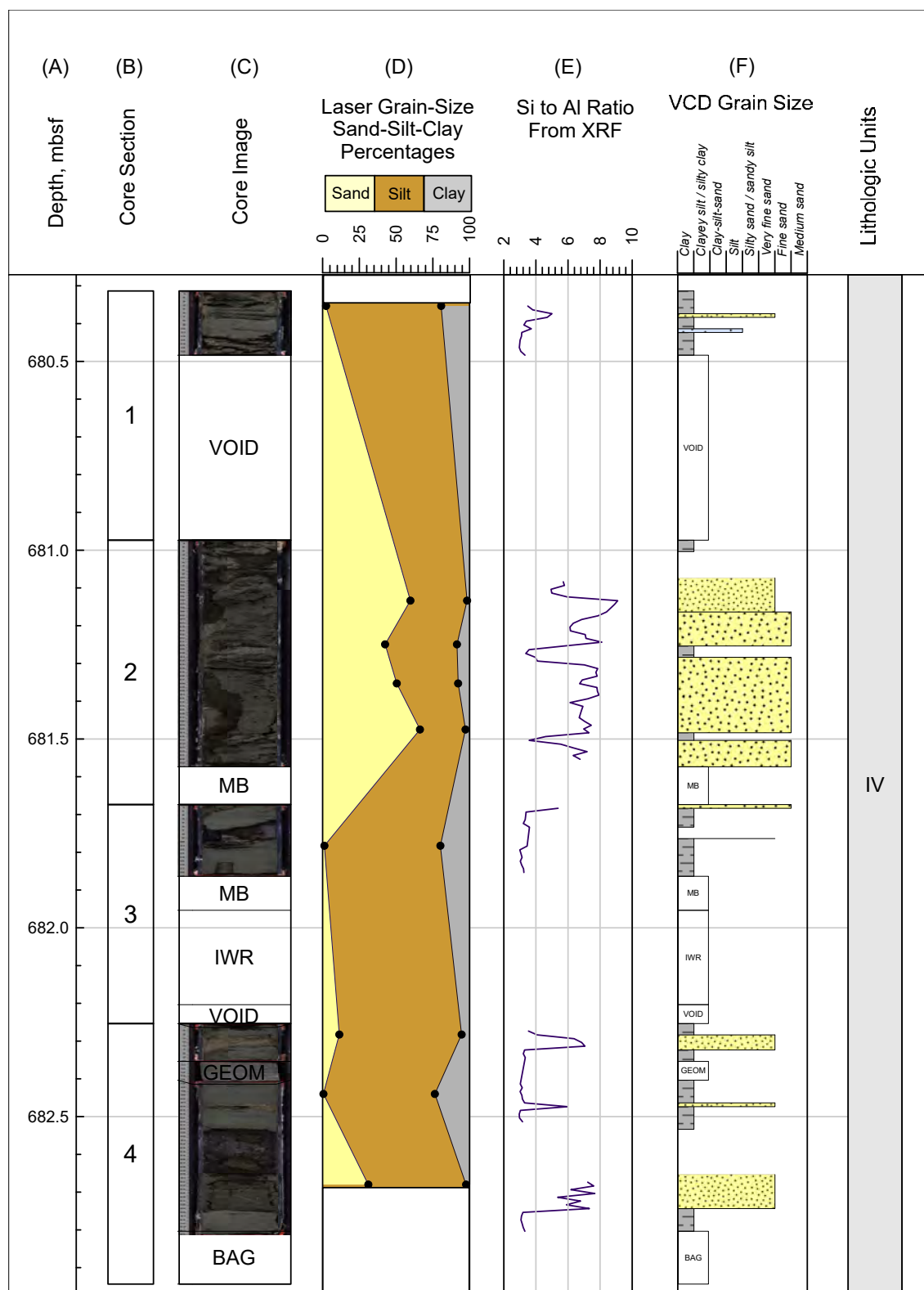


Figure F28: Expanded view of Lithologic Unit IV (Upper Blue sand) showing Core H002-04FB 680.3-683.3 mbsf (the larger interval is illustrated in Figure F26). This core was recovered at atmospheric pressure (Figure F26, column J) and thus, could be split, sampled, and described. A) Measured depth in meters below the seafloor (mbsf); B) Core section number; C) Split core images from a line scanner; D) Grain size from laser particle analysis using the geoscience classification; E) Uncalibrated silicon to aluminum ratio calculated from X-ray fluorescence (XRF); F) Visual Core Description (VCD) of grain size: sands = yellow, silts = blue, clay = gray. Whole-round samples removed before VCD are shown including samples for microbiology (sample code MB), routine pore water (sample code routine interstitial water or IWR). Voids (VOID) are also marked and were not described or scanned. Core H002-4FB recovery was less than the core throw, therefore archived and compressed measured depths are the same; all columns are plotted in archived depth.

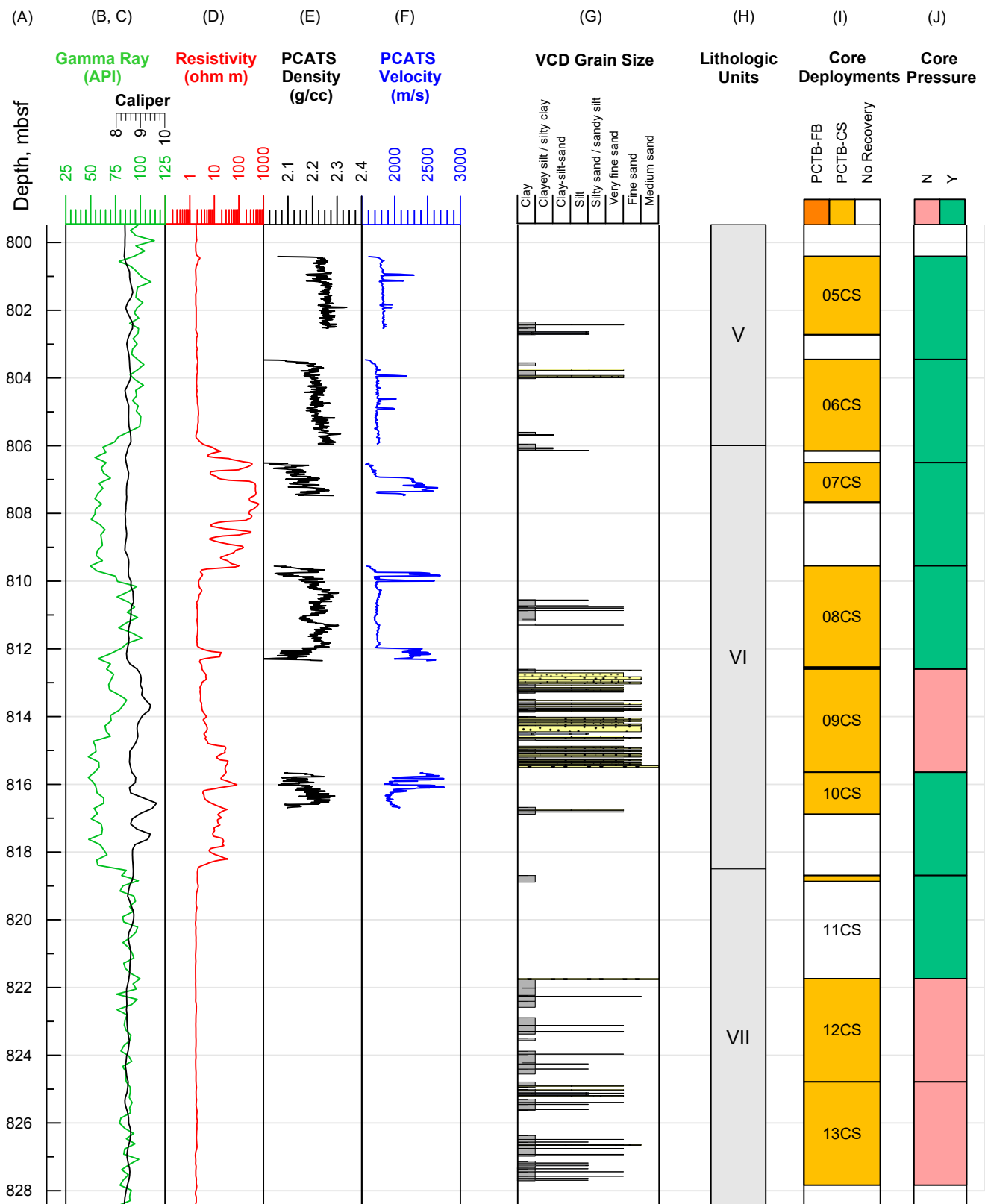


Figure F29: View of Lithologic Units V, VI and VII. Lithologic Unit VI is composed of the Mud and Sand lithofacies and is also called the Orange sand. A) Measured depth in meters below the seafloor (mbsf); B) Logging while drilling (LWD) gamma ray in green; C) LWD caliper in black; D) LWD resistivity in red; E) Pressure Core Analysis and Transfer System (PCATS) pressure core gamma density in black; F) PCATS pressure core p-wave velocity in blue; G) Visual Core Description (VCD) of grain size: sands = yellow, silts = blue, clay = gray. H) Lithologic units; I) Core deployments using the Pressure Coring Tool with ball valve in the Cutting Shoe configuration (PCTB-CS) shown in dark yellow; J) Recovery pressure for the pressure cores measured with a pressure gauge on the rig. Cores recovered at elevated pressure are shown as green and atmospheric pressure are shown as pink; An expanded view of Lithologic Unit VI Core H002-09CS is presented in Figure F30.

Figure [F30](#)). The analyzed samples show a bimodal distribution with the sand beds being a sandy silt and the mud beds being a clayey silt (orange circles in Figure [F23](#) A). These sediments are composed of mainly quartz and feldspar with some lithics (orange circles Figure [F23](#) B).

Lithologic Unit VII – Mud & Silt (> 818.5 mbsf)

Unit VII is composed of mud and is similar to Unit III and Unit V (Figures [F22](#) and [F29](#)).

Detailed sedimentology from visual core description

Visual core descriptions are summarized in full page core lithostratigraphic summaries produced with the software Strater are shown in Appendix D: Lithostratigraphy Core Summaries. During core description, a major and a minor lithology was determined based on the relative abundance of the lithology in the core on the describing table. The major lithology was most often mud (Figure [F23](#) A). In a few cases, the major lithology was silt- and sand-sized material.

Cores from Hole H003 (0-296.4 mbsf) penetrated Lithologic Units I, II and the upper part of Lithologic Unit III (Figures [F12](#) and [F22](#)). Unit I contains the thickest sand beds and occurs at the top of Core H003-01H (Figure [F8](#)). This material reappears as fall-in material in the tops of Cores H003-3H, H003-4CS (all of core), H003-6H, H003-12H, H003-13CS, H003-15CS, H003-18H, and H003-25H.

Lithologic Units II and III are predominantly composed of variably colored muds with silt to fine sand laminations (mm scale) and a few beds (up to ~10 cm). The coarser material is interspersed throughout the hole, but more common in the deeper strata (at the base of Lithologic Unit II and in Lithologic Unit III). Sand and/or silt beds (Figure [F24](#) C and E) are present as minor lithologies in Cores H003-1H, H003-2H, H003-3H, H003-7H, H003-11H, H003-12H, H003-16H, H003-17H, H003-25H, H003-26X, H003-29CS, and notably most abundant from 114-

145 mbsf (Cores H003-20H though H003-23H, Base of Unit II) (See Appendix D: Lithostratigraphy Core Summaries).

Laminations and bioturbation are variably preserved throughout Lithologic Unit II and the upper part of Unit III (Figure [F24](#) A and B), reflecting potential bottom water oxygenation changes through time. Bioturbation is variable throughout the clays and notably present within many of the silt and sand laminations and beds (e.g. Figure [F24](#) E, 80 cm). The color variation in the muds throughout Lithologic Units II and III (Figure [F24](#)) appears to be largely driven by changes in the proportions of calcium carbonate biogenic grains relative to the clay-sized lithogenic particles (Figure [F25](#)). Iron sulfide precipitation presents as a black colored overprint on the sediments that amplifies the bioturbation and laminations (Figure [F24](#) H and I) and occurs as framboidal pyrite and iron sulfide aggregates in smear slide and pyritized burrows and micronodules (up to 1 cm) on some split core surfaces, but more visible in XCT images.

Three sharp contacts were mapped by abrupt changes in lithology (e.g. Figure [F24](#) G): at 82 mbsf (Core H003-14H-1, 123.5 cm), 152 mbsf (Core H003-25H-4 to 5, at the section break), and 156 mbsf (Core H003-25H-10, 40 cm).

Pressure cores were acquired intermittently over a measured depth range from 644.6-859.6 mbsf (Figure [F12](#) I). These cores spanned Lithologic Units IV, V, VI, and VII (Figure [F22](#)). A large fraction of the sediment recovered from these cores was stored in pressure vessels for later analyses or designated as whole-round samples for interstitial water and/or geomechanics samples (e.g. Figure [F27](#) G and Figure [F28](#) F). Thus, much of the sediment within Lithologic Units IV to VII has not been described. Specifically, more than half of Cores H002-1FB, H002-3FB, H002-5CS, H002-6CS, H002-8CS, H002-10CS, H002-15CS, and all of core H002-7CS were not described.

Cores H002-1FB to H002-4FB penetrated Unit IV (the Blue unit) (e.g. Figures [F12](#) and [F26](#)). The thickest sand bed in Lithologic Unit IV occurs in the bottom

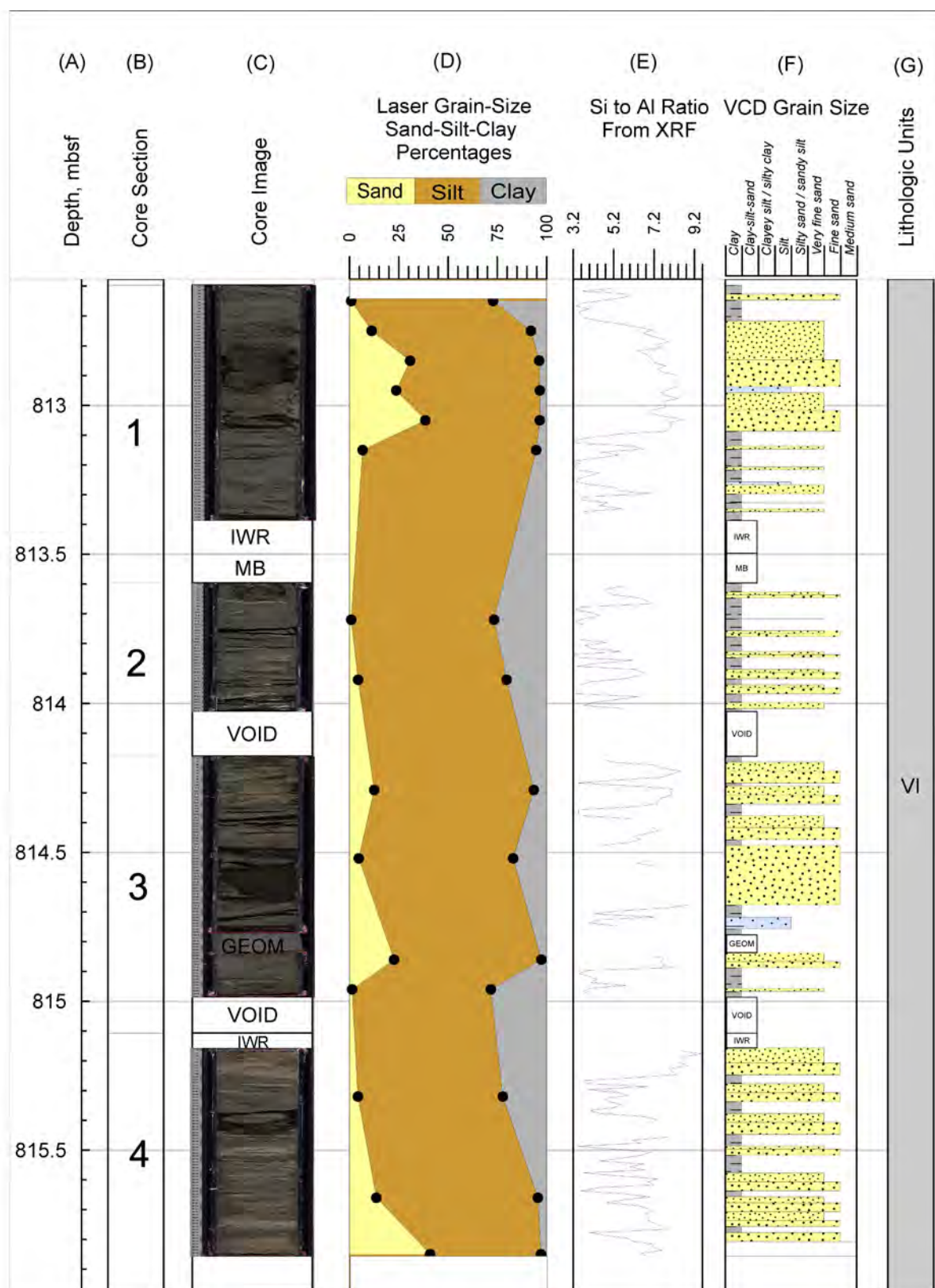


Figure F30: Expanded view of Lithologic Unit VI which is composed of Sand and Mud lithofacies. This is also part of the Orange sand (Core H002-09CS (812.6 to 815.6 mbsf)). This core was recovered at atmospheric pressure (Figure F29, column J) and thus could be split, sampled, and described. A) Measured depth in meters below seafloor (mbsf); B) Section number; C) Split core images from the Geotek Line scanner; D) Grain size from laser particle analysis using the geoscience classification; E) Uncalibrated silicon to aluminum ratio calculated from X-ray fluorescence (XRF); F) Visual Core Description (VCD) of grain size: sands = yellow, silts = blue, clay = gray. Whole-round samples included microbiology (sample code MB) and routine pore water (sample code routine interstitial water or IWR). Voids (VOID) are marked and were not described or scanned; Core H002-09CS recovery was greater than the core throw; all columns are plotted using archived measured depth.

of Core H002-2FB (Figure [F26](#)). Sharp bases and normal grading are common in the silt and sand beds. Iron sulfide precipitation presents as a black colored overprint on the sediments that amplifies the bioturbation in Core H002-01FB and occurs as framboidal pyrite in smear slide and at a macroscale as pyritized burrows on some split core surfaces.

Cores H002-5CS and H002-6CS penetrate Lithologic Unit V, immediately above Lithologic Unit VI (the Orange sand) (Figure [F29](#) H, I). Although the LWD GR and resistivity suggest this interval is mud prone, there were several centimeter to decimeter thick fine sands present (Figure [F29](#)).

Cores H002-7CS to H002-10CS penetrate Lithologic Unit VI (the Orange sand) (Figure [F29](#) H, I). Recovery was poor in this interval (Figure [F29](#)). Core H002-09-CS illustrates the sand-rich nature of the Orange Sand. Interbedded sand and mud are observed throughout 644.6-859.6 mbsf in Lithologic Unit VI (Figure [F30](#)). Millimeter- to centimeter-scale interbedded sand and mud laminations are common; the muds are typically medium-gray colored (e.g. Figure [F30](#), 813.2-813.3 m) and the thicker sands are typically dark-brown colored (e.g. Figure [F30](#), 812.8-812.9 m). Silt-sized grains dominate the particle size even in the finer grained intervals, suggesting mud- and coarser-sediment gravity flows dominate the depositional regime. High Si to Al ratios correspond to sand-rich intervals (quartz-rich sands) and low ratios correspond to clay-rich intervals (aluminum-rich phyllosilicates) (Figure [F30](#) E). Individual sand and clay laminae are indicated by the step-like breaks in grain size. Visual grain-size determinations tend to record the size of coarser fraction of the particle size distribution. In this case, the sands are visually interpreted to have a maximum grain size of fine sand (Figure [F30](#), 125-250 μm).

Cores H002-11CS, H002-12 CS, and H002-13CS are interpreted to penetrate Lithologic Unit VII (Figure [F29](#) H, I). As in Lithologic Unit V, the LWD GR and resistivity suggests this interval is mud prone, yet there are several centimeter to decimeter fine sands present (Figure [F29](#)). Bioturbation is variably

preserved throughout Lithologic Units IV, V, VI, and VII, 644.6-859.6 mbsf (Hole H002), and more commonly observed in the clays than in the coarser beds. The color variation in the mud is less variable throughout Lithologic Units IV, V, VI, and VII, compared to Units I, II, and III. Only one sharp color boundary is observed (H002-8CS-3, 27 cm).

Core-disturbance biscuits are common throughout the core. However, they can be masked in uniform intervals of dark colored clay. Laminations are present in some intervals; however, care should be taken not to confuse them with the core disturbance biscuit slurry that bounds individual biscuits. Light colored, well sorted silt lamina (1 mm) infilling fractures in the cores are most likely desiccated barite from the drilling mud. Care should be taken to not to confuse these features with similar scale primary lithogenic silt and sand lamina and beds (e.g. Figure [F24](#) C). Ba from XRF scanning can be used to identify injections of barite into the core .

Gas hydrate, preserved in a recovered core, was observed in Core H002-11CS after it was cryogenically frozen, depressurized, thawed, and split open in Salt Lake City. The resulting archived sediment is fluidized due to gas hydrate dissociation.

Sediment composition from smear slides

Fifty-nine smear slides were collected. Compositional determinations from smear slides are summarized in full page core lithostratigraphic summaries produced in Strater and shown in Appendix D: Lithostratigraphy Core Summaries.

In Lithologic Unit II (4.5-160 mbsf, Figure [F22](#)), calcareous nannofossil oozes +/- foraminifera, which we refer to as oozes, are interbedded with mud. The mud is dominated by clay minerals but also contains clay-sized quartz, carbonate lithics, feldspar (microcline and plagioclase), and igneous lithics (Table [T10](#)). In smear slide, the clay content within the oozes may be underestimated due to the presence of isotropic clay minerals. Initial calculations of calcium carbonate content by difference of total

carbon and total organic carbon (See [Sedimentary geochemistry](#)) suggest carbonate content within the oozes may be less abundant than the smear slides indicate. Carbonate content is often overestimated in smear slide observations, especially in smectite-rich sediments (Phillips and Littler, [2022](#)). The ternary diagram in Figure [F23](#) B, summarizes this range in composition throughout Lithologic Unit II. The transition between the mud and ooze is gradational; the muds contain trace to bearing amounts of calcareous nannofossils and the ooze contains trace to bearing amounts of quartz, and carbonate lithic grains. The downhole variation in composition between carbonate oozes (rich in calcareous nannofossils and foraminifers) and muds (rich in mineral and lithic grains) is illustrated in Figure [F25](#).

Smear slide photomicrographs in Figure [F31](#) highlight the major compositional variations throughout 0-296.4 mbsf (Hole H003). The muds are dominated by clay-sized particles, but there is a significant fraction of silt-sized particles present (e.g. Figure [F31](#) B). Their composition is similar to the coarser sand and silt laminations and beds. The sand and silt laminations and beds that commonly occur within the muds (e.g. Figure [F31](#) E) are less often present in the ooze. Trace foraminifera were present, often containing framboidal pyrite.

The bulk composition of the silt and sand beds is dominated by quartz, two types of feldspar (microcline and plagioclase, although untwinned K-feldspar was difficult to distinguish from quartz in smear slide and may also be present), carbonate lithic grains, and igneous lithic grains (Figure [F31](#) C, E, and F). Opaque and heavy minerals such as zircon were present in trace amounts. Volcanic glass and plant debris are rare but observed in some samples. A significant fraction of the silt and sand materials are dominated by detrital carbonate and igneous lithics (Figure [F31](#) C, E, and F)).

Pressure cores were acquired intermittently over a measured depth range from 644.6-859.6 mbsf (Figure [F12](#) I). These cores spanned Lithologic Units IV, V, VI, and VII (Figure [F22](#)). In this interval, the

major lithology was mud. Once again, the muds are dominated by clay-sized particles but have significant fractions of silt and coarser grains within them (e.g. Figure [F31](#) B). The composition of the coarser grained material varied between quartz-rich and carbonate lithic-rich muds with variable amounts of feldspars (microcline and plagioclase) and igneous lithics, with trace mica and calcareous nannofossils (Figure [F23](#) B). Down core variation in the major lithology for individual mineral and lithic grains is summarized in Figure [F32](#).

Slightly subrounded dolomite rhombs were observed in trace amounts. Trace calcareous nannofossils are also present in this interval. Mineral fragments were notably angular compared to rock fragments that were subrounded. Post-depositional diagenesis is dominated by iron sulfide precipitation in porosity afforded by the coarse beds (644.6-859.6 mbsf, Hole H002). Down core variation in the major lithology for individual mineral and lithic grains is summarized in Figure [F21](#).

Environment of deposition

In Lithologic Unit II, the repeated variation between oozes and mud with coarse lamina and beds is consistent with dilution of a pelagic rich carbonate marine environment by lithogenic sediment fluxes. The oozes represent a high primary productivity pelagic, ocean environment with little suspended lithogenic materials. These paleo-environmental conditions appear to be interrupted by lithogenic sediment fluxes in both the suspended and basal sediment loads, which are consistent with a range of dilute to concentrated sediment gravity flows. Most of the coarse sediment deposits in Lithologic Unit II and III are consistent with turbidity current deposition. The lack of biogenic fossil fragments or intact foraminifer within the muds is interpreted to result from the gravity flows overwhelming the flux from surface ocean biologic productivity. The abundance of reworked Cretaceous calcareous nannofossils (See [Calcareous nannofossil biostratigraphy](#)) throughout the record is consistent with these lateral terrigenous fluxes as well. The consistent composition of the

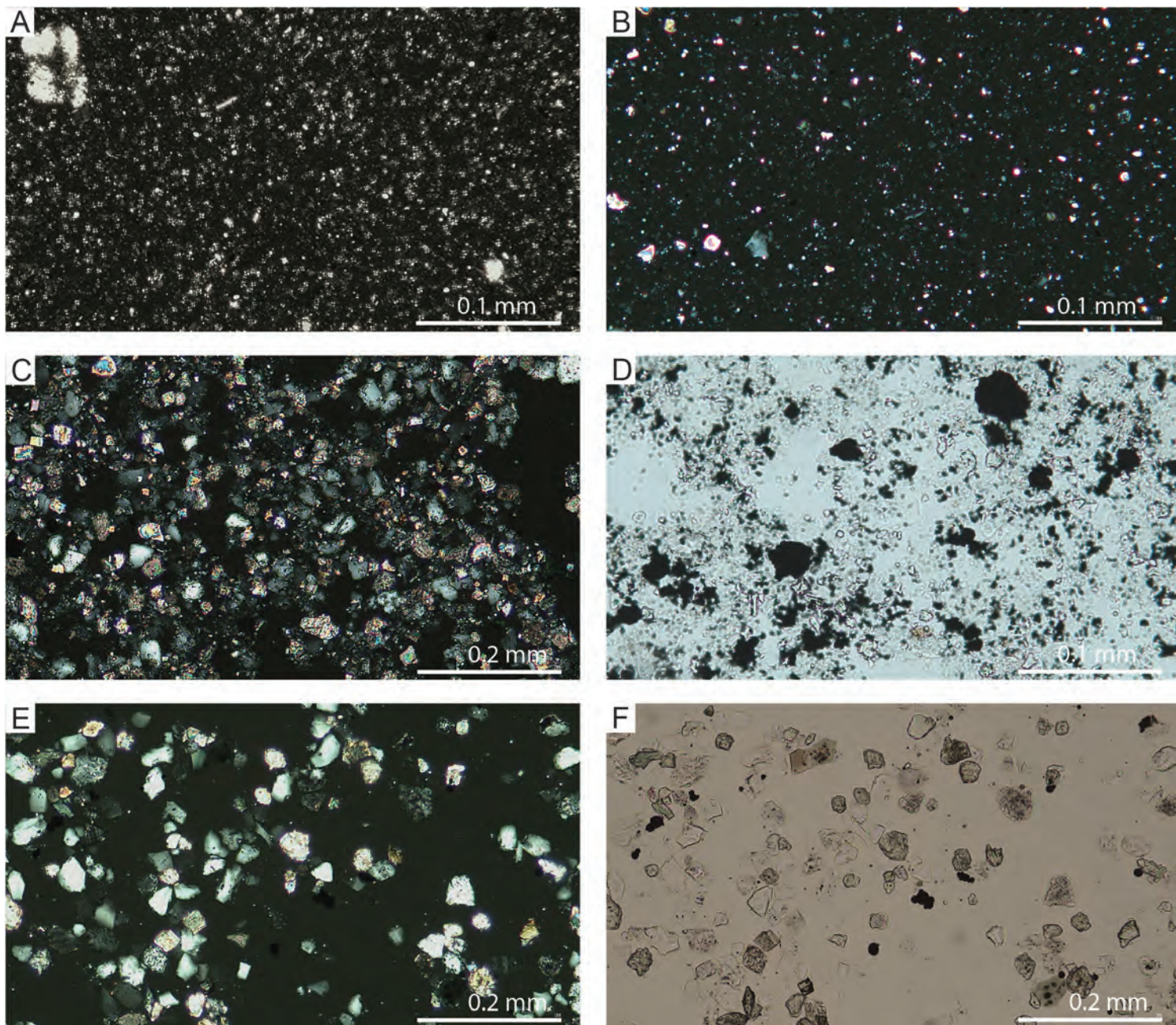


Figure F31: Example smear slide photomicrographs. A) Calcareous nannofossil ooze with foraminifer fragments (larger grains) (Smear slide H003-12H-2a-70cm, 200x magnification, cross polarized light); B) Quartz-rich, mud; larger quartz (gray) and carbonate lithics (brassy yellow) seen in lower left of image (Smear slide H003-10H-6-76cm, 200x magnification, cross polarized light); C) Quartz-rich (gray), carbonate lithic-rich (brassy yellow), sandy silt (Smear slide H003-7H-CC-50cm, 100x magnification, cross polarized light); D) Iron sulfide rich, quartz-rich, carbonate lithic rich clay; iron sulfides are variably sized, black aggregates (Smear slide H003-9H-4A1-8cm, 200x magnification, plain polarized light); E) and F) Quartz-rich, carbonate lithic-rich, pyrite bearing, silt*, with igneous lithics; notice the igneous and carbonate lithic grains are subrounded to rounded and the mineral grains (e.g. quartz and feldspars) are subangular to angular (Smear slide H003-21H-5-17cm-100x magnification, cross polarized light (E) and plain polarized light (F)). *Predominantly sand sized grains in this part of the slide are shown for ease of identification, see smear slide table for the sand, silt, and clay % estimate for this entire sample. See Methods: Smear slide description (Flemings et al., [2025b](https://doi.org/10.5281/zenodo.14518170)). Datasets: <http://doi.org/10.5281/zenodo.14518170>.

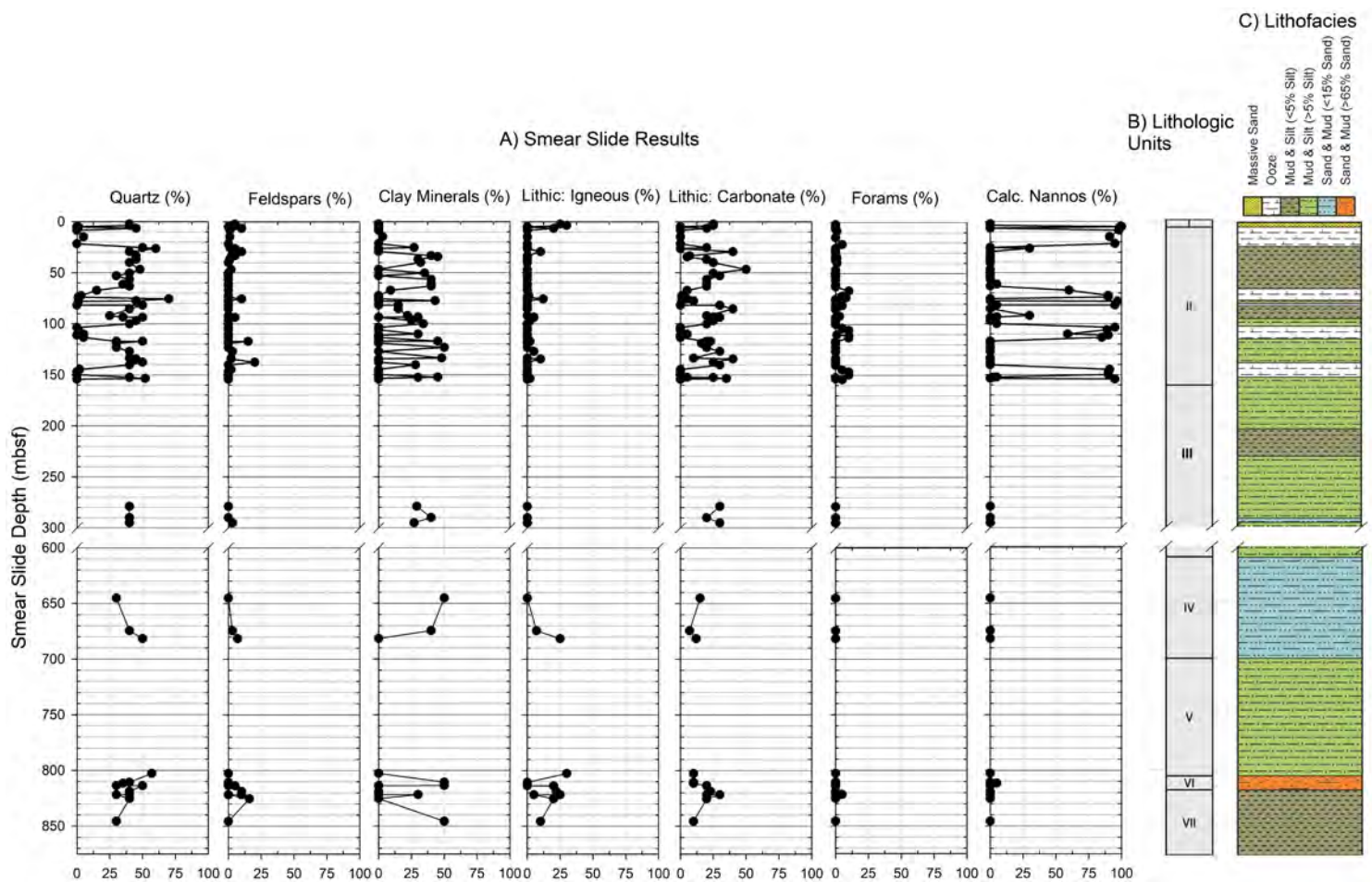


Figure F32: H003 and H002 downhole smear slide results for the major and minor lithologies plotted using compressed measured depths in meters below the seafloor (mbsf). See Methods: Smear slide description (Flemings et al., [2025b](#)). Datasets: <http://doi.org/10.5281/zenodo.14518170>.

muds and the sand and silt turbidite beds suggests they are from the same source. It is possible that the muds are genetically related to the turbidites as overbank suspended loads or distal deposits in waning turbidity current energy on the seafloor.

The abundance of muds with coarse lamina and beds in Lithologic Units IV to VII, 644.6-859.6 mbsf, is consistent with a slope depositional environment, where lithogenic sediments are delivered to the seafloor in both suspended and basal sediment loads. The bulk composition and core stratigraphy are consistent with a range of dilute to concentrated sediment gravity flows. Most of the coarse sediment deposits are consistent with turbidity current deposition.

Lithostratigraphy post-expedition analysis plan

A split core sampling (See Methods: Split core sampling (Flemings et al., [2025b](#))) and post-expedition measurement plan for the prioritized standard set was developed. Additional samples beyond the standard set were also planned for the top 68 mbsf. Table [T11](#) shows the post-expedition activity, responsible institution, sample codes, and the scientific objective for each of these sample types. Additional special sample requests were fulfilled around the Red, Blue and Orange sands. A photograph of each split core was taken after sampling, showing the location of each sample with the sample type. These images are available in the core images dataset: <http://doi.org/10.5281/zenodo.14261688>.

A. Post-expedition Activity	B. Responsible Party	C. Sample Codes	D. Scientific Goal
Primary coarse fraction microscopy	UNH	CF	Supplemental Sediment Composition
Authigenic sulfide nodule sampling for isotope measurements	UNH	PYR	Diagenetic origin
CHNS, TOC, & C and S isotopic analysis	UNH	CNS	Org. C, CaCO ₃ , and S variation, and origin
Moisture and density (MAD), X-ray diffraction (XRD), and X-ray fluorescence (XRF) analysis	Tufts/UNH	MDX	MAD, Bulk mineralogy and ground truthing elemental variation
Rock magnetics	USGS/UNH	RMG & ARM	Magnetic mineralogy and variation
Biostratigraphy	UT	PAL	Age model and degree of reworking
Biogenic Silica	UNH	BSI	Paleo-productivity
Oxygen and Carbon Isotope Stratigraphy	UNH	ISO	Age model down to 68 mbsf
⁴ He measurements	Ohio State	4HE	Assessing noble gas fractionation

Table T11: UT-GOM2-2 Split core sample post-expedition work. A) Post-expedition activity; B) responsible party, University of New Hampshire (UNH), Tufts university (Tufts), U.S. Geological Survey (USGS), The University of Texas at Austin (UT), The Ohio State University (Ohio State); C) Sample codes; D) Scientific goal for each measurement. See Methods: Split core sampling (Flemings et al., [2025b](#)).



Conventional cores prepped and ready for shipping to The University of Texas at Austin (UT). Photo credit: Joel E. Johnson

Calcareous nannofossil biostratigraphy

Discrete samples were collected onboard from core-catchers (32 samples) and dockside from split core sampling (308 samples). All samples collected during onboard operations and a subset of 68 samples collected dockside were examined for calcareous nannofossil assemblages (See Methods: Biostratigraphy (Flemings et al., [2025b](#)). Calcareous nannofossils were observed in nearly every sample examined. The preservation of in-situ specimens was very good to excellent over the entire depth of the recovered core section. The background assemblage indicated a Pleistocene age (<0.91 Ma) through the entirety of the borehole.

Reworked (RW) calcareous nannofossils were accounted for and considered part of the detritus rather than of the in-situ Pleistocene microfossil assemblage. RW specimens were predominantly Cretaceous in age, but specimens from the Neogene and Paleogene were also observed. All RW specimens were lumped together according to their respective geologic period. There is an inverse relationship between assemblages dominated by RW Cretaceous and in-situ Pleistocene nannofossils indicating variable environmental conditions, particularly pulses of continental river runoff and increased sediment load from runoff due to melting of the North American Laurentide Ice Sheets.

0-296.4 mbsf (Hole H003)

Abundances ranged from barren or very rare (10-20 specimens per traverse of a microscope slide coverslip) to microfossil ooze (pure fossil assemblage; >10,000 specimens per traverse). The preservation of in situ specimens was very good; whole coccospheres were regularly observed.

Four Pleistocene calcareous nannofossil biohorizons were observed between 0-296.4 mbsf (Figure [F34](#) and Table [T12](#)). The youngest age datum is the crossover in dominance from *Gephyrocapsa* spp. to *Emiliania huxleyi* (Constans and Parker, [1986](#); Gradstein et al., [2012](#)). The first appearance datum (FAD, evolution) of *E. huxleyi* is from Gradstein et al. ([2012](#)). The other two age datums, the last appearance datum (LAD, extinction) of *Pseudoemiliana lacunosa* A and the LAD of *P. lacunosa* B, are cited from Waterman et al. ([2017](#)). The LAD of *P. lacunosa* is a globally recognized age datum, but the LAD of *P. lacunosa* B is specific to the Gulf and was statistically interpolated from the extensive onshore and offshore bioevent databases collected and curated by micropaleontologists at Paleo Data, a PetroStrat company (Waterman et al., [2017](#)).

The first core sample collected for micropaleontological examination was sample H003-01H-4a1_57-59 cm at 5.10 mbsf and revealed an assemblage dominated by *Emiliania huxleyi*, *Reticulofenestra minuta*, and *Florisphaera profunda* indicating a geologic age within the *Emiliania huxleyi* biozone (<0.29 Ma) (Figure [F33](#), Table [T12](#)).

The youngest biohorizon, marked by the cross-over from the dominance of *Gephyrocapsa* spp. to *E. huxleyi*, occurs between samples H003-02H-CC_37-39 cm at 16.78 mbsf (Table [T12](#)) and H003-02H-CC_18-20.5 cm at 16.63 mbsf; a margin of error of 15 centimeters. This event is dated at 0.085 Ma in the Gulf (Gradstein et al., [2012](#)).

The FAD of *E. huxleyi* is dated to 0.29 Ma and is interpreted at 35.63 mbsf in sample H003-06H-4a_40-42.5 cm.

The next oldest biohorizon, the LAD of *P. lacunosa* A, refers to the extinction of the species *P. lacunosa* dated at 0.44 Ma. This biohorizon is observed in sample H003-10H-2_118-120.5 cm at 58.98 mbsf.

The first statistically interpolated biohorizon after *P. lacunosa* A is *P. lacunosa* B (0.66 Ma), which is marked by the last occurrence (LO) of a morphotype of *P. lacunosa* observed in sample H003-24CS-2_55.5-58

cm at 145.04 mbsf. This sample appears to simultaneously represent a geological event that disturbed the local stratigraphy as the assemblage also includes significant counts of one slightly older Gulf marker species, *Pseudoemiliana pacifica*. This event is observed down through sample H003-24CS-5_25-27.5 cm at 146.83 mbsf, for a total of approximately 1.79 meters. A similar assemblage was observed approximately 100 feet higher in one sample, H003-19CS-5a_12.5-15 cm at 113.19 mbsf, in the *P. lacunosa* A biozone. The out-of-place marker specimens observed in each of these three samples cease to be observed in the remainder of Hole H003, supporting an interpretation of reworking by some type of geological disturbance. No additional biohorizons were observed in Hole H003 (Figure [F34](#), Table [T12](#)).

644.6 to 859.6 mbsf (Hole H002)

Two Pleistocene calcareous nannofossil biohorizons were observed from 644.6 to 859.6 mbsf (Figure [F34](#)). The LADs of *P. pacifica* and *P. lacunosa* C are specific to the Gulf and are also statistically interpolated from the extensive onshore and offshore bioevent databases collected and curated by micropaleontologists at Paleo Data, a PetroStrat company (Waterman et al., [2017](#)).

The first sample in Hole H002, H002-01FB-1b_41-43.5 cm at 645.09 mbsf, contained the marker species, *P. pacifica* (LAD 0.82 Ma), suggesting that the hole and section is already within the *P. pacifica* biozone; older than 0.82 Ma (Figure [F34](#), Table [T12](#)).

P. pacifica is regularly observed in samples through the remainder of Hole H002. The oldest biohorizon observed, the *P. lacunosa* C biohorizon, is defined by an ACME event of *P. pacifica* and is observed in sample H002-09CS-4b_66.5-69 cm at 815.45 mbsf (Figure [F33](#), Plate 1). The *P. lacunosa* C biohorizon is interpreted to occur at 0.83 Ma and is the oldest biohorizon observed.

The next calcareous nannofossil biohorizon would mark 0.91 Ma, but it was not observed. Therefore, the stratigraphy in the rest of the borehole is

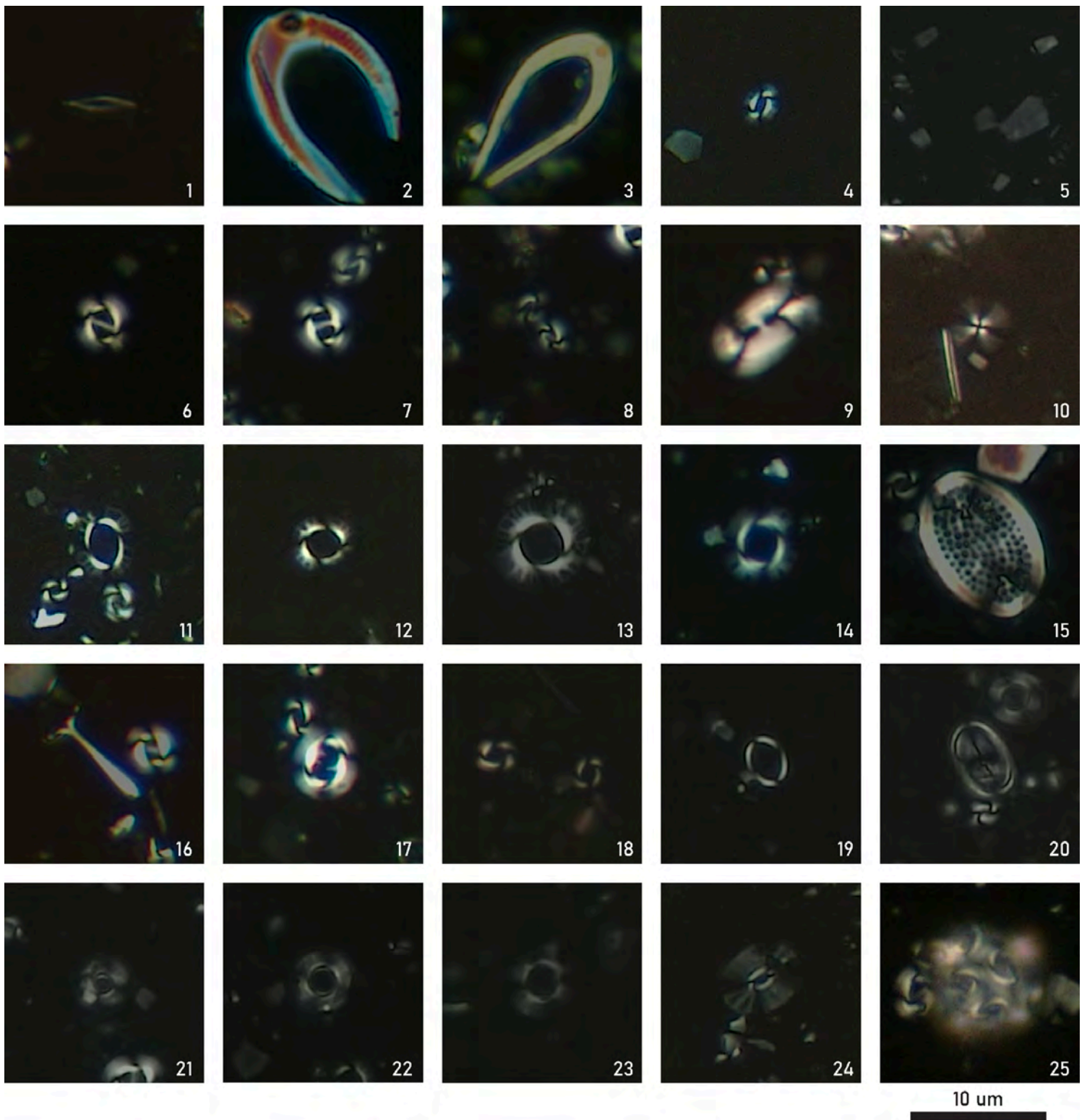


Figure F33: Biostratigraphy plate under polarized light: 1) *Calciosolenia* spp., 2) *Ceratolithus cristatus*, 3) *Ceratolithus telesmus*, 4) *Emiliania huxleyi*, 5) *Florisphaera profunda*, 6) *Gephyrocapsa oceanica*, 7) *Gephyrocapsa caribbeanica*, 8) *Gephyrocapsa* spp. (2–4 μ m), 9) *Helicosphaera carteri*, 10) *Oolithus fragilis*, 11) *Pseudoemiliana ovata*, 12) *Pseudoemiliana lacunosa* A, 13) *Pseudoemiliana lacunosa* B, 14) *Pseudoemiliana pacifica*, 15) *Pontosphaera multipora*, 16) *Rhabdosphaera clavigera*, 17) *Reticulofenestra haqii*, 18) *Reticulofenestra minuta*, 19) *Syracosphaera hystrix*, 20) *Syracosphaera pulchra*, 21) *Umbilicosphaera foliosa*, 22) *Umbilicosphaera sibogae*, 23) *Umbilicosphaera rotula*, 24) *Umbellosphaera tenuis*, 25) Coccosphere of *Gephyrocapsa caribbeanica*. See Methods: Biostratigraphy (Flemings et al., 2025b). Dataset: <http://doi.org/10.5281/zenodo.14143460>.

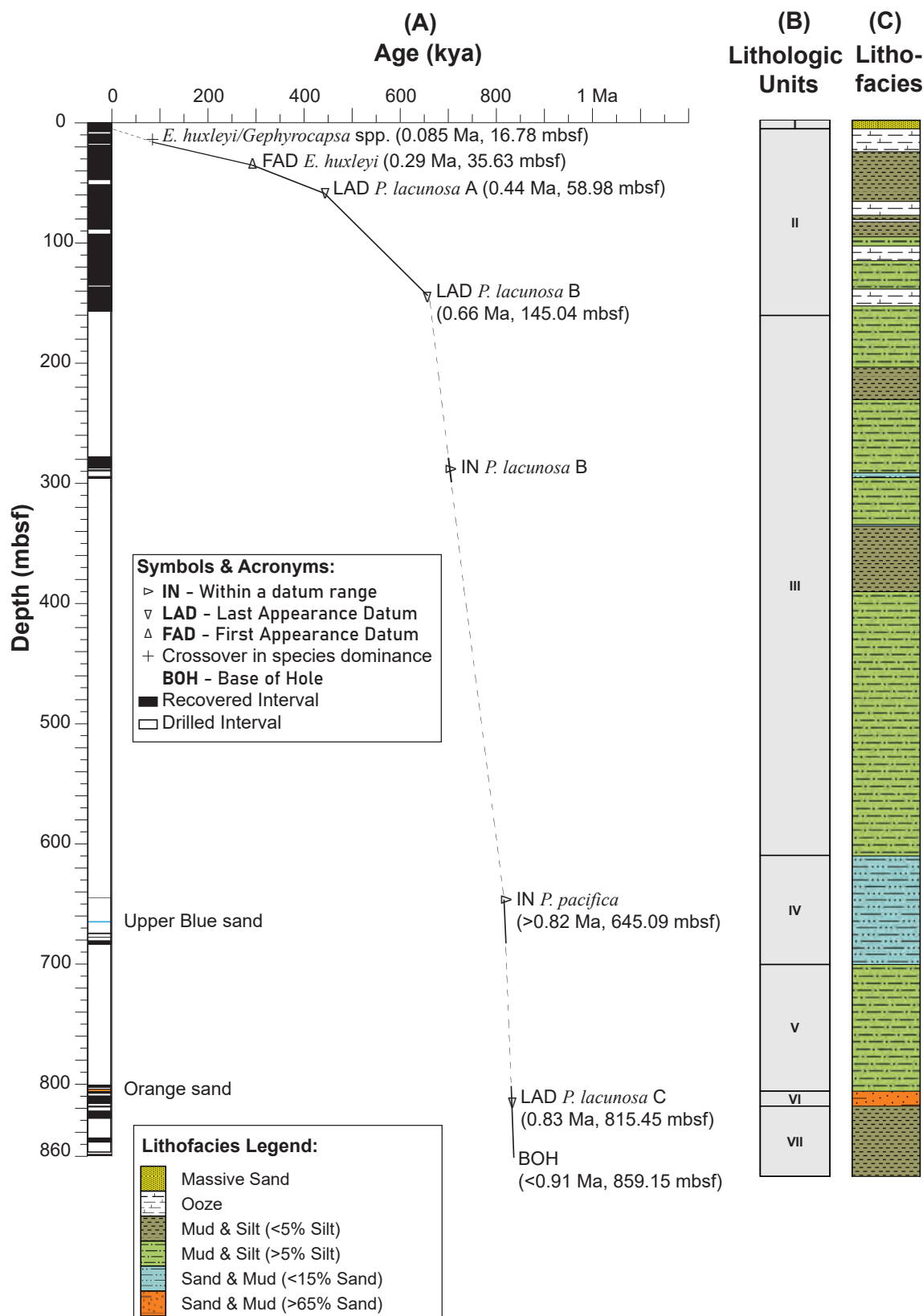


Figure F34: Composite time-depth plot of calcareous nannofossil biohorizons through Hole H003 and Hole H002 using compressed measured depths in meters below the seafloor (mbsf). Calcareous nannofossil events are from the Biostratigraphic Chart – Gulf Basin, USA (Waterman et al., 2017). On the age-depth curve, solid black lines correlate with recovered intervals where samples were taken regularly for biostratigraphic analysis. Dashed black lines correlate with drilled intervals through which sediment samples were not recovered and biostratigraphic analysis could not be performed. Each first appearance datum (FAD, evolution) is shown as an upright triangle, and each last appearance datum (LAD, extinction) is shown as an inverted triangle. See Methods: Biostratigraphy (Flemings et al., 2025b). Dataset: <http://doi.org/10.5281/zenodo.14143460>.

(A) Sample Name	(B) Depth, bottom (mbsf)	(C) Compressed Depth, bottom (mbsf)	(D) BIOSTRATIGRAPHIC EVENT (Calcareous Nannofossils)	(E) GEO AGE (Ma)
UT-GOM2-2-WR313-H003-01H-4a1_57-59.5cm	5.10	5.10	First PAL Sample; IN <i>Emiliana huxleyi</i> biozone	<0.29
UT-GOM2-2-WR313-H003-02H-CC_37-39 cm	18.28	16.76	<i>E. huxleyi</i> / <i>Gephyrocapsa</i> spp. crossover in dominance	0.085
UT-GOM2-2-WR313-H003-04CS-3c_123-125cm	35.63	35.63	FAD <i>E. huxleyi</i> biozone	0.29
UT-GOM2-2-WR313-H003-10H-2_118-120.5cm	59.40	58.98	LAD <i>Pseudoemiliana lacunosa</i> A biozone	0.44
UT-GOM2-2-WR313-H003-24CS-2-55.5-58cm	145.12	145.04	LAD <i>P. lacunosa</i> B biozone	>= 0.66
UT-GOM2-2-WR313-H003-29CS-5e_79-81cm	296.44	296.44	Base of Hole H003, IN <i>P. lacunosa</i> B biozone	-
UT-GOM2-2-WR313-H002-01FB-1b_41-43.5cm	645.09	645.09	IN <i>Pseudoemiliana pacifica</i> biozone; first PAL sample in Hole H002	>0.82
UT-GOM2-2-WR313-H002-09CS-4b_66.5-69cm	816.02	815.45	LAD <i>P. lacunosa</i> C biozone	0.83
UT-GOM2-2-WR313-H002-15CS-2a1_6.5-9cm	859.18	859.18	Base of Hole H002; Last PAL Sample	<0.91

Table T12: Calcareous nannofossil biohorizons. A) Biostratigraphy sample (sample code PAL); B) Archived measured depth in meters below the seafloor (mbsf); C) Compressed measured depth in mbsf; D) Biostratigraphic event based on calcareous nannofossils; E) Assessed age. See Methods: Biostratigraphy (Flemings et al., [2025b](#)). Dataset: <http://doi.org/10.5281/zenodo.14143460>.

younger than 0.91 Ma. The last sample examined for biostratigraphy was H002-15CS-2a1_6.5-9 cm at 859.18 mbsf (Figures [F33](#) and [F34](#), Table [T12](#)).

Biostratigraphy post-expedition analysis plan

Over 312 samples were collected for calcareous nannofossil examination. Over time, these samples will be examined to fill in additional potential biohorizons for future Pleistocene biostratigraphy applications. They will also be used to produce high resolution (every 30 cm) biostratigraphy of both the in-situ and reworked calcareous nannofossils through to the bottom of the continuously cored section (~155 mbsf), to investigate meltwater pulses from the continent.



Steve Phillips of the USGS, Rick Colwell of Oregon State, Monica Korsha of The University of Texas, and Camille Sullivan of the University of New Hampshire onboard the Q4000. Photo credit: Jackson School of Geosciences

Physical properties

Samples were collected to characterize the physical properties of sediment as a function of depth at high resolution. The measurements included the following: thermal conductivity; in-situ temperature/thermal gradient; multi-sensor core logging (pressure coring logging and imaging, conventional whole core logging and imaging, and split core logging and imaging); undrained shear strength; index properties; and rock magnetism.

Thermal conductivity

We conducted thermal conductivity measurements on sediment whole-round sections using the needle probe method (See Methods: Thermal conductivity (Flemings et al., [2025b](#))). In most cases, we made three to five measurements at each measurement position. The conductivity measurements were very challenging because of the many voids in the core. The plotted value represents the mean of the measurements, and the horizontal bar shows the standard deviation of the measurements. The general trend is that thermal conductivity increases with depth: 0.9 – 1.1 W/[mK] close to the seafloor and at shallower depths [~5 – 50 mbsf] and 1.1 – 1.4 W/[mK] at deeper depths [~280 – 860 mbsf] (Figure [F35](#) and Table [T13](#)). The low thermal conductivity data points (~0.9 W/[mK] at 670-680 mbsf) are in poor-quality cores due to coring disturbances resulting in high water content as evidenced by their soft, disturbed soupy state.

The thermal conductivity estimates using the geometric mean model were acquired. Modeling results are based on Hole H001 log porosity data (Flemings et al., [2025a](#)) and use $TC_{\text{bulk}} = (1.92)^{(1-n)} + (0.58)^n$; where, n is porosity, 0.58 W/[mK] is thermal conductivity for water, and 1.92 W/[mK] is thermal conductivity for marine mud grains

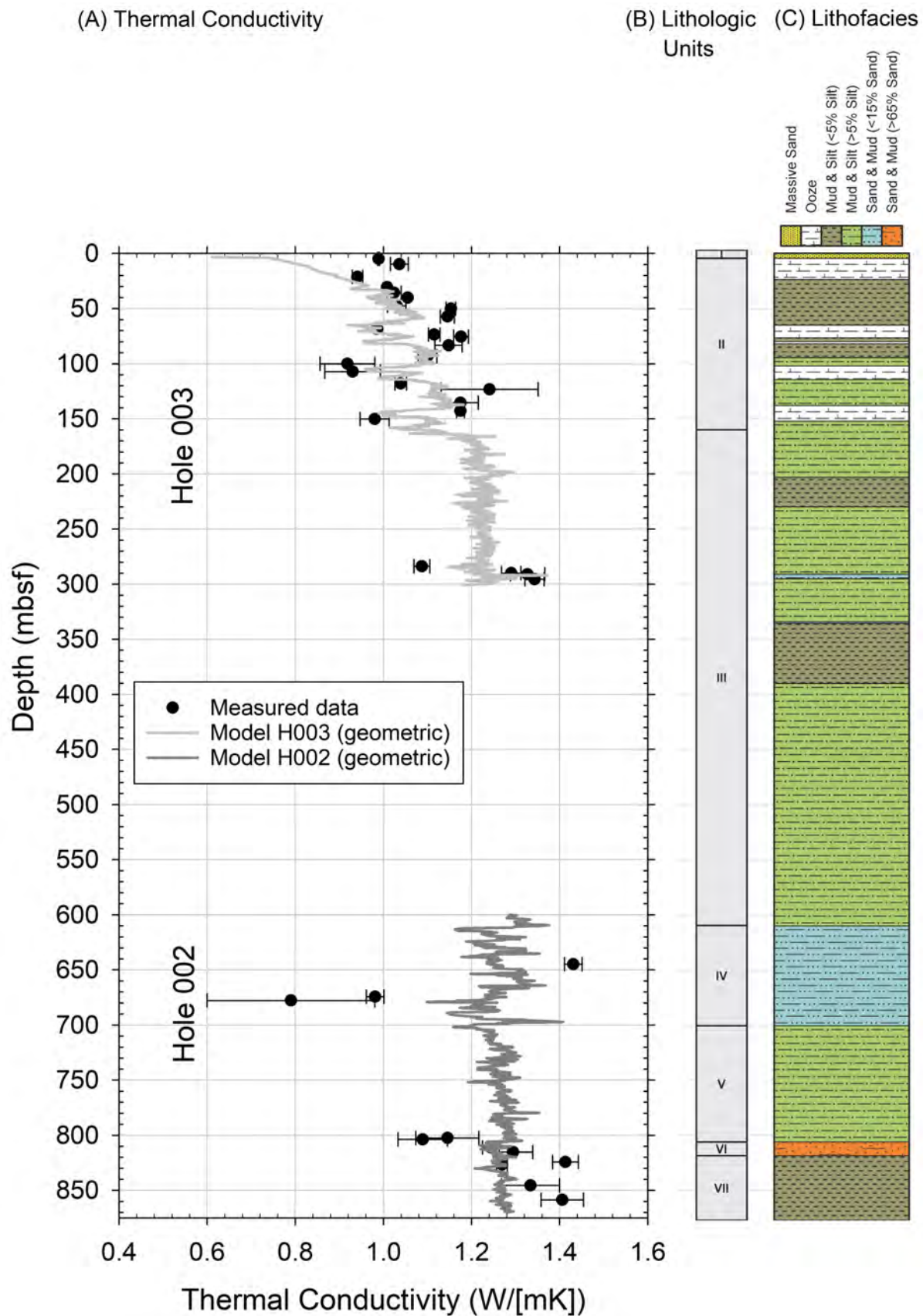


Figure F35: Thermal conductivity with compressed measured depth from core measurements for Hole H003 and Hole H002. A) Measured and modeled thermal conductivity. The gray lines show the thermal conductivity estimates based on the projected Hole H001 log data using the geometric mean model. The depth projection of Hole H001 LWD data onto Hole H002 and Hole H003 is discussed in Plotting H001, H002, and H003 downhole data; B) Lithologic units (See Lithostratigraphy); C) Lithofacies (Table T10). Dataset: <http://doi.org/10.5281/zenodo.14171332>.

A. Core Section/ Piece	B. Depth	C. Compressed Depth	D. Thermal Conductivity	E. Standard Deviation
	mbsf	mbsf	W/[mK]	W/[mK]
H003-01H-4	4.92	4.92	0.989	0.002
H003-02H-2	10.08	9.80	1.036	0.020
H003-03H-3	21.86	21.32	0.941	0.012
H003-05CS-1	30.58	30.55	1.008	0.000
H003-06H-4	37.36	35.71	1.024	0.016
H003-07H-1	40.32	40.18	1.055	0.000
H003-08CS-2	47.63	47.63	1.030	0.021
H003-09H-1	50.29	50.16	1.153	0.011
H003-10H-1	57.39	57.28	1.145	0.016
H003-11H-5	70.20	68.63	0.986	0.000
H003-12H-3	74.61	73.68	1.115	0.013
H003-12H-5	77.10	75.56	1.176	0.017
H003-14H-3	84.13	83.49	1.148	0.031
H003-16H-2	93.63	93.15	1.100	0.021
H003-17H-3	100.87	100.09	0.918	0.062
H003-18H-3	108.40	107.15	0.930	0.063
H003-20H-4	118.71	117.97	1.039	0.013
H003-21H-2	123.55	123.33	1.241	0.110
H003-22H-5	135.49	135.49	1.175	0.040
H003-23H-5	143.85	142.89	1.175	0.009
H003-25H-4	151.26	150.25	0.980	0.033
H003-26X-5	283.77	283.77	1.087	0.018
H003-27CS-5	289.96	289.96	1.290	0.022
H003-28CS-1	291.14	291.14	1.327	0.039
H003-29CS-3	295.53	295.53	1.343	0.022
H002-1FB-1a	644.90	644.90	1.431	0.020
H002-2FB-1	674.33	674.33	0.981	0.020
H002-3FB-2c	677.70	677.70	0.790	0.190
H002-5CS-3c	802.46	802.46	1.145	0.072
H002-6CS-2	803.75	803.75	1.089	0.056
H002-8CS-3a	811.09	811.09	1.244	0.019
H002-9CS-4b	815.64	815.31	1.294	0.045
H002-12CS-3a	824.64	824.29	1.413	0.029
H002-13CS-2a	826.82	826.59	1.269	0.012
H002-14CS-2a	845.55	845.44	1.334	0.066
H002-15CS-1a	858.52	858.52	1.406	0.048

Table T13: Thermal conductivity measurements in cores from Hole H003 and Hole H002. We made three to five measurements at each measurement location. A) Sample hole, core, section and/or piece; B) Measured depth in meters below the seafloor; C) Compressed measured depth in meters below the seafloor (mbsf); D. Thermal conductivity; E. Standard deviation of the 3-5 measurements at each location. Dataset: <http://doi.org/10.5281/zenodo.14171332>.

(Quartz = 27 %) (Portnov et al., [2023](#)). Measured values are well within the range of values (1.08 – 1.28 W/[mK]; measured depth 15.8 – 478.4 m) determined by Davis et al. ([1990](#)) for sediment from the northern Cascadia accretionary sedimentary prism off Vancouver Island.

In-situ temperature/thermal gradient

Temperature measurements

Discrete measurements of in-situ temperature at multiple depths in Hole H003 were made with the Advanced Piston Corer Temperature Tool (APCT-3), as described in Methods: Downhole tools (Flemings et al., [2025b](#)).

The APCT-3 was deployed twelve times in Hole H003, but only ten of those included a dwell time long enough to infer the in-situ temperature. Table [T14](#) summarizes these deployments, including date and time, depth, and dwell time. During Deployment H003-06H, the descent of the coring tool was stopped at the seafloor while the drilling fluid pumps were turned off to record a temperature measurement of the drilling fluid after it had equilibrated to the ocean temperature at the seafloor.

Figure [F36](#) shows the temperature evolution with time for every deployment. All deployments show the temperature rise associated with the G-APC shot. Deployments H003-01H and -02H did not include a dwell time; thus, there is no evident thermal decay. These two deployments were intended to assess the performance of the APCT-3 downhole, rather than to measure temperature. See in Methods: Extrapolating the APCT-3 temperature measurement (Flemings et al., [2025b](#)).

Temperature measurements from 27.1 mbsf (Deployment H003-03H) to 144.5 mbsf (Deployment H003-23H) all show a gradual thermal decay after the frictional heating caused by the G-APC insertion (Figure [F36](#)) and were used to infer the in-situ temperature. Deployments H003-03H, H003-06H, H003-12H, H003-14H, and H003-17H display a sharp

A. Core	B. Date	C. G-APC firing	D. Depth	E. Dwell time	F. Seafloor stop	G. Lowest temperature recorded
		hh:mm	mbsf	Min	°C	
H003-01H	4 August 2023	12:22	8.2	0	No	4.13
H003-02H	4 August 2023	19:11	16.8	0	No	4.13
H003-03H	5 August 2023	00:04	27.1	5	No	4.13
H003-06H	5 August 2023	16:11	39.3	10	Yes	4.17
H003-07H	5 August 2023	20:00	46.6	10	No	4.17
H003-09H	7 August 2023	18:10	56.7	10	No	4.17
H003-10H	7 August 2023	21:58	63.7	10	No	4.17
H003-12H	8 August 2023	06:45	77.7	10	No	4.17
H003-14H	8 August 2023	17:15	88.4	10	No	4.16
H003-17H	9 August 2023	07:00	104.2	10	No	4.16
H003-21H	9 August 2023	19:51	129.2	10	No	4.16
H003-23H	10 August 2023	02:44	144.5	10	No	4.32

Table T14: Summary for all Advance Piston Corer Temperature Tool (APCT-3) deployments in Hole H003. A) Core deployment; B) Date and C) time the Advanced Piston Coring tool (G-APC) was fired; D) Measured depth of the bottom of the cored interval in meters below the seafloor (mbsf); E) Time after firing the tool before the coring tool was retrieved; Stop at the seafloor included during the deployment; G) Lowest temperature recorded; Dataset: <http://doi.org/10.5281/zenodo.14171354>.

second temperature peak associated with the retrieval of the tool. Conversely, Deployments H003-07H, H003-09H, H003-10H, H003-21H and H003-23H depict a more erratic temperature increase after thermal decay. We attribute this behavior to the attempts to retrieve the tool from the formation.

Seafloor temperature

Deployment H003-06H included a stop at the seafloor. During this stop, the drilling fluid pumps were stopped to allow the fluid in the drill pipe near the temperature sensor to thermally equilibrate with the seafloor. The measured seafloor temperature was 4.17 °C. This is the lowest recorded temperature throughout the entire 06H deployment (See Methods: Extrapolating the APCT-3 temperature measurement (Flemings et al., 2025b)). A Q4000 ROV also provided temperature measurements near the seafloor. The lowest temperature recorded by the ROV is 5.53 °C, which is significantly higher than APCT-3. The ROV's temperature probe is uncalibrated, so we attribute the difference to erroneous ROV temperature

measurements.

Interpreted formation temperature

We use the temperature decrease data shown as red lines in Figure F36 to extrapolate the in-situ temperature (Table T15, column D) from the measured temperatures acquired during the dwell time (Table T15, column C). An extrapolation was used because the dwell times required to reach equilibrium temperature were not obtainable in the borehole (See Drilling challenges). Extrapolations were conducted according to the procedure in Methods: Extrapolating the APCT-3 temperature measurement (Flemings et al., 2025b) for all deployments. Initial temperature data was not used for Deployment H003-23H because it exhibited an abrupt decay in temperature after the G-APC deployment (Figure F36, lower right). In this case, we disregard this initial effect and consider data after ~2 minutes of the first temperature peak.

The inferred in-situ temperature with true vertical depth for Site H is shown in Figure F37. The temperature gradient is 25 °C/km. This value was

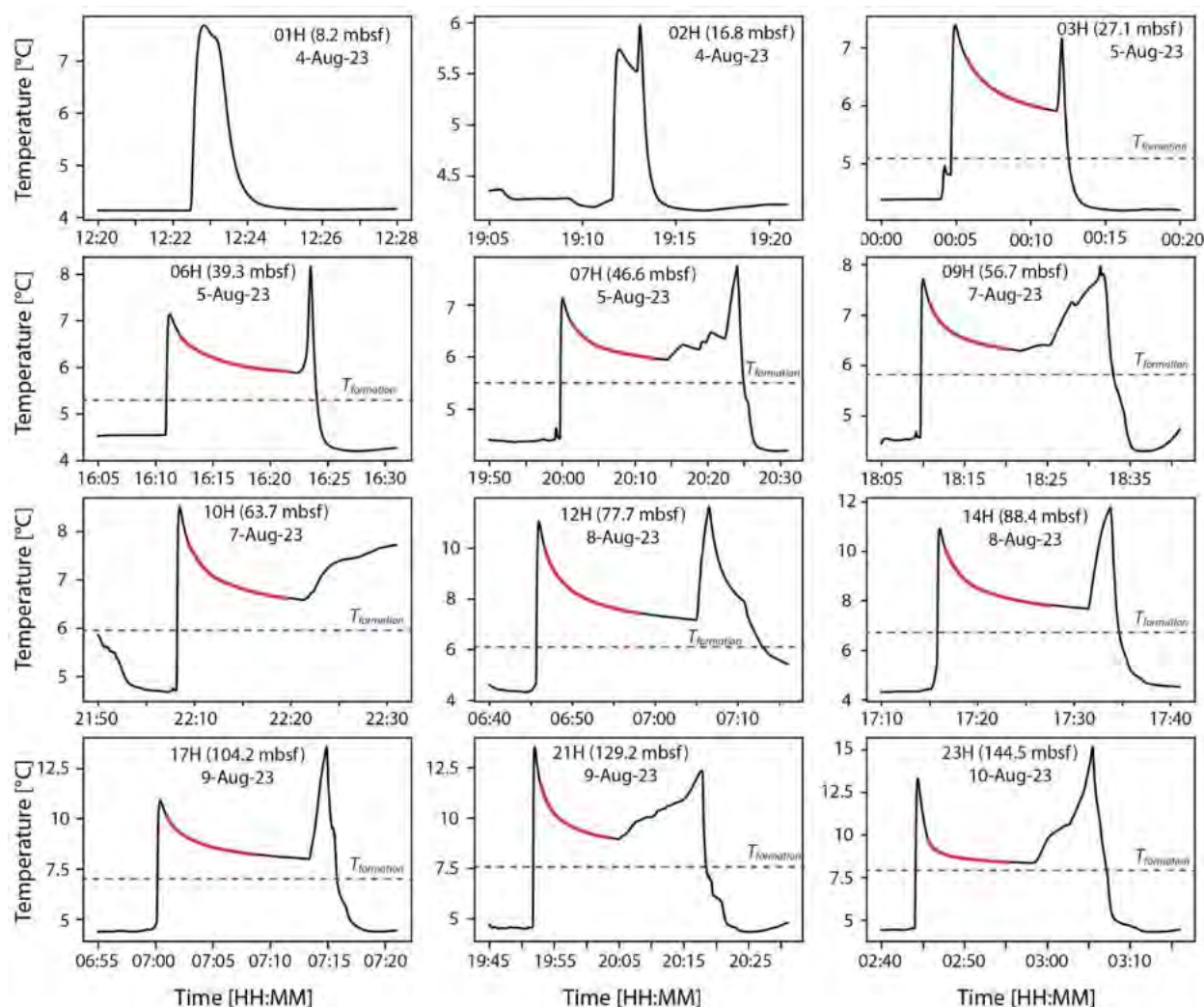


Figure F36: Temperature record for each Advanced Piston Corer Temperature Tool (APCT-3) deployment in Hole H003. The archived measured depth of the measurement is shown in the label for each record in meters below the seafloor (mbsf). See in Methods: Extrapolating the APCT-3 temperature measurement (Flemings et al., [2025b](https://doi.org/10.5281/zenodo.14171354)). Dataset: [http://doi.org/10.5281/zenodo.14171354](https://doi.org/10.5281/zenodo.14171354).

obtained by fitting a linear trend of temperature with depth and disregarding the seafloor temperature, as the temperature at the seafloor may be more sensitive to environmental changes (e.g., ocean currents). True vertical depth in meters below the seafloor (mbsf, Table [T15](#), column C) was used rather than the archived measured depth (Table [T15](#), column B) to infer the temperature with depth. True vertical depth was calculated assuming a constant inclination of 7 degrees (See [True vertical depth below seafloor](#)).

The temperature gradient based on the depth of the BSR was estimated to be 17.5 °C/km (Figure [F38](#), solid black line, See Summary: Geothermal gradient and Thermodynamic conditions (Flemings et al., [2025a](#)). This value was based on the assumptions that (1) the base of the gas hydrate stability is at

three-phase stability, (2) the pore water has seawater salinity (3.5 wt.%), (3) the pore pressure is hydrostatic (water density of 1.07 g/cm³), and (4) the seafloor temperature equals 4.2 °C. The gradient of 17.5 °C/km is an average value across the entire hydrate stability zone up to the BSR at ~895 mbsf. By contrast, our measurement-based temperature gradient of 25 °C/km is for the first ~150 mbsf.

Temperature Dual Pressure Penetrometer (T2P) and Penetrometer Deployment Tool (PDT)

We attempted to conduct a Temperature Dual Pressure Penetrometer (T2P) deployment test (See Methods: Temperature Dual Pressure Penetrometer (Flemings et al., [2025b](#))) inside the drill pipe without

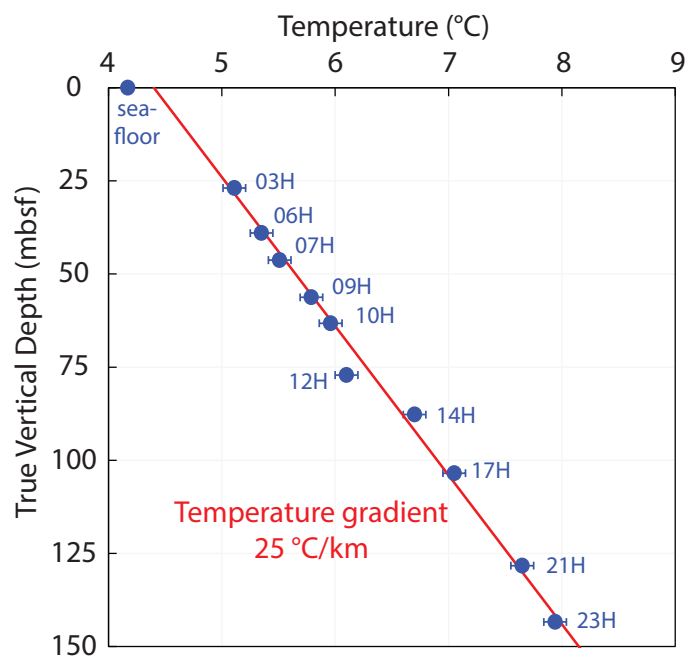


Figure F37: Interpreted in-situ temperatures from seafloor to 150 mbsf, using true vertical depth in meters below the seafloor (mbsf), based on Advanced Piston Corer Temperature Tool (APCT-3) measurements. The red line is a linear fit using least square regression, with an error of $R^2 = 0.99$. The seafloor temperature was excluded in this fitting procedure. Dataset: <http://doi.org/10.5281/zenodo.14171354>.

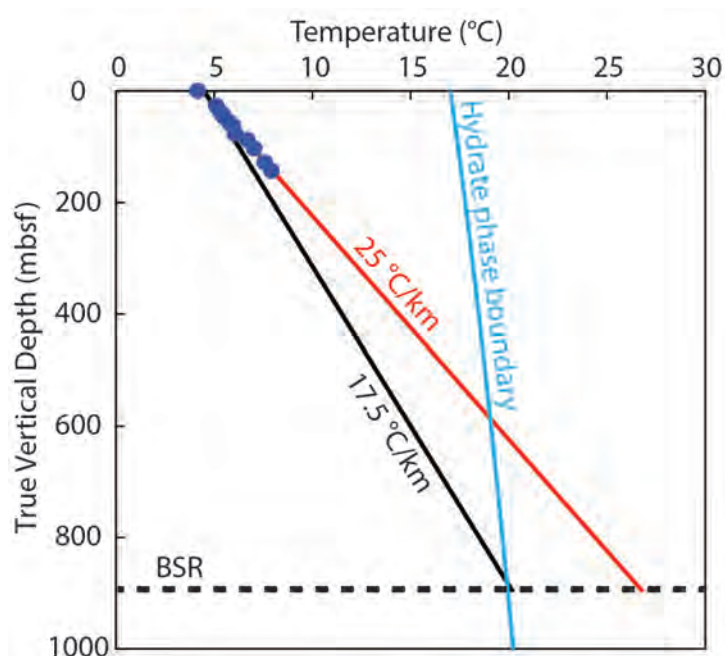


Figure F38: Temperatures with true vertical depth in meters below the seafloor (mbsf). The gradient of 25 °C/km (red line) is a linear fit using measured temperature values (blue circles). The black line is the inferred linear temperature with depth by considering the intersection between the bottom-simulating reflector (BSR) depth (black dashed line), the hydrate phase boundary (light blue line), and the seafloor temperature. Dataset: <http://doi.org/10.5281/zenodo.14171354>.

A. Core	B. Depth	C. True Vertical Depth	D. Time window for data fitting with model	E. Interpreted in-situ temperature
	mbsf	mbsf	hh:mm-hh:mm	°C
Seafloor (06H)	0	0	NA	4.17
H003-03H	27.1	26.9	00:06-00:11	5.11
H003-06H	39.3	39.0	16:11-16:21	5.34
H003-07H	46.6	46.3	20:01-20:11	5.50
H003-09H	56.7	56.3	18:11-18:27	5.78
H003-10H	63.7	63.2	22:10-22:20	5.96
H003-12H	77.7	77.1	06:47-06:58	6.06
H003-14H	88.4	87.7	17:16-17:27	6.69
H003-17H	104.2	103.5	07:02-07:08	7.03
H003-21H	129.2	128.3	19:54-20:04	7.57
H003-23H	144.5	143.4	02:45-02:55	7.92

Table T15: Interpreted in-situ temperature for Site H. A) Coring deployment; B) Archived measured depth of the bottom of the cored interval in meters below the seafloor (mbsf); C) True vertical depth of the bottom of the cored interval in mbsf calculated assuming a constant inclination of 7 degrees (See [True vertical depth below seafloor](#)); D) time interval used for fitting the measured temperature with the theoretical impulse response; E) Interpreted in-situ temperature. Dataset: <http://doi.org/10.5281/zenodo.14171354>.

inserting the probe into the formation. The objective of this test was to confirm the deployment operation procedure, latching and unlatching performance, and stability of T2P under downhole conditions.

On 4 August 2023, the T2P was connected to the Penetrometer Deployment Tool (PDT). The PDT was then placed on the drill pipe and held in place with a clamp. There was a strong current and there was significant vibration in the drill pipe due to the current. Thereafter, the Running Pulling Tool (RPT) was lowered into the PDT and latched. Latching was confirmed as the top drive assembly was able to lift the RPT-PDT-T2P assembly and hold it at the top of the drill pipe with the clamp. Then, we started to lower the system inside the drill pipe. During this procedure, the drilling crew felt a noise and vibration in the pipe, and it was confirmed by the ROV that the tool was sitting in the bottom the BHA (Figure F39). The RPT had accidentally unlatched from the PDT-T2P assembly. The PDT-T2P assembly free fell approximately ~6,500 feet. A fishing operation using the GS Fishing Tool was required to retrieve the tool, which successfully picked up the tool to the surface. It is unclear why the RPT unlatched from the assembly.

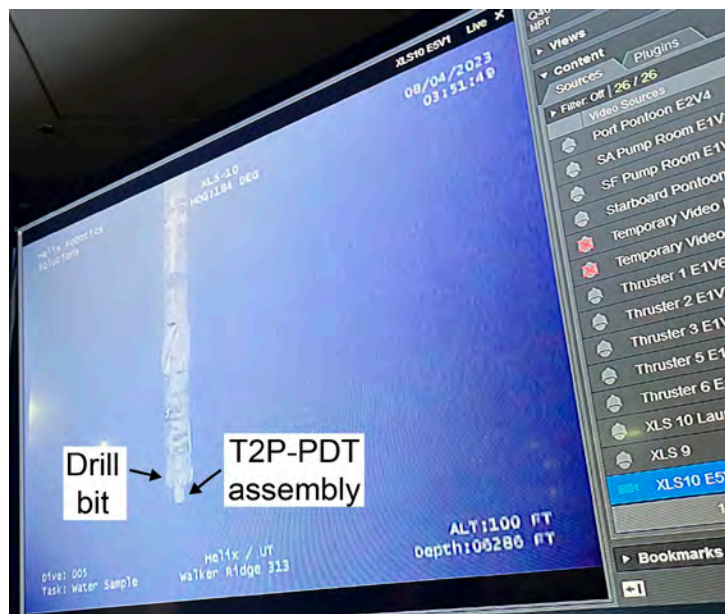


Figure F39: Image from a remote operating vehicle showing the Temperature Dual Pressure Penetrometer and Penetrometer Deployment Tool assembly (T2P-PDT) protruding from the bottom hole assembly (BHA) after an accidental unlatch of the RPT. Dataset: <http://doi.org/10.5281/zenodo.14680720>.

The T2P recovered data while free falling inside the drill pipe. Figure F40 shows the entire data set for the water column test. First, the tool is laying on the pipe rack and it is picked up at ~2:41 AM (Figure F40, acceleration data). Then, the T2P pressure starts to sharply increase and temperature decrease at 2:48 AM and reaches a constant value at 2:56 AM. This implies the free fall of the tool lasted for 8 min. The average drop velocity was 812 ft/min (4.1 m/s).

After the T2P-PDT assembly was returned to the rig floor, the T2P probe was detached from the PDT and placed in the Conex office for data collection and visual evaluation. The collected data were downloaded and analyzed. After inspection, the T2P was seen to be mechanically intact and reprogrammed for possible redeployment. For the examination of the PDT, the latching mechanism was removed from the assembly and a full mechanical teardown was undertaken. During the inspection of the latching mechanism, it was determined that the alignment roll pin (maintains the proper orientation of the latching mechanism in its landing sleeve housing) had become dislodged and stuck inside of the latching mechanism itself. No determination was able to ascertain when or how the pin had become dislodged. In addition to the dislodged roll pin, it was also discovered that that latching mechanism was full of heavy-scale rust fragments. No definitive source of the heavy-scale rust was able to be found but it was determined that the rust was not from the PDT assembly itself. The RPT was also disassembled to attempt to determine a cause for the premature release of the PDT-T2P during deployment. No damage was found. All of the springs and collets for both the PDT and RPT mechanisms were found to be in operational condition without any deformation or damage. The PDT latching mechanism was reassembled according to the technical manual instructions. All components were cleaned and lubricated with Fluid Film lanolin. The RPT was cleaned and reassembled in the same manner. After reassembly of the RPT and PDT latching mechanism, the PDT latching mechanism underwent extensive testing to ensure proper operation. This involves

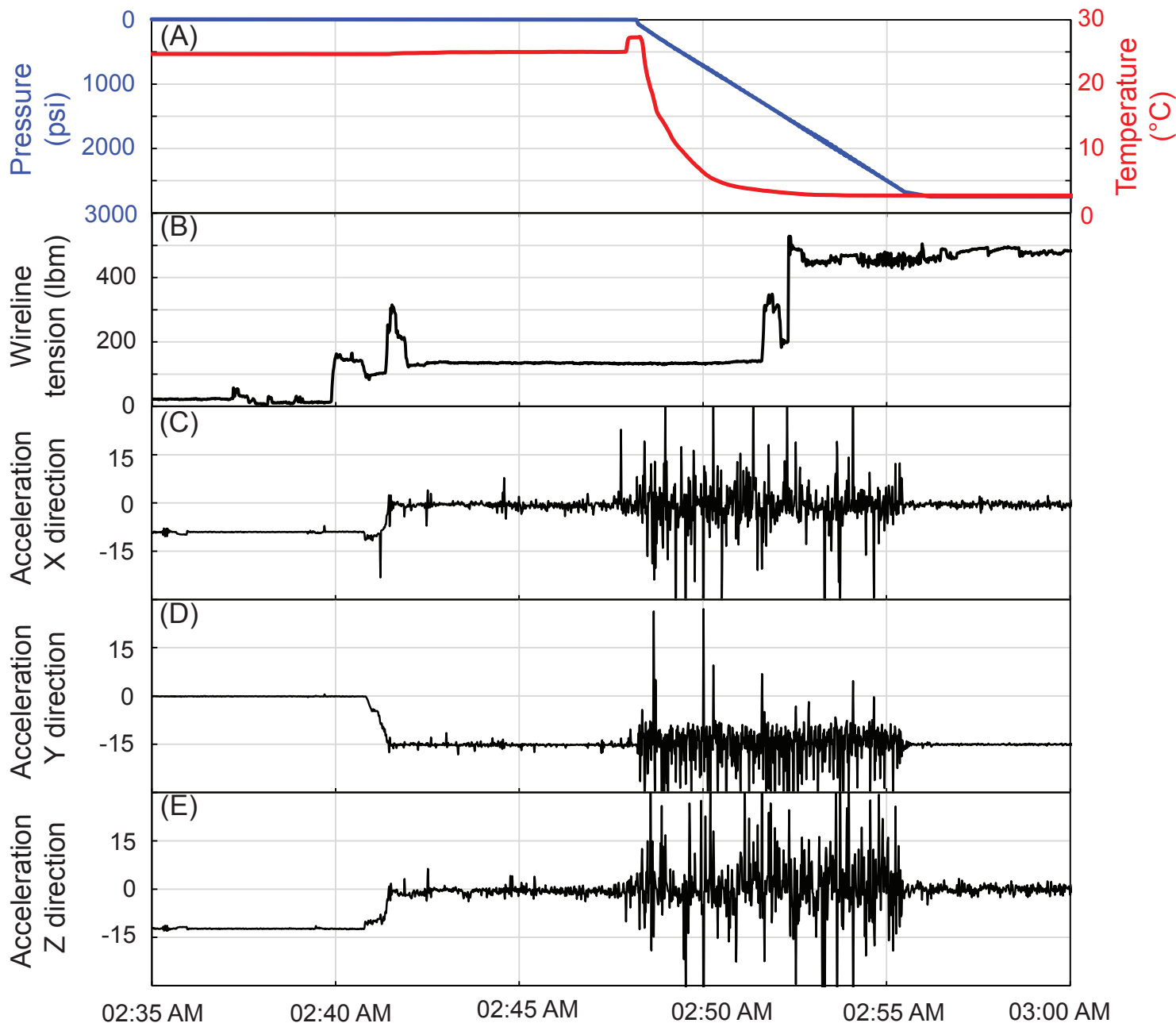


Figure F40: Temperature Dual Pressure Penetrometer (T2P) and rig data during T2P water column test. A) Pressure and temperature measured at the T2P tip; B) Wireline tension. The T2P also records acceleration in the C) X-direction, D) y-direction, and E) z-direction. The T2P and Penetrometer Deployment Tool (PDT) assembly unlatched from the Running Pulling Tool (RPT) at ~02:48 AM and free fell inside the borehole. Dataset <http://doi.org/10.5281/zenodo.14680720>.

using the RPT to properly exercise the mechanics of the latch for both deployment and recovery of the T2P-PDT assembly. After extensive testing, the PDT latching mechanism performed as intended. The latching mechanism was reattached to the PDT assembly for possible redeployment but was not deployed for the rest of the expedition.

Pressure coring logging and imaging

Pressure cores that sealed were logged and imaged using PCATS to collect gamma density, P-wave velocity, 2D radiography, 2D computed laminography, and 3D CT imaging (See Methods: Pressure core logging and imaging (Flemings et al., [2025b](#))). Core logs, images, and cuts were plotted using Strater

software. Figure [F41](#) shows the logging and imaging data for Core H003-08CS. All pressure core logs can be found in Appendix E: Pressure Core Logs.

Cores H003-05CS, H003-08CS, H003-19CS, H003-27CS, H003-28CS, and H002-05SC (Appendix E: Pressure Core Logs) all show very homogeneous P-wave velocity and gamma density (e.g., Figure [F41](#), column K and L). P-wave velocity and gamma density increased with depth. For example, the average gamma densities for Cores H003-8CS (46.6 mbsf) and H003-28CS (290.8 mbsf) are 1.95 and 2.29 g/cm³, respectively. Similarly, the velocity increases from 1520 to 1760 m/s.

Core H003-13CS (Appendix E: Pressure Core Logs) is filled with fluid in the first 30 cm and the velocity and density gradually increase to the expected sediment values. In Core H003-24CS, there is a periodic oscillation in the velocity ranging from 1,540-1,570 m/s.

For the deeper Hole H003 cores (Appendix E: Pressure core logs), Core H003-29CS has the highest range in velocity and density, varying from 2.15-2.3 g/cm³ and 1,700-1,900 m/s, respectively. In Cores H003-27CS through H003-29CS the velocity is still well below the ~2,500-3,300 m/s expected for pore-filling gas hydrate.

In Hole H002, Upper Blue sand Cores H002-02FB, H002-03FB have a gamma density of 2.0-2.2 g/cm³, and P-wave velocity between 1,600 to 1,800 m/s. These cores have intervals of 10-20 cm with higher P-wave velocities of 1,850 to 2,650 m/s (Appendix E: Pressure Core Logs).

Orange sand pressure cores have 10-25 cm intervals of P-wave velocity starting at 2,000-2,100 m/s in Core H002-06CS and increasing from 2,500 to 2,700 m/s (Appendix E: Pressure Core Logs). The longest recovered interval of high P-wave velocity is in Core H002-07CS. The interval is 41 cm long and velocities range from 2,100-2,700 m/s (Appendix E: Pressure Core Logs).

Conventionalized whole core logging

Conventionalized cores (depressurized pressure cores) were scanned for magnetic susceptibility, κ , using a standalone loop sensor. See Methods: Conventionalized pressure core logging (Flemings et al., [2025b](#)).

Figure [F42](#) shows the magnetic susceptibility logged on conventionalized pressure core sections. In H003, κ ranges up to 114 SI x 10⁻⁵, with an average of 29 SI x 10⁻⁵ (Figure [F42](#), 0-296.4 mbsf). In Hole H002, κ ranges up to 160 SI x 10⁻⁵ with an average of 53 SI x 10⁻⁵ (Figure [F42](#), 644.6-859.6 mbsf).

As possible, conventionalized core logs were created with the same format as the conventional core logs (See [Conventionalized whole core logging](#)). These logs can be found in Appendix E: Pressure Core Logs.

Conventional whole core logging and imaging

Conventional cores were extracted from the G-APC or G-XCB and imaged with an IR scanner. The cores were then sectioned, with whole-round samples being cut from the sections for pore water and microbiology analyses. Index properties and strength measurements were made on the ends of each section. Core sections were transported to College Station, TX for Multi-Sensor Core Logger (MSCL) logging and CT imaging. Core sections were then transported to Salt Lake City, UT and whole-round samples were cut from these cores for geomechanics. See Methods: Core processing (Flemings et al., [2025b](#)) for more details.

Figure [F43](#) shows an example of the variety of logs and images collected on one conventional core, Core H003-01H. Downhole trends are presented in Figure [F44](#). Logging included volume-dependent magnetic susceptibility (gamma density (Figure [F43](#), column J, red line), natural gamma radiation (Figure [F43](#), column J, green line), P-wave velocity (Figure

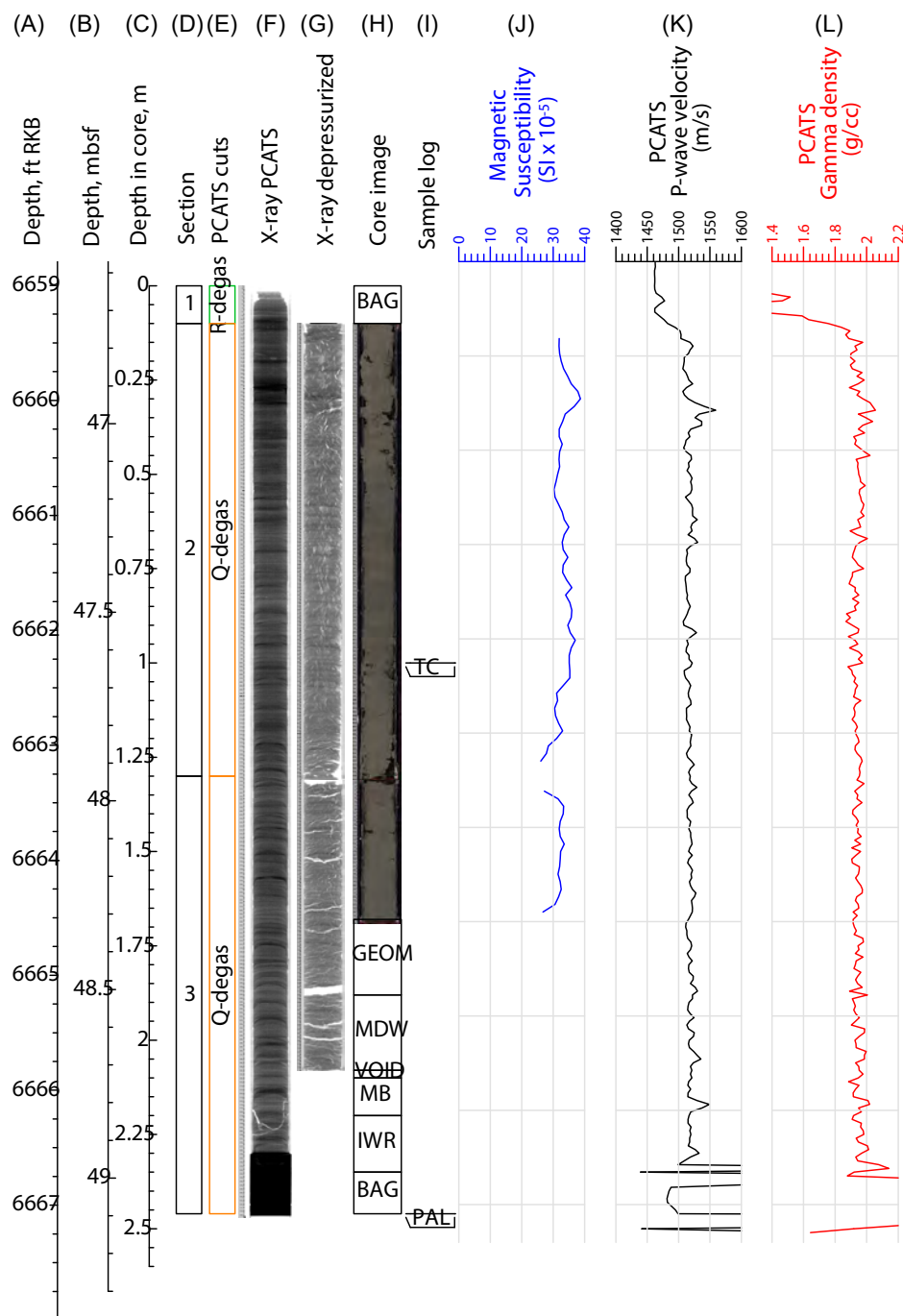


Figure F41: Example pressure core log for Core H003-08CS. A) Measured depth in feet below the rig floor (ft RKB); B) Measured depth in meters below the seafloor (mbsf); C) Measured depth in core; D) Section number (number in black box); E) Core allocation (text in colored box). Core H003-08CS was cut at elevated pressure into two sections for quantitative degassing (Q-Degas, orange boxes). The remaining pressure core section, Section 1, was rapidly depressurized in the Pressure Core Analysis and Transfer System (PCATS) (R-degas) and bagged for later assessment (sample code BAG) and a biostratigraphy sample (sample code PAL) was collected from the bagged material; F) PCATS X-ray image (slab view of computed tomography (CT) data). Core H003-08CS was imaged and logged before depressurization using PCATS at close to in-situ pressure and temperature; G) Multi-Sensor Core Logger (MSCL) X-ray image (slab view of CT after depressurization). After quantitative degassing, whole-round samples were cut from section 3 for routine pore water analysis (sample code IWR) and microbiology (sample code MB). The remaining whole-round sections were imaged. Whole-round sections were then cut for geomechanical testing (sample code GEOM) and moisture and density (sample code MDW) from section 3, and a thermal conductivity measurement was made on section 2 (code TC). Magnetic susceptibility was then measured on Sections 2 and 3; H) Split core images and identification of samples collected before splitting; I) measurement locations; J) magnetic susceptibility using an MSCL loop scanner measured after depressurization but before splitting in blue; K) PCATS P-wave velocity in black measured before depressurization; L) PCATS gamma density in red measured before depressurization. PCATS Dataset: <https://doi.org/10.5281/zenodo.14518408>, Core Images Dataset: <http://doi.org/10.5281/zenodo.14261688>.

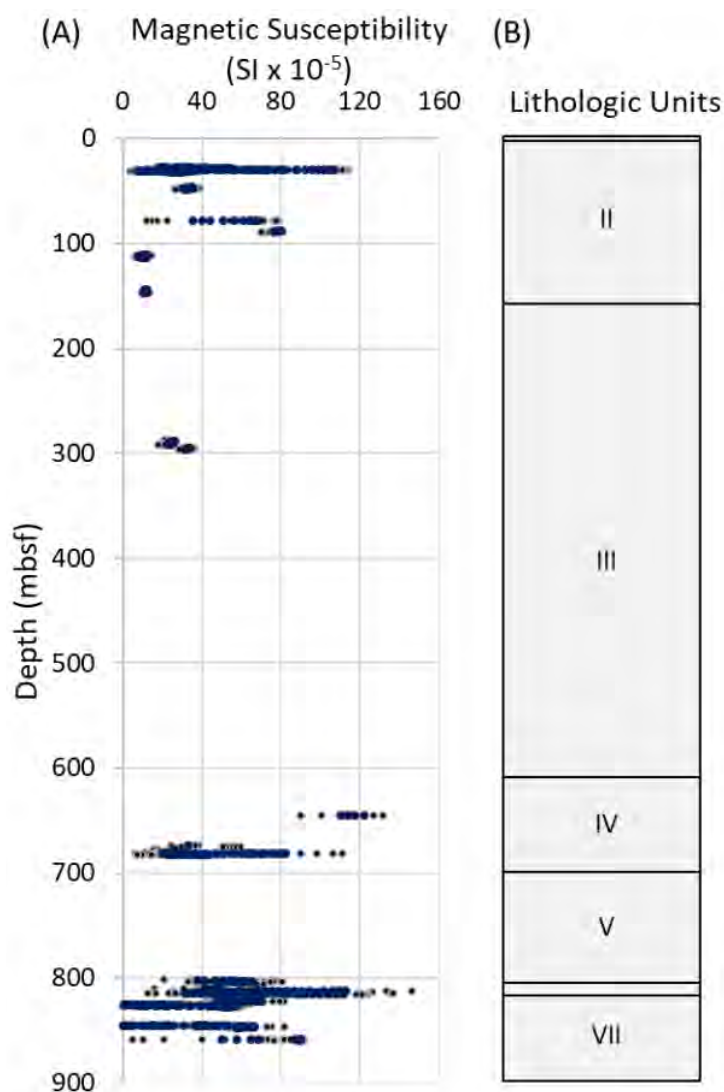


Figure F42: Conventionalized core magnetic susceptibility. Gray dots show actual measurements which integrate magnetic susceptibility over a core length of approximately 5 cm. The blue dots show the 10-point running means. Dataset: <http://doi.org/10.5281/zenodo.14518437>.

[F43](#), column K), and electrical resistivity (Figure [F43](#), column L). A core log for each core can be found in Appendix F: Conventional Core Logs.

IR scans did not reveal any temperature anomalies in any core. There may be multiple reasons for this: 1) temperatures were high in both the upper water column and on deck, warming the core before the IR scan and 2) significant concentrations of hydrate were not expected in conventionally cored sections.

A variety of 2D and 3D X-ray images were collected on the whole-round core. See Methods: Conventional whole core logging and imaging (Flemings et al., [2025b](#)). Both the CT slab image (Figure [F43](#), column

F) and the visible line scan image from the split core (Figure [F43](#), column G, See [Split core imaging and logging](#)) can provide an idea of core recovery and core quality. In general, X-ray images emphasize layers or veins with higher density and higher atomic number. Roughly, white areas in the scans are usually air-filled and low density while darker black indicates high density.

Gamma density (Figure [F44](#), column A) is on average 1.7 g/cm^3 with a maximum of 2.2 g/cm^3 . There are numerous low values down to $\sim 0 \text{ g/cm}^3$ due to the presence of cracks, voids, and mousse-like/soupy textures in the sediments. Detailed analyses using these data should take care to interpret these low values with core photos and descriptions to identify these disturbances. There are broad trends in these data (Figure [F44](#)). Density decreases with depth over the upper 20 m from ~ 2 to 1.4 g/cm^3 and then steeply increases from 1.4 to 1.8 g/cm^3 between 20 and 41 mbsf. From 41 mbsf to the bottom of the continuous section at 158 mbsf, there is an overall very slight increase in density with maxima at 51, 90, and 123 mbsf. The deeper core (Core H003-26X) from 278 to 277 mbsf has a higher overall density compared to the shallower cores. Individual spikes in density at the top of cores may be related to sandy fall-in material and the core description can provide context.

Natural gamma radiation exhibits a wide scatter but presents down-core trends when the running mean is plotted (Figure [F44](#)). Natural gamma radiation ranges up to 19 counts s⁻¹, but the running mean is constrained between 2 and 10 counts s⁻¹. There is a local maximum at 21 mbsf and below this point there are broad trends with some similarity to gamma density.

Magnetic susceptibility (κ) shows a strong peak at 3 mbsf ($93 \text{ SI} \times 10^{-5}$) and decreases to a low interval ($\kappa < 20 \text{ SI} \times 10^{-5}$) between 5 and 19 mbsf (Figure [F44](#)). κ is relatively higher between 20 and 62 mbsf and 71 and 101 mbsf. κ is relatively low in most of the deeper cores in Hole H003 between 105 and 158 mbsf, and 278 and 296 mbsf. Individual spikes in κ at the top of cores are likely related to sand-rich fall-in material.

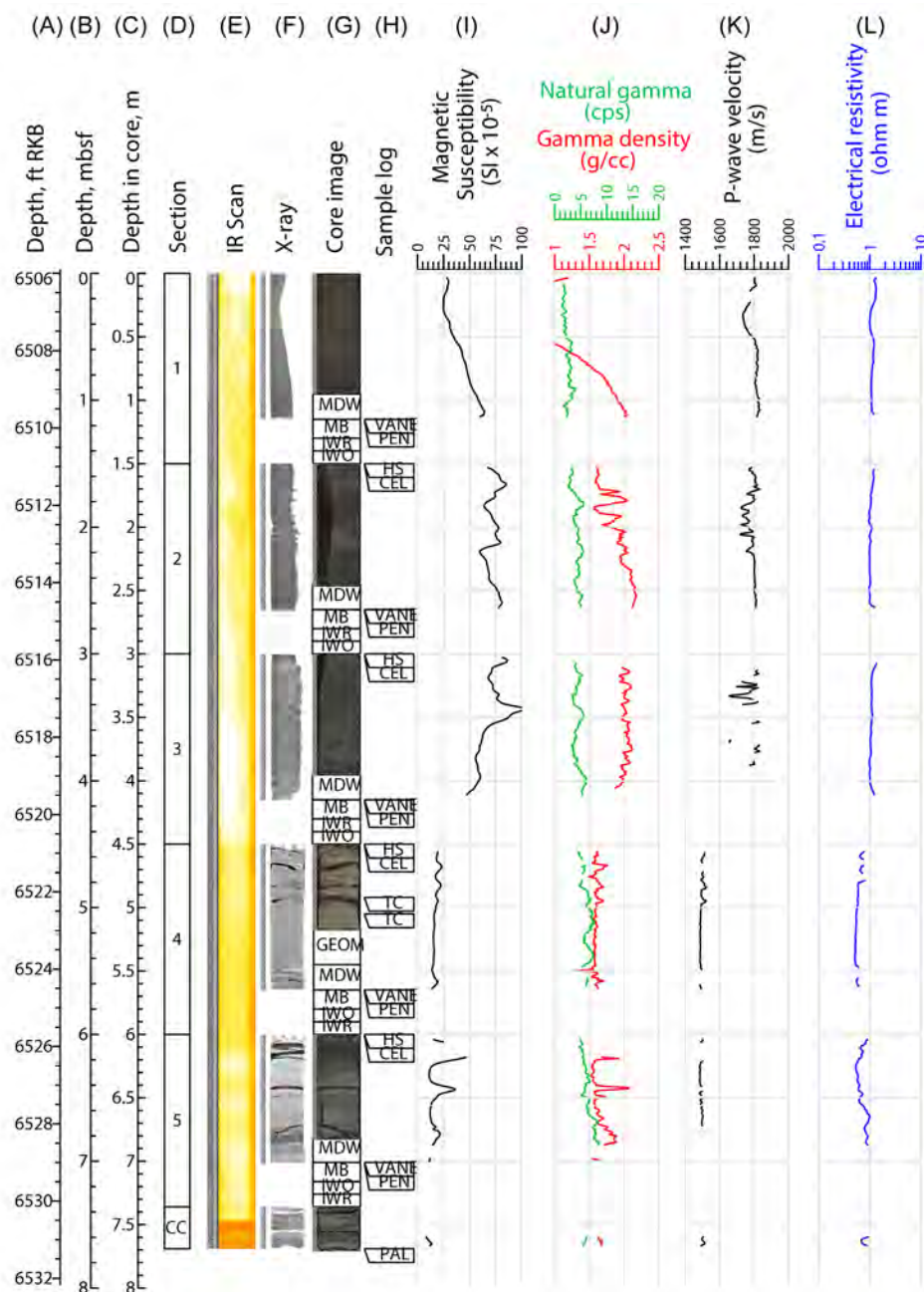


Figure F43: Example conventional core log for Core H003-01H. This mudline core penetrated the massive Sand lithofacies. A) Measured depth in feet below the rig floor (ft RKB); B) Measured depth in meters below the seafloor (mbsf); C) Measured depth in core (0 m is set at the top of the core sediment); D) section identification (number in black box); E) thermal image, darker yellow areas are warmer; F) Multi-Sensor Core Logger (MSCL) x-ray image (slab view of Computed Tomography (CT) after depressurization); G) split core images of the archival halves. Whole-round samples were cut from all sections except the core catcher (CC) section. A biostratigraphy sample (sample code PAL) was collected from the core catcher. Whole-round samples included microbiology (sample code MB), routine pore water (sample code IWR), and organic pore water (sample code IWO). Headspace gas (sample code HS) and microbiology cell count (sample code CEL) samples were extracted from the top of sections 2-5. Sediment strength was measured using a hand-held vane (code VANE) and a pocket penetrometer (code PEN) at the bottom of sections 1-5. The remaining parts of the sections were logged using the MSCL and CT images. The geomechanics (sample code GEOM) and moisture and density (sample code MDW) whole-round samples were cut from sections after CT imaging but before splitting. Sediment strength measurements were again made on the ends of sections 1-5 using a table vane and fall-cone (locations not shown) before splitting; H) identification of whole-round sampling and measurement locations taken before splitting, including a pair of thermal conductivity measurements (TC) in section 4; I) MSCL magnetic susceptibility; J) MSCL natural gamma and gamma density; K) MSCL P-wave velocity, and L) MSCL electric resistivity. Conventional Core Log Dataset: <https://doi.org/10.5281/zenodo.14518382>, Core Image Dataset: <http://doi.org/10.5281/zenodo.14261688>.

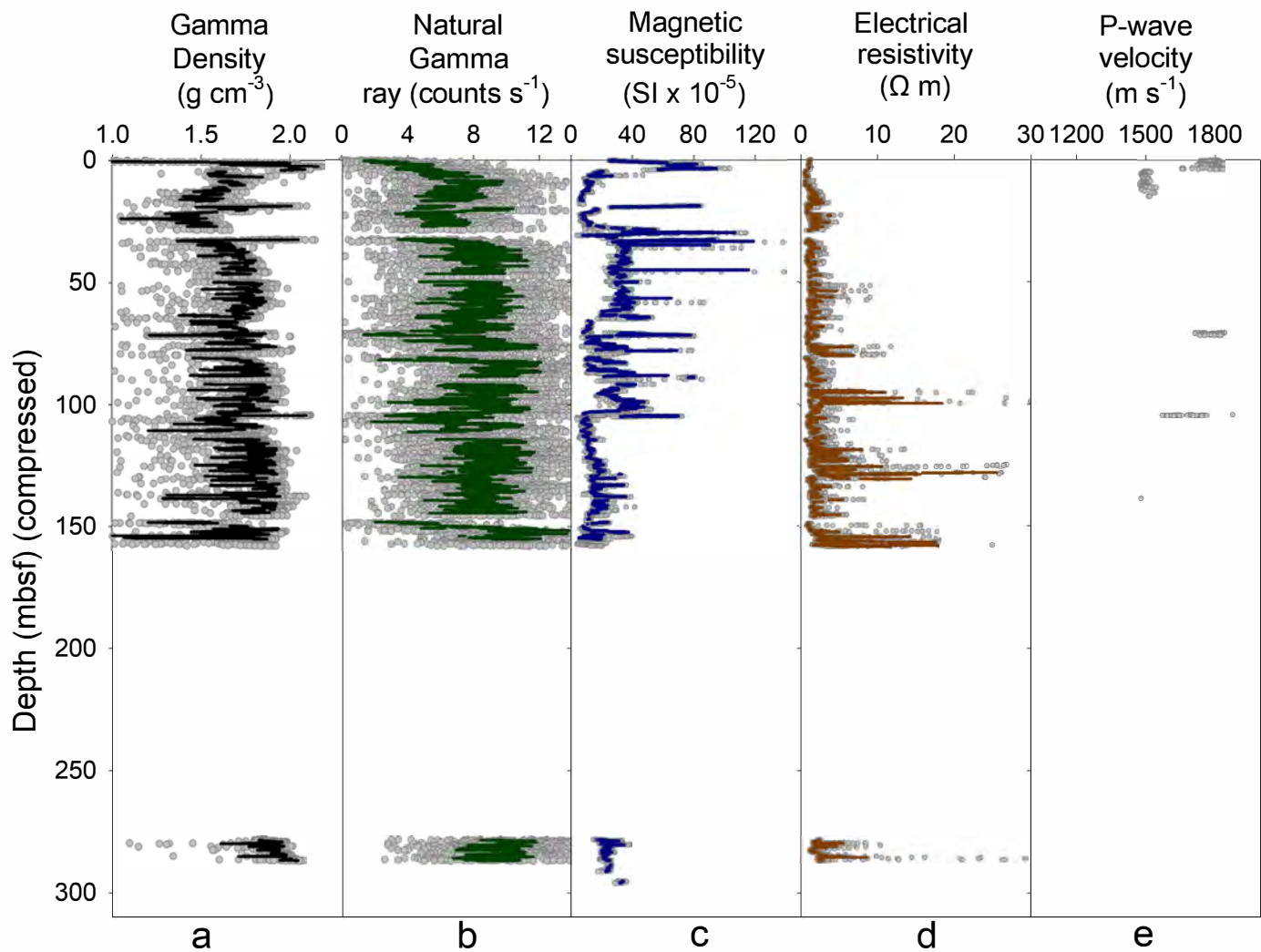


Figure F44: Downcore trends in MSCL-S measured conventional core properties using compressed measured depth in meters below the seafloor (mbsf). A) gamma density B) natural gamma ray C) magnetic susceptibility D) electrical resistivity E) P-wave velocity. Gray dots show actual measurement points, while the colored lines show 10-point running means. Dataset: <https://doi.org/10.5281/zenodo.14518382>.

Electrical resistivity is below 4 Ωm for most of the record with multiple intervals containing spikes up to 10 to 26 Ωm (Figure F44). These are likely due to cracks and voids in the sediment.

Very few scanned intervals generated quality P-wave velocity measurements due to a lack of contact between the core and liner. Where P-wave velocity was measured, velocities ranged from 1,475 to 1,878 m s^{-1} (Figure F44).

Split core logging and imaging

All split cores were scanned for color spectrophotometry, magnetic susceptibility, and X-ray

fluorescence.

Color spectrophotometry

Color spectrophotometry was acquired on all split core sections according to the method in Methods: 2.8.6 Conventional whole core logging and imaging (Flemings et al., 2025b).

Color spectrophotometry scans (Figure F45) reveal cyclic variation in the continuous section 0-296.4 mbsf (Hole H003). Sediment lightness (L^*) has prominent spikes at 21, 68, 105, 112, and 164 mbsf. Color spectrophotometry scans generally have lower variation from 644.6 to 859.6 mbsf (Hole H002) compared to the overlying interval from 0-296.4 mbsf (Hole H003). Green to red color space (a^*) and blue

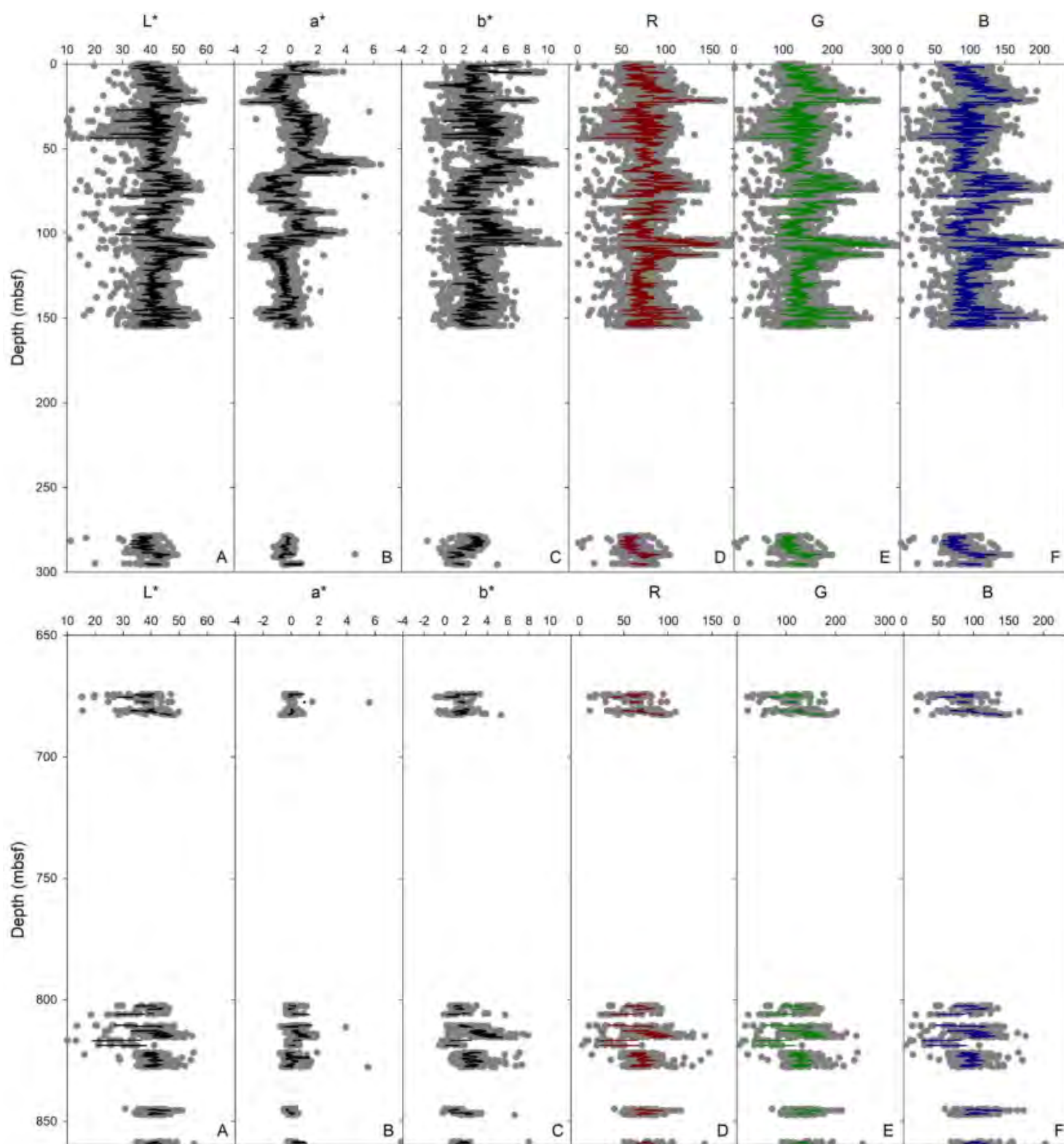


Figure F45: Color spectrophotometry results from Hole H003 (top) and Hole H002 (bottom). A) Sediment lightness (L^*), B) green to red color space (a^*), C) blue to yellow color space (b^*), D) red color range (650 to 700 nm) (R). E) green color range (490 to 590 nm) (G), and F) blue color range (400 to 480 nm) (B). All depths are compressed measured depth in meters below the seafloor (mbsf). Dataset: <http://doi.org/10.5281/zenodo.14277995>.

to yellow color space (b^*) follow a pattern inverse to L^* . Raw red (R), green (G), and blue (B) color ranges follow a pattern largely similar to L^* and show increased variation in the Orange sand interval.

Magnetic susceptibility

Point magnetic susceptibility (volume-dependent magnetic susceptibility), κ was measured on all split

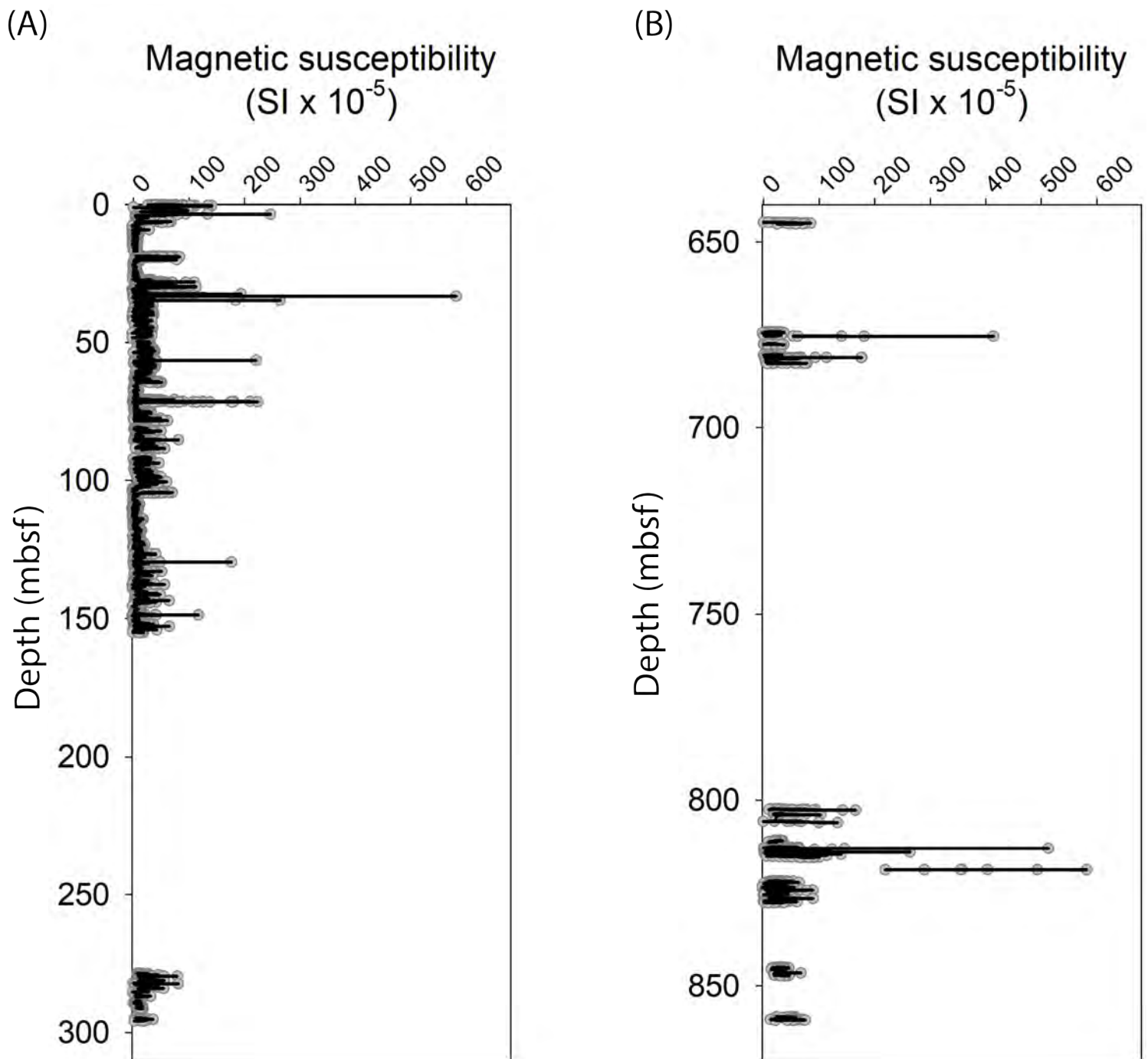


Figure F46: Point magnetic susceptibility from split cores. Gray dots are each measurement, and the black lines are a running mean of 10 measurements. A) Hole H003; B) Hole H002 data; All depths are compressed measured depth in meters below the seafloor (mbsf). Dataset: <http://doi.org/10.5281/zenodo.14277995>.

core sections according to the method in Methods: Conventional whole core logging and imaging (Flemings et al., 2025b).

In Hole H003 (0-296.4 mbsf, Figure F46, left), κ decreases over the upper 4 mbsf and remains relatively low ($< 15 \text{ SI} \times 10^{-5}$) down to 24 mbsf (Figure F46). κ increases to 30-60 $\text{SI} \times 10^{-5}$ between 24 and 63 and 75 to 102 mbsf. κ is low between 102 mbsf and

increases slightly between 121 and 158 mbsf. There are numerous spikes in κ throughout the record, some of which correspond to intervals of sandy fall-in material.

In Hole H002, κ is generally less than 90 $\text{SI} \times 10^{-5}$, but ranges up to 582 $\text{SI} \times 10^{-5}$, increasing in thin coarse layers associated with the Blue and Orange sands (Figure F46, column B, 644.6-859.6 mbsf).

Uncalibrated X-ray fluorescence

X-ray fluorescence was measured on all split core sections according to the method in Methods: Conventional whole core logging and imaging (Flemings et al., 2025b). Measurements are presented uncalibrated. These data will be calibrated against XRF measurements from discrete samples at UNH.

Si and Zr show numerous spikes downcore, many of them corresponding to spikes in κ , and corresponding to sandy fall-in intervals (Figures F47 and F48). Al, Ti, Fe, and K show a similar pattern downcore from 0-296.4 mbsf (Hole H003) (Figure F47). Ca and Si show a record that is somewhat inverse of the other siliciclastic-associated elements. S, P, and Ba are elevated in distinct intervals that do not correspond to records of more siliciclastic elements (Figures F47 and F48).

Due to the intermittent coring of Hole H002 (644.6-859.6 mbsf), it is hard to determine any downhole variation, but we can see higher variation in elemental abundance within the Orange sand (Figures F47 and F48, 805-819 mbsf). Some elements show anomalies in Core H002-09CS including Si, Zr, Ti, Al, and Pb (Figures F47 and F48, 812.6-815.6). These may be associated with thin sand intervals in the middle of the Orange sand. There is also an increase in Si and Zr associated with a coarse-grained bed as part of the Upper Blue sand (Figures F47 and F48, 664-688 mbsf). There is an anomaly in Ba and S in the lower bound of the Orange sand (Figures F47 and F48, 805-819 mbsf).

Undrained shear strength

Undrained shear strength (S_u) of cohesive, mud-dominated sediments was measured on conventional and conventionalized pressure cores acquired on UT-GOM2-2 (See Methods: Core processing (Flemings et al., 2025b)). This subsection presents the strength measurements obtained from the onboard and dockside phases.

While onboard the *Q4000*, a handheld shear vane and a pocket penetrometer provided an estimate of the undrained shear strength and aided in evaluating

sample quality and the consistency of the sampling process. Measurement frequency was generally one measurement location at the bottom of each section of core (See Methods: Undrained shear strength (Flemings et al., 2025b)). In most cases, one handheld shear vane measurement and three pocket penetrometer measurements were obtained at each sample location, and an average value was calculated (avg. strength reported in Table 1).

Hole H003: 0-296.4 mbsf

During the onboard phase, a total of 108 locations were measured for undrained shear strength with the majority (103) from depths 0-153 mbsf corresponding to G-APC cores 01H – 25H. An additional five measurements were obtained in G-XCB core 26X from 280-286 mbsf. Dockside, a total of 160 lab vane and fall cone measurements were collected for undrained shear strength with the majority corresponding to G-APC cores. All data are plotted in Figure F49 and included in Appendix G: Undrained Strength Table 1 (onboard data) and Appendix G: Undrained Strength Table 2 (dockside data). Undrained shear strength generally increases with depth, although not linearly, reaching above 200 kPa. This increase is expected, since the porosity decreases with depth and the material compacts with depth. Overall, the strengths measured with handheld vane are lower than the strengths measured with pocket penetrometer for the onboard measurements. In the dockside measurements, the strengths measured with fall cone are generally lower than the strengths measured with lab vane. The strength measured with fall cone is the lowest, and the strength measured with pocket penetrometer is the highest at most depths. The strength measured with fall cone is the lowest, and the strength measured with pocket penetrometer is the highest in most locations. The G-XCB core 26X from 280-286 mbsf exhibited wide variations in the strengths measured compared to the G-APC cores 01H – 23H.

Hole H002: 644.6 to 859.6 mbsf

A total of 23 lab vane and fall cone measurements were collected for undrained shear strength of Hole

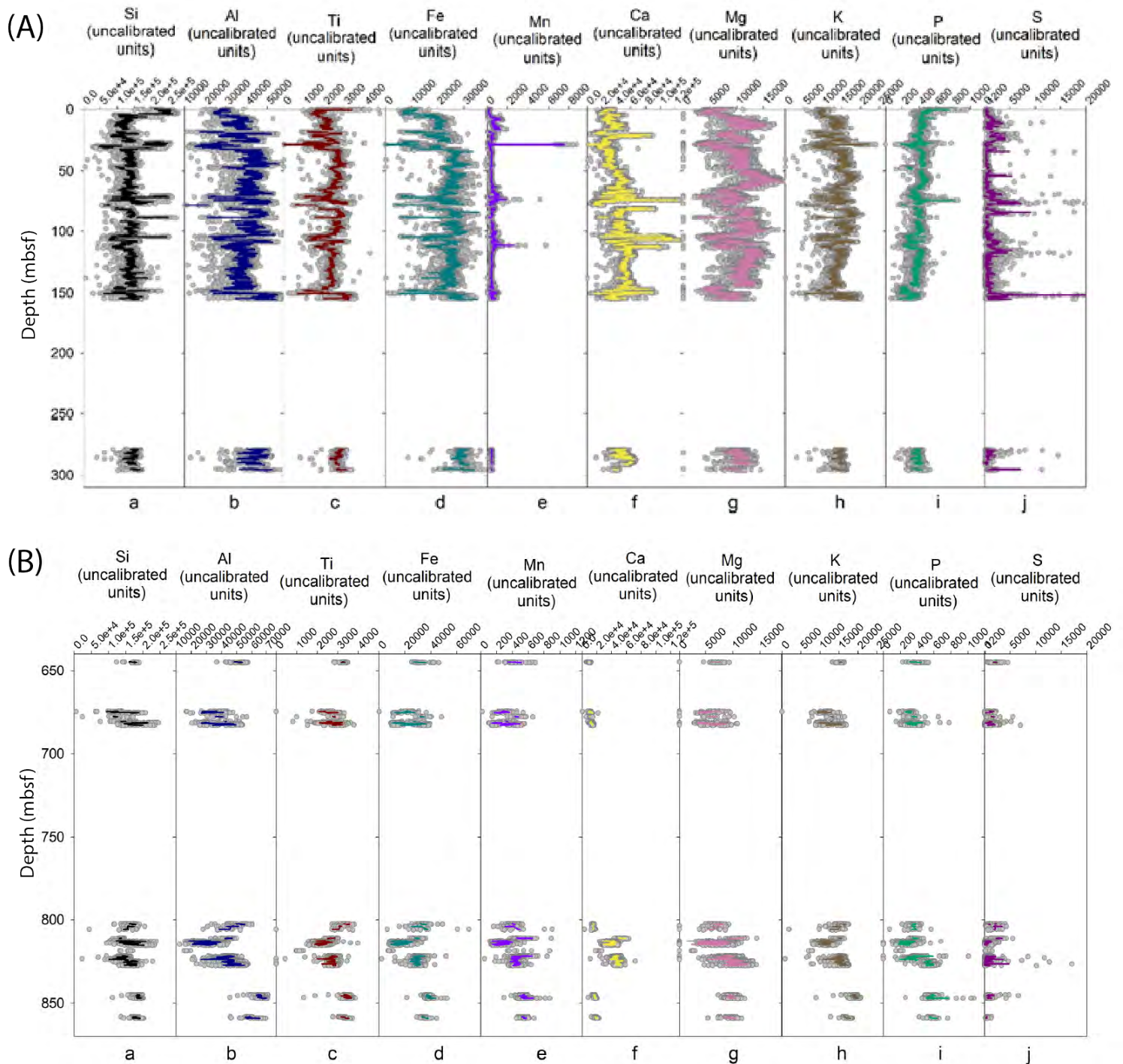


Figure F47: Major and minor elements as measured by X-ray fluorescence on split cores. A) Data from Hole H003 (0-296.4 mbsf); B) Data from Hole H002 (644.6-859.6 mbsf); Columns a) silicon, Si b) aluminum, Al c) titanium, Ti, d) iron, Fe e) manganese, Mn f) calcium, Ca g) magnesium, Mg h) potassium, K i) phosphorus, P; and j) sulfur, S. Gray dots are individual measurements, and the colored lines are a running mean of 10 points. All depths are in compressed measured depths in meters below the seafloor (mbsf). Dataset: <http://doi.org/10.5281/zenodo.14277995>.

H002 cores during the dockside phase. All data are plotted in Figure F49 and included in Appendix G: Undrained Strength Table 3. In both measurements, the undrained shear strength varies more than two-orders of magnitude.

Appendix H: Index Properties Table 2 provides a summary of the location of the 33 whole-round samples for mechanical strength testing (sample code GEOM). These sections were selected based on CT scan evaluation with priority given to locations with the least cracking and most uniform fine-grained

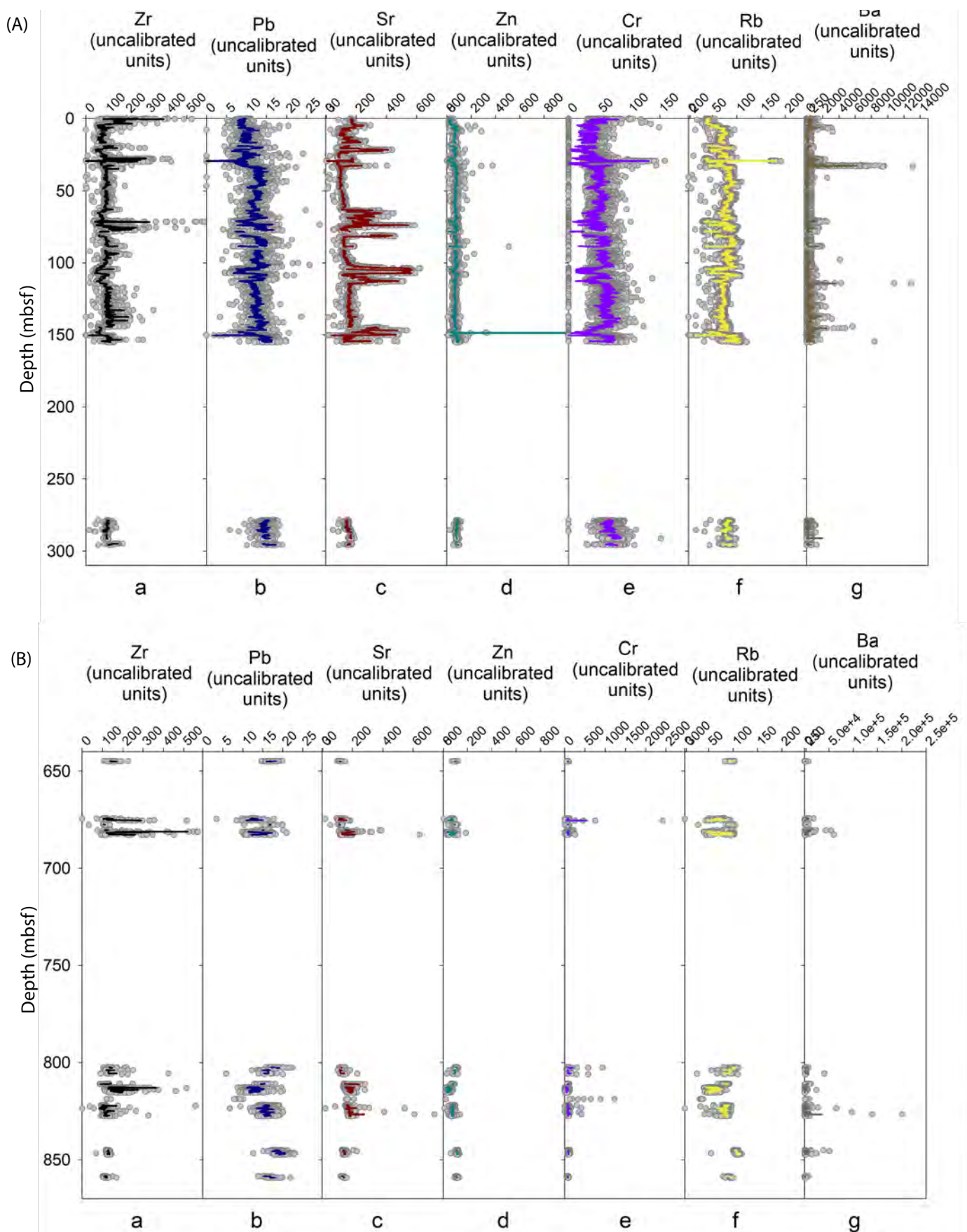


Figure F48: Trace elements as measured by X-ray fluorescence on split cores. A) Data from Hole H003 (0-296.4 mbsf); B) Data from Hole H002 (644.6-859.6 mbsf); Columns a) zirconium, Zr b) lead, Pb c) strontium, Sr d) zinc, Zn e) chromium, Cr f) rubidium, Rb and g) barium, Ba. Gray dots are individual measurements, and the colored lines are a running mean of 10 points. All depths are in compressed measured depths in meters below the seafloor (mbsf). <http://doi.org/10.5281/zenodo.14277995>.

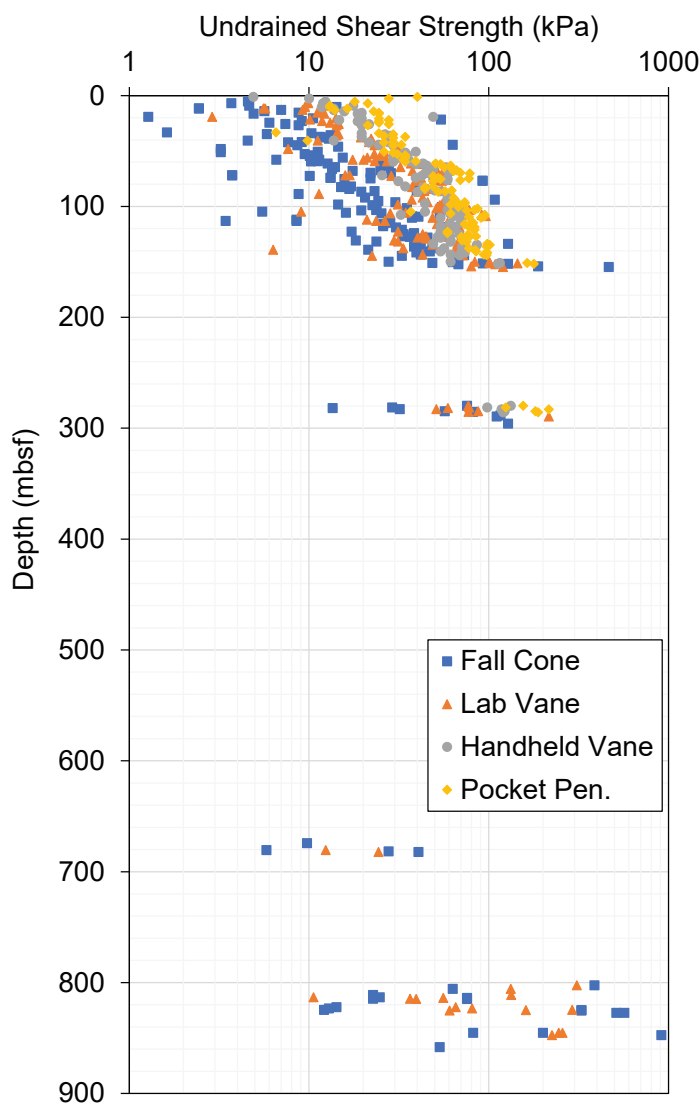


Figure F49: Undrained shear strength measurements. A pocket penetrometer and a handheld vane shear were deployed onboard. A lab vane and a fall cone were deployed dockside. Advanced Piston Corer (G-APC) coring ended at 153 mbsf (Core H002-25H). Measurement methods are in Methods: Undrained shear strength (Flemings et al., [2025b](#)). All depths are in compressed measured depths in meters below the seafloor (mbsf). Dataset: <http://doi.org/10.5281/zenodo.14107263>.

material. Samples were shipped to UT in cold core storage. Mechanical testing will be completed at UT and Tufts.

Index properties

Physical property measurements are being made at Tufts and UT on samples acquired during core processing at the Geotech facility in Salt Lake City, Utah. The results are still considered preliminary pending modification based on measured grain density and salinity values. See Methods: Index

<https://doi.org/10.5281/zenodo.13971276>

properties (Flemings et al., [2025b](#)) for all sampling and allocation methods.

Measurements were made on core plug samples acquired from split core sections from 0-859.6 mbsf (Holes H002 and H003) and oriented perpendicular to the axis of the core. Moisture and density measurements were made on split core plugs (sample code MDX). Results are reported in Moisture and density. Particle size distribution was measured using laser particle analysis on different split core plugs (sample code GSL). Results are reported in Laser particle analysis and Lithostratigraphy.

Moisture and density, as well as particle size distribution measurements, were also made on whole-round samples (sample code MAD, cut from the MDW whole-round samples, See Appendix H: Index Properties Table 2) from 0-296.4 mbsf (Hole H003). Measurements were made on the whole-round samples before subsampling and on plugs, wedges, and blended material after subsampling (See Methods: Moisture and density (Flemings et al., [2025b](#)) for subsampling method and Moisture and Density for results). Plugs from the MAD whole-round samples were oriented perpendicular to the axis of the core. Blended material was used for analyses requiring larger amounts of material, including particle size distribution by hydrometer and grain density by water submersion (See [Hydrometer](#) and [Grain density](#)).

Particle size distribution

Particle size distribution was measured using both the laser and hydrometer methods (Appendix H: Index Properties Table 4 and Table 7, Figures [F50](#) and [F51](#)) (See Methods: Particle size distribution (Flemings et al., [2025b](#))). The fraction of sand, silt, and clay was reported, based on both the geoscience and geotechnical engineering classifications of grain size: 1) The engineering definition is that clay particles are less than 2.0 μm ; silt-sized particles are between 2.0 – 75 μm , and sand particles are larger than 75 μm ; 2) The geoscience definition is that clay particles are smaller than 3.9 μm and sand particles are larger

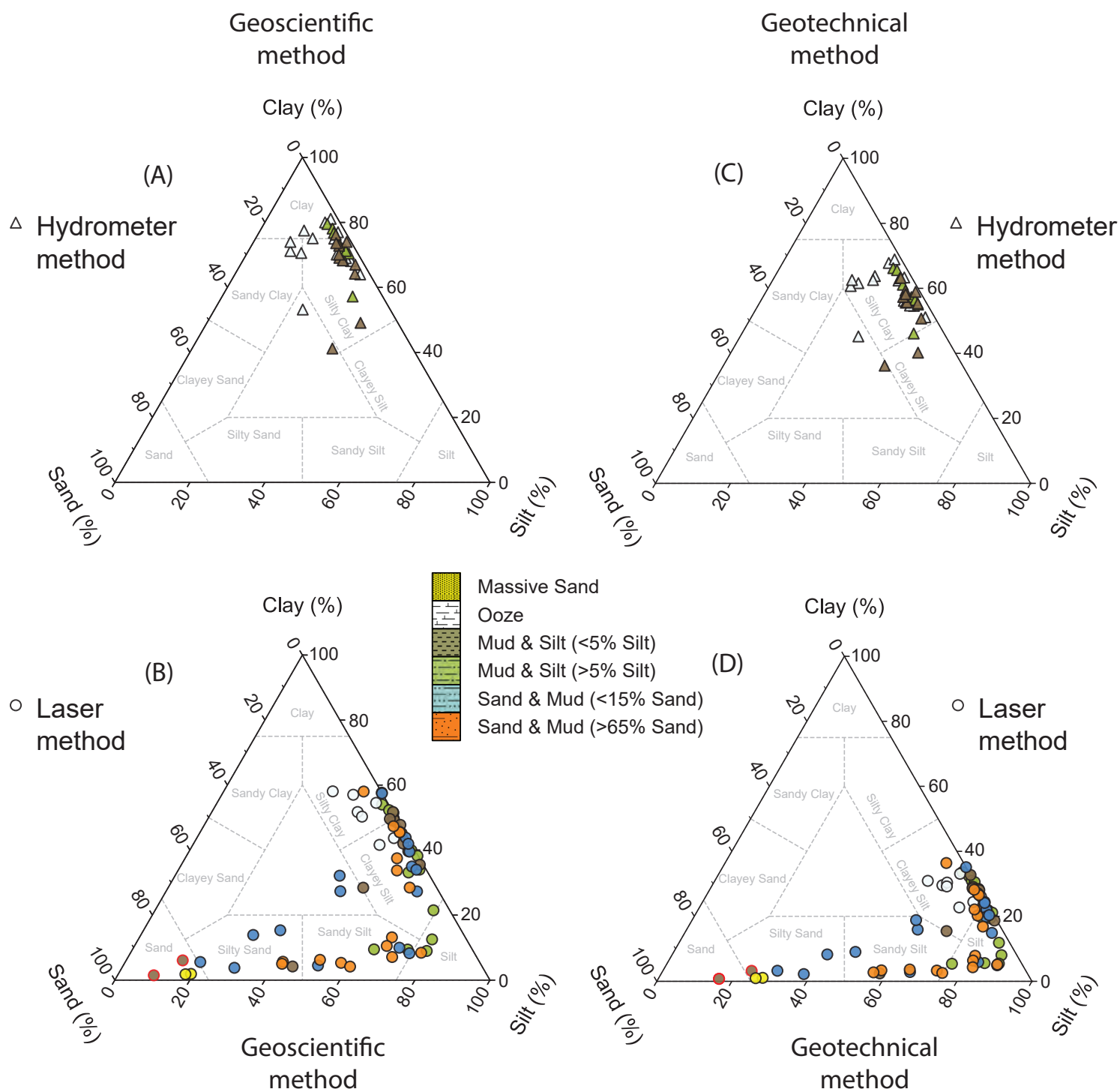


Figure F50: Ternary diagrams of particle size distribution using different measurement and classification methods. A) Hydrometer and B) Laser results using the geoscientific classification with particle size cutoffs of clay = <3.9 μm , silt = 3.9–62.5 μm , sand = >62.5 μm ; C) Hydrometer, and D) Laser results using the geotechnical classification with particle size cutoffs of clay = <2 μm , silt = 2–75 μm , sand = >75 μm . The two brown circles outlined in red are samples of fall-in from H003-04CS. Particle Size Distribution Dataset: <http://doi.org/10.5281/zenodo.14109861>.

than 62.5 μm (See Methods: Grain size classification (Flemings et al., 2025b)).

Figure F50 shows a breakdown of the particle distribution results by method and classification. The largest difference is between the hydrometer (Figure

F50, top row) and the laser particle measurements (Figure F50, bottom row) when comparing fine particles (Figure F50, brown, green, and white markers). This difference occurs because the laser method reports a value weighted towards the average particle dimension, whereas the hydrometer

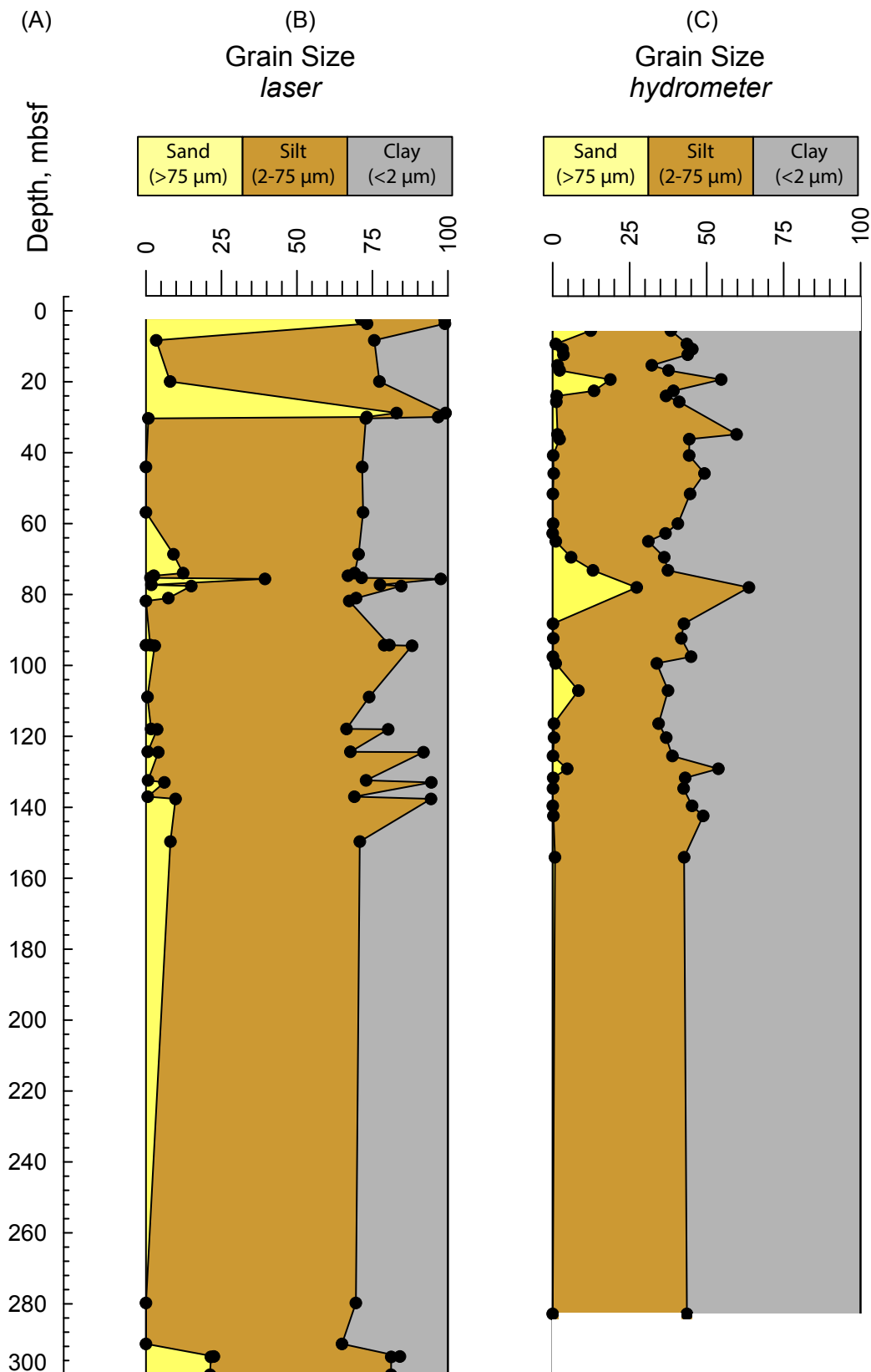


Figure F51: Sand, silt and clay fractions with depth. A) Compressed measured depth in meters below seafloor (mbsf); B) Laser particle analysis of discrete samples (sample code GSL). The large sand fraction 28-29 mbsf is fall-in from Core H003-04CS; C) Hydrometer tests on the MAD blended material. Grain size was determined using the geotechnical classification with particle size cutoffs of clay = <2 μm, silt = 2-75 μm, sand = >75 μm. The finer-grained lithofacies (Mud and Silt, Table T10) plot as a clayey silt when measured with the laser method whereas they plot as silty clay with the hydrometer method. Systematic laser and hydrometer method comparison studies have shown that the laser method typically reports a larger particle size for plate-shaped clay particles than does the hydrometer method (Di Stefano et al., 2010; Ferro and Mirabile, 2009; Wen et al., 2002). Dataset: <http://doi.org/10.5281/zenodo.14109861>.

method reports a value weighted towards the thin (short) dimension (Di Stefano et al., [2010](#); Ferro and Mirabile, [2009](#)). A majority of Site H fine particles are classified as silty clay using the hydrometer and clayey silt when using the laser particle method. A smaller but still significant shift is seen between the geoscience classification (Figure [F50](#) A) and the geotechnical classification (Figure [F50](#) B). Using the geotechnical classification, none of the fine sediments were classified as clay or sandy clay using the hydrometer. Using the geoscience classification, a few fine sediments were classified as clay or sandy clay. Samples of coarser material (Figure [F50](#), orange and yellow markers) were only measured using the laser particle method. A slight difference between the number of samples characterized as sand or silty sand can be seen between the two classifications (Figure [F50](#) bottom row). A very large difference can be seen in the fine particles between the hydrometer results with the geoscience classification (Figure [F50](#) A) and the laser results with the geotechnical classification (Figure [F50](#) D). Most of the fines using the hydrometer and the geoscience classification and none of the fines using the laser and the geotechnical classification were classified as clay, sandy clay, or silty clay. In Lithostratigraphy, fines are described based on Figure [F50](#) C, the hydrometer results using the geotechnical classification.

Laser particle analysis

Laser particle size distribution was measured on 69 sediment samples collected from the split cores (sample code GSL). Thirty-five of these samples were obtained from Hole H003, from 0-296.4 mbsf. Thirty-four were obtained from Hole H002 from 644.6-859.6 mbsf. The analyses were performed at UT (See Methods: Laser particle analysis and grain size classifications (Flemings et al., [2025b](#))).

Cumulative particle size distributions are shown for 0-296.4 mbsf (Hole H003, Figure [F52](#)) and 644.6-859.6 mbsf (Hole H002, Figure [F53](#)). Sediment particle sizes generally range from 0.4 μm to 1000 μm . Sediments display two endmembers of particle size distributions. One endmember represents fine-grained sediments,

with clay fractions ($<2\ \mu\text{m}$) ranging from ~20%-40%. The other endmember represents coarse-grained sediments, with clay fractions ($<2\ \mu\text{m}$) ranging from 0-10% which include coarse-grained sediments from the sandy top at Site H (samples H003-01H-2a, and H003-01H-3a), fall-in from the sandy top (samples H003-04CS-2 and H003-04CS-3c, and possibly fractions of other samples from Hole H003), and coarse-grained sediments from the Upper Blue and Orange sands.

Hydrometer

Particle size distributions from Hole H003 made from blended material from the moisture and density whole-round samples (MAD blended) were measured using the sedimentation by hydrometer method at Tufts (See Methods: Hydrometer (Flemings et al., [2025b](#))). Results are presented in Appendix H: Index Properties Table 4, Figure [F23](#) A ternary diagram, and Figure [F54](#). The data are clustered in the silty clay region of the diagram (i.e. above the 50 % finer line in Figure [F54](#)) and include a few outliers with less clay.

Moisture and density

Figures [F55](#) and [F56](#), and Appendix H: Index Properties Table 1, and Table 3 show the moisture and density properties at Site H. Measurements were made on discrete plug samples from split cores (sample code MDX), whole-round samples (sample code MAD), and subsamples from the MAD whole-round samples (MAD plugs, MAD wedges, and MAD blended material, See sampling details in Methods: Moisture and density (Flemings et al., [2025b](#))).

Properties of wet density, water content, water saturation, and porosity were determined (See measurement methods in Methods: Moisture and density (Flemings et al., [2025b](#))). Core porosity was calculated using the measured wet density, assuming a grain density of 2.7 g/cm^3 , and that the pores are filled with fresh water. The porosity was also calculated using the measured water saturation and assuming a water saturation of 100%.

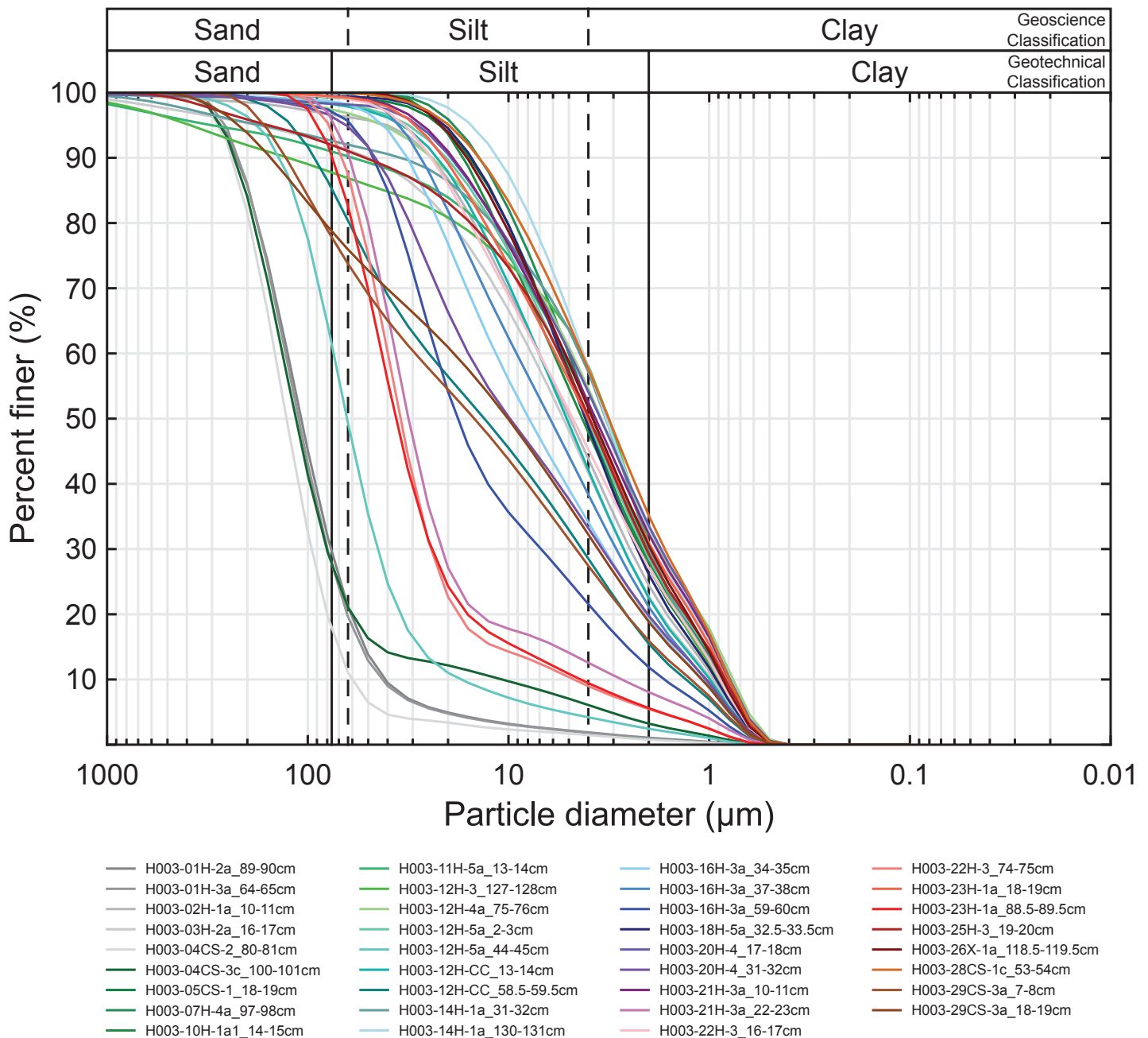
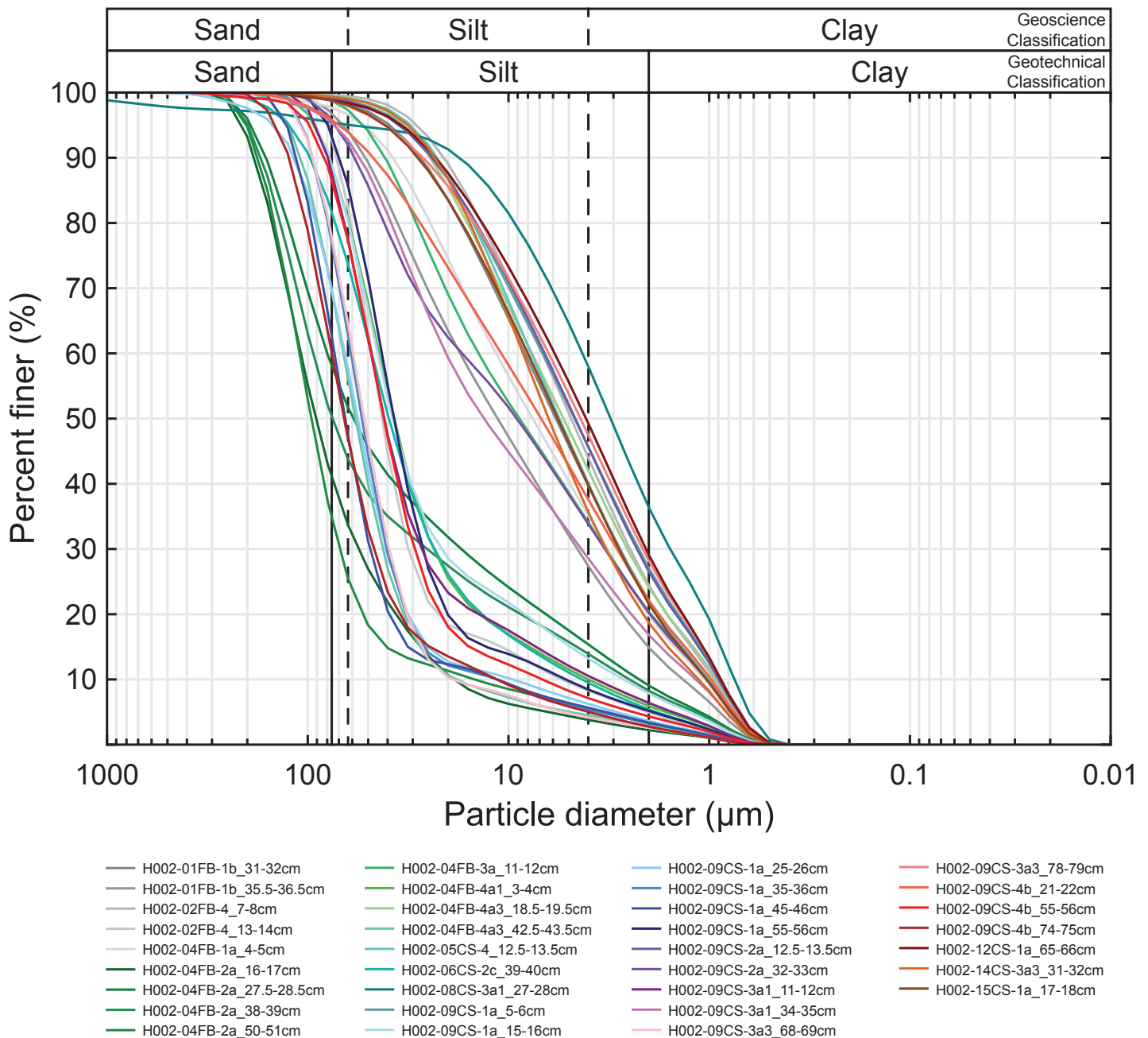


Figure F52: Cumulative laser particle size distributions for Hole H003 (measured depths of 0 to 296.4 meters below the seafloor) determined using laser particle analysis. Particle size cutoffs of the geotechnical (solid vertical lines; clay = <2 μm , silt = 2-75 μm , sand = >75 μm) and geoscience (dashed vertical lines; clay = <3.9 μm , silt = 3.9-62.5 μm , sand = >62.5 μm) classifications are shown with vertical black and dashed black lines, respectively. Samples of fall-in material (H003-04CS-2 and H003-04CS-3c) were kept in the dataset. Measurement method and particle size cutoffs are further described in Methods: Laser particle analysis and Grain size classification, respectively (Flemings et al., [2025b](#)). Dataset: <http://doi.org/10.5281/zenodo.14109861>.

Wet density

Wet density (sometimes called bulk or total density) measurements (Figures [F55](#) and [F56](#), column A) were obtained from mass and volume measurements of split core plugs (orange circles), whole-round samples (gray circles), and whole-round plugs (black circles). All plugs were collected perpendicular to

the axis of the cores (See Methods: Moisture and density (Flemings et al., [2025b](#)) for method and sample collection details). Wet density increases with compressed measured depth to a value of just over 2.0 g/cm³ at about 200 mbsf. Wet density in this interval is also related to lithostratigraphy, with lower density values being observed in the ooze intervals, as shown in Figure [F25](#) (See [Lithostratigraphy](#)).



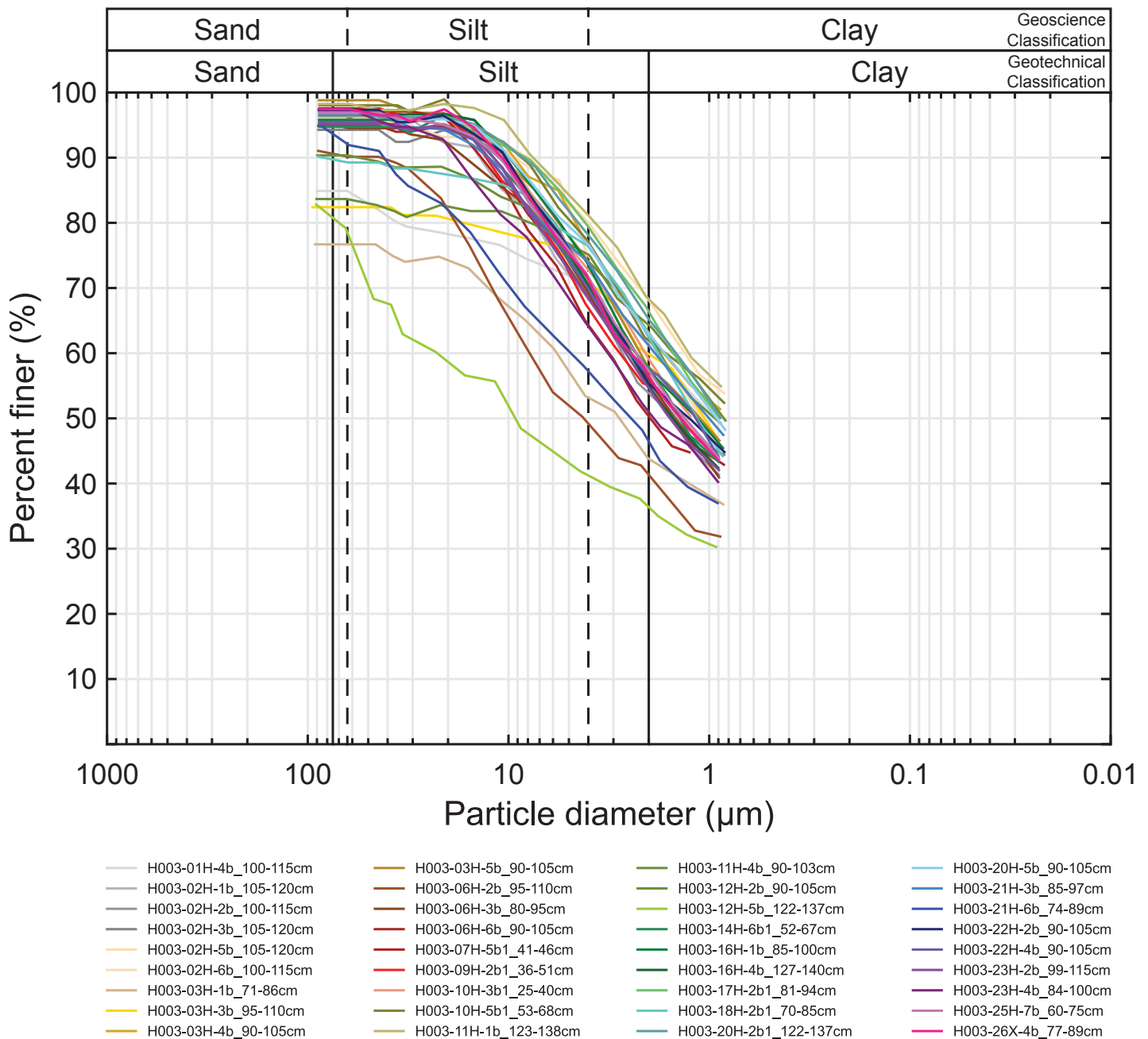


Figure F54: Cumulative hydrometer particle size distributions for Hole H003 (measured depth of 0 to 296.4 meters below the seafloor). Particle size cutoffs of the geotechnical (solid vertical lines; clay = <2 μm, silt = 2-75 μm, sand = >75 μm) and geoscience (dashed vertical lines; clay = <3.9 μm, silt = 3.9-62.5 μm, sand = >62.5 μm) classifications are shown with vertical black and dashed black lines, respectively. Measurement method and particle size cutoffs are further described in Methods: Hydrometer and Grain size classification, respectively (Flemings et al., [2025b](#)). Dataset: <http://doi.org/10.5281/zenodo.14109861>.

y-slope is 1.050 (Figure [F57 B](#)). Much of the offset in Figure [F57 B](#), is due to the measurements on one core with fall-in (Core H003-03H).

Water content

Water content with compressed measured depth (Figures [F55](#) and [F56](#), column B) was obtained from mass and volume measurements of split core plugs (orange circles), whole-round plugs (black circles),

whole-round wedges (green circles), and MAD blended material (Appendix H: Index Properties Table 3, not shown in the figure). See Methods: Moisture and density (Flemings et al., [2025b](#)) for measurement method details.

The overall trend is consistent with depth, with the values decreasing from around 80% near the mudline to around 25% at depth. Hole H003 (0.296.4 mbsf)

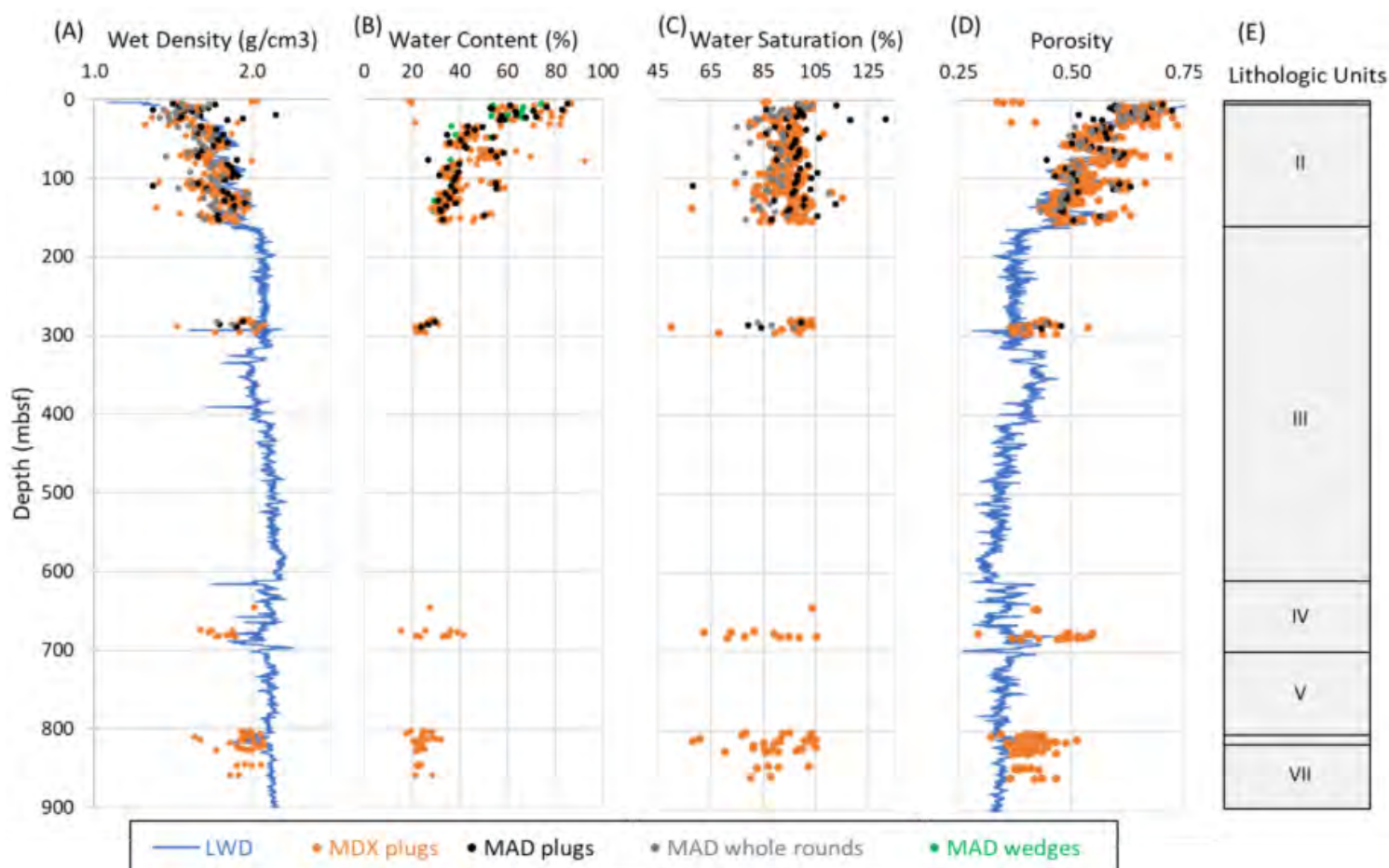


Figure F55: Measured moisture and density properties of A) Wet (bulk) density; B) Water content; C) Water saturation; and D) Porosity; Data from discrete split core plugs (MDX plugs) are shown as orange circles. Data from discrete plugs taken from moisture and density whole-round samples (MAD plugs) are shown as black circles, the entire whole-round sample before subsampling (MAD whole rounds) are shown as gray circles, and from whole-round wedges (MAD wedges, water content only) are shown as green circles. Samples were collected from Hole H002 but have not been measured yet. Depths are compressed measured depth in meters below the seafloor (mbsf). Any measurements of samples containing fall-in or thin interbedded sand were not removed. Core porosity was determined assuming fresh-water and a grain density of 2.7 g/cm³. Projected Hole H001 Logging while drilling (LWD) data are shown as a blue line. Data was projected to equivalent stratigraphic depths (See [Projection of Hole H001 to Site H measured depth](#)). The method for calculating the porosity from the LWD data is discussed in the Summary (Flemings et al., 2025a). E) Lithologic units (See [Lithostratigraphy](#)). Dataset: <http://doi.org/10.5281/zenodo.14107593>.

trends with lithostratigraphy (See [Lithostratigraphy](#)) with ooze intervals having higher water content. Some deeper cores from Hole H002 have higher water content due to gas hydrate dissociation. Figure [F58](#) compares the water content measured on the whole-round plug and whole-round blended material against the whole-round wedge material. Wedge and blended values are very consistent with a slope of 1.0029 (Figure [F58](#), black circles and trendline). The whole-round plug values are also consistent but have more scatter (Figure [F58](#), red circles and trendline).

Water saturation

Water saturation with compressed measured depth (Figures [F55](#) and [F56](#), column C) was calculated for the split core plugs (orange circles), whole-round plugs (black circles), and whole-round entire sample (gray circles). See Methods: Moisture and density (Flemings et al., 2025b) for calculation methods.

The average water saturation for the whole-round plugs from the center of the whole-round samples is 98.8% (96.7% with two outliers removed from the core with noted fall-in Core, H003-03H) while the average water saturation for the entire whole-round

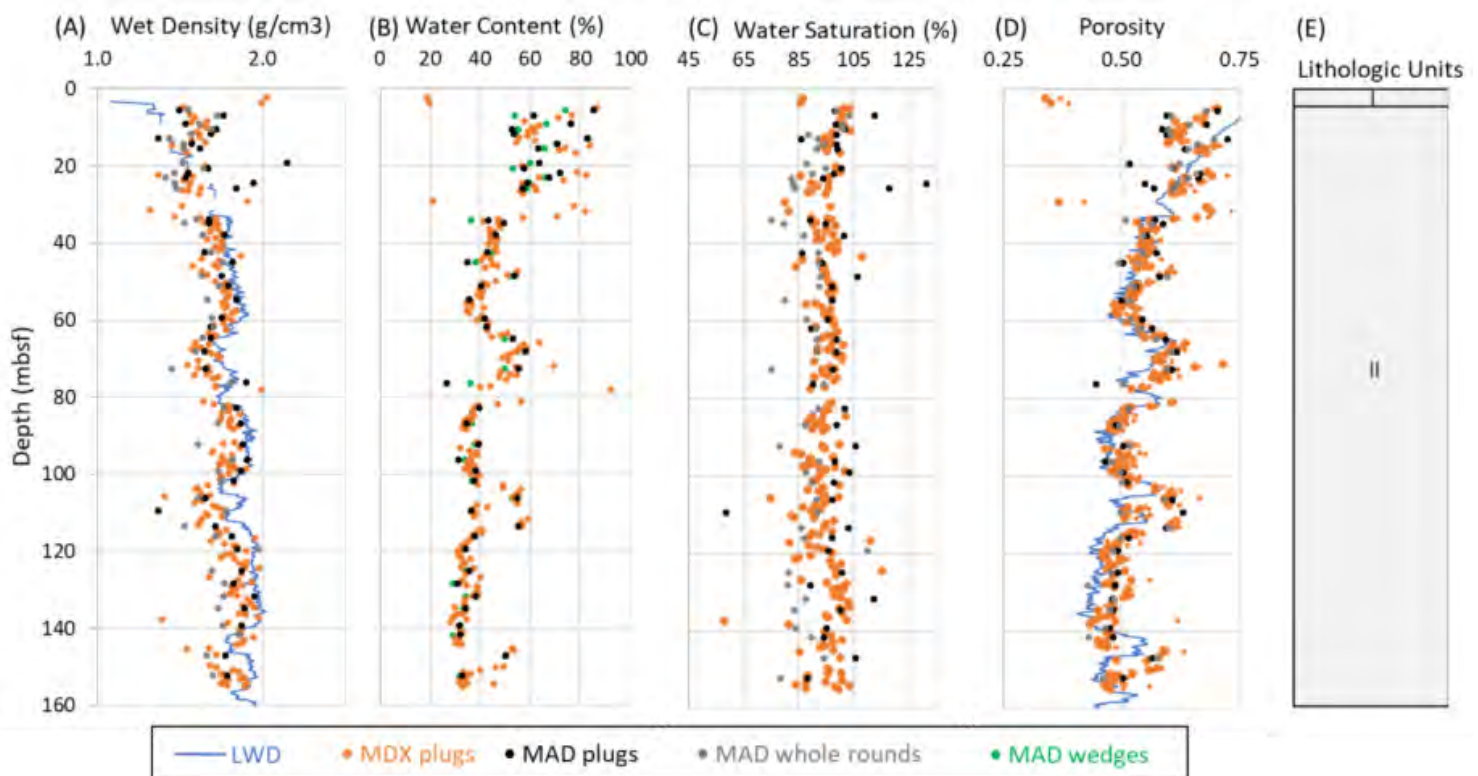


Figure F56: Expanded view of the measured moisture and density properties of A) Wet (bulk) density; B) Water content; C) Water saturation; and D) Porosity; Data from discrete split core plugs (MDX plugs) are shown as orange circles. Data from discrete plugs taken from moisture and density whole-round samples (MAD plugs) are shown as black circles, the entire whole-round sample before subsampling (MAD whole rounds) are shown as gray circles, and from whole-round wedges (MAD wedges, water content only) are shown as green circles. Depths are compressed measured depth in meters below the seafloor (mbsf). Any measurements of samples containing fall-in or thin interbedded sand were not removed. Core porosity was determined assuming a fresh-water saturation of 100% and a grain density of 2.7 g/cm³. Projected Hole H001 Logging while drilling (LWD) data are shown as a blue line. Data was projected to equivalent stratigraphic depths (See [Projection of Hole H001 to Site H measured depth](#)). The method for calculating the porosity from the LWD data is discussed in the Summary (Flemings et al., 2025a). E) Lithologic units (See [Lithostratigraphy](#)). Dataset: <http://doi.org/10.5281/zenodo.14107593>.

samples before subsampling is only 89.0%. Values over 100% are likely from cracking within the core.

Porosity

Porosity values are computed using two methods (See Methods: Moisture and density (Flemings et al., 2025b)). The first porosity calculation for each sample type assumes 100 % water saturation. This eliminates errors in the volume measurement because the porosity is only a function of water content and specific gravity. The second method makes use of the volume measurement through the calculation of the water saturation. All porosity values are based on an assumed grain density of 2.7 g/cm³ and we did not account for salinity in the pore fluid (pore fluid assumed to be fresh water). This assumed grain

density will be updated once we have sufficient grain density values.

Appendix H: Index Properties Table 1 provides the two values of porosity computed from the wet density measurement on each split core plug. Appendix H: Index Properties Table 3 provides four values of porosity computed from the wet density measurements on each whole-round sample; two from the plugs from the center of the whole-round sample and two from the entire whole-round before subsampling.

Figure F59 presents a cross plot of porosity between the two methods of calculation along with a linear regression line. Measurements made on the whole-round plugs are the most consistent between the methods. The whole-round sample values generally

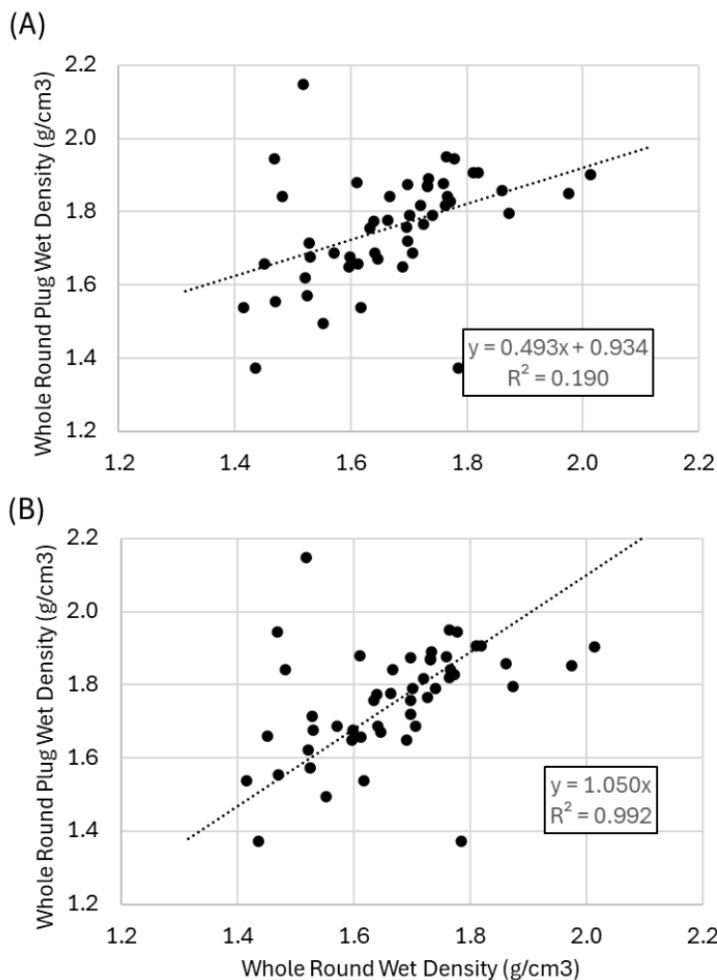


Figure F57: Comparison of the (A) wet (bulk) density of the whole-round plug (MAD plug) to the (B) wet (bulk) density of the entire whole-round sample (MAD). Measurements of samples containing fall-in or thin interbedded sands were not removed. Dataset: <http://doi.org/10.5281/zenodo.14107593>.

agree with the whole-round plug values when assuming 100% saturation due to the consistent water content.

Porosity calculated using the measured volume and calculated water saturation versus compressed measured depth is shown in Figures F55 and F56, column D for the split core plugs (orange circles), whole-round plugs (black circles), whole-round entire sample (gray circles). The Hole H003 (0-296.4 mbsf) porosity trends with the Hole H001 LWD-derived porosity and variations are driven by the lithology as shown in Figure F25. Porosity in Hole H002 (644.6-859.6 mbsf) is higher than the Hole H001 LWD from gas hydrate dissociation.

Porosity using an assumed water saturation of 100% is shown with depth for the first 150 m in Figure F56,

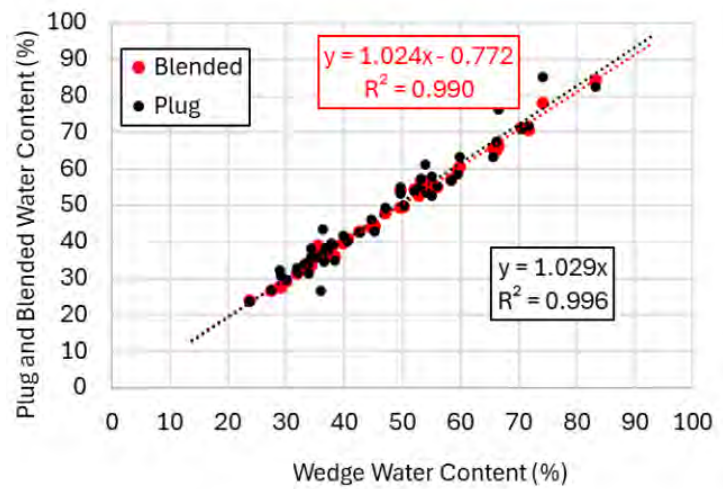


Figure F58: Cross plot of the water content measurements obtained on whole-round plugs (MAD plugs) and whole-round blended material (MAD Blended) vs the whole-round wedges (MAD wedges). Dataset: <http://doi.org/10.5281/zenodo.14107593>.

column D. The porosity trends with the LWD-derived data and variations are driven by the lithology as shown in Figure F25.

Grain density

The grain density was measured using two methods (Methods: Moisture and density (Flemings et al., 2025b)).

Submersion method

The results of initial grain density measurements performed on samples from Hole H003 (0-296.4 mbsf) on the whole-round blended material (MAD blended) using the water submersion method are presented in Appendix H: Index Properties Table 5. The average grain density is 2.798 g/cm³ with a standard deviation of 0.048, slightly higher than the assumed grain density of 2.7 g/cm³ using for the porosity calculations. There appears to be a slight trend of decreasing grain density with depth but there are also a pair of low and a pair of high values.

Pycnometer

The results of grain density measurements performed using a gas pycnometer on oven dried and pulverized split core plugs (sample code MDX) from 0-296.4 mbsf (Hole H003) and 644.6-859.6 mbsf (Hole H002) are presented in Appendix H: Index Properties Table

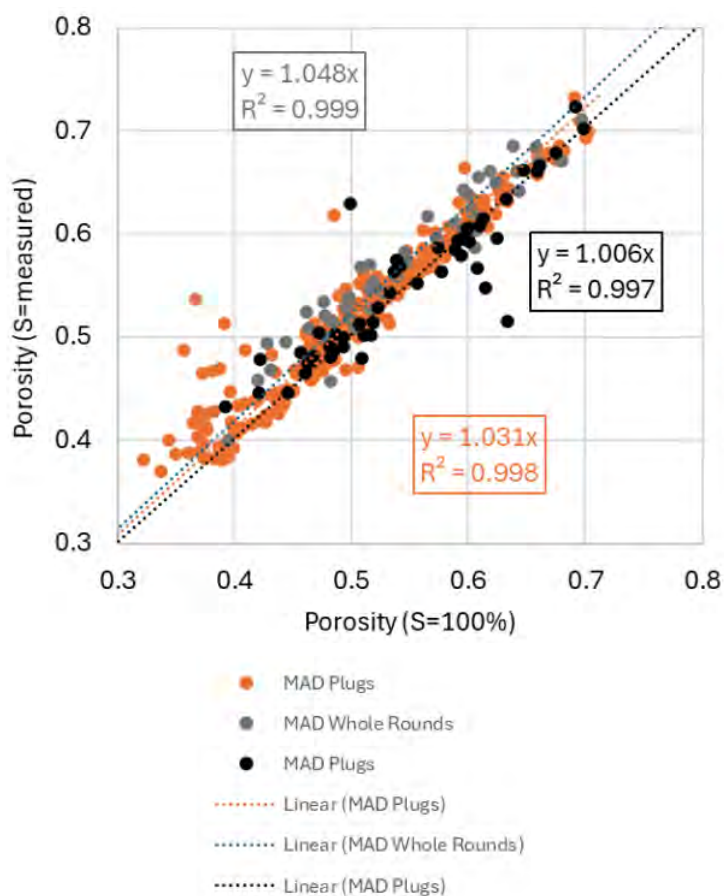


Figure F59: Cross plot of porosity calculated using the measured water saturation versus using an assumed water saturation of 100% for three datasets: the split core plugs (MAD plugs), the whole-round sample before subsampling (MAD whole-rounds), and the plugs from the whole-round samples (MAD plugs). Dataset: <http://doi.org/10.5281/zenodo.14107593>.

6. There are only a few tests performed to date on 7 different samples. The average grain density (Hole H002 and Hole H003 combined) is 2.704 g/cm^3 with a standard deviation of 0.014.

Rock magnetism

Magnetic susceptibility

Magnetic susceptibility (χ , Figure F60, column A) can provide insights into changes in sediment composition, particularly the presence of ferrimagnetic minerals, which have a magnetic susceptibility several orders of magnitude higher than other sedimentary components. Small differences in the low and high frequency χ can be used to determine the relative superparamagnetic mineral fraction.

A total of 372 paleomagnetic cube samples were collected and measured from either split cores (270 samples) or from pore water squeeze cakes (102 samples, sample code RMG). All discrete cube measurements are mass-normalized to avoid artefacts from porosity and squeezing of samples. Thirty-one of the split core samples were collected from observed anomalies in magnetic susceptibility values such as spikes, low values, or transitions (sample code ARM). Measurement methods are described in Methods: Split core sampling and Rock magnetics (Flemings et al., 2025b).

χ ranges from 1.96×10^{-8} to $1.43 \times 10^{-6} \text{ m}^3 \text{ kg}^{-1}$ with a mean of $1.29 \times 10^{-7} \text{ m}^3 \text{ kg}^{-1}$ (Figure F60). High frequency χ ranges from 1.60×10^{-8} - $1.43 \times 10^{-6} \text{ m}^3 \text{ kg}^{-1}$ with a mean of $1.24 \times 10^{-7} \text{ m}^3 \text{ kg}^{-1}$.

All samples were stored vacuum sealed and frozen for additional post-expedition analysis of room-temperature magnetic properties and low and high temperature magnetic properties.

Dissolved gas concentrations and hydrate saturation

Overview

Quantitative measurement of the volume of gas and liquid produced during the stepwise depressurization of pressure cores to atmospheric pressure (quantitative degassing) was conducted on 22 pressure core sections. Most degassing experiments were performed over ~6 to ~12 hours with a few lasting ~16 to ~30 hours. See Methods: Dissolved methane and hydrate saturation (Flemings et al., 2025b).

All quantitative degassing on samples from 0-296.4 mbsf (Hole H003) were performed on mud rich material. All quantitative degassing on samples from 644.6-859.6 mbsf (Hole H002) were performed on cores from the bounding muds of the Upper Blue and Orange sands. One sample contains a transition from mud to sand rich layers of the Upper Blue sand at 675.13-675.33 mbsf (Section H002-02FB-4).

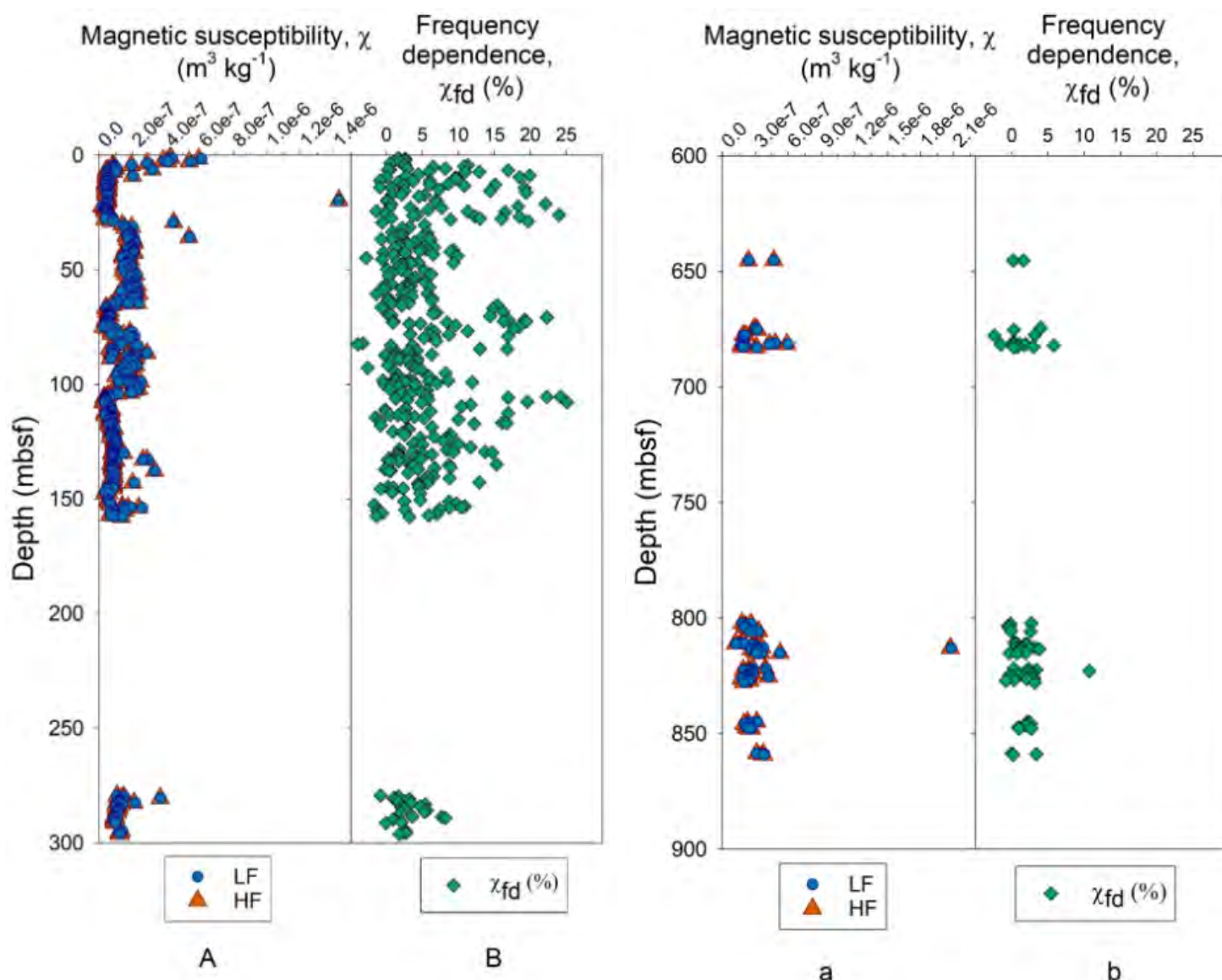


Figure F60: Magnetic susceptibility with compressed measured depth for Holes H003 (left) and H002 (right). A and a) Mass-normalized magnetic susceptibility (χ). Low frequency measurements (LF) are shown as blue circles and high frequency (HF) measurements as orange triangles; B and b) Frequency dependence of magnetic susceptibility (χ_{fd}). All depths are compressed measured depth in meters below the seafloor (mbsf). Dataset: <http://doi.org/10.5281/zenodo.14775361>.

Once the total volume of methane produced from a sample is known, the concentration of methane present or methane hydrate saturation is calculated based on the volume of the sample, a calculated porosity, a typical Structure I hydrate stoichiometry, and a typical Structure I hydrate density (Sloan and Koh, 2008). If the total amount of methane present is less than the in-situ maximum solubility of methane in water, the sample did not contain methane hydrate, and we calculate the dissolved methane concentration. If the total amount of methane is greater than the in-situ maximum solubility of methane in water, the consequent hydrate saturation

of the pore space is calculated from the amount of methane exceeding the solubility limit requirement.

Gases produced during quantitative degassing were analyzed and found to all be > 99.99% methane (See [Gas geochemistry](#)). The total volume of gas produced can therefore be used to determine the in-situ concentration of dissolved methane in the pore water, the presence of methane hydrate, and the pore space saturation of methane hydrate.

Table T16 shows the primary degassing results. These data include pressure-volume relationships, total methane content, and calculated values of dissolved

Hole	Core	Section	Depth in core	Depth in core	Section length	Section volume	Total methane	Degassing duration
			<i>top</i>	<i>bottom</i>				
			(cm)	(cm)	(cm)	(L)	(L)	(hr)
H003	05CS	1	0	110	110	1.72	0.09	2.1
H003	05CS	2	110	229	119	2.01	0.95	3.6
H003	08CS	2	10	130	120	2.53	1.44	20.9
H003	08CS	3	130	246	116	2.44	1.25	16.6
H003	13CS	1	0	42	42	0.86	0.14	16.2
H003	19CS	3	7	120	113	2.47	1.86	17
H003	19CS	4	120	240	120	2.67	1.84	10.2
H003	19CS	5	240	346	106	2.29	1.57	11.3
H003	24CS	2	6	100	94	1.93	1.66	11.7
H003	24CS	5	240	346	106	2.1	2.16	13.3
H003	27CS	4	146	230	84	1.81	3.16	0.6
H003	27CS	5	230	321	91	2.01	1.97	2.1
H003	28CS	1	0	75	75	1.57	2.18	18.1
H003	29CS	3	95	160	65	1.47	4.28	5
H003	29CS	5	180	261	81	1.83	2.69	4.8
H002	02FB	1	0	15	15	0.25	0.13	4.4
H002	02FB	4	91	111	20	0.31	4.4	29.9
H002	03FB	2	10	45	35	0.73	0.63	1.4
H002	05CS	3	160	212	52	1.02	1.11	1.4
H002	06CS	2	10	60	50	0.67	0.8	5.9
H002	06CS	5	215	250	35	0.56	0.8	6
H002	08CS	3	120	200	80	1.57	3.97	5.7

Table T16: Quantitative degassing results for pressure cores acquired in Hole H003 and Hole H002. Dataset: <http://doi.org/10.5281/zenodo.14775236>.

methane concentration, and hydrate saturation. The length of degassed sections ranged from 18 to 120 cm, whereas the volume of gas produced ranged from 0.09 to 4.28 L (standard temperature and pressure) (Table [T16](#)).

Dissolved methane concentration increases with depth and reaches 100% saturation at 146.6-147.5 mbsf (Section H003-24CS-5, Table [T17](#)). In the muds bounding the Red sand interval, 287.1 to 296.4 mbsf (Cores H003-27CS to H003-29CS), methane hydrate exists in small saturations of ~1 to 6% (Table [T17](#) and Figure [F61](#)).

Section H002-02FB-4 (675.13-675.33 mbsf) represents a transition from the bounding mud to a hydrate-bearing sand bed associated with the Upper Blue sand, as shown by an increase in P-wave velocity in the lower part of the sample. The bulk hydrate saturation of this sample is 24.4%. The hydrate saturation of the sand is higher than the bulk saturation in a section of mud 2 m below (677.4-677.7 mbsf, Section H002-03CF-2), the dissolved methane concentration is 72% of solubility (Table [T17](#) and Figure [F61](#)).

Three sections were degassed in the interval 802.0-805.7 mbsf from the seal of the Orange sand (Sections H002-05CS-3, -06CS-2, and -06CS-5). Sections

Hole	Core	Section	Compressed Depth	Average PCATS bulk density	Average core diameter	Average calculated porosity	Total methane	Methane concentration	Methane solubility	Dissolved methane saturation	Hydrate saturation
			<i>Top</i>							(% of solubility)	(% of pore space)
			(mbsf)	(g cm ⁻³)	(mm)	(%)	(mmol)	(mM)	(mM)		
H003	05CS	1	30.18	1.54	44.5	67.3	3.9	3.4	75.8	4	0
H003	05CS	2	31.20	1.88	46.3	46.7	40.7	43.5	75.7	57	0
H003	08CS	2	46.73	1.94	51.8	43	62.1	57.1	77.5	74	0
H003	08CS	3	47.93	2.02	51.7	38.2	53.9	57.9	77.6	75	0
H003	13CS	1	77.72	2.19	51	27.9	6	25.3	81	31	0
H003	19CS	3	111.01	1.91	52.7	44.8	81.3	73.5	85	87	0
H003	19CS	4	112.00	1.94	53.3	43	79.7	69.4	85.1	82	0
H003	19CS	5	113.06	1.94	52.4	43	68	69.3	85.3	81	0
H003	24CS	2	144.53	1.92	51.2	44.2	72	84.3	89.1	95	0
H003	24CS	5	146.59	1.95	50.2	42.4	93.7	105.2	89.4	>100	0.2
H003	27CS	4	288.58	2.23	52.3	25.5	137.7	308.6	109.6	>100	2.6
H003	27CS	5	289.42	2.25	53	24.2	85	176.4	109.8	>100	0.9
H003	28CS	1	290.78	2.27	51.6	23	81.9	229.1	110.1	>100	1.6
H003	29CS	3	294.78	2.26	53.6	23.6	184.4	559.9	110.6	>100	5.8
H003	29CS	5	295.63	2.26	53.6	23.6	116	268.7	110.7	>100	2.2
H002	02FB	1	674.22	2.03	49.6	37.6	5.6	59.5	181.1	33	0
H002	02FB	4	675.13	2.21	51.6	26.7	165.1	1976.5	181.3	>100	24.4
H002	03FB	2	677.37	2.18	51.7	28.5	27.2	130	181.8	72	0
H002	05CS	3	802.00	2.26	50	23.6	47.6	197.4	210.4	94	0
H002	06CS	2	803.55	2.2	50.1	27.3	30	174.8	210.8	83	0
H002	06CS	5	805.60	2.26	45.1	23.6	34.3	260.2	211.2	>100	0.7

Table T17: Interpreted methane concentration and hydrate saturation for pressure core sections acquired at Site H. Sections H003-05CS-1, H003-13CS-1, and H002-02FB had substantial air contamination and cannot be used for reliable methane calculations. The sections with contamination are shown with red text. All calculations are from measured compressed depths and the thermal gradient from H003. Post expedition analysis will account for the true vertical depth and a more nuanced interpretation of the thermal gradient. Dataset: <http://doi.org/10.5281/zenodo.14775236>.

H002-05CS-3 and H002-06CS-2 have methane concentrations of 94 and 83% of methane solubility, respectively (Table T17 and Figure F61). Section H002-06CS-5 has a methane hydrate saturation of less than 1% and the clay-rich interval of the Orange sand (810.8-811.3 mbsf, Section H002-08CS-3) was also characterized with a methane hydrate saturation of less than 1% (Table T17 and Figure F61).

Individual quantitative degassing results

Figure F62 illustrates the difference in the total volume of methane produced for three samples, one where the dissolved methane concentration of the pore water is below the solubility limit (thus without methane hydrate, Figure F62 H003-24CS-2 brown circles) and two where the dissolved

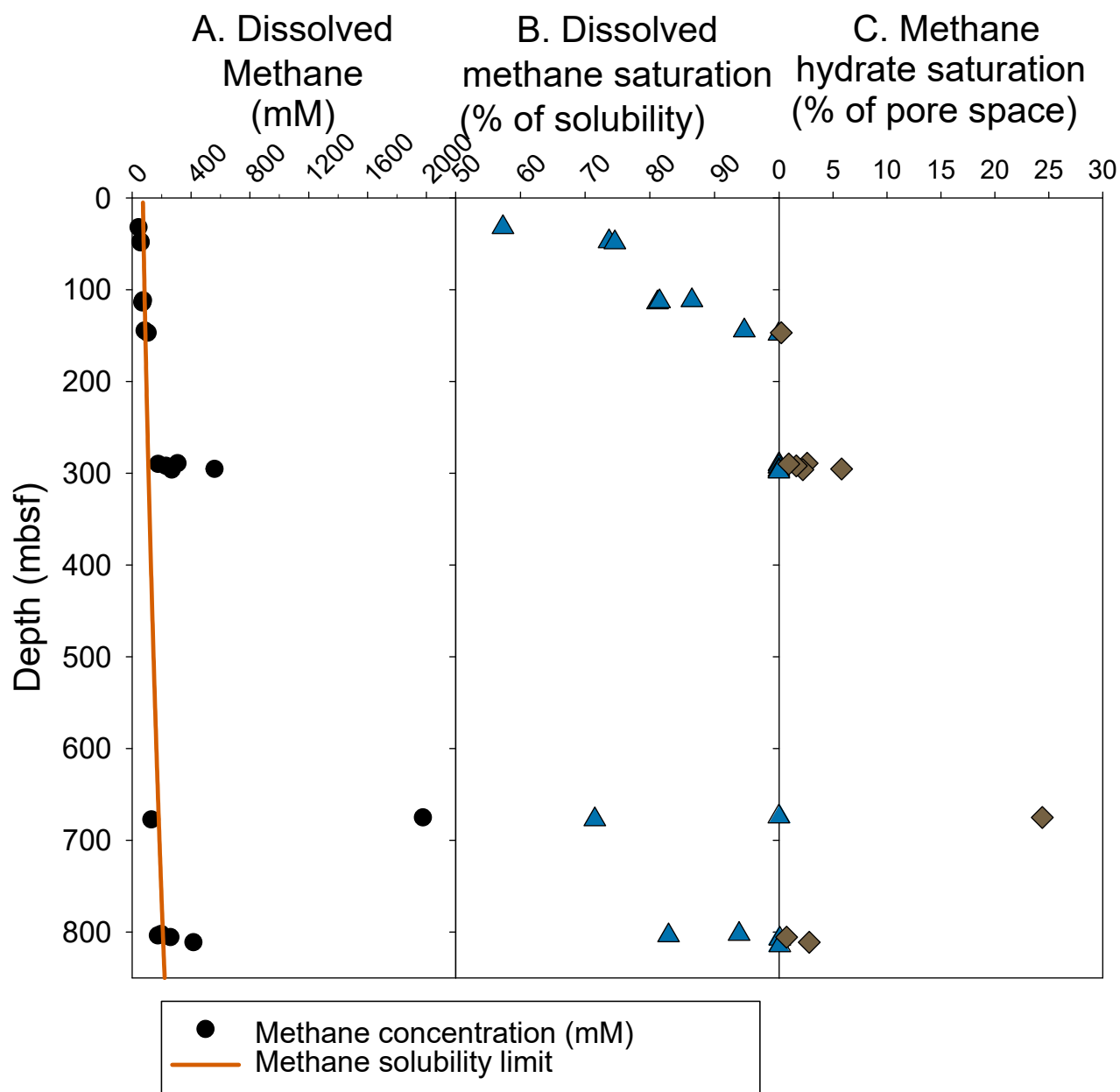


Figure F61: Dissolve methane and hydrate saturation with compressed measured depth in meters below the seafloor (mbsf). A) Methane concentration (black dots) and calculated methane solubility (red line); B) Dissolved methane as a percent of the solubility limit; C) Methane hydrate saturation as a percentage of the pore space. All calculations are from measured depths and the thermal gradient from H003. Post expedition analysis will account for the true vertical depth and a more nuanced interpretation of the geothermal gradient. Dataset: <http://doi.org/10.5281/zenodo.14775236>.

methane concentration of the pore water exceeds the solubility limit and the recovered core contains methane hydrate (Figure F62, H003-29CS-3 orange diamonds and H002-02FB-4 blue triangles). During depressurization of the low-concentration sample, H003-24CS-3, the change in total volume of methane as the pressure is decreased is initially driven by water displacement by gas under pressure and finally from gas displacement as methane solubility decreases with decreasing pressure. A total of only 1.66 L of

methane is produced from this 94 cm long section of pressure core. When the pore water is saturated with methane and methane hydrate is present, as during the depressurization of H003-29CS-3, the change is similar except the collected methane accumulates at a pressure that approximately follows the hydrate stability boundary (~ 6 MPa in this example) as hydrate dissociates into methane and water. From this sample, a total of 4.28 L of methane is produced from a 65 cm long section of pressure core. A similar

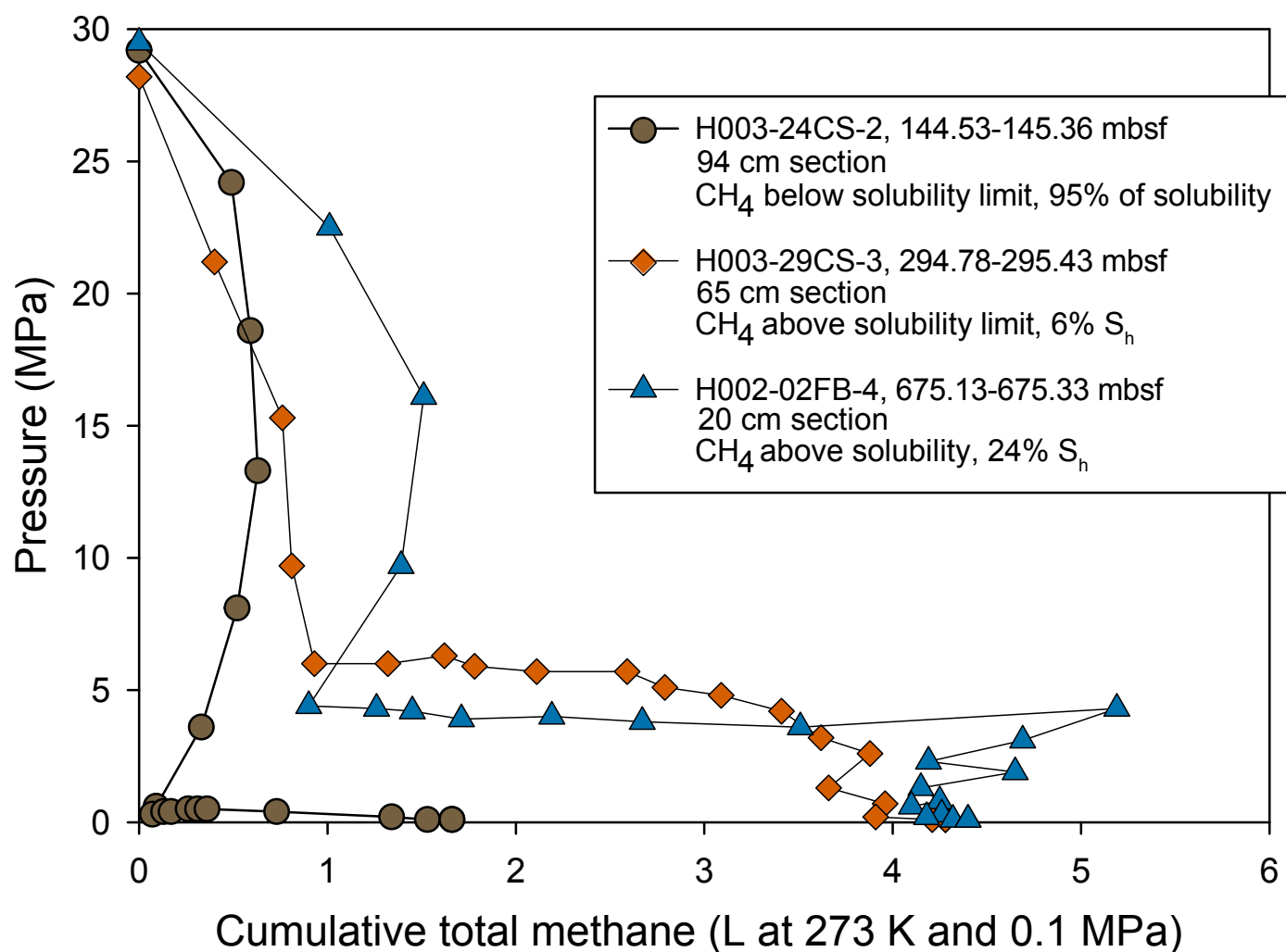


Figure F62: Total volume of methane produced from a pressure core as the pressure is decreased in steps for a sample under-saturated with methane (without hydrate, Section H003-24CS-2, gray dots) and two samples saturated with methane and containing methane hydrate (Section H003-29CS-3, orange diamonds; Section H002-02FB-4, blue triangles). Dataset: <http://doi.org/10.5281/zenodo.14775236>.

volume of methane is produced from the 20 cm section, H002-02FB-4, due to its higher hydrate saturation.

The degassing information from all samples can be found in Appendix I: Quantitative Degassing.



Post-doc Tanner Mills of The University of Texas and graduate student Kelly Shannon of Oregon St. University make their way to the Q4000 via helicopter. Photo Credit: Jackson School of Geosciences

Microbiology

Samples were collected to investigate microbial communities in recovered sediments from both coarse- and fine-grained materials, where hydrates occur and where they are absent, and from below the hydrate-bearing sediments (below the bottom-simulating reflector). Though challenging because of both the low biomass and the low levels of microbial activity known to occur in deep seafloor systems, we are using approaches most likely to yield measurable results. See Methods: Microbiology (Flemings et al., [2025b](#)).

Using these samples, the following will be determined as part of the continuing post-expedition laboratory studies:

- DNA-based microbial community diversity and genetic/functional capacity of single microbial cells at Oregon State University (Table [T18](#), column D1)
- Complex organic matter degradation capacity at the University of South Alabama (Table [T18](#), column D2)
- Calcium carbonate-precipitating capacity of microbial cells at UT (Table [T18](#), column D3)
- Presence and type of foraminifera as well as visual evidence of carbonates or sulfides at USGS (Table [T18](#), column D4)
- Heterotrophic organisms at the University of Chicago (Table [T18](#), column D5)
- Microbial cell counts at Japan Agency for Marine-Earth Science and Technology (JAMSTEC) (Table [T18](#), column D6)

All samples collected for these microbiological determinations were obtained from samples adjacent to other measurements or core samples acquired for pore water geochemistry, sediment texture, hydrate analysis, and

(A) Sample	(B) Archived Depth - Top (mbsf)	(C) Compressed Depth- Top (mbsf)	(D) Sub-coring and Allocation					
			(1) Oregon St: DNA, RNA	(2) US Alabama: Single-Amplified Genomics	(3) UT: Microbial- induced carbonate precipitation	(4) USGS: Foraminifera	(5) U of Chicago: Heterotrophic microorganisms	(6) JAMSTEC: Cell counts
H003-01H-1c, 115-130 cm, MB	1.15	1.15	1c	1c	1c	1c		
H003-01H-2a, 0-5 cm, CEL	1.50	1.50						2a
H003-01H-2c, 115-130 cm, MB	2.65	2.65	2c	2c	2c	2c		
H003-01H-3a, 0-5 cm, CEL	3.00	3.00						3a
H003-01H-3c, 115-130 cm, MB	4.15	4.15	3c	3c	3c	3c		
H003-01H-4a1, 0-5 cm, CEL	4.50	4.50						4a
H003-01H-4c, 115-130 cm, MB	5.65	5.65	4c	4c	4c	4c		
H003-01H-5a, 0-5 cm, CEL	6.00	6.00						5a
H003-01H-5c, 101-116 cm, MB	7.01	7.01	5c	5c	5c	5c	5c	
H003-02H-1c, 120-130 cm, MB	9.43	9.25	1c	1c	1c	1c		
H003-02H-2a, 0-5 cm, CEL	9.73	9.50						2a
H003-02H-2c, 120-130 cm, MB	10.93	10.52	2c	2c	2c	2c		
H003-02H-3a, 0-5 cm, CEL	11.23	10.78						3a
H003-02H-3c, 120-130 cm, MB	12.43	11.80	3c	3c	3c	3c		
H003-02H-4a, 0-5 cm, CEL	12.73	12.05						4a
H003-02H-4c, 120-130 cm, MB	13.93	13.07	4c	4c	4c	4c		
H003-02H-5a, 0-5 cm, CEL	14.23	13.32						5a
H003-02H-5c, 120-130 cm, MB	15.43	14.34	5c	5c	5c	5c		
H003-02H-6a, 0-5 cm, CEL	15.73	14.60						6a
H003-02H-6c, 120-130 cm, MB	16.93	15.62	6c	6c	6c	6c		
H003-02H-7, 0-5 cm, CEL	17.23	15.87						7
H003-03H-1c, 86-96 cm, MB	19.45	19.31	1c	1c	1c	1c		
H003-03H-2a, 0-5 cm, CEL	20.04	19.80						2a
H003-03H-2c, 110-120 cm, MB	21.14	20.72	2c	2c	2c	2c		
H003-03H-3a2, 0-5 cm, CEL	21.54	21.06						3a2
H003-03H-3c, 110-120 cm, MB	22.64	21.97	3c	3c	3c	3c		
H003-03H-4a, 0-5 cm, CEL	23.04	22.31						4a
H003-03H-4c, 110-125 cm, MBC	24.14	23.23					4c	
H003-03H-4d, 125-135 cm, MB	24.29	23.35	4d	4d	4d	4d		
H003-03H-5a, 0-5 cm, CEL	24.69	23.69						5a
H003-03H-5c, 110-120 cm, MB	25.79	24.61	5c	5c	5c	5c		
H003-03H-6a, 0-5 cm, CEL	26.19	24.94						6a
H003-03H-6c, 110-120 cm, MB	27.29	25.86	6c	6c	6c	6c		
H003-03H-7, 0-5 cm, CEL	27.69	26.19						7
H003-05CS-2a, 0-10 cm, MB	31.28	31.20	2a	2a	2a	2a		

(A) Sample	(B) Archived Depth - Top (mbsf)	(C) Compressed Depth- Top (mbsf)	(D) Sub-coring and Allocation					
			(1) Oregon St: DNA, RNA	(2) US Alabama: Single-Amplified Genomics	(3) UT: Microbial- induced carbonate precipitation	(4) USGS: Foraminifera	(5) U of Chicago: Heterotrophic microorganisms	(6) JAMSTEC: Cell counts
H003-05CS-2cde, 25-30 cm, CEL	31.53	31.43						2cde
H003-06H-2c, 110-120 cm, MB	34.91	34.06	2c	2c	2c	2c		
H003-06H-3a, 0-5 cm, CEL	35.31	34.33						3a
H003-06H-3c, 100-110 cm, MB	36.31	35.00	3c	3c	3c	3c		
H003-06H-4a, 0-5 cm, CEL	36.81	35.34						4a
H003-06H-6c, 110-120 cm, MB	40.91	38.09	6c	6c	6c	6c		
H003-06H-7, 0-5 cm, CEL	41.31	38.36						7
H003-07H-3c, 80-90 cm, MB	43.12	42.60	3c	3c	3c	3c	3c	
H003-07H-4, 0-5 cm, CEL	43.82	43.21						4
H003-07H-5c, 73-83 cm, MB	46.05	45.13	5c	5c	5c	5c		
H003-07H-6, 0-5 cm, CEL	46.60	45.61						6
H003-08CS-3e, 80-90 cm, MB	48.73	48.73	3e	3e				
H003-09H-2c, 62-72 cm, MB	51.80	51.35	2c	2c	2c	2c		
H003-09H-3a, 0-5 cm, CEL	52.34	51.77						3a
H003-09H-5c, 70-80 cm, MB	56.04	54.68	5c	5c	5c	5c		
H003-09H-6a, 0-5 cm, CEL	56.45	55.00						6a
H003-10H-3c, 55-65 cm, MB	60.24	59.69	3c	3c	3c	3c		
H003-10H-4, 0-5 cm, CEL	60.67	60.05						4
H003-10H-5c, 84-105 cm, MB	62.99	62.01	5c	5c	5c	5c		
H003-10H-6, 0-5 cm, CEL	63.52	62.46						6
H003-11H-1d, 155-165 cm, MB	65.25	64.88	1d	1d	1d	1d		
H003-11H-3a, 0-5 cm, CEL	67.68	66.72						3a
H003-11H-4c, 110-120 cm, MB	69.61	68.19	4c	4c	4c	4c		
H003-11H-5a, 0-5 cm, CEL	70.06	68.53						5a
H003-12H-2c, 110-120 cm, MB	73.31	72.69	2c	2c	2c	2c		
H003-12H-3, 0-5 cm, CEL	73.71	72.99						3
H003-12H-5c, 142-152 cm, MB	78.13	76.35	5c	5c	5c	5c		
H003-12H-6a, 0-5 cm, CEL	78.53	76.65						6a
H003-14H-2c, 91-101 cm, MB	83.23	82.76	2c	2c		2c		
H003-14H-3a2, 0-5 cm, CEL	83.73	83.17						3a2
H003-14H-6c, 83-93 cm, MB	88.47	87.00	6c	6c		6c		
H003-14H-7, 0-5 cm, CEL	88.99	87.42						7
H003-15CS-2a, 0-5 cm, CEL	88.39	88.39						2a
H003-15CS-2b, 50-60 cm, MB	88.89	88.89	2b	2b		2b		
H003-16H-1d, 121-131 cm, MB	92.65	92.38	1d	1d	1d	1d		

(A) Sample	(B) Archived Depth - Top (mbsf)	(C) Compressed Depth- Top (mbsf)	(D) Sub-coring and Allocation					
			(1) Oregon St: DNA, RNA	(2) US Alabama: Single-Amplified Genomics	(3) UT: Microbial- induced carbonate precipitation	(4) USGS: Foraminifera	(5) U of Chicago: Heterotrophic microorganisms	(6) JAMSTEC: Cell counts
H003-16H-2, 0-5 cm, CEL	93.20	92.81						2
H003-16H-4d, 152-162 cm, MB	97.72	96.34	4d	4d		4d		
H003-16H-5, 0-5 cm, CEL	98.13	96.66						5
H003-17H-2d, 126-137 cm, MB	99.79	99.29	2d	2d	2d	2d		
H003-17H-3b1, 4-9 cm, CEL	100.23	99.61						3b1
H003-17H-4d, 160-170 cm, MB	103.29	101.88	4d	4d		4d		
H003-17H-5, 0-5 cm, CEL	103.69	102.18						5
H003-18H-2c, 111-121 cm, MB	107.42	106.47	2c	2c	2c	2c		
H003-18H-3a, 0-5 cm, CEL	107.82	106.75						3a
H003-18H-5a, 0-5 cm, CEL	110.57	108.67						5a
H003-18H-5c, 111-121 cm, MB	111.68	109.45	5c	5c		5c	5c	
H003-18H-6, 0-5 cm, CEL	112.19	109.81						6
H003-19CS-5c, 55-60 cm, CEL	113.90	113.55						5c
H003-19CS-5d, 60-69 cm, MB	113.95	113.59	5d	5d	5d			
H003-20H-2c, 137-148 cm, MB	116.47	116.08	2c	2c	2c	2c		
H003-20H-3, 0-5 cm, CEL	116.95	116.48						3
H003-20H-5c, 110-120 cm, MB	120.48	119.46	5c	5c		5c		
H003-20H-6, 0-5 cm, CEL	120.88	119.80						6
H003-21H-3c, 107-120 cm, MB	125.69	125.20	3c	3c	3c	3c		
H003-21H-4, 0-5 cm, CEL	126.12	125.58						4
H003-21H-6c, 94-104 cm, MB	129.26	128.35	6c	6c		6c		
H003-21H-7, 0-5 cm, CEL	129.66	128.71						7
H003-22H-2c, 110-120 cm, MB	131.84	131.84	2c	2c	2c	2c		
H003-22H-3, 0-5 cm, CEL	132.24	132.24						3
H003-22H-4c, 110-120 cm, MB	134.82	134.82	4c	4c		4c		
H003-22H-5, 0-5 cm, CEL	135.22	135.22						5
H003-23H-2d, 138-148 cm, MB	139.90	139.48	2d	2d		2d		
H003-23H-3a, 0-5 cm, CEL	140.57	140.05						3a
H003-23H-4d, 109-119 cm, MB	142.59	141.79	4d	4d		4d		
H003-23H-5, 0-5 cm, CEL	143.10	142.23						5
H003-24CS-3, 0-20 cm, CRYO	145.48	145.36	3					3
H003-24CS-5c, 58-63 cm, CEL	147.46	147.10						5c
H003-24CS-5e, 80-91 cm, MB	147.68	147.29	5e	5e				
H003-25H-7b, 75-80 cm, CEL	154.12	152.33						7b
H003-25H-7c, 75-85 cm, MB	154.17	152.37	7c	7c	7c	7c	7c	

(A) Sample	(B) Archived Depth - Top (mbsf)	(C) Compressed Depth- Top (mbsf)	(D) Sub-coring and Allocation					
			(1) Oregon St: DNA, RNA	(2) US Alabama: Single-Amplified Genomics	(3) UT: Microbial- induced carbonate precipitation	(4) USGS: Foraminifera	(5) U of Chicago: Heterotrophic microorganisms	(6) JAMSTEC: Cell counts
H003-26X-4c, 97-107 cm, MBC	282.97	282.97					4c	
H003-26X-4d, 107-117 cm, MB	283.07	283.07	4d	4d	4d	4d		
H003-26X-5a, 0-5 cm, CEL	283.37	283.37						5a
H003-26X-6c, 81-91 cm, MB	285.64	285.64	6c	6c		6c		
H003-26X-7a, 0-5 cm, CEL	285.98	285.98						7a
H003-27CS-3, 0-20 cm, CRYO	288.38	288.38	3					3
H003-27CS-4c, 37-46 cm, MB	288.95	288.95	4c	4c		4c		
H003-27CS-4e, 71-76 cm, CEL	289.29	289.29						4e
H003-29CS-4, 0-20 cm, CRYO	295.43	295.43	4					4
H003-29CS-5d, 68-80 cm, MB and CEL	296.31	296.31	5d	5d		5d		5d
H002-01FB-1d, 77-87 cm, MB and CEL	645.42	645.42	1d	1d		1d		1d
H002-02FB-2, 0-20 cm, CRYO	674.37	674.37	2					2
H002-02FB-5, 0-20 cm, CRYO	675.33	675.33	5					5
H002-03FB-2c, 27-32 cm, CEL	677.64	677.64						2c
H002-04FB-2b, 60-70 cm, MB	681.57	681.57	2b	2b		2b		2b
H002-04FB-3b, 19-28 cm, MB and CEL	681.86	681.86	3b	3b		3b		3b
H002-05CS-4, 0-20 cm, CRYO	802.52	802.52	4					4
H002-06CS-6, 0-20 cm, CRYO	805.95	805.95	6					6
H002-08CS-2, 0-20 cm, CRYO	810.55	810.55	2					2
H002-09CS-1c, 90-100 cm, MB	813.50	813.40	1c	1c				1c
H002-10CS-2, 0-20 cm, CRYO	816.68	816.68	2					2
H002-11CS-1, 0-18 cm, CRYO	818.69	818.69	1					1
H002-12CS-1d, 96-106 cm, MB	822.70	822.58	1d	1d				1d
H002-12CS-2d, 77-88 cm, MB	823.82	823.57	2d	2d				2d
H002-13CS-1d, 144-154 cm, MB	826.23	826.06	1d	1d				1d
H002-14CS-1a, 0-15 cm, MB	844.60	844.60	1a	1a				1a
H002-14CS-2c, 114-124 cm, MB	846.58	846.36	2c	2c				2c
H002-15CS-1c, 32-43 cm, MB	858.64	858.64	1c	1c				1c

Table T18: Investigator and analysis for each microbiology whole-round subsample. Sample name, MB=microbiology whole-round sample, MBC= extra microbiology whole-round sample for the University of Chicago, CEL=cell counts sample (See Methods: Core processing (Flemings et al., [2025b](#))), CRYO= cryogenically frozen and depressurized core (see Methods: Cryogenic freezing and depressurization (Flemings et al., [2025b](#))). The coring tool used to acquire each whole-round core can be identified in the core name (H = Advanced piston corer, X = Extended core barrel rotary coring, FB= Pressure Coring Tool in the Face Bit configuration, CS = Pressure Coring Tool in the Cutting Shoe configuration; B) Archived measured depth of the top of the sample in meters below the seafloor (mbsf); C) Compressed measured depth of the top of the sample in mbsf; D) Green highlighted cells show how each sample was sub-cored and/or allocated. Dataset: <https://doi.org/10.5281/zenodo.14767822>

geophysical properties. Throughout the sampling we collected control samples to assess the degree of drilling fluid contamination in the cores, if any, and the potential for lab-based contamination from confining waters and lab airborne contaminants.

Curation of microbiology samples

Samples for determining the calcium carbonate-precipitating capacity of microbial cells and the presence and type of foraminifera were collected above, within, and below the SMTZ to a measured depth of approximately 279 mbsf (Table [T18](#), columns D3 and 4). Samples for the analysis of DNA-based microbial community diversity, complex organic matter degradation capacity, and microbial cell counts were collected above, within, and below the SMTZ to a depth of approximately 293 mbsf (above and within hydrate-bearing sediments) (Table [T18](#), columns D1,2, and 5).

All samples collected are shown in Table [T18](#). Whole-round samples from conventional and conventionalized cores were subsampled onboard. Cryogenically frozen and depressurized whole-round samples (sample code CRYO) were subsampled in Salt Lake City using JAMSTEC's mini coring device (See Methods: Dockside sub-coring for microbiology (Flemings et al., [2025b](#))).

Control samples were gathered to assess multiple sources of contamination during microbiological sampling, including the air where whole-round cores were processed and sub-sampled, PCATS fluid concurrent with pressure coring, drilling fluid (seawater and drilling mud), and the shavings and mud which surrounded G-XCB biscuits (Table [T19](#)) (See Methods: Microbiology (Flemings et al., [2025b](#))). Each of these control samples was stored at -80 °C and sent to Oregon State University for DNA extractions and 16S rRNA gene Illumina MiSeq high throughput sequencing to establish contaminant microbial communities.

Extraction and amplification of DNA

Several UT-GOM2-2 sediment samples collected for microbiological analyses were amplified and extracted in the Colwell Geomicrobiology Lab at Oregon State University. The amount of extracted DNA is shown in Table [T20](#). The extraction was done using the methods described in Methods: DNA extraction and amplification (Flemings et al., [2025b](#)). These samples were extracted in the clean environment (the lab “greenhouse” described), using a PowerSoil DNA Extraction Kit (Qiagen) modified to include the reagent G2 (Jacobsen et al., [2018](#)) to adsorb to clay microsites. For each sample, 0.25 to 0.4 g of sediment was used for each kit extraction, and this was replicated five times for each sample to yield a total of 1.25 to 2.0 g of extracted sediment. The DNA extracted from all of the replicates of a single sediment sample was then pooled, precipitated, and concentrated (10x the initial concentration) using linear polyacrylamide and a Savant SpeedVac (ThermoFisher), and quantified using gel electrophoresis and a Qubit Fluorometer (ThermoFisher).

Prior to DNA precipitation and concentration, the genomic DNA (gDNA) was too low to quantify from either of these samples. However, steps were taken to increase the quantity of sample extracted, adsorb clay microsites that bind nucleic acids, and to concentrate the DNA which yielded quantifiable amounts of DNA. These early results are promising as there was some DNA recovered from considerable depth (154 mbsf). Extracted gDNA concentrations from H003 1H-4C and H003 25H-7C totaled 0.28 and 0.35 µg/mL, respectively. These values compare to and are higher than other low-biomass systems (Simpson et al., [2023](#)). Findings still need to be compared to controls and samples with known levels of DNA and tested by polymerase chain reaction to assure that the DNA can be amplified to verify that we have quantities required for amplification and sequencing.

Date	Time	Type	Corresponding cores	Investigator
230805	7:00	seawater	2H, 3H, 6H, 7H	Colwell
230805	9:45	drilling mud	2H, 3H, 6H, 7H	Colwell
230806	9:00	seawater	7H	Colwell
230806	9:00	drilling mud	7H	Colwell
230807	8:45	seawater	5CS, 7H, 9H, 10H	Colwell
230807	8:45	drilling mud	5CS, 7H, 9H, 10H	Colwell
230807	01:00-04:00	MB lab air	5CS, 7H, 9H, 10H	Colwell
230808		Geotek lab air		Colwell
230808	14:00	parings	12H	Colwell
230808	15:45	PCATS fluid	8CS	Colwell
230808	23:00	PCATS fluid	13CS	Colwell
230808	8:30	seawater	11H, 12H, 14H	Colwell
230808	9:30	drilling mud	11H, 12H, 14H	Colwell
230809	8:45	drilling mud	16H, 17H, 18H, 20H, 15CS	Colwell
230809	8:45	seawater	16H, 17H, 18H, 20H, 15CS	Colwell
230810	15:00	PCATS fluid		Colwell
230810	7:00	seawater	21H, 22H, 23H, 25H	Colwell
230810	7:00	drilling mud	21H, 22H, 23H, 25H	Colwell
230810	21:00	PCATS fluid	19CS	Colwell
230811	9:30	seawater	8CS	Colwell
230811	9:30	drilling mud	8CS	Colwell
230812	7:15	seawater	?	Colwell
230812	7:15	drilling mud	?	Colwell
230813	9:30	seawater	24CS	Colwell
230813	9:30	drilling mud	24CS	Colwell
230814	15:15	seawater	19CS, 26X	Colwell
230814	15:15	drilling mud	19CS, 26X	Colwell
230814	15:15-19:25	Laminar Flow Hood		Colwell
230814		26X-4d Shavings		Ruff/Colwell
230814		26X-4c Shavings		Colwell
230814		26X-6c Shavings		Colwell
230815	7:30	seawater	24CS	Colwell
230815	8:30	drilling mud	24CS	Colwell
230817		PCATS fluid	27CS	Colwell
230817		PCATS fluid	28CS	Colwell
230817		PCATS fluid	29CS	Colwell
230820	9:15	Mud	1FB	Colwell
230820	7:00	Mud	1FB	Colwell
230824	18:30	Mud		Colwell
230825	12:30	Mud		Colwell
230825		PCATS fluid	2FB	Colwell

Date	Time	Type	Corresponding cores	Investigator
230825		PCATS fluid	5CS	Colwell
230825		PCATS fluid	7CS	Colwell
230825		PCATS fluid	8CS	Colwell
230825		PCATS fluid	10CS	Colwell
230826	8:15	Mud		Colwell
230827	7:00	Mud		Colwell
230827		PCATS fluid	11CS	Colwell
230827		PCATS fluid	6CS	Colwell
230827		PCATS fluid	5CS	Colwell

Table T19: Types and collection dates of microbiology control samples taken to assess sources of microbial contamination. Dataset: <http://doi.org/10.5281/zenodo.14767822>

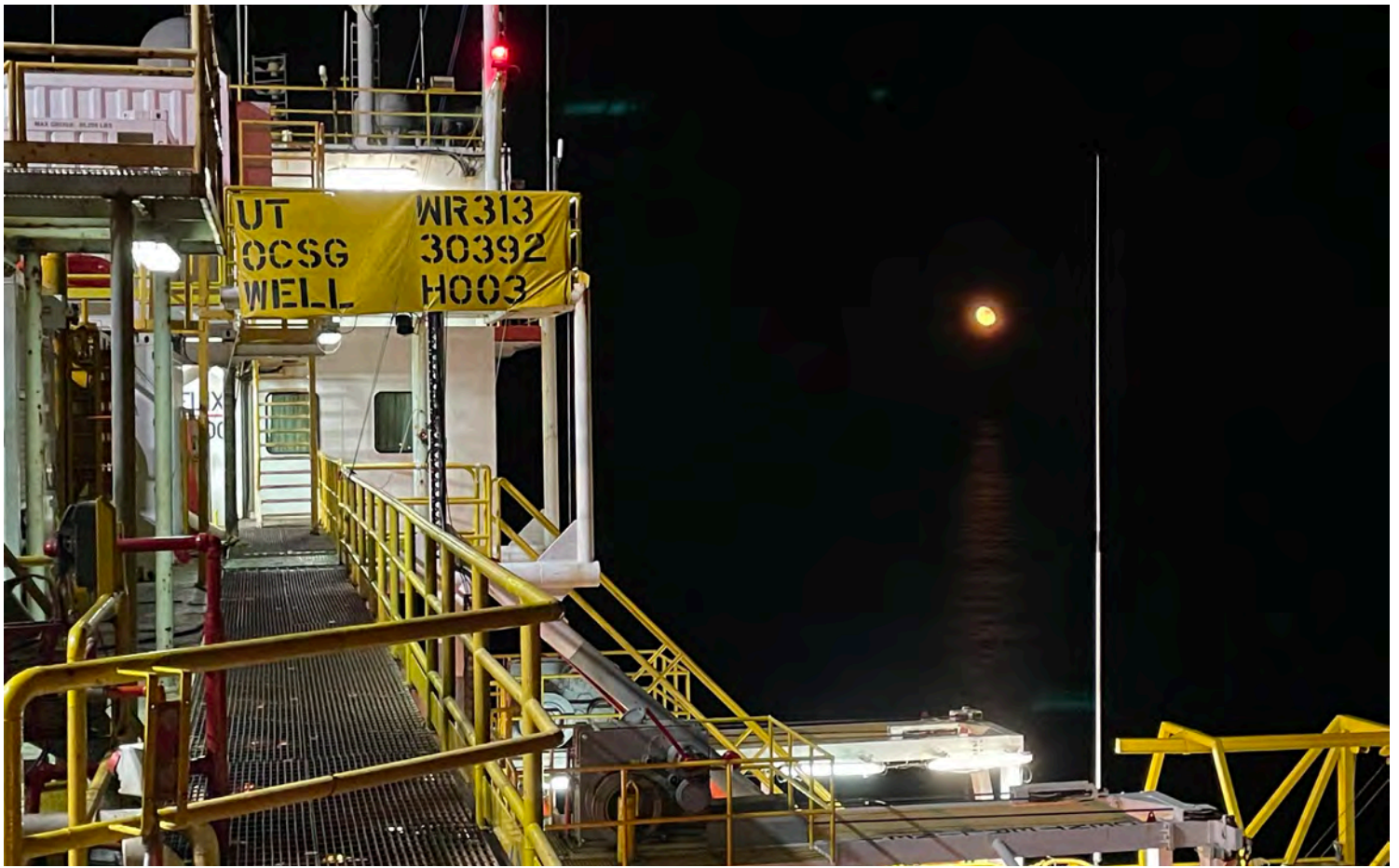
Sample	Lab ID	Archived Depth, Center (mbsf)	Compressed Depth, Center (mbsf)	gDNA Concentration (ng/ul)	LPA Concentrated	Amplicon Concentration (mg/ul)
H003-01H-4c, 115-130 cm	1H 4C	5.73	5.73	0.234	Yes	3.82
H003-02H-2c, 120-130 cm	2H 2C	10.98	10.57	0.116	Yes	3.63
H003-02H-3c, 120-130 cm	2H 3C	12.48	11.84	0.052	Yes	1.79
H003-06H-3c, 100-110 cm	6H 3C	36.36	35.03	0.29	Yes	1.10
H003-14H-2c, 91-101 cm	14H 2C	83.28	82.8	0.248	Yes	1.30
H003-25H-7c, 75-85 cm	25H 7C	154.22	152.4	0.158	Yes	1.66
WBM 5-AUG-2023	Mud 8/5	NA	NA	7.44	No	38.9
Seawater 5-AUG-2023	Seawater 8/6	NA	NA	1.62	Yes	1.30
m3 Lab Air 6-AUG-2024	m3 Lab Air	NA	NA	too low	Yes	0.71
m3 LFH Air 14-AUG-2024	m3 LFH Air	NA	NA	too low	Yes	1.69
PCATS Fluid 28CS	Pcats28CS	NA	NA	0.215	Yes	0.64
PCATS Fluid 29CS	Pcats29CS	NA	NA	2.2	No	1.33
PCATS Fluid 24CS	Pcats24CS	NA	NA	2.4	Yes	1.16
GlassFloss Bubble LFH Filter	filter	NA	NA	too low	Yes	1.87
Extraction Neg 6-DEC-2023	12/6 Neg	NA	NA	0.595	Yes	1.83
Extraction Neg 24-FEB-2024	2/24 Neg	NA	NA	too low	Yes	3.28
Extraction Neg 24-FEB-2024	2/27 Neg	NA	NA	too low	Yes	1.07

Table T20: Extracted DNA. These samples were submitted for 16S ribosomal DNA sequencing as a preliminary assessment of sediment community characteristics and potential sources of contamination. DNA samples originated from sub-cored sediments acquired from several depths as well as selected contamination controls (i.e., drilling mud, lab air, PCATS fluid), and lab blanks. Depths are measured depths in meters below the seafloor (mbsf). LFH = laminar flow hood. LPA = Linear Polyacrylamide. Dataset: <http://doi.org/10.5281/zenodo.14767822>

Microbiology post-expedition analysis plan

Further microbial community characterization will be performed by Oregon State University. Microbial cell numbers and distribution will be determined at JAMSTEC by density-based separation of microbes in a clean room and fluorescence microscopy.

The assessment of degradation potential of macromolecules will be performed at the Woods Hole Marine Biological Lab (MBL) through enrichment culture-based studies. The functional potential of methanotrophs will be assessed at the Dauphin Island Sea Lab (DISL) of the University of South Alabama with the use of cell sorting and single-cell genomics. The potential for microbes to induce carbonate precipitation will be examined at UT by growing and enriching viable microbes from the sediments that are able to carry out this process.



Despite this serene moonlight scene, night operations are in full swing at Site WR313 Hole H003. Photo Credit: Stephen C. Phillips

Geochemistry

Figure [F63](#) summarizes many of the geochemical measurements made to date. Figure [F64](#) shows an expanded view of the top 300 mbsf.

Pore water geochemistry

The focus of the shipboard pore water geochemistry program during the UT-GOM2-2 expedition was to conduct time-sensitive chemical analyses onboard and to preserve pore water samples for shore-based analyses of solutes and isotope ratios. Pore water whole-round samples were collected onboard the *Q4000* in Hole H003 on most Cores 1-29, but not in Cores H003-04CS, H003-13CS, and H003-28CS. In Hole H002, whole-round samples were collected on the *Q4000* from Cores H002-1FB to H002-15CS. Due to time limitations, whole-round samples for cores 5CS to 15CS were processed shore-based in Salt Lake City (See Dockside sampling in Salt Lake City in Methods: Pore water geochemistry (Flemings et al., [2025b](#))).

A total of 56 routine pore water whole-round samples (sample code IWR) samples of 10-45 cm length were collected and squeezed for shipboard and shore-based chemical analyses from 0-296.4 mbsf (Hole H003). See Methods: Pore water geochemistry (Flemings et al., [2025b](#)). Of the 56 IWR samples, 47 were from G-APC cores, 2 were from G-XCB cores, and 7 were from pressure cores. The volume of pore water recovered varies with core type, depth, and lithology, and ranged between 4-43 mL in G-APC cores, 13-18 mL in G-XCB cores, and 12-34 mL in pressure cores (Table [T21](#)). 16 routine pore water whole-round samples (IWR) of 5-30 cm length were collected from pressure cores in Hole H002. Pore water volume recovered ranged from 2-27 mL (Table [T21](#)).

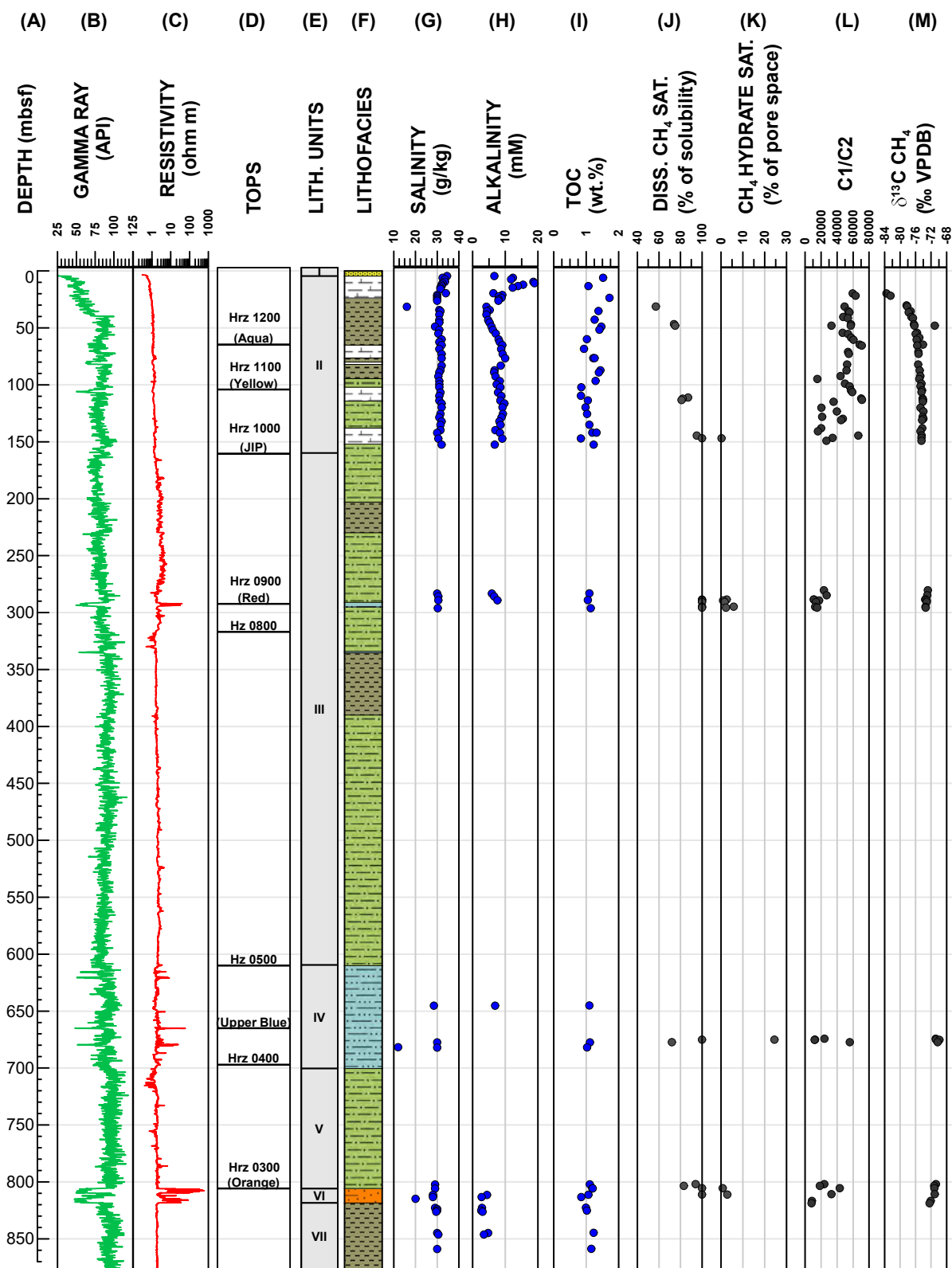


Figure F63: Geochemistry Summary. A) Measured depth in meters below the seafloor (mbsf); B) Projected Hole H001 logging while drilling (LWD) gamma ray in green. The depth projection of Hole H001 LWD data onto Hole H002 and Hole H003 is discussed in [Plotting H001, H002, and H003 downhole data](#); C) Projected LWD resistivity in red; D) Seismic reflectors (Hrz = Horizon) and stratigraphic tops as described in Table T4; E) Lithologic unit; F) Lithofacies (Table T10); G) Uncorrected salinity (See [Pore water geochemistry](#)); H) Uncorrected alkalinity (See [Pore water geochemistry](#)); I) Total Organic Carbon (TOC, See [Sediment geochemistry](#)); J) Dissolved methane saturation as a percent of solubility (See [Dissolved gas concentrations and hydrate saturation](#)); K) Methane hydrate saturation of the pore space (See [Dissolved gas concentrations and hydrate saturation](#)); L) Methane to ethane ratio (C₁:C₂) ratio (See [Gas geochemistry](#)); M) Carbon-13 isotopes ($\delta^{13}\text{C}$) of methane (CH₄) measured post-expedition using a cavity ringdown spectrometer (CRDS, See [Gas geochemistry](#)). G through M used compressed measured depths in mbsf.

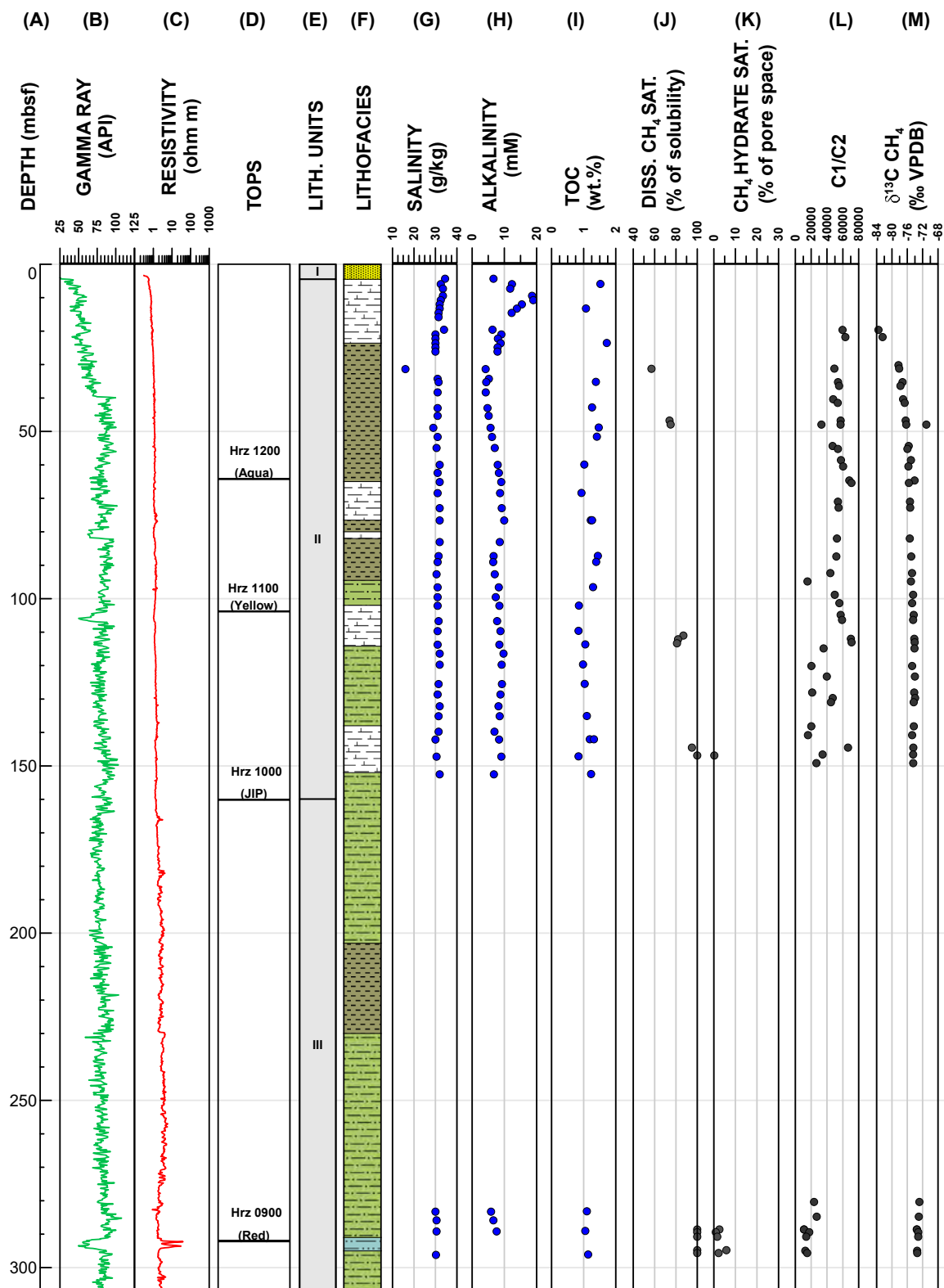


Figure F64: Expanded view of the Geochemistry Summary 0-300 mbsf. A) Measured Depth in Hole H003 meters below the seafloor (mbsf); B) Projected Hole H001 logging while drilling (LWD) gamma ray in green. The depth projection of Hole H001 LWD data onto Hole H002 and Hole H003 is discussed in [Plotting H001, H002, and H003 downhole data](#); C) Projected LWD resistivity in red; D) Seismic reflectors (Hrz = Horizon) and stratigraphic tops as described in Table [T4](#); E) Lithologic units; F) Lithofacies (Table [T10](#)); G) Uncorrected salinity (See [Pore water geochemistry](#)); H) Uncorrected alkalinity (See [Pore water geochemistry](#)); I) Total Organic Carbon (TOC, See [Sediment geochemistry](#)); J) Dissolved methane saturation as a percent of solubility (See [Dissolved gas concentrations and hydrate saturation](#)); K) Methane hydrate saturation of the pore space (See [Dissolved gas concentrations and hydrate saturation](#)); L) Methane to ethane ratio ($C_1:C_2$) ratio (See [Gas geochemistry](#)); M) Carbon-13 isotopes ($\delta^{13}C$) of methane (CH_4) measured post-expedition using a cavity ringdown spectrometer (CRDS, See [Gas geochemistry](#)). G through M used compressed measured depths in mbsf.

Hole	Core	Type	Section	Top (cm)	Bot (cm)	Archived Depth (mbsf)	Compressed Depth (mbsf)	Volume (mL)	Salinity	Alkalinity (mM)
H003	1	H	1	130	140	1.35	1.35	4		
H003	1	H	2	130	140	2.85	2.85	6		
H003	1	H	3	130	140	4.35	4.35	12	34.5	6.62
H003	1	H	4	140	150	5.95	5.95	35	32.5	12.33
H003	1	H	5	126	136	7.31	7.31	43	33.5	11.81
H003	2	H	1	140	150	9.68	9.46	36	33.5	18.59
H003	2	H	2	140	150	11.18	10.73	36	32.5	18.95
H003	2	H	3	140	150	12.68	12.01	34	32	15.43
H003	2	H	4	140	150	14.18	13.28	36	32	13.87
H003	2	H	5	140	150	15.68	14.56	34	31.5	12.24
H003	2	H	6	140	150	17.18	15.83	33	31.5	
H003	3	H	1	111	126	19.78	19.58	42	34	6.33
H003	3	H	2	135	150	21.47	20.99	36	30	9.06
H003	3	H	3	135	150	22.97	22.25	27	30	8.00
H003	3	H	4	150	165	24.62	23.62	30	30	8.84
H003	3	H	5	135	150	26.12	24.88	35	30	7.91
H003	3	H	6	135	150	27.62	26.13	32	30	7.87
H003	5	CS	2	10	25	31.45	31.36	30	16	4.21
H003	6	H	2	135	150	35.23	34.28	32	31	5.19
H003	6	H	3	125	150	36.68	35.25	26	31.5	4.37
H003	6	H	6	135	150	41.23	38.31	28	31	4.23
H003	7	H	3	105	150	43.59	43.01	34	31	4.77
H003	7	H	5	83	113	46.30	45.35	29	31	5.15
H003	8	CS	3	90	105	48.91	48.91	34	29	5.72
H003	9	H	2	87	116	52.20	51.66	36	31	6.18
H003	9	H	5	95	111	56.37	54.94	30	30.5	7.03
H003	10	H	3	80	98	60.58	59.98	29	32	7.95
H003	10	H	5	120	137	63.44	62.39	30	31	8.31
H003	11	H	1	180	195	65.58	65.13	31	32	9.04
H003	11	H	4	135	155	69.96	68.45	13	31	8.68
H003	12	H	2	135	150	73.64	72.94	40	32	9.17
H003	12	H	5	167	182	78.46	76.60	14	32	9.94
H003	14	H	2	117	141	83.61	83.07	27	32	8.57
H003	14	H	6	108	124	88.80	87.27	31	31.5	6.67
H003	15	CS	2	60	75	89.07	89.07	19	31	6.55
H003	16	H	1	146	176	93.05	92.70	24	30.5	7.01
H003	16	H	4	177	193	98.05	96.60	26	31	8.28
H003	17	H	2	152	166	100.12	99.53	28	31	7.34

Hole	Core	Type	Section	Top (cm)	Bot (cm)	Archived Depth (mbsf)	Compressed Depth (mbsf)	Volume (mL)	Salinity	Alkalinity (mM)
H003	17	H	4	185	200	103.62	102.12	29	31	8.46
H003	18	H	2	136	151	107.75	106.69	30	31.5	7.74
H003	18	H	5	136	162	112.06	109.72	29	31	8.77
H003	19	CS	5	69	91	114.15	113.77	28	31	8.46
H003	20	H	2	170	185	116.87	116.42	29	32	9.73
H003	20	H	5	135	150	120.80	119.74	28	32	9.14
H003	21	H	3	136	150	126.05	125.52	24	31.5	9.25
H003	21	H	6	119	134	129.58	128.64	29	31	8.80
H003	22	H	2	135	150	132.16	132.16	29	32	8.16
H003	22	H	4	135	150	135.14	135.14	30	31.5	8.53
H003	23	H	2	163	184	140.25	139.78	26	31.5	6.92
H003	23	H	4	135	160	142.97	142.13	28	30	8.36
H003	24	CS	5	63	80	147.59	147.22	29	30.5	9.07
H003	25	H	7	85	102	154.36	152.50	26	32	6.74
H003	26	X	4	117	137	283.27	283.27	13	30	5.87
H003	26	X	6	91	115	285.86	285.86	18	30.5	6.60
H003	27	CS	4	46	71	289.17	289.17	23	30.5	7.59
H003	29	CS	5	45	68	296.19	296.19	12	30.25	
H002	1	FB	1	47	77	645.27	645.27	19	28.5	6.8420
H002	3	FB	2	7	27	677.54	677.54	10	30	
H002	4	FB	2	60	70	681.62	681.62	2	12	
H002	4	FB	3	28	53	682.08	682.08	15	30	
H002	5	CS	3	9	34	802.22	802.22	6	29	
H002	6	CS	5	8	35	805.82	805.82	12	29	
H002	8	CS	3	56	80	811.43	811.43	27	28	4.3706
H002	9	CS	1	79	90	813.44	813.35	21	28	2.7487
H002	9	CS	4	0	5	815.13	814.86	6	20	
H002	12	CS	1	106	131	822.93	822.78	19	29	2.8632
H002	12	CS	2	88	113	824.06	823.77	19	30	
H002	13	CS	1	48	57	825.31	825.25	15	30	2.6197
H002	13	CS	1	154	179	826.45	826.26	22	29.5	3.0030
H002	14	CS	1	15	40	844.88	844.84	22	30	4.7132
H002	14	CS	2	89	114	846.46	846.24	16	30.5	3.4490
H002	15	CS	1	46	67	858.88	858.88	12	30	

Table T21: Routine whole-round pore water sample results. H= Advance Piston Corer, X= Extended Core Barrel. CS = Pressure Coring Tool with Ball Valve in the Cutting Shoe configuration, FB= Pressure Coring Tool in the Face Bit configuration. Salinity is in dimensionless IAPSO practical salinity units. All depths are measured depths in meters below the seafloor (mbsf). Dataset: <https://doi.org/10.5281/zenodo.14146527>.

Hole	Core	Type	Section	Top (cm)	Bot (cm)	Depth (mbsf)	Volume (mL)
H003	1	H	1	140	150	1.45	2
H003	1	H	2	140	150	2.95	4
H003	1	H	3	140	150	4.45	38
H003	1	H	4	130	140	5.95	20
H003	1	H	5	116	126	7.21	20
H003	2	H	1	130	140	9.5796	33
H003	2	H	2	130	140	11.0796	33
H003	2	H	3	130	140	12.5796	28
H003	2	H	4	130	140	14.0796	32
H003	2	H	5	130	140	15.5796	29
H003	2	H	6	130	140	17.0796	34
H003	3	H	1	96	111	19.6278	36
H003	3	H	2	120	139	21.3178	34
H003	3	H	3	120	135	22.8178	32
H003	3	H	4	135	150	24.4678	-
H003	3	H	5	120	135	25.9678	34
H003	3	H	6	120	135	27.4678	33
H003	6	H	2	120	135	35.0838	28
H003	6	H	3	110	125	36.4838	28
H003	6	H	6	120	135	41.0838	-
H003	7	H	3	90	105	43.2942	-
H003	7	H	5	113	128	46.2992	28
H003	9	H	2	72	87	51.9774	30
H003	9	H	5	80	95	56.2174	26
H003	10	H	3	65	80	60.4178	30
H003	10	H	5	105	120	63.2778	22
H003	11	H	1	165	180	65.4282	28
H003	11	H	4	120	135	69.7882	17
H003	12	H	2	120	135	73.4886	30
H003	12	H	5	152	167	78.3086	18
H003	14	H	2	101	117	83.412	29
H003	14	H	6	93	108	88.647	29
H003	16	H	1	131	146	92.825	25
H003	16	H	4	162	177	97.895	25
H003	17	H	2	137	152	99.9758	27
H003	17	H	4	170	185	103.4658	22
H003	18	H	2	121	136	107.5966	37
H003	18	H	5	121	136	111.8566	26
H003	20	H	2	154	170	116.7152	29

Hole	Core	Type	Section	Top (cm)	Bot (cm)	Depth (mbsf)	Volume (mL)
H003	20	H	5	120	135	120.6502	28
H003	21	H	3	120	136	125.8952	22
H003	21	H	6	104	119	129.4302	25
H003	22	H	2	120	135	132.0102	24
H003	22	H	4	120	135	134.9902	-
H003	23	H	2	148	163	140.0702	25
H003	23	H	4	119	135	142.7652	19

Table T22: Organic whole-round pore water sample results for H003. H= Advance Piston Corer, X= Extended Core Barrel. CS = Pressure Coring Tool with Ball Valve (PCTB) in the Cutting Shoe configuration. FB= PCTB in the Face Bit configuration. Salinity is in dimensionless IAPSO practical salinity units. All depths are measured depths in meters below the seafloor (mbsf). Dataset: <https://doi.org/10.5281/zenodo.14146527>

Date Collected	Time Collected	Bottle #	Salinity	Alkalinity (mM)
8/5/2023	7:00	1	31	2.65
8/6/2023	9:00	2	35	2.39
8/7/2023	8:45	3	-	2.31
8/8/2023	8:30	4	36	2.32
8/9/2023	8:45	6	36	2.45
8/10/2023	7:00	5	36	2.58
8/11/2023	9:20	7	36	2.39
8/13/2023	9:30	8	35.5	2.59
8/14/2023	15:15	10	36	2.48
8/15/2023	7:30	9	36	2.45

Table T23: Seawater drilling fluid sample results. Salinity is in dimensionless IAPSO practical salinity units. Dataset: <https://doi.org/10.5281/zenodo.14146527>

Date Collected	Time Collected	Salinity	Alkalinity (mM)
8/6/2023	9:00	32	-
8/7/2023	8:45	32	-
8/8/2023	8:30	33	-
8/9/2023	8:45	32	-
8/10/2023	7:00	35	-
8/11/2023	9:20	32	-
8/12/2023	7:15	32	-
8/13/2023	9:30	34	-
8/14/2023	15:15	34	-
8/15/2023	7:30	33	-

Table T24: Water-based mud drilling fluid sample results. Salinity is in dimensionless IAPSO practical salinity units. Dataset: <https://doi.org/10.5281/zenodo.14146527>

Hole	Core	Type	Salinity	Alkalinity (mM)
H003	5	CS	0	2.11
H003	8	CS	-	-
H003	13	CS	-	-
H003	19	CS	0	0.63
H003	24	CS	0	-
H003	27	CS	0	0.73
H003	28	CS	5	1.42
H003	29	CS	0	1.04
H002	3	FB	0	0.32
H002	5	CS	55	0.00
H002	6	CS	4	-
H002	8	CS	0	6.12
H002	10	CS	15	2.95
Sample				
Sample		Date	Salinity	Alkalinity (mM)
PCATS Feedwater		8/12/2023	0	1.71
PCATS Mixing Tank		8/12/2023	0	-

Table T25: PCATS fluid sample results. CS = Pressure Coring Tool with Ball Valve (PCTB) in the Cutting Shoe configuration. FB= PCTB in the Face Bit configuration. Salinity is in dimensionless IAPSO practical salinity units. Dataset: <https://doi.org/10.5281/zenodo.14146527>

A total of 46 organic whole-round samples (sample code IWO) samples of 10-16 cm length were collected immediately adjacent to the IWR whole-round samples and squeezed for shore-based analysis of trace metal concentrations, trace metal isotope ratios, dissolved organic carbon characterization, dissolved sulfide concentrations, and sulfate concentrations (See Methods: Pore water geochemistry (Flemings et al., [2025b](#))) from 0-152 mbsf. IWO samples were only collected from G-APC cores due to potential contamination with drilling fluid and PCATS fluid in G-XCB and pressure cores. The volume of pore water recovered ranged from 2-38 mL (Table [T22](#)).

Daily samples of drilling seawater and drilling mud were collected while drilling (Tables [T23](#) and [T24](#)). Dissolved sulfate will be used as a tracer of contamination for drilling seawater and drilling mud below the sulfate-methane transition zone (SMTZ). Sulfate concentrations will be determined shore-based, thus the salinity and alkalinity data presented in Table [T21](#) and Figure [F65](#) are not corrected for drilling contamination. Samples of PCATS confining

fluids were collected for pressure cores that went through PCATS (Table [T25](#)). The confining fluid was spiked with 10 ppm cesium chloride to track contamination. Cesium concentrations will be determined on shore. As such, the pressure core data presented are not corrected for PCATS contamination.

Salinity and alkalinity were measured in pore water extracted from routine whole-round samples (IWR), drilling seawater (IWSW), drilling mud (IWDM), and PCATS fluids (IWPCATS) shipboard and at Geotek in Salt Lake City (See Methods: Pore water geochemistry (Flemings et al., [2025b](#))). The data are presented in Tables [T21](#), [T23](#), [T24](#), and [T25](#) and Figure [F65](#).

Uncorrected salinity decreases from 34.5 at 4.35 mbsf to 30 at 21 mbsf, then remains relatively constant to 296.4 mbsf (Hole H003 total depth) (Figure [F65](#)). There is a salinity minimum of 16 (dimensionless IAPSO practical salinity units) at 30.2 mbsf, corresponding to pressure core 5CS. Successful pressure cores were first passed through PCATS before routine sampling in the core receiving laboratory. The PCATS confining

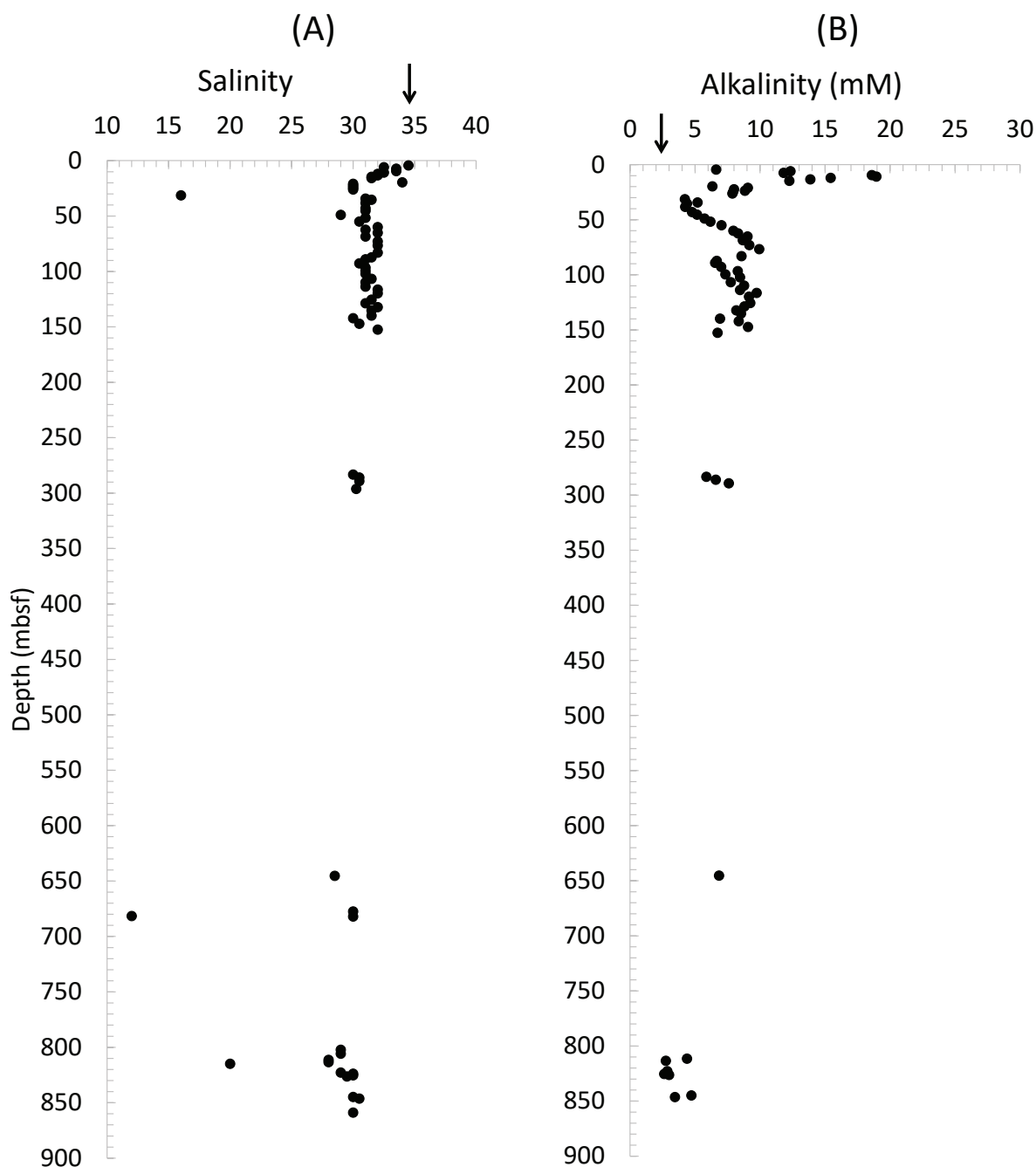


Figure F65: Uncorrected salinity and alkalinity with depth. The arrows indicate seawater values. Values will be corrected for contamination in the future. All depths are compressed measured depth in meters below the seafloor (mbsf). A) Salinity is in dimensionless IAPSO practical salinity units; B) Alkalinity Units = mM. Dataset: <https://doi.org/10.5281/zenodo.14146527>.

fluid was sourced from the potable freshwater supply on the *Q4000*. As such, the low salinity value likely reflects contamination with PCATS fluid prior to whole-round sampling in the core receiving laboratory. Contamination of the IWR sample from core 5CS with PCATS fluid will be confirmed by shore-based cesium concentration analyses.

Background salinity ranges from 28 to 30.5 from 644.6-859.6 mbsf (Hole H002). There are two distinct

salinity anomalies from the background profile. The first occurs at 681.6 mbsf with a salinity of 12, and the second is a salinity of 20 at 814.9 mbsf. These two salinity anomalies indicate the occurrence of methane hydrate at relatively high saturations. Shore-based chloride concentration analyses will be used to quantify the average methane hydrate saturations in the two whole-round samples.

The alkalinity with compressed measured depth

0-296.4 mbsf (Hole H003) contains three distinct concentration maxima in the upper ~80 m of the sediment column (Figure F65). Alkalinity concentrations increase sharply from 6.6 mM at 4.4 mbsf to the first concentration maxima of 19 mM at 10.7 mbsf. Alkalinity concentrations then decrease to 6.3 mM at 19.6 mbsf and increase abruptly to the second concentration maxima of 9.1 mM at 30 mbsf. Alkalinity concentrations then decrease sharply to 4.2 mM at 31.4 mbsf and increase more gradually to the third concentration maxima of 9.9 mM at 76.6 mbsf. Alkalinity concentrations again decrease sharply below the third concentration maxima to 6.7 mM at 87.3 mbsf. Below this depth, alkalinity concentrations are variable but do not exhibit sharp increases or decreases to TD, with concentrations ranging between 5.9 and 9.7 mM. The reason for the sharp changes in alkalinity concentrations in the upper ~80 m of the sediment column will be one of the major focuses of the shore-based pore water geochemistry program. Alkalinity concentrations 644.6-861.3 mbsf (H002) range from 2.6 mM to 6.8 mM, with the lowest measured concentrations between 813-825 mbsf and the highest concentration at 645 mbsf.

Pore water geochemistry post-expedition analysis plan

The concentration of dissolved species in pore water and their isotopic composition will be used to characterize fluid-sediment reactions, the formation of authigenic minerals, microbially-mediated reactions, biogeochemical cycling, fluid sources, and fluid flow pathways. In addition, pore water solute and isotope ratio profiles are essential for quantifying fluid flow rates and the rates of chemical reactions, including methanogenesis and methanotrophy.

Gas geochemistry

Headspace gases

A total of 54 gas samples desorbed from headspace sediment stored in glass vials from Holes H003 and H002 were analyzed for C₁-C₆ hydrocarbon composition, atmospheric gases, carbon dioxide,

hydrogen sulfide, helium, and hydrogen. See Methods: Headspace gas collection and gas chromatography (Flemings et al., 2025b). Methane (C₁ or CH₄) content ranged from 0.01 to 4% (mean: 0.74%) (compared to 2 ppm in the atmosphere) (Figure F66). Ethane (C₂) ranged from 0.12 to 7.4 ppm (mean: 1.1 ppm). Propane (C₃) was below detection in most samples but ranged from 0.1 to 5.6 ppm when detected. Butane (C₄), pentane (C₅), and hexane (C₆) were not detected. The methane/ethane ratio (C₁/C₂) is generally highest in the upper 150 mbsf compared to deeper sediments but doesn't exhibit a clear trend down core (Figure F67), likely due to the large variation in recovery times and lags between sampling that result in loss of gas from the core.

Argon (Ar) ranged from 0.79 to 1.19 % with a mean of 1.01%, near the atmospheric average of 0.93 %. Nitrogen (N₂) ranged between 77.4 to 96.6% (mean: 89%), while oxygen varied between 0.79 and 21.6% (mean: 8.05 %) (Figure F66). Even though headspace gases contain only a few percent methane, this methane gas is representative of the sediment sample with only trace contribution of atmospheric methane. Atmospheric C₁/Ar is 0.0002, while the headspace gas C₁/Ar ranges from 0.01 to 3.9. Oxygen (O₂) was clearly depleted in the headspace vials during storage, either due to sulfide mineral oxidation or decomposition of organic matter despite saturation with 1 M potassium chloride (KCl). Atmospheric O₂/Ar is 22.5 while much lower values were observed in the headspace gas (Figure F67). Helium (He) ranged from 3.0 to 17.0 ppm (mean: 6.0 ppm) and hydrogen (H₂) ranged from 11.8 to 122.8 ppm (mean: 33.0 ppm). Both He and H₂ are slightly elevated in the upper 150 mbsf, possibly due to the faster recovery of these shallower cores resulting in less loss of these light gases.

Hydrogen sulfide (H₂S) was below detection in the majority of samples. When detected, it ranged from 14.5 to 29.1 ppm (mean: 22.9 ppm). The presence of H₂S below the sulfate-methane transition zone (SMTZ) suggests drilling fluid contamination.

Void, pressure core, and hydrate gases

Syringe samples

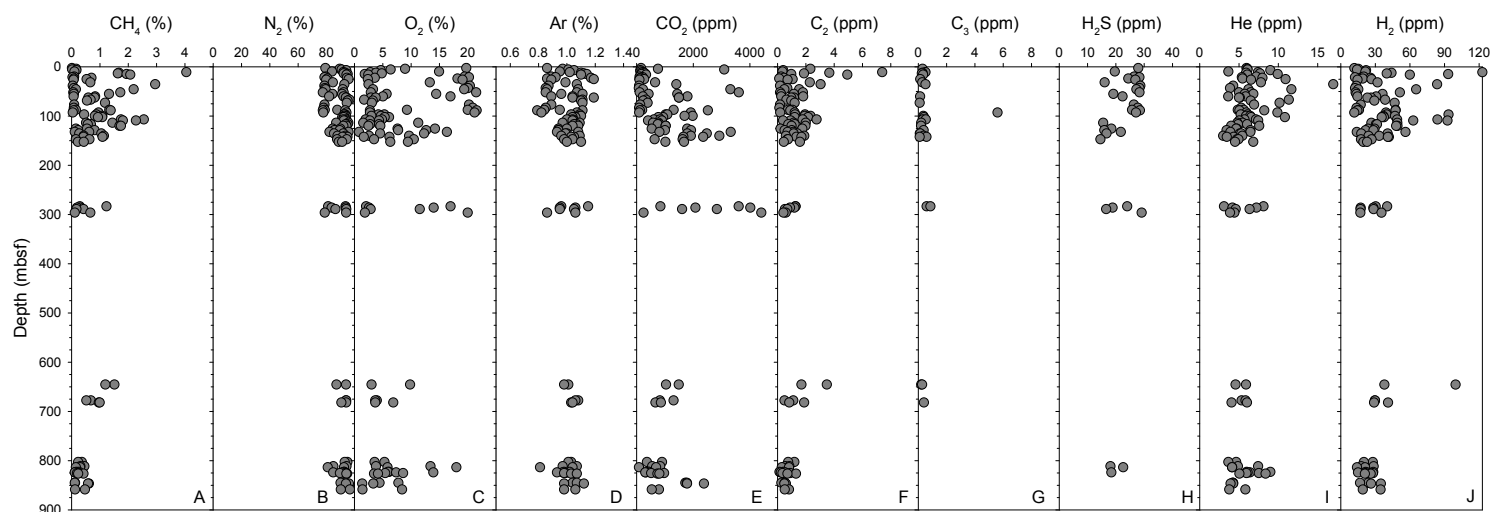


Figure F66: Composition of headspace gas samples. A) methane (CH_4), B) nitrogen (N_2), C) oxygen (O_2), D) argon (Ar), E) carbon dioxide (CO_2), F) ethane (C_2), G) propane (C_3), H) hydrogen sulfide (H_2S), I) helium (He), and hydrogen (H_2). All depths are compressed measured depth in meters below the seafloor (mbsf). Dataset: <https://doi.org/10.5281/zenodo.14518633>.

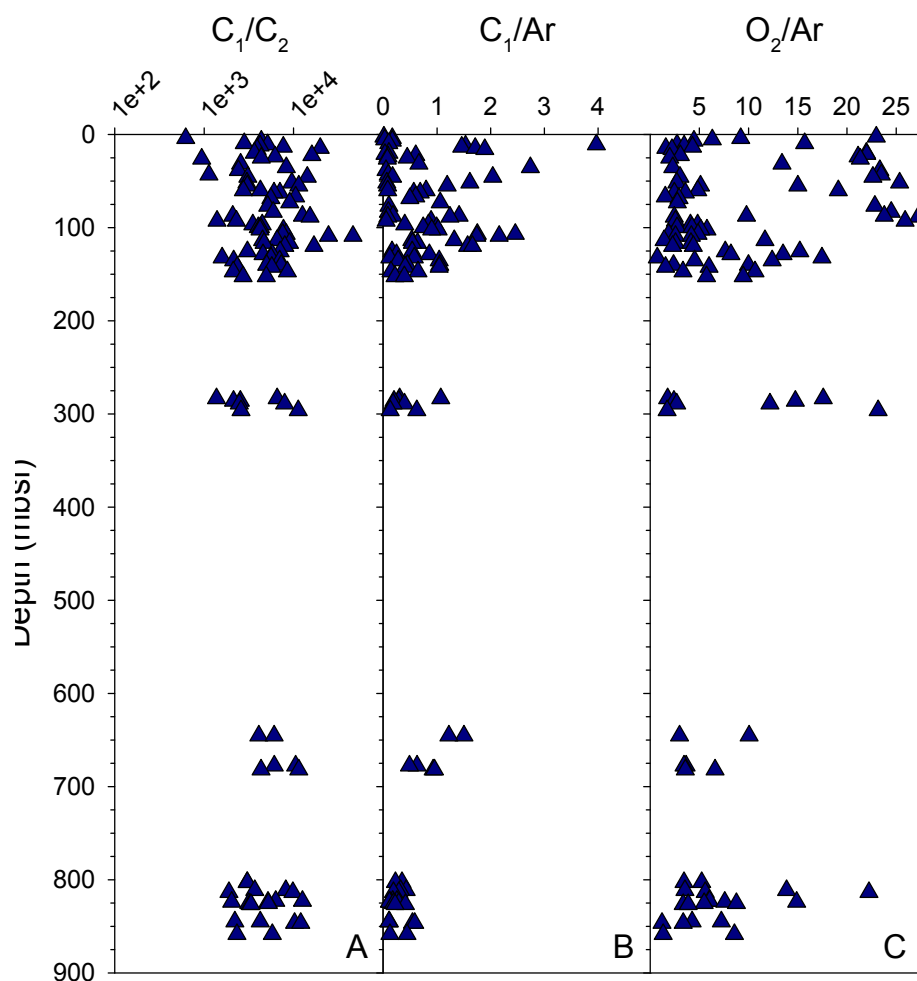


Figure F67: Constituent ratios from headspace gas samples. A) methane/ethane (C_1/C_2), B) methane/argon (C_1/Ar), and oxygen/argon (O_2/Ar). All depths are compressed measured depth in meters below the seafloor (mbsf). Dataset: <https://doi.org/10.5281/zenodo.14518633>.

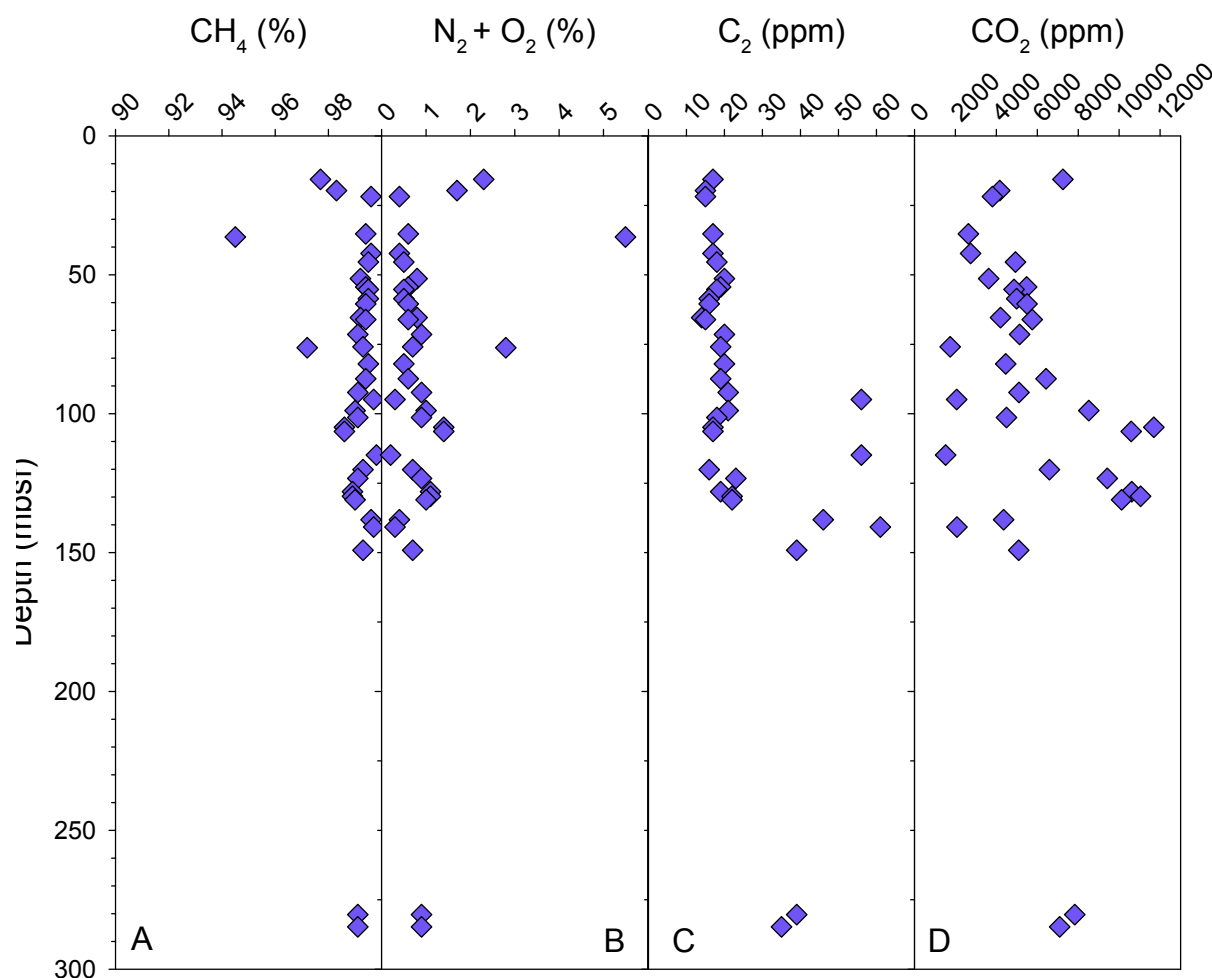


Figure F68: Composition of void gas samples measured on the *Q4000* and in Salt Lake City via gas chromatography with a thermal conductivity detector (GC-TCD). A) methane, (CH_4); B) nitrogen + oxygen ($\text{N}_2 + \text{O}_2$); C) ethane (C_2); and D) carbon dioxide (CO_2). All depths are compressed measured depth in meters below the seafloor (mbsf). Dataset: <https://doi.org/10.5281/zenodo.16689630>

A total of 36 void gas samples collected in syringes were measured via gas chromatography with a thermal conductivity detector (GC-TCD) within hours of collection on the *Q4000* and in Salt Lake City. See Methods: Void gases and Geotek gas analysis (Flemings et al., [2025b](#)). Void gases could only be collected on conventional cores from Hole H003. These samples are primarily methane (94.5 to 99.8% CH_4 ; mean: 99.0%) with relatively small amounts of atmospheric contamination (less than 1% $\text{N}_2 + \text{O}_2$ on average; range: 0.2 to 5.5%) (Figure [F68](#)). Ethane ranges from 14 to 61 ppm (mean: 24 ppm). Ethane is less than 25 ppm above 100 mbsf and increases below 100 mbsf. CO_2 ranges from 1,519 to 11,692 ppm (mean: 5,763 ppm). CO_2 reaches a relative minimum around 40 mbsf and becomes higher and more variable between 60 and 160 mbsf.

Similar to the void gas samples, 67 pressure core

gas samples collected in syringes were measured via GC-TCD within hours of collection on the *Q4000* and in Salt Lake City. See Methods: Pressure core produced gases and Geotek gas analysis (Flemings et al., [2025b](#)). These are primarily methane (89% on average) with some samples with higher amounts of atmospheric contamination (1 to 98% $\text{N}_2 + \text{O}_2$) (Figure [F69](#)). Ethane ranges from 4 to 89 ppm (mean: 35 ppm) with a large increase starting below 289 mbsf. CO_2 ranges from 94 to 1,498 ppm (mean: 630 ppm) with generally high values shallower than 160 mbsf. Ethane and CO_2 exhibit large variability during quantitative degassing, either increasing or decreasing systematically during depressurization. No propane, butane, or pentane was observed in these samples.

Hydrate gas samples were only collected in gas bags for post-expedition analyses and were not analyzed immediately. See Methods: Hydrate-bearing sediment

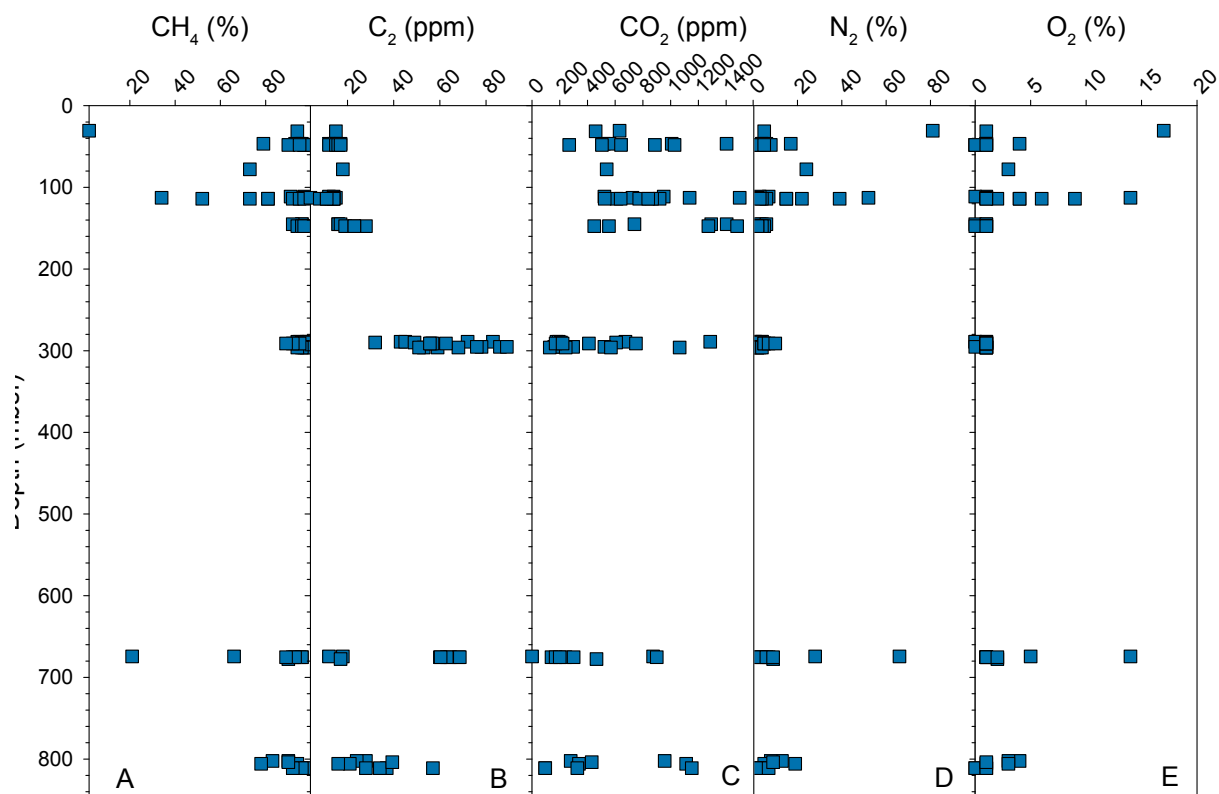


Figure F69: Composition of pressure core gas samples measured on the Q4000 and in Salt Lake City via gas chromatography with a thermal conductivity detector (GC-TCD). A) methane (CH₄); B) ethane (C₂); C) carbon dioxide (CO₂); D) nitrogen (N₂); and E) oxygen (O₂). All depths are compressed measured depth in meters below the seafloor (mbsf). Dataset: <https://doi.org/10.5281/zenodo.16689630>

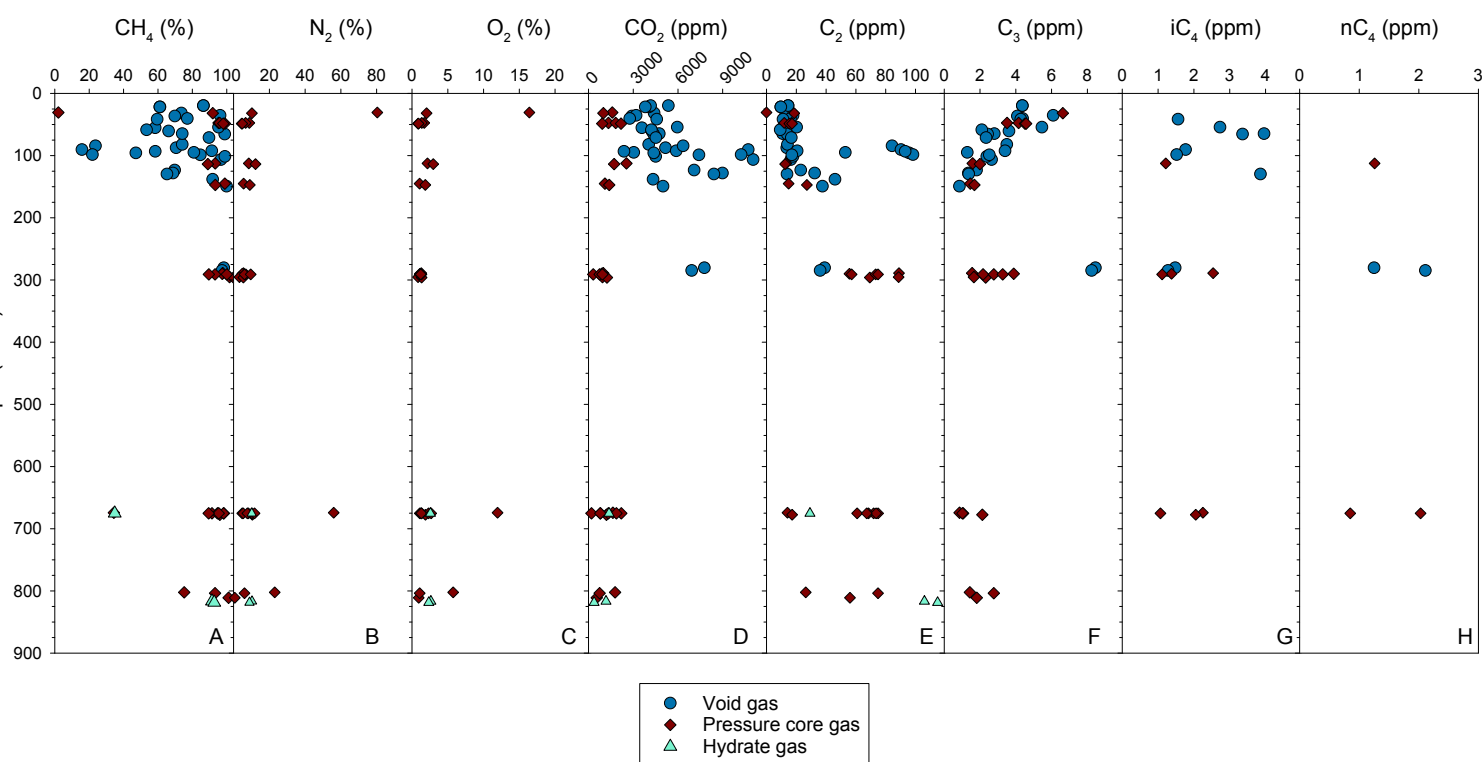


Figure F70: Composition of void, pressure core, and hydrate gas samples measured via gas chromatography with a flame ionization detector (GC-FID), via gas chromatography with a thermal conductivity detector (GC-TCD), and a cavity ringdown spectrometer (CRDS). A) methane (CH₄); B) nitrogen (N₂); C) oxygen (O₂); D) carbon dioxide (CO₂); E) ethane (C₂); F) propane (C₃); G) isobutane (iC₄); and H) normal butane (nC₄). All depths are compressed measured depth in meters below the seafloor (mbsf). Dataset: <https://doi.org/10.5281/zenodo.16689630>

dissociation gases (Flemings et al., [2025b](#)).

Gas bag samples

All void gas samples were collected in Cali-5 bond gas bags and a subset of degassing steps were sampled into gas bags for post-expedition analysis. See Methods: Gas geochemistry (Flemings et al., [2025b](#)). All three hydrate or hydrate-bearing sediment samples were collected only in gas bags for post-expedition analyses. Void gas samples in gas bags have relatively higher atmospheric contamination (mean: 22.5% $N_2 + O_2$; range: 4.6 to 49.9%) compared to the syringe samples. This is most likely due to the fact syringe samples were collected first from voids and may have drawn in atmospheric contamination before the gases were collected in bags. However, the overall high hydrocarbon content of the samples (mean: 81.4% CH_4 , range: 53.4 to 99.9% CH_4) allow for quality analysis of hydrocarbon molecular and isotopic composition. Pressure core gas samples in gas bags had relatively lower atmospheric contamination (mean 11.8 % $N_2 + O_2$). Hydrate gas and hydrate-bearing sediment gas samples had moderate atmospheric contamination (mean: 12.3 % $N_2 + O_2$).

In all three types of samples, ethane increases with depth over the upper 160 mbsf and is highest on average below 280 mbsf (Figure [F70](#)). The highest values of ethane (106 and 115 ppm) were measured in hydrate/hydrate-bearing sediment from the Orange sand (Sections H002-10CS-2 and H002-11CS-1, ~818 mbsf). CO_2 is highest in the upper 160 mbsf and generally increases over the continuously cored interval. Propane decreases over the upper 160 mbsf and increases again between 280 and 300 mbsf. All concentrations of propane are less than 8 ppm. i-Butane and n-butane were measured in a small number of samples at values less than 5 ppm. There is no observable trend in butane with depth.

Methane to ethane (C_1/C_2) and methane to ethane and propane ($C_1/(C_2+C_3)$) decrease with depth, mainly driven by the increase in ethane with depth (Figure [F71](#)). This trend exists in both the GC-TCD and higher sensitivity gas chromatography with flame ionization detector (GC-FID) measurements. All values of C_1/C_2

and $C_1/(C_2+C_3)$ are relatively high (>1000). $\delta^{13}C-CH_4$ increases with depth, but all values are lighter than -69.3 ‰ Vienna Pee Dee Belemnite (VPDB) (mean: -73.9 ‰ VPDB). The decrease in C_1/C_2 and increase in $\delta^{13}C-CH_4$ is most apparent in the continuously cored section (Figure [F72](#)) but the values near the Red sand (Figure [F73](#)) and through the Upper Blue sand (Figure [F74](#)) are consistent with the overall trend of the shallower sediments (Figure [F71](#)). The highest variability was observed in the cores through the Orange sand interval (Figures [F71](#) and [F75](#)). It is unclear at this point whether there is a trend through this interval. No gas samples have yet been collected from quantitative degassing of the high-saturation intervals.

Overall, the gas composition of light $\delta^{13}C-CH_4$ and high $C_1/(C_2+C_3)$ is consistent with a mainly microbial source of methane with only very minor thermogenic components. Future analyses will be necessary to determine the specific methanogenesis pathways, possible secondary methane generation, or the possible presence of microbial ethane.

Gas geochemistry post-expedition analysis plan

The gases remaining in Cali-5 bond gas bags and a subset of these gas bags will be used for additional methane and ethane carbon and hydrogen isotopic analyses, as well as carbon dioxide carbon isotopic analyses. An additional subset will be used for clumped methane isotopologue analyses. Copper tubes were collected from four pressure core sections and will be used for noble gas and isotopic analyses. Additional gas samples are planned to be collected from preserved pressure cores from the Orange and Upper Blue sands at UT.

Sedimentary geochemistry

CNS elemental measurements

Elemental analysis of bulk sediment from IWR whole-round squeeze cakes (n=36) were completed (Figures [F76](#) and [F77](#); Table [T26](#)). See Methods: Sedimentary geochemistry (Flemings et al., [2025b](#))

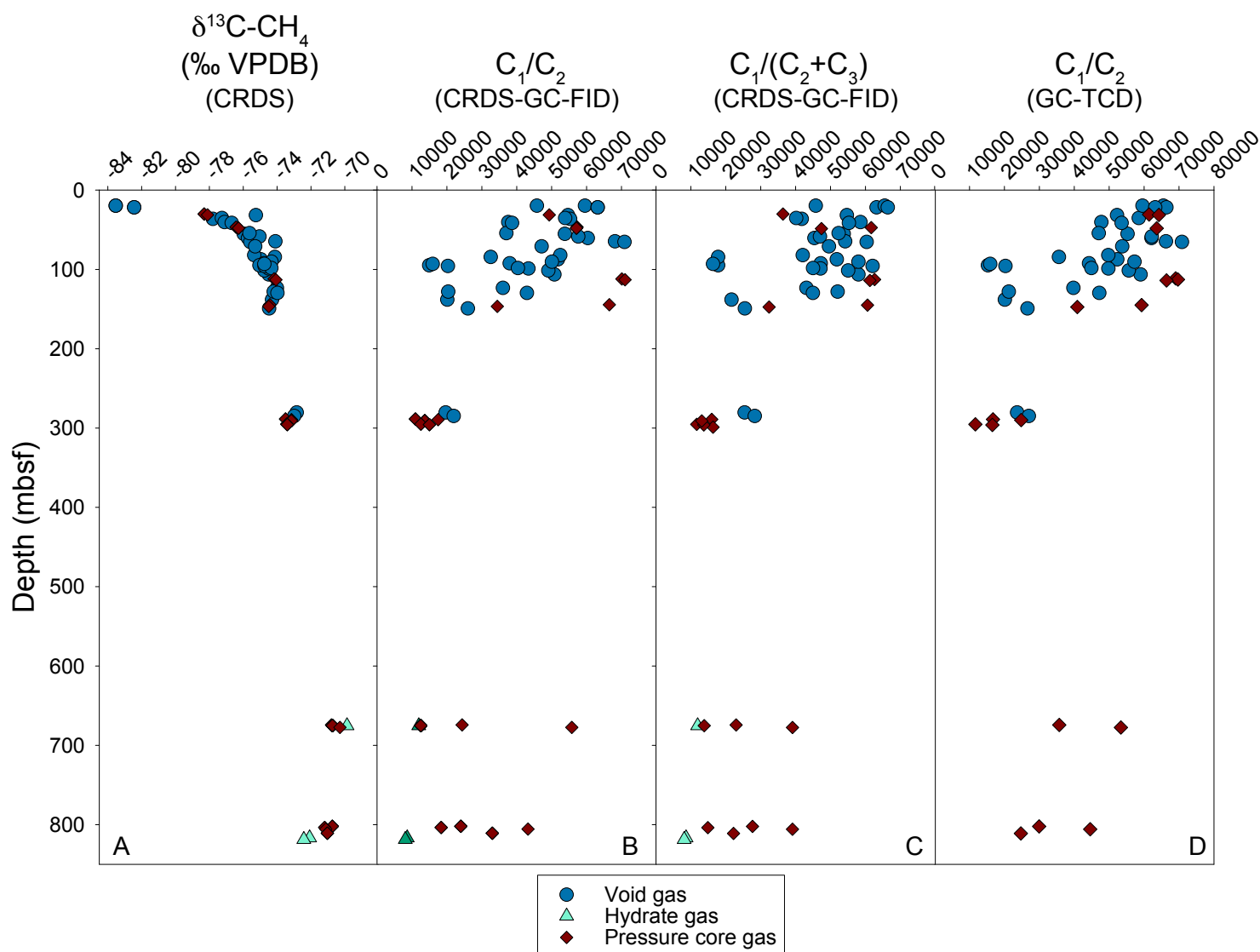


Figure F71: Carbon isotopes of methane ($\delta^{13}\text{C}$) and molecular ratios for methane (C_1), ethane (C_2) and propane (C_3) from void, pressure core, and hydrate gas samples from Site H. A) $\delta^{13}\text{C}\text{-CH}_4$ measured by cavity ringdown spectrometer (CRDS) and reported relative to a Vienna Pee Dee Belemnite (VPDB) standard; B) C_1/C_2 measured by CRDS and gas chromatography with a flame ionization detector (GC-FID); C) $\text{C}_1/(\text{C}_2+\text{C}_3)$ measured by CRDS and GC-FID; and D) C_1/C_2 measured within hours of collection via gas chromatography with a thermal conductivity detector (GC-TCD). All depths are compressed measured depth in meters below the seafloor (mbsf). Dataset: <https://doi.org/10.5281/zenodo.15626975>.

Total organic carbon (TOC) measurements 0-296.4 mbsf (H003) vary between 0.84 wt.% and 1.72 wt.%, with a mean of 1.19 wt.% ($1\sigma = 0.22$ wt.%) (Figure F76 A). The variation in the TOC content is driven largely by the relative contributions and dilution effects of pelagic versus hemipelagic sedimentation (See [Environment of deposition](#)). The origin of the TOC is determined initially by its atomic TOC/TN. The mean atomic TOC/TN is 15.59 ($1\sigma = 3.42$) and ranges from 10.40 to 23.79. TOC measurements 644.6-859.6 mbsf (Hole H002) vary between 0.85 wt.% and 1.29 wt.%, with a mean of 1.09 wt.% ($1\sigma = 0.11$ wt.%). The TOC values 644.6-859.6 mbsf (Hole H002) are noticeably

less variable compared to 0-296.4 mbsf (Hole H003).

The mean atomic TOC/TN is 12.84 ($1\sigma = 1.67$) and ranges from 10.92 to 16.99 (Figure F76 B). The TOC/TN measurements document a mixed origin for the TOC from both terrestrial and marine organic carbon.

The CaCO_3 content 0-296.4 mbsf (H003) ranges from 1.50 to 26.82 wt.%, with a mean of 14.59 wt.% ($1\sigma = 5.57$) (Figure F76 C). The CaCO_3 content 644.6-859.6 (H002) ranges from 0.00 to 20.66 wt.%, with a mean of 7.00 wt.% ($1\sigma = 7.35$). These amounts and presence are consistent with detrital carbonate lithic

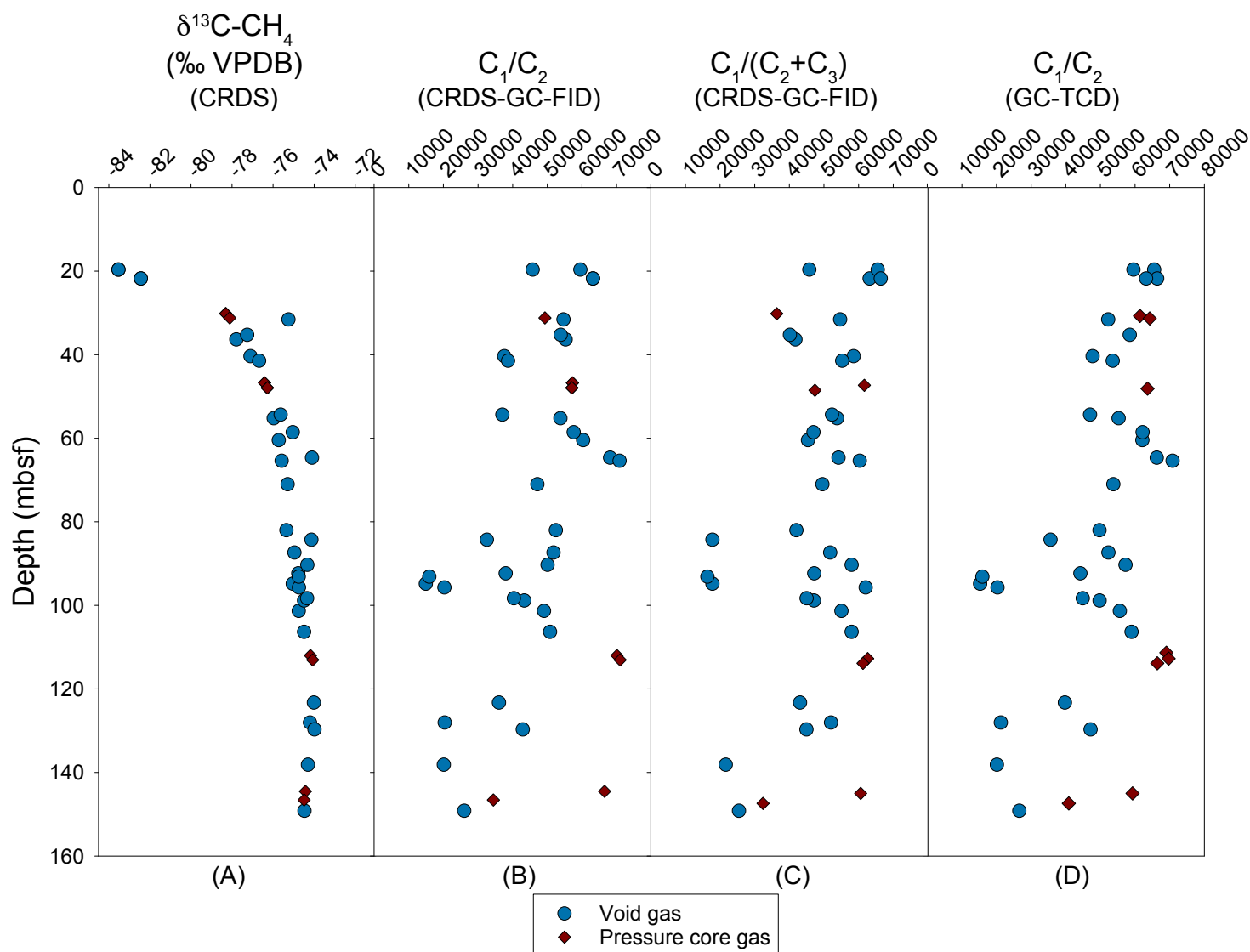


Figure F72: $\delta^{13}\text{C}$ isotopic ratio of methane and molecular ratios 0-1,601 mbsf for methane (C_1), ethane (C_2) and propane (C_3) from void and pressure core gas samples from the upper continuously cored section at Hole H003 (Cores H003-01H through H003-25H). A) $\delta^{13}\text{C}-\text{CH}_4$ measured by cavity ringdown spectrometer (CRDS) and reported relative to a Vienna Pee Dee Belemnite (VPDB) standard; B) C_1/C_2 measured by CRDS and via gas chromatography with a flame ionization detector (GC-FID); C) $\text{C}_1/(\text{C}_2+\text{C}_3)$ measured by CRDS and GC-FID; and D) C_1/C_2 measured via gas chromatography with a thermal conductivity detector (GC-TCD). All depths are compressed measured depth in meters below the seafloor (mbsf). Dataset: <https://doi.org/10.5281/zenodo.15626975>.

fragments, foraminifera, and calcareous nannofossils observed in smear slides (See [Sediment composition from smear slides](#)).

Total sulfur (TS) measurements 0-296.4 mbsf (H003) are variable (Figure [F76 D](#)), with a mean of 0.49 wt.% ($1\sigma=0.68$) and range of 0.07 wt.% to 3.14 wt.%. Intervals of elevated TS relative to a low background level may be diagnostic of sulfides produced via AOM (Borowski et al., [2013](#); Peketi et al., [2012](#)). Cyclic variation in TS in the upper 150 m of the hole H003 also appears to be anticorrelated with magnetic susceptibility (See [Physical properties](#)) suggested

AOM influenced diagenesis in this interval (Johnson et al., [2021](#)). AOM diagenetic overprints occurred in the presence of pore water sulfate and methane and thus occurred during early diagenesis, prior to compaction/dewatering.

Total sulfur (TS) measurements 644.6-859.6 mbsf (H002) are lower and less variable (Figure [F76, D](#)) with a mean TS of 0.14 wt.% ($1\sigma=0.12$) and range of 0.06 to 0.48 wt.%. The lack of intervals with elevated TS suggested OSR is the dominant pathway for sulfide mineralization.

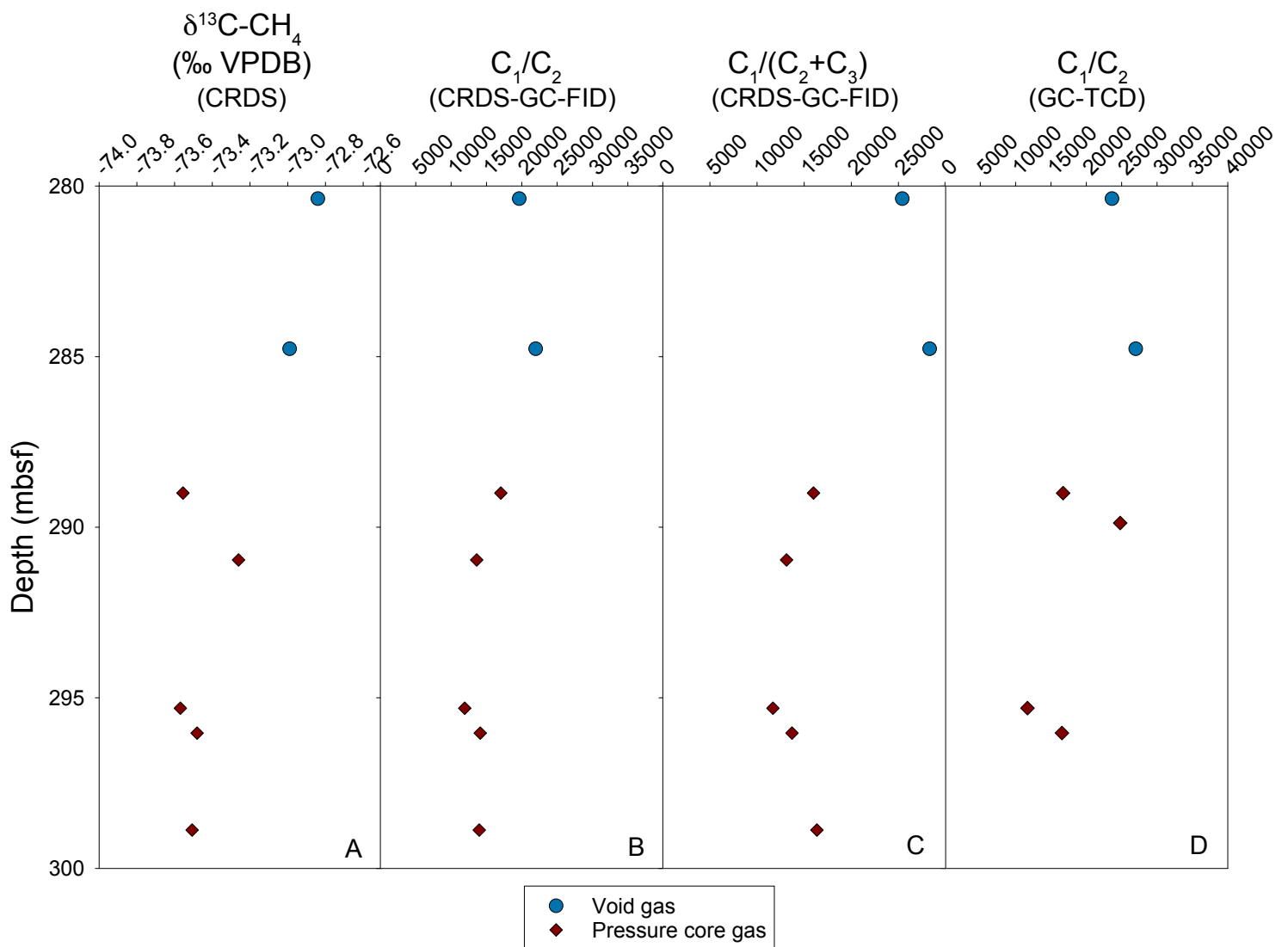


Figure F73: $\delta^{13}\text{C}$ isotopic ratio of methane and molecular ratios 280-300 mbsf for methane (C_1), ethane (C_2) and propane (C_3) from void and pressure core gas samples from the interval targeting the Red sand (Cores H003-26X through H003-29CS). A) $\delta^{13}\text{C}-\text{CH}_4$ measured by cavity ringdown spectrometer (CRDS) and reported relative to a Vienna Pee Dee Belemnite (VPDB) standard; B) C_1/C_2 measured by CRDS and via gas chromatography with a flame ionization detector (GC-FID); C) $\text{C}_1/(\text{C}_2+\text{C}_3)$ measured by CRDS and GC-FID; and D) C_1/C_2 measured via gas chromatography with a thermal conductivity detector (GC-TCD). All depths are compressed measured depth in meters below the seafloor (mbsf). Dataset: <https://doi.org/10.5281/zenodo.15626975>.

TS vs TOC

In marine sediments, both organoclastic sulfate reduction (OSR) and anaerobic oxidation of methane (AOM) produce hydrogen sulfide, which can precipitate pyrite, greigite, and iron monosulfide minerals in the presence of reactive iron (Larrasoana et al., 2007; Riedinger et al., 2005). As observed in modern seafloor methane-seep environments and at sulfate-methane transition zones (SMTZs) (Kaneko et al., 2010; Sato et al., 2012), measurements of TS are elevated relative to that expected to be produced by OSR (Berner and Raiswell, 1983). This excess TS

is driven by methane transported toward the SMTZ, where it is consumed during AOM.

Measured TS/TOC (Figure F77, black dots) is compared to values of typical marine sediments and phytoplankton. Intervals of elevated TS (relative to TOC) above the typical marine sediment (Berner and Raiswell, 1983) (Figure F77, solid black line) are consistent with the occurrence of early, AOM-related diagenesis in the sediments. Low TS data points (relative to TOC) below typical marine sediments and close to the marine phytoplankton end member line (Suits and Arthur, 2000) (Figure F77, dashed black

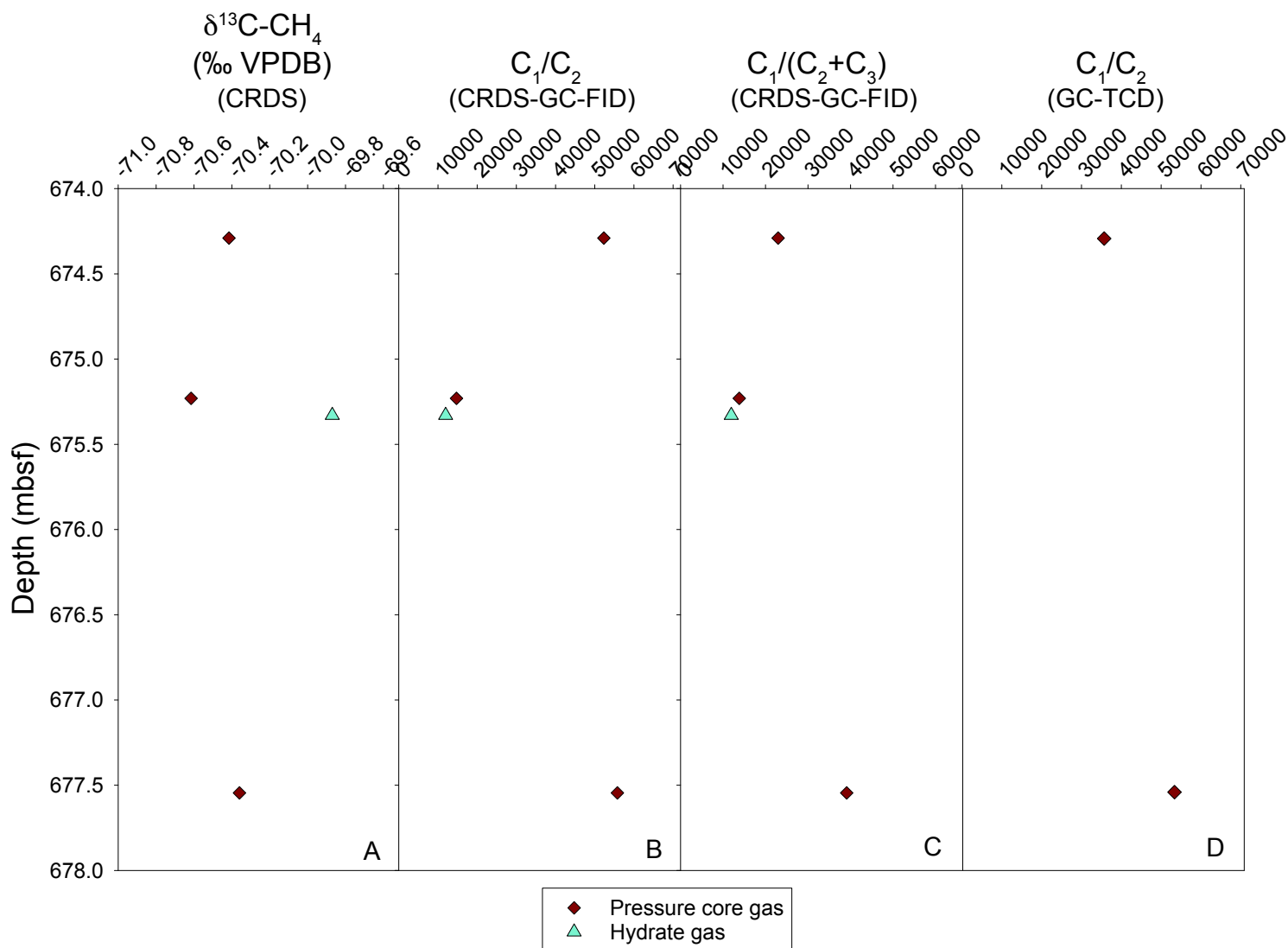


Figure F74: $\delta^{13}\text{C}$ isotopic ratio of methane and molecular ratios 674-678 mbsf for methane (C_1), ethane (C_2) and propane (C_3) from pressure core and hydrate gas samples from the interval targeting the Upper Blue sand (Cores H002-01FB through H002-4FB). A) $\delta^{13}\text{C}-\text{CH}_4$ measured by cavity ringdown spectrometer (CRDS) and reported relative to a Vienna Pee Dee Belemnite (VPDB) standard; B) C_1/C_2 measured by CRDS and via gas chromatography with a flame ionization detector (GC-FID); C) $\text{C}_1/(\text{C}_2+\text{C}_3)$ measured by CRDS and GC-FID; and D) C_1/C_2 measured via gas chromatography with a thermal conductivity detector (GC-TCD). All depths are compressed measured depth in meters below the seafloor (mbsf). Dataset: <https://doi.org/10.5281/zenodo.15626975>.

line), suggest a dominance of OSR for these sediment samples.

Sediment geochemistry post-expedition analysis plan

Future analyses will include high resolution measurements (1-2 samples per section) of TOC, CaCO_3 , TN, and TS, as well as a subset of these

samples for $\delta^{13}\text{C}_{\text{TOC}}$ and $\delta^{34}\text{S}_{\text{bulk}}$.

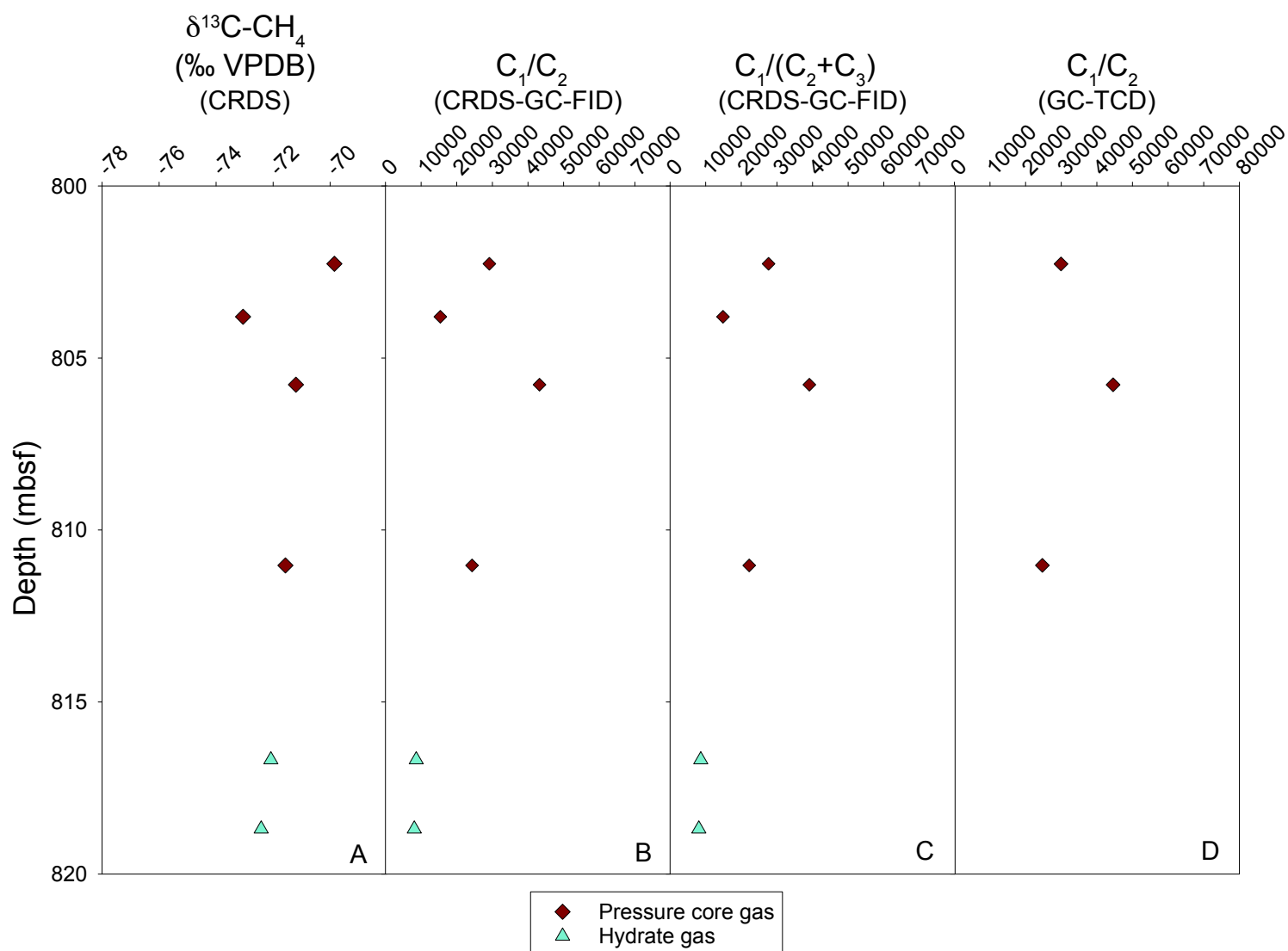


Figure F75: $\delta^{13}\text{C}$ isotopic ratio of methane and molecular ratios 800-820 mbsf for methane (C_1), ethane (C_2) and propane (C_3) from void and hydrate gas samples from the interval targeting the Orange sand (Cores H002-05CS through H002-15CS). A) $\delta^{13}\text{C}-\text{CH}_4$ measured by cavity ringdown spectrometer (CRDS) and reported relative to a Vienna Pee Dee Belemnite (VPDB) standard; B) C_1/C_2 measured by CRDS and via gas chromatography with a flame ionization detector (GC-FID); C) $\text{C}_1/(\text{C}_2+\text{C}_3)$ measured by CRDS and GC-FID; and D) C_1/C_2 measured via gas chromatography with a thermal conductivity detector (GC-TCD). All depths are compressed measured depth in meters below the seafloor (mbsf). Dataset: <https://doi.org/10.5281/zenodo.15626975>.

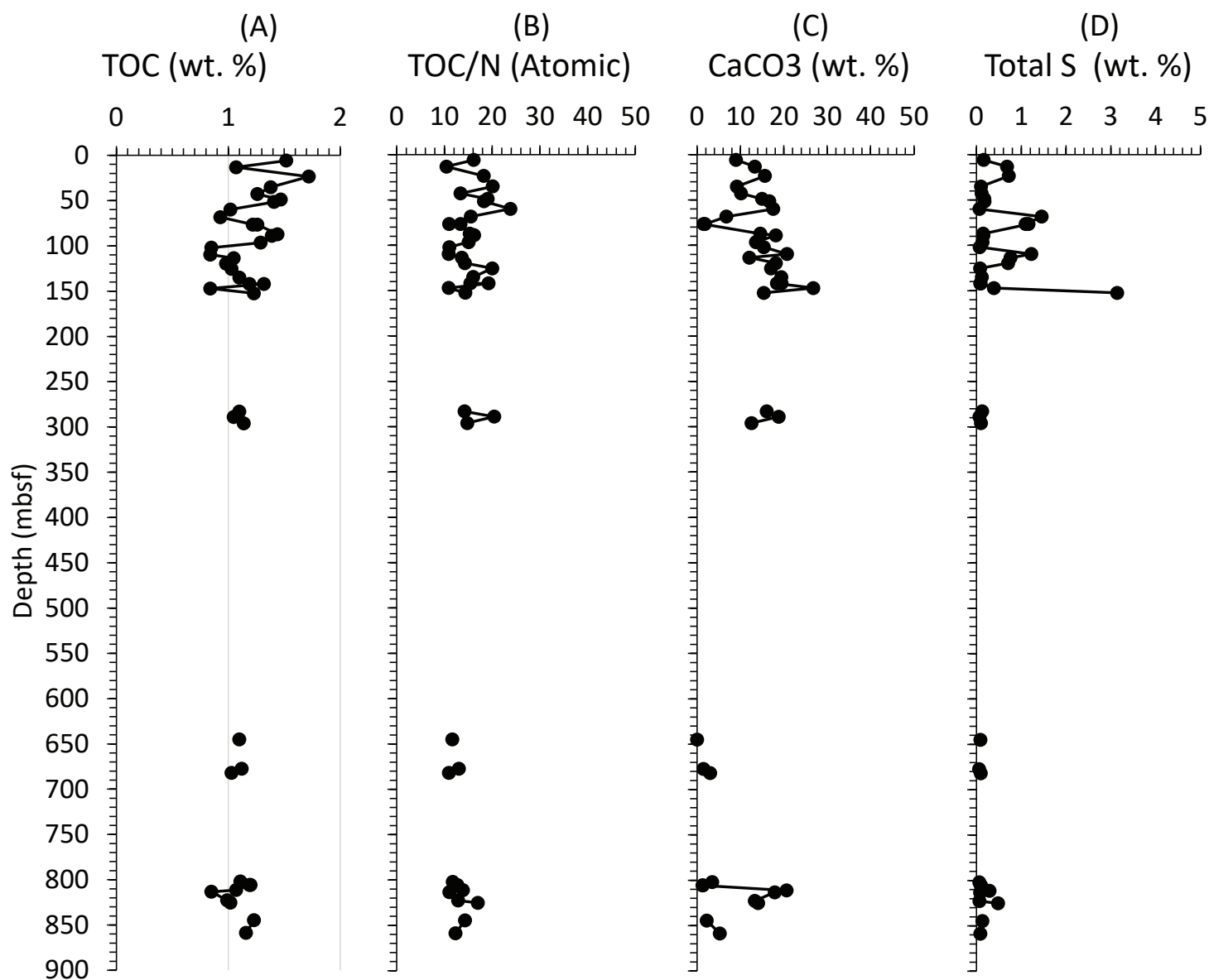


Figure F76: Initial CHNS element analysis results. TOC = Total Organic Carbon. TN = Total Nitrogen. TS = Total Sulfur. All depths are compressed measured depth in meters below the seafloor (mbsf). Dataset: <https://doi.org/10.5281/zenodo.14146049>.

Sample Name	Depth (mbsf)	Compressed Depth (mbsf)	TN (wt. %)	TC (wt. %)	TS (wt. %)	TOC (wt. %)	TOC/TN (Atomic)	CaCO3 (wt. %)
H003-1H-4e, 140-150cm	5.90	5.90	0.11	2.60	0.16	1.52	16.11	9.00
H003-2H-4e, 140-150cm	14.13	13.24	0.12	2.67	0.68	1.07	10.40	13.33
H003-3H-4f, 150-165cm	24.54	23.56	0.11	3.60	0.73	1.72	18.23	15.66
H003-6H-3e, 125-150cm	36.56	35.17	0.08	2.48	0.10	1.38	20.12	9.16
H003-7H-3e, 105-150cm	43.37	42.82	0.11	2.48	0.12	1.26	13.36	10.16
H003-8CS-3f, 90-105cm	48.83	48.83	0.09	3.27	0.17	1.47	19.05	14.99
H003-9H-2e, 87-116cm	52.05	51.55	0.09	3.41	0.18	1.41	18.27	16.66
H003-10H-3e, 80-98cm	60.49	59.90	0.05	3.13	0.07	1.02	23.79	17.58
H003-11H-4e, 135-155cm	69.86	68.38	0.07	1.74	1.46	0.93	15.49	6.75
H003-12H-5e, 167-182cm	78.38	76.54	0.13	1.44	1.10	1.22	10.94	1.83
H003-12H-5e, 167-182cm (replicate)	78.38	76.54	0.11	1.44	1.16	1.26	13.36	1.50
H003-14H-6e, 108-124cm	88.72	87.20	0.11	3.19	0.15	1.44	15.27	14.58
H003-15CS-2c, 60-75cm	88.99	88.99	0.10	3.57	0.15	1.39	16.21	18.16
H003-16H-4f, 177-193cm	97.97	96.54	0.10	2.92	0.14	1.29	15.04	13.58
H003-17H-4f, 180-200cm	103.54	102.07	0.09	2.70	0.07	0.85	11.01	15.41
H003-18H-5e, 136-162cm	111.93	109.62	0.09	3.33	1.23	0.84	10.88	20.74
H003-19CS-5e, 69-91cm	114.04	113.67	0.09	2.50	0.76	1.05	13.61	12.08
H003-20H-5e, 135-150cm	120.73	119.67	0.08	3.16	0.71	0.98	14.29	18.16
H003-21H-3e, 136-150cm	125.98	125.46	0.06	3.08	0.08	1.03	20.02	17.08
H003-22H-4e, 135-150cm	135.07	135.07	0.08	3.43	0.12	1.10	16.04	19.41
H003-23H-4f, 135-160cm	142.85	142.02	0.09	3.53	0.09	1.19	15.42	19.49
H003-23H-4f, 135-160cm (replicate)	142.85	142.02	0.08	3.53	0.09	1.32	19.24	18.41
H003-24CS-5d, 63-80cm	147.51	147.14	0.09	4.06	0.39	0.84	10.88	26.82
H003-25H-7d, 85-102cm	154.27	152.44	0.10	3.08	3.14	1.23	14.34	15.41
H003-26X-4e, 117-137cm	283.17	283.17	0.09	3.03	0.13	1.10	14.25	16.08
H003-27CS-4d, 46-71cm	289.04	289.04	0.06	3.31	0.07	1.05	20.41	18.83
H003-29CS-5c, 45-68cm	296.08	296.08	0.09	2.65	0.10	1.14	14.77	12.58
H002-1FB-1c, 47-77cm	645.12	645.12	0.11	1.10	0.09	1.10	11.66	0.00
H002-3FB-2b, 7-27cm	677.44	677.44	0.10	1.30	0.06	1.12	13.06	1.50
H002-4FB-3c, 28-53cm	681.95	681.95	0.11	1.39	0.10	1.03	10.92	3.00
H002-5CS-3b, 9-34cm	802.09	802.09	0.11	1.53	0.07	1.11	11.77	3.50
H002-6CS-5b, 8-35cm	805.68	805.68	0.11	1.34	0.10	1.19	12.62	1.25
H002-6CS-5b, 8-35cm (replicate)	805.68	805.68	0.11	1.36	0.10	1.20	12.72	1.33
H002-8CS-3b, 56-80cm	811.31	811.31	0.09	3.55	0.29	1.07	13.86	20.66
H002-9CS-1b, 79-90cm	813.39	813.30	0.09	3.00	0.08	0.85	11.01	17.91
H002-12CS-1e, 106-131cm	822.80	822.67	0.09	2.59	0.07	0.99	12.83	13.33
H002-13CS-1b, 48-57cm	825.27	825.21	0.07	2.71	0.48	1.02	16.99	14.08
H002-14CS-1b, 15-40cm	844.75	844.73	0.10	1.50	0.13	1.23	14.34	2.25
H002-15CS-1e, 46-67cm	858.78	858.78	0.11	1.79	0.09	1.16	12.30	5.25

Table T26: Sediment geochemistry results. Measured depth in meters below the seafloor (mbsf). TN = Total Nitrogen. TC = Total Carbon, TS = Total Sulfur. TOC = Total Organic Carbon. Dataset: <https://doi.org/10.5281/zenodo.14146049>.

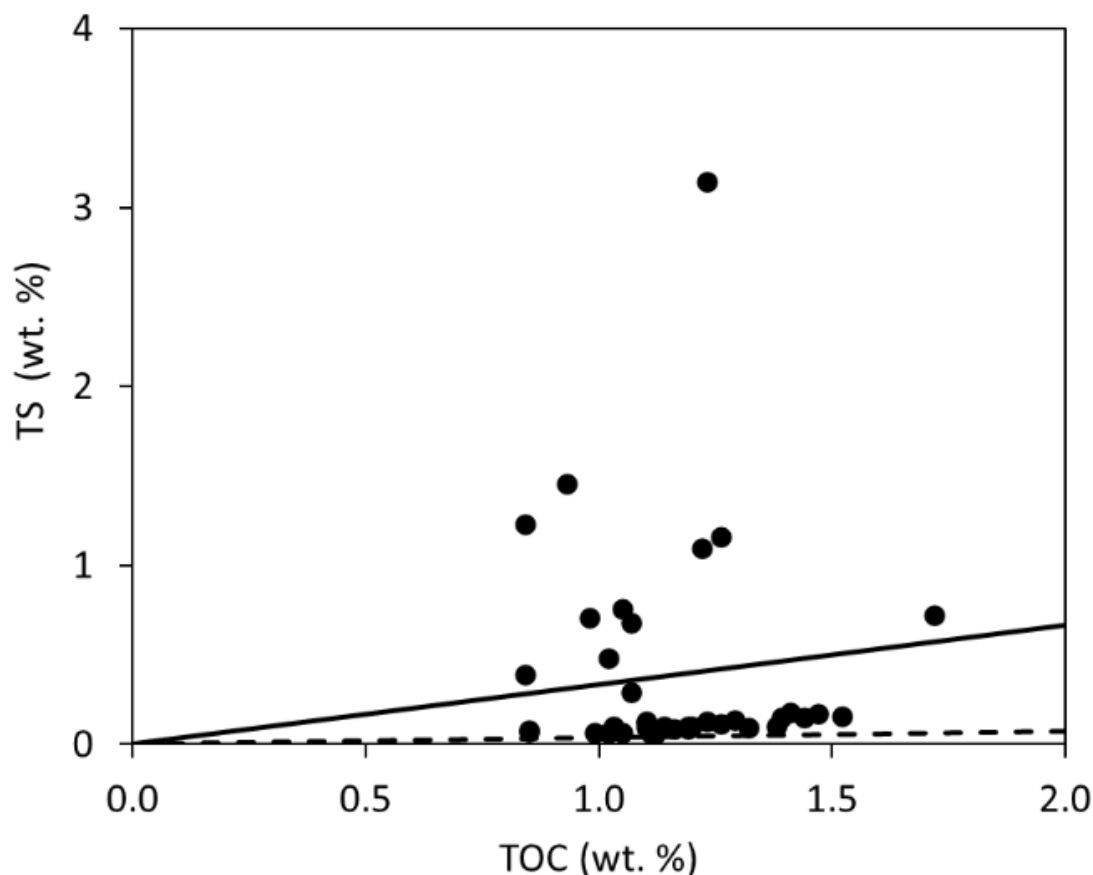


Figure F77: Initial Total Sulfur (TS) vs Total Organic Carbon (TOC) cross-plot using compressed measured depths (WR313 H003). The solid black line expresses the typical marine sediment ratio expected to be produced by organoclastic sulfate reduction (OSR) (Berner and Raiswell, [1983](#)). The dashed black line is the phytoplankton end member TS/TOC relationship of Suits and Arthur ([2000](#)). Dataset: <https://doi.org/10.5281/zenodo.14146049>.

Appendices

The following appendices contain data from Site H activities and are available in the same repository as the main report—whether that’s [OSTI](#), [Zenodo](#), or the [UT-GOM2-2 website](#).

Appendix A: UT-GOM2-02 Post-Drill Operation Report and Daily Log

Appendix B: Daily Science Reports

Appendix C: Pressure Coring Deployments

Appendix D: Lithostratigraphy Core Summaries

Appendix E: Pressure Core Logs

Appendix F: Conventional Core Logs

Appendix G: Undrained Strength

Appendix H: Index Properties

Appendix I: Quantitative Degassing

References

ASTM International, 2017, ASTM D2487-17e1: Standard Practice for Classification of Soils for Engineering Purposes (Unified Soil Classification System): Annual Book of ASTM Standards, <https://doi.org/10.1520/D2487-17E01>.

Berner, R. A., and Raiswell, R., 1983, Burial of organic carbon and pyrite sulfur in sediments over phanerozoic time: a new theory: *Geochimica et Cosmochimica Acta*, v. 47, no. 5, p. 855-862, [https://doi.org/10.1016/0016-7037\(83\)90151-5](https://doi.org/10.1016/0016-7037(83)90151-5).

Borowski, W. S., Rodriguez, N. M., Paull, C. K., and Ussler, W., 2013, Are 34S-enriched authigenic sulfide minerals a proxy for elevated methane flux and gas hydrates in the geologic record?: *Marine and Petroleum Geology*, v. 43, p. 381-395, <https://doi.org/10.1016/j.marpetgeo.2012.12.009>.

Boswell, R., Collett, T. S., Frye, M., Shedd, W., McConnell, D. R., and Sheldner, D., 2012a, Subsurface gas hydrates in the northern Gulf of Mexico: *Marine and Petroleum Geology*, v. 34, no. 1, p. 4-30, <https://doi.org/10.1016/j.marpetgeo.2011.10.003>.

Boswell, R., Frye, M., Sheldner, D., Shedd, W., McConnell, D. R., and Cook, A., 2012b, Architecture of gas-hydrate-bearing sands from Walker Ridge 313, Green Canyon 955, and Alaminos Canyon 21: Northern deepwater Gulf of Mexico: *Marine and Petroleum Geology*, v. 34, no. 1, p. 134-149, <https://doi.org/10.1016/j.marpetgeo.2011.08.010>.

BSEE, 2024, BSEE Data Center, <https://www.data.bsee.gov/>.

Collett, T. S., Boswell, R., Frye, M., Shedd, W., Godfriaux, P., Dufrene, R., McConnell, D., Mrozewski, S., Guerin, G., Cook, A., Jones, E., and Roy, R., 2009, Gulf of Mexico Gas Hydrate Joint Industry Project Leg II: Operational Summary: Proceedings of the Drilling and Scientific Results of the 2009 Gulf of Mexico Gas Hydrate Joint Industry Project Leg II, p. 27, <https://netl.doe.gov/sites/default/files/netl-file/OpSum%5B1%5D.pdf>.

Collett, T. S., Lee, M. W., Zyrianova, M. V., Mrozewski, S. A., Guerin, G., Cook, A. E., and Goldberg, D. S., 2012, Gulf of Mexico Gas Hydrate Joint Industry Project Leg II logging-while-drilling data acquisition and analysis: *Marine and Petroleum Geology*, v. 34, no. 1, p. 41-61, <https://doi.org/10.1016/j.marpetgeo.2011.08.003>.

Constans, R. E., and Parker, M. E., 1986, Calcareous nanofossil biostratigraphy and paleoclimatic indices for the late Quaternary, Deep Sea Drilling Project, Leg 96, Gulf of Mexico, Initial Reports of the Deep Sea Drilling Project, 96, p. 601-630, <https://doi.org/10.2973/dsdp.proc.96.132.1986>.

Davis, E. E., Hyndman, R. D., and Villinger, H., 1990, Rates of fluid expulsion across the Northern Cascadia Accretionary Prism: Constraints from new heat flow and multichannel seismic reflection data: *Journal of Geophysical Research*, v. 95, no. B6, <https://doi.org/10.1029/JB095iB06p08869>.

Di Stefano, C., Ferro, V., and Mirabile, S., 2010, Comparison between grain-size analyses using laser diffraction and sedimentation methods: *Biosystems Engineering*, v. 106, no. 2, p. 205-215, <https://doi.org/10.1016/j.biosystemseng.2010.03.013>.

Ferro, V., and Mirabile, S., 2009, Comparing Particle Size Distribution Analysis by Sedimentation and Laser Diffraction Method: *Journal of Agricultural Engineering*, v. 40, no. 2, <https://doi.org/10.4081/jae.2009.2.35>.

Flemings, P. B., 2020, Phase 3 Report (Period ending 9/30/2019), Deepwater Methane Hydrate Characterization and Scientific Assessment, DOE Award No.: DE-FE0023919, <https://www.osti.gov/servlets/purl/1615748>.

Flemings, P. B., Pettigrew, T., Houghton, J., Phillips, S. C., Price, A., Murphy, Z., Fang, Y., and Santra, M., 2020, GOM2 Pressure Coring Tool with Ball Valve (PCTB) Land Test II Report, https://ig.utexas.edu/wp-content/uploads/2020/08/PCTB_Land_Test_II_Report_wAppendices.pdf.

Flemings, P. B., Cook, A. E., Houghton, J., Morrison, J., Portnov, A., Pettigrew, T., Phillips, S. C., Polito,

P., Santra, M., and Thomas, C., 2023, UT-GOM2-2 Operations Plan, https://ig.utexas.edu/wp-content/uploads/2023/06/OperationsPlan_Rev2.3.pdf.

Flemings, P. B., Thomas, C., Phillips, S. C., Collett, T. S., Cook, A. E., Solomon, E., Colwell, F. S., Johnson, J. E., Awwiller, D., Aylward, I., Bhandari, A. R., Brooks, D., Buser-Young, J. Z., Cardona, A., Casso, M., Coyte, R., Darrah, T., Davis, M., Dugan, B., Duncan, D., Germaine, J. T., Holland, M., Houghton, J., Martin, S., Mills, N. T., Mimitz, M., Minarich, D., Morono, Y., Murphy, Z., O'Connell, J., Petrou, E., Pettigrew, T., Pohlman, J. W., Portnov, A., Phillips, M. P., Redd, T., Sawyer, D. E., Schultheiss, P., Shannon, K., Sullivan, C., Small, C., Tozier, K., Tsang, M.-Y., Maal, C. V. D., Waite, W. F., and Walton, T., 2025a, Expedition UT-GOM2-2 Summary, in Flemings, P. B., ed., Proceedings of the Deepwater Hydrate Coring Expedition UT-GOM2-2: The University of Texas at Austin, University of Texas Institute for Geophysics, <https://doi.org/10.5281/zenodo.13971076>.

Flemings, P. B., Thomas, C., Phillips, S. C., Collett, T. S., Cook, A. E., Solomon, E., Colwell, F. S., Johnson, J. E., Awwiller, D., Aylward, I., Bhandari, A. R., Brooks, D., Buser-Young, J. Z., Cardona, A., Casso, M., Coyte, R., Darrah, T., Davis, M., Dugan, B., Duncan, D., Germaine, J. T., Holland, M., Houghton, J., Martin, S., Mills, N. T., Mimitz, M., Minarich, D., Morono, Y., Murphy, Z., O'Connell, J., Petrou, E., Pettigrew, T., Pohlman, J. W., Portnov, A., Phillips, M. P., Redd, T., Sawyer, D. E., Schultheiss, P., Shannon, K., Sullivan, C., Small, C., Tozier, K., Tsang, M.-Y., Maal, C. V. D., Waite, W. F., and Walton, T., 2025b, Expedition UT-GOM2-2 Methods, in Flemings, P. B., ed., Proceedings of the Deepwater Hydrate Coring Expedition UT-GOM2-2: The University of Texas at Austin, University of Texas Institute for Geophysics, <https://doi.org/10.5281/zenodo.13971228>.

Frye, M., Shedd, W., and Boswell, R., 2012, Gas hydrate resource potential in the Terrebonne Basin, Northern Gulf of Mexico: Marine and Petroleum Geology, v. 34, no. 1, p. 150-168, <https://doi.org/10.1016/j.marpetgeo.2011.08.001>.

Gradstein, F. M., Ogg, J. G., Schmitz, M. D., and Ogg, G. M., 2012, Geologic Time Scale 2012 -- 2 volume book, <https://www.sciencedirect.com/book/9780444594259/the-geologic-time-scale>.

Hutchinson, D. R., Sheldner, D., Dai, J., McConnell, D., Shedd, W., Frye, M., Ruppel, C., Boswell, R., Jones, E., Collett, T., Rose, K., Dugan, B., Wood, W., and Latham, T., Site Selection for DOE/JIP Gas Hydrate Drilling in the Northern Gulf of Mexico, in Proceedings 6th International Conference on Gas Hydrates (ICGH 2008), Vancouver, British Columbia, Canada, July 6-10, https://netl.doe.gov/sites/default/files/2018-12/ICGH_5506_1_41330_0.pdf.

Jacobsen, C. S., Nielsen, T. K., Vester, J. K., Stougaard, P., Nielsen, J. L., Voriskova, J., Winding, A., Baldrian, P., Liu, B., Frostegard, A., Pedersen, D., Tveit, A. T., Svenning, M. M., Tebbe, C. C., Ovreas, L., Jakobsen, P. B., Blazewicz, S. J., Hubalek, V., Bertilsson, S., Hansen, L. H., Cary, S. C., Holben, W. E., Ekelund, F., and Baelum, J., 2018, Inter-laboratory testing of the effect of DNA blocking reagent G2 on DNA extraction from low-biomass clay samples: Sci Rep, v. 8, no. 1, p. 5711, <https://doi.org/10.1038/s41598-018-24082-y>.

Johnson, J. E., Phillips, S. C., Clyde, W. C., Giosan, L., and Torres, M. E., 2021, Isolating Detrital and Diagenetic Signals in Magnetic Susceptibility Records From Methane-Bearing Marine Sediments: Geochemistry, Geophysics, Geosystems, v. 22, no. 9, <https://doi.org/10.1029/2021gc009867>.

Kaneko, M., Shingai, H., Pohlman, J. W., and Naraoka, H., 2010, Chemical and isotopic signature of bulk organic matter and hydrocarbon biomarkers within mid-slope accretionary sediments of the northern Cascadia margin gas hydrate system: Marine Geology, v. 275, no. 1-4, p. 166-177, <https://doi.org/10.1016/j.margeo.2010.05.010>.

Larrasoana, J. C., Roberts, A. P., Musgrave, R. J., Gràcia, E., Piñero, E., Vega, M., and Martínez-Ruiz, F., 2007, Diagenetic formation of greigite and pyrrhotite in gas hydrate marine sedimentary systems: Earth and Planetary Science Letters, v. 261, no. 3-4, p. 350-366, <https://doi.org/10.1016/j.epsl.2007.06.032>.

Peketi, A., Joshi, R. K., Patil, D., Rao, P., and Dayal, A., 2012, Tracing the Paleo sulfate-methane transition zones and H₂S seepage events in marine sediments: An application of C-S-Mo systematics: *Geochemistry, Geophysics, Geosystems*, v. 13, <https://doi.org/10.1029/2012GC004288>.

Phillips, S. C., and Littler, K., 2022, Comparison of sediment composition by smear slides to quantitative shipboard data: a case study on the utility of smear slide percent estimates, *IODP Expedition 353, northern Indian Ocean: Scientific Drilling*, v. 30, p. 59-74, <https://doi.org/10.5194/sd-30-59-2022>.

Portnov, A., Flemings, P. B., You, K., Meazell, K., Hudec, M. R., and Dunlap, D. B., 2023, Low temperature and high pressure dramatically thicken the gas hydrate stability zone in rapidly formed sedimentary basins: *Marine and Petroleum Geology*, v. 158, p. 106550, <https://doi.org/10.1016/j.marpetgeo.2023.106550>.

Price, A., Flemings, P., Thomas, C., Cardona, A., Murphy, Z., Garcia, A., Savage, A., Houghton, J., and Pettigrew, T., 2021, GOM2 Pressure Coring Tool with Ball Valve (PCTB Land Test III Report, https://ig.utexas.edu/wp-content/uploads/2021/07/PCTB_Land_Test_III_UT_06.17.21-shrunk.pdf).

Riedinger, N., Pfeifer, K., Kasten, S., Garman, J. F. L., Vogt, C., and Hensen, C., 2005, Diagenetic Alteration of Magnetic Signals by Anaerobic Oxidation of Methane Related to a Change in Sedimentation Rate: *Geochimica et Cosmochimica Acta*, v. 69, no. 16, p. 4117-4126, <https://doi.org/10.1016/j.gca.2005.02.004>.

Sato, H., Hayashi, K.-i., Ogawa, Y., and Kawamura, K., 2012, Geochemistry of deep sea sediments at cold seep sites in the Nankai Trough: Insights into the effect of anaerobic oxidation of methane: *Marine Geology*, v. 323-325, p. 47-55, <https://doi.org/10.1016/j.margeo.2012.07.013>.

Shedd, W., Frye, M., Godfriaux, P., Dufrene, R., McConnell, D., Boswell, R., Collett, T., Mrozewski, S., Guerin, G., Cook, A., Shelandar, D., and Dai, J., 2010, Gulf of Mexico Gas Hydrates Joint Industry Project Leg II: Results from the Walker Ridge 313

Site, Offshore Technology Conference, <https://doi.org/10.4043/20806-MS>.

Shepard, F. P., 1954, Nomenclature based on sand-silt-clay ratios: *Journal of Sedimentary Petrology*, v. Vol. 24, p. 151-158, <https://doi.org/10.1306/D4269774-2B26-11D7-8648000102C1865D>.

Simpson, A. C., Tighe, S., Wong, S., Leo, P., Parker, C., Chander, A. M., Williams, M., Wu, H. W., Venkateswaran, K., and Singh, N. K., 2023, Analysis of Microbiomes from Ultra-Low Biomass Surfaces Using Novel Surface Sampling and Nanopore Sequencing: *J Biomol Tech*, v. 34, no. 3, <https://doi.org/10.7171/3fc1f5fe.bac4a5b3>.

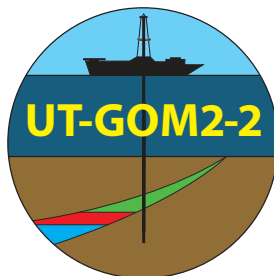
Sloan, E. D., and Koh, C. A., 2008, *Clathrate Hydrates of Natural Gases*, Boca Raton, FL, CRC Press, <https://doi.org/10.1201/9781420008494>.

Suits, N. S., and Arthur, M. A., 2000, Sulfur diagenesis and partitioning in Holocene Peru shelf and upper slope sediments: *Chemical Geology*, v. 163, no. 1, p. 219-234, [https://doi.org/10.1016/S0009-2541\(99\)00114-X](https://doi.org/10.1016/S0009-2541(99)00114-X).

Thomas, C., Phillips, S. C., Flemings, P. B., Santra, M., Hammon, H., Collett, T. S., Cook, A. E., Pettigrew, T., Mimitz, M., Holland, M., and Schultheiss, P., 2020, Pressure coring operations during The University of Texas-Gulf of Mexico 2-1 (UT-GOM2-1) Hydrate Pressure Coring Expedition in Green Canyon Block 955, northern Gulf of Mexico: *AAPG Bulletin*, v. 104, no. 9, p. 1877-1901, <https://doi.org/10.1306/02262019036>.

Waterman, A. S., Weber, R. D., Lu, Y., Smith, V. E., George, R. A., Reilly, T. M., Roederer, R. V., Edmunds, J. A., Parker, B. W., Myers, N. R., and Avery, A. J., 2017, *Biostratigraphic Chart - Gulf Basin, USA, Quaternary and Neogene*: Paleo-Data, Inc., <https://www.paleodata.com/chart/>.

Wen, B., Aydin, A., and Duzgoren-Aydin, N. S., 2002, A comparative study of particle size analyses by sieve-hydrometer and laser diffraction methods: *Geotechnical Testing Journal*, v. 25, no. 4, <https://doi.org/10.1520/GTJ11289J>.



Expedition UT-GOM2-2 Site H

Proceedings of the UT-GOM2-2 Deepwater Hydrate Coring Expedition

Terrebonne Basin (Walker Ridge Block 313)

WR313 H002 (API 608124014800) and WR313 H003 (API 608124014900)

July 30–September 28, 2023 | Expedition UT-GOM2-2 Scientists

University of Texas Institute for Geophysics | 2025

<https://doi.org/10.5281/zenodo.13971276>